

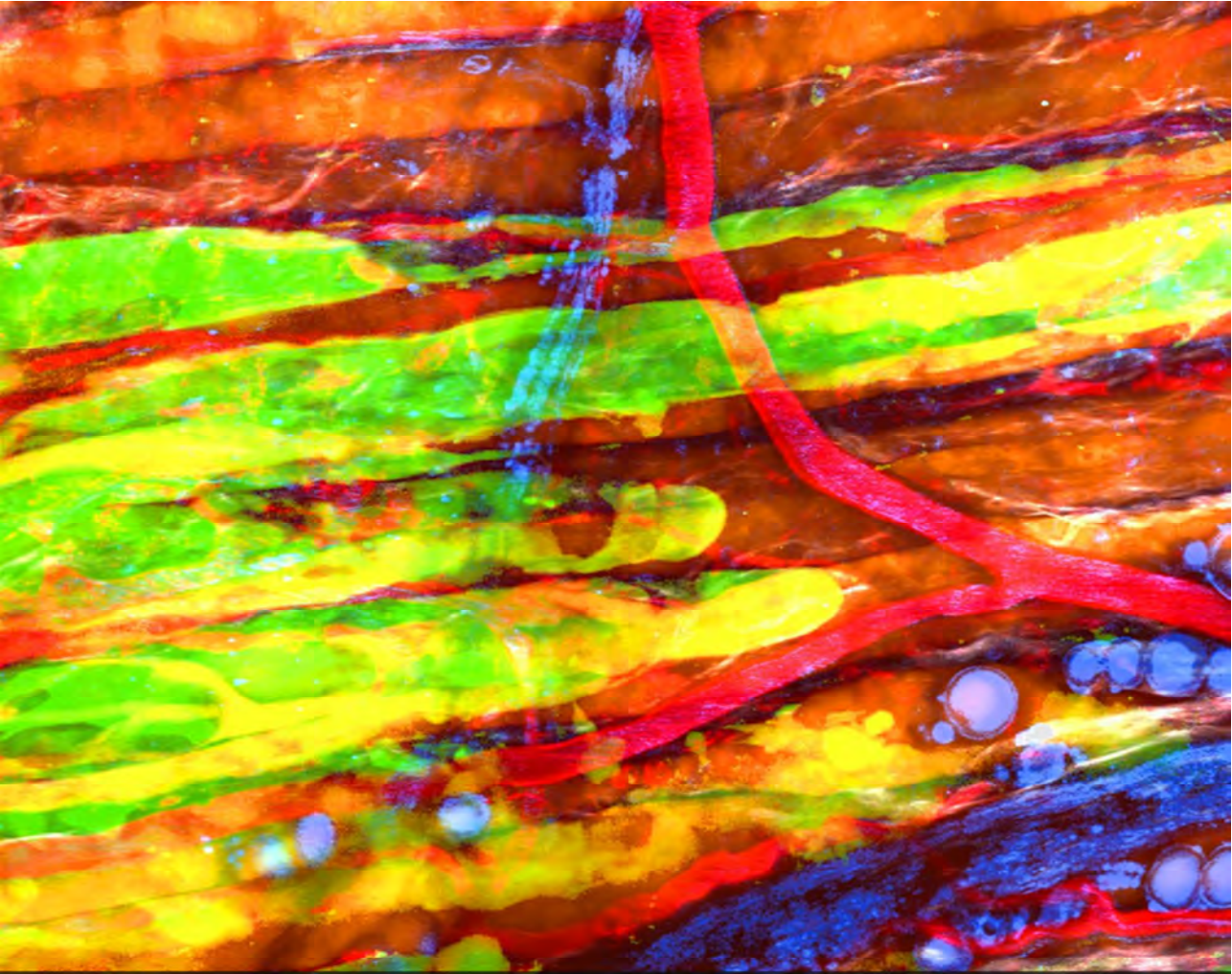
PDF hosted at the Radboud Repository of the Radboud University Nijmegen

The following full text is a publisher's version.

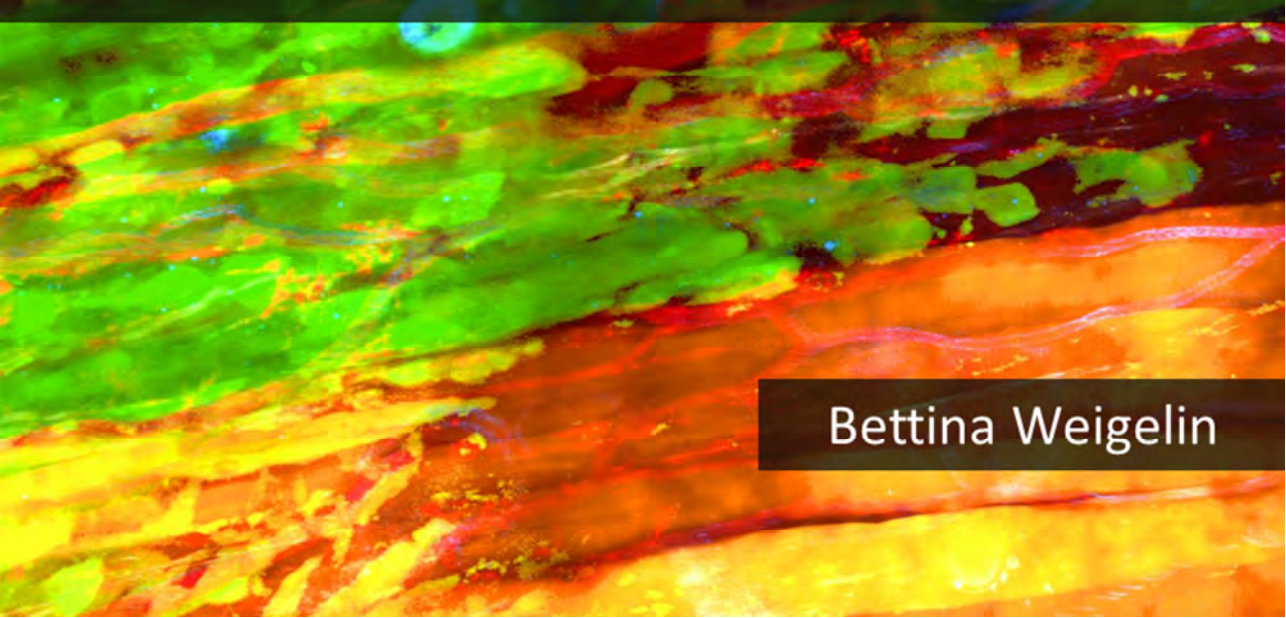
For additional information about this publication click this link.

<http://hdl.handle.net/2066/145309>

Please be advised that this information was generated on 2017-12-05 and may be subject to change.



Cytotoxic T Cell Function in Solid Tumors:
Principles and Implications for Immunotherapy



Bettina Weigelin

**Cytotoxic T Cell Function in Solid Tumors:
Principles and Implications for Immunotherapy**

Bettina Weigelin

The research described in this thesis was performed at the Department of Cell Biology, RIMLS, Radboud University Medical Center Nijmegen, The Netherlands and the Rudolf Virchow Center for Experimental Biomedicine and the Department of Dermatology, University of Würzburg, Germany.

The work was supported by the Dutch Cancer Foundation (KWF 2008-4031), FP7 of the European Union (ENCITE HEALTH TH-15-2008-208142), Netherlands Science Organization (NWO-VICI 918.11.626) and DFG (FR1155/7-3).

Cover design and layout: Bettina Weigelin

Cover image: The image shows a mouse melanoma (green) growing in the mouse dermis. Melanoma cells collectively invade the tissue in between and along nerve fibers and fat cells (blue), collagen fibers (grey), striated muscles (orange) and blood vessels (red).

Copyright © by Bettina Weigelin, 2015.

Printed by: Gildeprint Drukkerijen www.gildeprint.nl

**Cytotoxic T Cell Function in Solid Tumors:
Principles and Implications for Immunotherapy**

PROEFSCHRIFT

ter verkrijging van de graad van doctor
aan de Radboud Universiteit Nijmegen
op gezag van de rector magnificus prof. dr. Th.L.M. Engelen,
volgens besluit van het college van decanen
in het openbaar te verdedigen op dinsdag 24 november 2015
om 14.30 uur precies

door

Bettina Weigelin
geboren op 20 maart 1982
te Bernburg, Duitsland

Promotor

Prof. dr. P. Friedl

Copromotor

Dr. M. M. Zegers

Manuscriptcommissie

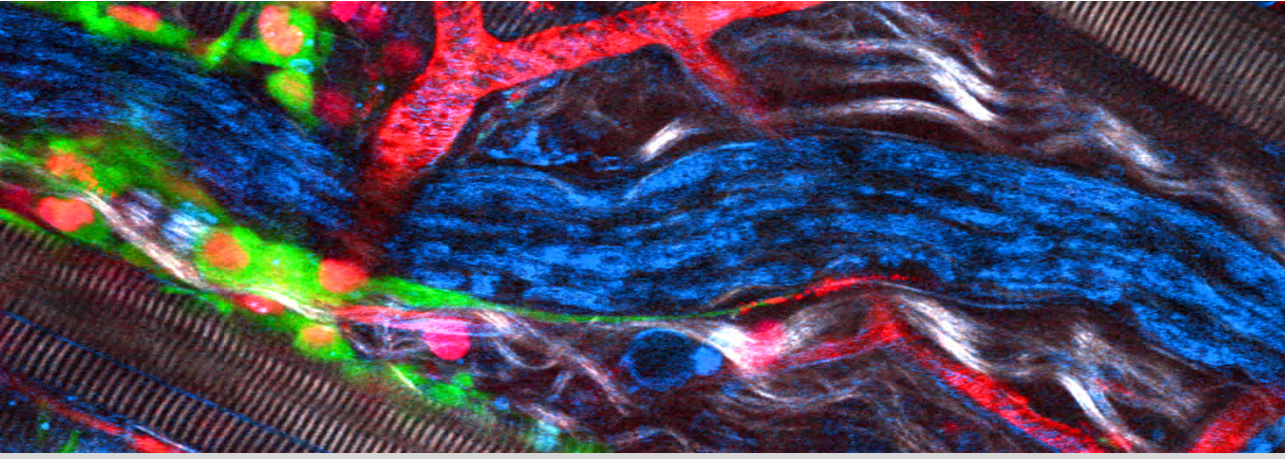
Prof. dr. G. J. Adema

Prof. dr. H. Dolstra

Prof. dr. T. N. Schumacher (LUMC)

Table of Contents

Chapter 1	7
Introduction and Outline of the Thesis	
Chapter 2	15
Interstitial Leukocyte Migration and Immune Function	
Chapter 3	43
Intravital Third Harmonic Generation Microscopy of Collective Melanoma Cell Invasion: Principles of Interface Guidance and Microvesicle Dynamics	
Chapter 4	73
A Three-Dimensional Organotypic Assay to Measure Target Cell Killing by Cytotoxic T Lymphocytes	
Chapter 5	87
Cytotoxic T Lymphocyte Migration and Effector Function in the Tumor Microenvironment	
Chapter 6	95
Cytotoxic T Cell Cooperation is Required for Serial Killing of Cancer Cells	
Chapter 7	127
Focusing and Sustaining the anti-Tumor CTL Response by Agonist α CD137 mAb	
Chapter 8	159
Discussion and Implications	
Summary	174
Nederlandse Samenvatting	176
Acknowledgements	180
Curriculum Vitae	185
List of Publications	186



CHAPTER 1

Introduction and Outline of the Thesis

Cytotoxic T lymphocytes for immunotherapy of cancer

Immunotherapy is a promising therapeutic strategy for a range of cancer types with the potential to raise a specific, adaptive and long-lasting anti-cancer protection¹. The main effector cells of a successful antitumor immune response are cytotoxic T lymphocytes (CTL), which kill cancer cells in a cell-contact and antigen-specific manner². Besides activation and expansion of tumor-specific CTL, successful tumor elimination requires an efficient CTL effector phase in the tumor lesion³. Induction of target cell apoptosis thereby relies on a sequence of multiple events, including migration towards and scanning the surface of target cells, antigen recognition and formation of an immunological synapse, and execution of effector function followed by detachment and resumed migration². Consequently, interference at any step will ultimately compromise killing efficiency. In this thesis, *in vitro* and *in vivo* models for extended imaging of CTL-target cell interactions and outcome are developed, which facilitate monitoring of the full sequence of CTL effector function to deliver novel insight into rate limiting steps and interference mechanisms imposed by the immunosuppressive tumor microenvironment⁴. The acquired knowledge on the mechanisms of local immune response success or failure will contribute to the rational design of new therapy approaches to reactivate antitumor immunity for potent, long-lasting responses.

Interstitial migration is an integral part of CTL function

Chapter 2 summarizes molecular and biophysical mechanisms of immune cell migration and guidance. Interstitial migration represents an integral part of CTL effector function, by facilitating the search for target cells and the scanning of receptors expressed at the cell surfaces encountered. Consequently, the tumor may escape immune control by counteracting the migration of infiltrating CTL. This may comprise exclusion from entering the tissue, stop signals that arrest CTL motility, barriers created by extracellular matrix structures or signals that misroute CTL to some tumor regions while sparing others, thereby creating tumor survival niches. Thus, besides “immunological” mechanisms such as TCR-mediated recognition and signaling, effector function in tumors critically depends on coordinated CTL positioning and migration within the tumor tissue.

Multimodal intravital multiphoton microscopy to observe cellular dynamics within living tissues

The three-dimensional tissue topography of the tumor microenvironment can act as barrier⁵ or provide guidance⁶ for immune cell infiltration of solid tumors as well as for

tumor cells invading healthy tissue⁷. While *in vitro* models fail to mimic the complex matrix architecture of tumor environments, immunohistological analyses of intact tissues depict tissue complexity but are restricted to fixed samples, lacking the possibility to observe the dynamic nature of immune cells including cell migration as well as cellular interactions and outcome. To integrate the time- and space-dependent complexity, monitoring immunotherapy of solid tumors with intravital multiphoton microscopy (IV MPM) in living animals enables direct observation of CTL effector function in the context of the reactive host stroma. When applied longitudinally over days or weeks, IV MPM reveals long-term dynamics and turn-over of tumor progression, infiltrating immune cells and therapy response⁸.

In **Chapter 3** multimodal intravital MPM was established which includes infrared-excited two-photon fluorescence and second harmonic generation and, as novel modality in cancer research, third harmonic generation (THG) microscopy for label-free visualization of the structural microenvironment of melanoma growing in the mouse dermis. Destructive tissue invasion and distant metastasis formation are the main cause of fatal outcome in cancer disease and consequently, of particular importance to control cancer progression. Although studied extensively, the mechanisms driving initiation, mode and sustained progression of cancer cell dissemination from the primary tumor are not yet fully understood. By mapping melanoma cell invasion in relation to tissue organization, we identified that tumor cells preferentially navigate through connective tissue by taking routes of least resistance, including preexisting tissue tracks and open spaces along blood vessels, myofibers, nerves, between adipocytes and collagen bundles, without immediate anatomic tissue remodeling or destruction.

An organotypic assay to integrate CTL dynamics in the effector phase

To simulate the connective tissue environment in an *in vitro* assay we established a 3D collagen-based real-time imaging model of CTL function that allows the observation of active migration, interaction, dissociation and serial killing of single target cells over extended time periods (**Chapter 4**). CTL mediated cytotoxicity is commonly studied in 2D liquid cocultures of CTL and cancer cells^{9,10}, which promote passive aggregation and likely result in an overestimation of CTL killing efficacy. In contrast, *in vivo*, immune cells face structurally heterogeneous tissue architectures and complex interactions with diverse factors and cell types of the tumor microenvironment^{5,11-13}. This discrepancy likely explains the poor correlation of *in vitro* measured CTL killing capacities and their anti-tumor efficacy after adoptive transfer into patients⁴. The here established novel migration-based assay promotes the natural dynamic CTL behavior and thus provides improved physiologically relevant information on CTL killing kinetics.

Cytotoxic T cell cooperation is required for serial killing of cancer cells

In **Chapter 5** the mechanisms of CTL effector function are reviewed and fluorescent histone-2B labeling is established as readout for CTL-mediated apoptosis induction in tumor cells. While the molecular mechanisms of CTL effector response are well defined^{14,15}, the parameters determining CTL success or failure in established tumors remain less clear. In **Chapter 6** we used dynamic imaging of organotypic 3D assays of tumor cells confronted with migratory CTL and intravital multiphoton microscopy to identify a cooperation mechanism dependent on sequential CTL-tumor cell interactions and the accumulation of sub-lethal hits to overcome melanoma cell resistance to CTL-mediated apoptosis. Consistently, in orthotopic melanoma *in vivo*, tumor regions with high CTL density supported additive cytotoxicity and correlated with high local apoptosis rates. Highest CTL densities and apoptosis induction occurred at the invasive tumor front, where invading tumor cells and CTL both move and accumulate along the same anatomic trails of least resistance, suggesting invading tumor cells as target for immunotherapy. Thus, kinetic imaging shows CTL efficiency as function of the cumulative dwell time per target cell, which is dependent on local CTL density and coordinated CTL migration into and along niches of tumor-cell residence, both controlled by the topographic organization of the tumor microenvironment.

Agonist α -CD137 monoclonal antibodies focus and sustain anti-tumor CTL response

The amplitude and quality of CTL effector reaction towards target cells are controlled by stimulatory and inhibitory signals (“immune checkpoints”)¹⁶. Under physiological conditions, immune checkpoints are crucial to maintain an appropriate balance between self-tolerance to prevent tissue damage by autoimmunity and specific activation to eliminate malignant cells. Tumors co-opt inhibitory mechanisms of self-tolerance to escape immune control¹⁷. To activate anti-cancer immunity, immunomodulatory monoclonal antibodies (mAbs) are used to antagonize immune-repressor molecules¹⁸ or stimulate immune-activating receptors¹⁹. CD137 (4-1BB) is a TNFR family costimulatory receptor expressed by activated T cells and other immune cells and CD137 ligation by agonist mAbs promotes immune cell proliferation, survival, memory formation and enhanced effector function²⁰. Significant therapeutic effects of α -CD137 mAb against transplanted tumor models have provided a rationale for ongoing clinical trials; however, underlying mechanisms and which immune cells mediate the effect remain unclear. In **Chapter 7** we show a synergy of adoptive CTL transfer and α -CD137 mAb against mouse melanoma. Intravital microscopy provides direct evidence that α -CD137 mAb therapy

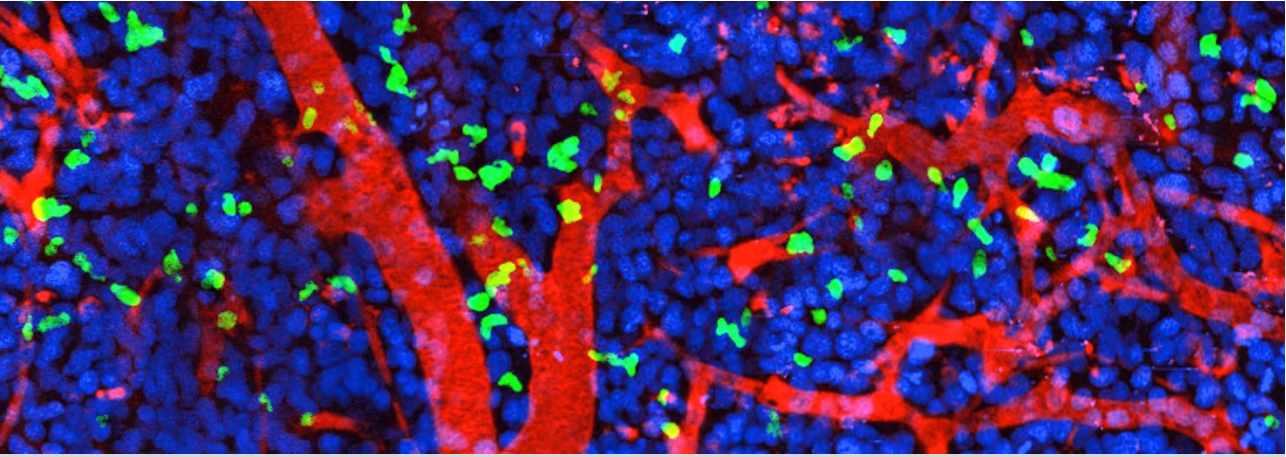
prolongs CTL contacts with target cells and sustains the efficacy of adoptively transferred CTL over extended time periods.

Chapter 8 summarizes findings and emerging concepts of this thesis and discusses their implications for understanding cancer invasion and improving cancer immunotherapy.

References:

1. Lizée, G. *et al.* Harnessing the Power of the Immune System to Target Cancer. *Annu. Rev. Med.* **64**, 71–90 (2013).
2. Weigelin, B., Krause, M. & Friedl, P. Cytotoxic T lymphocyte migration and effector function in the tumor microenvironment. *Immunol. Lett.* **138**, 19–21 (2011).
3. Quezada, S. a *et al.* Limited tumor infiltration by activated T effector cells restricts the therapeutic activity of regulatory T cell depletion against established melanoma. *J. Exp. Med.* **205**, 2125–38 (2008).
4. Gattinoni, L., Powell, D. J., Rosenberg, S. A. & Restifo, N. P. Adoptive immunotherapy for cancer: building on success. *Nat. Rev. Immunol.* **6**, 383–93 (2006).
5. Salmon, H. *et al.* Matrix architecture defines the preferential localization and migration of T cells into the stroma of human lung tumors. *J. Clin. Invest.* **122**, 899–910 (2012).
6. Boissonnas, A., Fetler, L., Zeelenberg, I. S., Hugues, S. & Amigorena, S. In vivo imaging of cytotoxic T cell infiltration and elimination of a solid tumor. *J. Exp. Med.* **204**, 345–56 (2007).
7. Friedl, P. & Wolf, K. Plasticity of cell migration: a multiscale tuning model. *J. Cell Biol.* **188**, 11–9 (2010).
8. Alexander, S., Weigelin, B., Winkler, F. & Friedl, P. Preclinical intravital microscopy of the tumour-stroma interface: invasion, metastasis, and therapy response. *Curr. Opin. Cell Biol.* **25**, 659–71 (2013).
9. Brunner, K. T., Mael, J., Cerottini, J.-C. & Chapuis, B. Quantitative assay of the lytic action of immune lymphoid cells of 51Cr-labelled allogeneic target cells in vitro; inhibition by isoantibody and by drugs. *Immunology* **14**, 181–196 (1968).
10. Jedema, I., Van Der Werff, N. M., Barge, R. M. Y., Willemze, R. & Falkenburg, J. H. F. New CFSE-based assay to determine susceptibility to lysis by cytotoxic T cells of leukemic precursor cells within a heterogeneous target cell population. *Blood* **103**, 2677–2682 (2004).
11. Mrass, P. *et al.* Random migration precedes stable target cell interactions of tumor-infiltrating T cells. *J. Exp. Med.* **203**, 2749–61 (2006).
12. Marangoni, F. *et al.* The Transcription Factor NFAT Exhibits Signal Memory during Serial T Cell Interactions with Antigen-Presenting Cells. *Immunity* **38**, 237–49 (2013).
13. Mempel, T. R. *et al.* Regulatory T cells reversibly suppress cytotoxic T cell function independent of effector differentiation. *Immunity* **25**, 129–41 (2006).
14. Barry, M. & Bleackley, R. C. Cytotoxic T lymphocytes: all roads lead to death. *Nat. Rev. Immunol.* **2**, 401–9 (2002).
15. Ritter, A. T. *et al.* Actin Depletion Initiates Events Leading to Granule Secretion at the Immunological Synapse. *Immunity* **42**, 864–876 (2015).
16. Pardoll, D. M. The blockade of immune checkpoints in cancer immunotherapy. *Nat. Rev. Cancer* **12**, 252–64 (2012).
17. Hanahan, D. & Weinberg, R. a. Hallmarks of cancer: the next generation. *Cell* **144**, 646–74 (2011).
18. Vasaturo, A. *et al.* Clinical Implications of Co-Inhibitory Molecule Expression in the Tumor Microenvironment for DC Vaccination: A Game of Stop and Go. *Front. Immunol.* **4**, 417 (2013).

19. Melero, I., Grimaldi, A. M., Perez-Gracia, J. L. & Ascierto, P. A. Clinical development of immunostimulatory monoclonal antibodies and opportunities for combination. *Clin. Cancer Res.* **19**, 997–1008 (2013).
20. Melero, I., Hirschhorn-Cymerman, D., Morales-Kastresana, A., Sanmamed, M. F. & Wolchok, J. D. Agonist antibodies to TNFR molecules that costimulate T and NK cells. *Clin. Cancer Res.* **19**, 1044–53 (2013).



CHAPTER 2

Interstitial Leukocyte Migration and Immune Function

Friedl P & Weigelin B

Nature Immunology 2008; 9:960–9.

Department of Cell Biology, Radboud University Nijmegen Medical Centre,
The Netherlands, and
Rudolf Virchow Center for Experimental Biomedicine and
Department of Dermatology, University of Würzburg, Germany

Abstract

The trafficking of leukocytes into and within lymphoid and peripheral tissues is central to immune cell development, immunosurveillance and effector function. Interstitial leukocyte trafficking is the result of amoeboid polarization and migration, guided by soluble or tissue-bound chemoattractant signals for positioning and local arrest. In contrast to other migration modes, amoeboid movement is particularly suited for scanning cellular networks and tissues. Here, we review mechanisms of leukocyte migration and sensing involved in diapedesis, tissue-based interstitial migration and egress, immune cell positioning in inflammation, and emerging therapeutic interference strategies.

An efficient immune reaction requires leukocytes to be at the right place at the right time. Nearly all steps, from maturation to activation and effector function, depend upon leukocyte migration and positioning in lymphoid and non-lymphoid tissues¹. Both innate and adaptive immune functions depend upon interstitial leukocyte migration²⁻⁵. After leaving the bone marrow by way of the blood, monocytes and granulocytes reach lymphoid or peripheral tissues, move toward their targets and execute effector functions. T lymphocytes emigrate from the thymus, become activated by a cascade of cell-cell interactions in secondary lymphoid organs and circulate to peripheral tissues for effector function. Similarly, B lymphocytes move within secondary lymphatic tissues to capture antigen, receive T cell help and recirculate and become resident in the bone marrow and other lymphoid organs as antibody-secreting plasma cells. Leukocyte entry into tissue through the vascular endothelium has been studied in detail (reviewed in refs.^{1,6}), whereas the mechanisms of leukocyte diapedesis into and navigation within and out of tissues are less clear. The density and position of leukocytes in tissues is a steady-state result of influx and migration, local activation, proliferation and death, and efflux (Supplementary Fig. 1 online), which together confers effector functions. Efficient pathogen elimination and resolution can be reached by either subthreshold non-inflamed immune surveillance⁷ or nondestructive short-term inflammation⁷. Persisting antigen, however, may lead to chronic inflammation, tissue remodeling and formation of de novo structures, such as tertiary lymphatic tissues or granulomas. In chronic inflammation, stepwise tissue destruction is followed by defective healing. Because of their role in mediating inflammatory reactions, interstitial migration and positioning of leukocytes represent therapeutic targets for either suppressing unwanted inflammation or boosting insufficient host responses⁸.

Mechanisms of amoeboid migration in leukocytes

Leukocytes use amoeboid cell migration mechanisms. Reminiscent of the amoeba *Dictyostelium discoideum*, polarized leukocytes develop a small leading edge consisting of short-lived pseudopods, followed by the cell body that contains the nucleus, and a posterior, near-cylindrical tail of 2 to 10 μm in length termed the uropod (Fig. 1a,b). Four steps mediate the amoeboid migration cycle: the leading edge protrudes one or several pseudopods by actin flow, protruding membrane and surface receptors interact with the substrate, actomyosin-mediated contraction of the cell body occurs in mid-region, and so the rear of the cell moves forward. These steps occur in a cyclic manner, generating forward movement. Amoeboid migration is very different from mesenchymal or collective migration modes employed by other cell types in three-dimensional models⁹. Amoeboid migration is used by leukocytes (and likely many stem cells), is fast (up to 30 $\mu\text{m}/\text{min}$), lacks strong adhesive interactions to the tissue and commonly preserves tissue integrity rather than degrading it¹⁰. Mesenchymal migration used by fibroblasts, smooth muscle cells and cancer cells is much slower (less than 1 $\mu\text{m}/\text{min}$), generates stronger adhesion sites and causes proteolytic extracellular matrix (ECM) remodeling¹¹. Collective cell migration is used by cells that retain their cell-cell junctions, remodel ECM, and move either as a two dimensional sheet, three-dimensional strand or compact cluster through tissue¹², as during branching morphogenesis, vascular sprouting and epithelial wound closure¹³. Compared to other migration types, amoeboid movement is special because it supports a uniquely fast capability to sense and integrate signaling input from the extracellular environment ('scanning')¹⁴. After polarization, the leading edge contains rapidly forming and rebuilding networks of filamentous actin that include abundant membrane ruffles indicative of dynamic probing of the environment. The leading edge is particularly sensitive to receptor engagement, including that by Fc receptors (FcRs), T cell antigen receptors (TCRs), chemokine receptors¹⁵ and β_2 integrins in intermediate or active state¹⁶, all of which serve to initiate contact with other cells, induce signal transduction¹⁷ and mediate phagocytosis after binding of bacteria and other particles¹⁸. If normalized to membrane area, the density of most surface and chemoattractant receptors on the leading edge is equal to that on other cell parts, at least at the light-microscopic level^{19,20}, but at ultrastructural resolution, other receptors, such as β_2 integrins in neutrophils, show discrete relocation toward the tips of ruffles²¹. The mid-region of amoeboid cells contains the nucleus and a relatively immobile cell region that maintains the front–rear axis. The trailing edge contains the highly glycosylated surface receptors CD43 and CD44, adhesion receptors including intercellular adhesion molecule (ICAM)-1, ICAM-3, β_1 integrins and ERM adaptor proteins, as well as GM-1-type

cholesterol-rich microdomains²². The uropod mediates cell–matrix and cell–cell interactions during migration and has a putative anchoring function¹⁰.

Polarization of cytoskeletal and signaling scaffolds

At the leading edge (Fig. 1c), pseudopod and lamellipod protrusion occurs either spontaneously or induced by migration-promoting factors binding to surface receptors. In leukocytes, polarization and migration to chemoattractant gradients, known as chemotaxis, are induced by various compound classes, including chemokines and cytokines, lipid mediators, bacterial factors and ECM degradation products including fragments of collagen, fibronectin and elastin^{23–25}. Many chemoattractants transmit signals through heterotrimeric G-protein-coupled receptors (GPCRs). In leukocytes, most GPCRs transmit through the α subunit of $G_{i\alpha}$, the subtype of G protein that can be inhibited by pertussis toxin. These GPCRs include the fMLP (N-formyl-Met-Leu-Phe) receptor and C5a receptor; chemokine receptors including CCR7, CXCR4, CXCR5 and CCR3; the leukotriene B4 receptor BLT1; sphingosine-1-phosphate receptors 1–4 (S1P1–4) and lysophosphatidic acid (LPA) receptors 1–3²⁶. All these GPCRs mediate promigratory signals but also enhance cell activation. A key GPCR-mediated pathway is signaling through class Ib phosphatidylinositol-3-kinase (PI(3)K), containing the p110 γ catalytic subunit). PI(3)K- γ is recruited to the inner leaflet of the plasma membrane by the G protein $\beta\gamma$ subunit, where it becomes activated, and then phosphorylates phosphatidylinositol phosphates (PIPs) and other effectors (reviewed in ref. 27). PIPs serve as docking sites for pleckstrin-homology domain-containing proteins, notably Akt (also known as protein kinase B), which is implicated in inducing actin polymerization and pseudopod protrusion by phosphorylating downstream effectors²⁸, such as the actin-binding protein girdin²⁹. A second pathway linked to PI(3)K activation is induced by ζ -chain-associated receptors, including TCRs and FcRs. These receptors signal through tyrosine kinases Lck and Zap-70 to class Ia PI(3)Ks (consisting of p110 δ) and activate downstream Akt, as well as the GTPases Rac and Cdc42³⁰. A third, PI(3)K-independent pathway induced by the fMLP receptor in neutrophils leads to the activation of p38 mitogen-associated protein kinase and downstream Rac activation⁷. Lastly, the Rac guanine nucleotide exchange factor DOCK-2 leads to Rac activation at the leading edge³¹. Ultimately, Rac induces actin polymerization through WAVE (Scar) and Arp2/3. WAVE, a member of the WASP family of actin-binding proteins, mediates actin filament formation³²; Arp2/3 causes sideward branching of actin filaments. Together, these activities generate interconnected, branched networks³³. Thus, promigratory signals received at the leading edge generate local Rac activation and actin network protrusion, pushing the plasma membrane outward. The mechanisms of preferential receptor

sensitivity at the leading edge are likely diverse and may include local signal amplification mechanisms³⁴ and the exclusion of counter-regulatory proteins.

The mid-region (Fig. 1d) generates actomyosin-based stiffness and contractility, limits lateral protrusions and thereby maintains a stable, bipolar cortex. The cytoskeletal motor protein myosin II located in the central and rear regions of leukocytes promotes actin filament contraction and limits lateral protrusions. Myosin II cross-links actin filaments in parallel, forming the contractile shell required to hold the extending cell together and propelling the cell nucleus, the most rigid part of the cell, forward³⁵. Inhibition of myosin II in neutrophils leads to ectopic lamellae on two-dimensional substrates³⁶ or the loss of rear-end retraction in three-dimensional tissues³⁷, resulting in impaired migration. Upstream of myosin II, by yet unclear mechanisms, PI(3)K- γ and possibly DOCK-2 suppress lateral protrusions³⁸; deletion of either protein enhances cell turning such that overall cell mobility is compromised³¹. The phosphatase PTEN also contributes to lateral stability by preventing ectopic protrusion formation⁷. PTEN is excluded from the leading edge but active in lateral and rear cell parts, where it dephosphorylates kinases, including PI(3)K and Akt, as well as phosphatidylinositol-(3,4,5)-tris-phosphate, and thereby counteracts protrusion formation^{7,39}. The uropod (Fig. 1e) extends rearward from the nucleus and contains the microtubule-organizing center and rearward-polarized microtubules, the Golgi, and abundant actin-binding ERM proteins. In association with microtubules, mitochondria localize to the rear of the cell, which, presumably owing to local ATP delivery to the region of ATP-dependent actomyosin contraction, is required for proper polarization, uropod retraction and migration⁴⁰. Amoeboid polarization thus generates a bipolar mechanosensory state with a dynamic leading edge to acquire new contacts and signals, a stiff mid-body, and a sticky uropod that is dragged along the substrate and stabilizes the cell position in complex environments^{10,41}.

Leukocyte migration in different environments

Leukocytes are able to migrate along or through most, if not all, tissues of the body. Both two-dimensional surfaces, such as inner vessel walls, the peritoneum and the pleura, and three-dimensional tissues, composed of mostly cellular (lymph node) or fibrillar ECM components, serve as 'substrates' for this migration (Fig. 2). As part of the amoeboid migration program, leukocytes use adhesion receptor-dependent mechanisms, known as haptokinesis, for migration across two-dimensional surfaces. Migration across two-dimensional ECM or an endothelial surface requires integrin-mediated attachment and polarized adhesion, notably through binding of integrins $\alpha 4\beta 1$ and LFA-1 to counterpart ligands VCAM-1 and ICAM-1 on the endothelial cell (Fig. 2a)⁶.

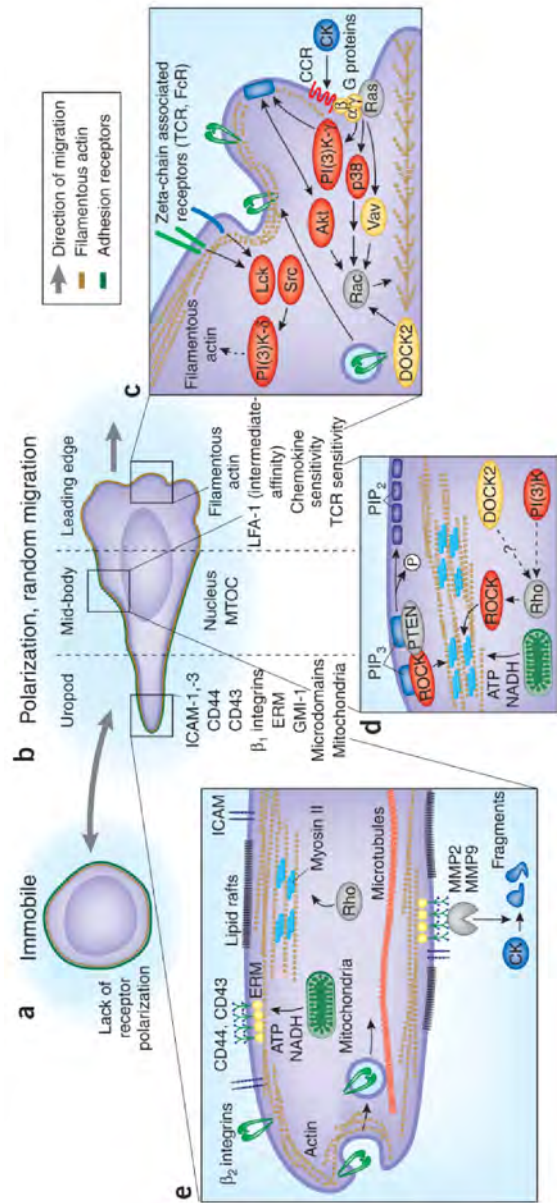


Figure 1. Morphology, surface receptors and signaling in amoeboid leukocyte migration. (a) Round morphology of immobile or freely floating leukocyte, including uniform distribution of surface receptors and cytoskeleton. (b) Amoeboid shape after polarization during random migration and chemotaxis. (c) Surface receptors, cytoskeletal structure and signaling events in the leading edge, lateral portion of the cell body and uropod. Class I PI(3)Ks are lipid kinases that phosphorylate phosphatidylinositol-(3,4)-bisphosphate (PIP2) to phosphatidylinositol-(3,4,5)-trisphosphate (PIP3). PIP3 is thought to form multimers at the inner leaflet of the plasma membrane that serve as docking and activation site for pleckstrin-homology (PH) domain-containing proteins, including Akt (protein kinase B). Other pathways directly and indirectly triggered by chemoattractant receptors are Ras and p38 and DOCK2. As central effector of these pathways, Rac mediates the formation of actin filaments that move the plasma membrane forward. Other surface receptors, including TCR and FcR, activate the tyrosine kinases Lck and Src and downstream PI(3)K- δ . (d) The mid-portion contains actomyosin filaments that are under the control of Rho and ROCK. (e) The uropod forms an adhesive and contractile rear that contains microtubules and mitochondria. CK, cytokine; ERM, adaptor proteins of the ezrin-radixin-moesin family; GM-1, monosialotetrahexosylganglioside; MTOC, microtubule-organizing center; Vav, Vav-family guanine-nucleotide exchange factor.

By contrast, in three-dimensional ECM environments, cells use weakly adhesive to nonadhesive interaction and traction mechanisms. Leukocyte migration within interstitial tissue *in vitro* and *in vivo* is integrin independent, being mediated instead by actin flow along the confining ECM scaffold structure, shape change, and squeezing (Fig. 2b)^{10,22,37}. In contrast to two-dimensional migration, the three-dimensional tissue network confines and mechanically anchors cells from all sides so they intercalate alongside and perpendicular to tissue structures^{10,37,42}; this differs from integrin-dependent mesenchymal and other migration modes⁹. How leukocytes distinguish substrate anatomy - that is, two-dimensional versus three-dimensional environments - and adjust their adhesion requirements is presently unknown.

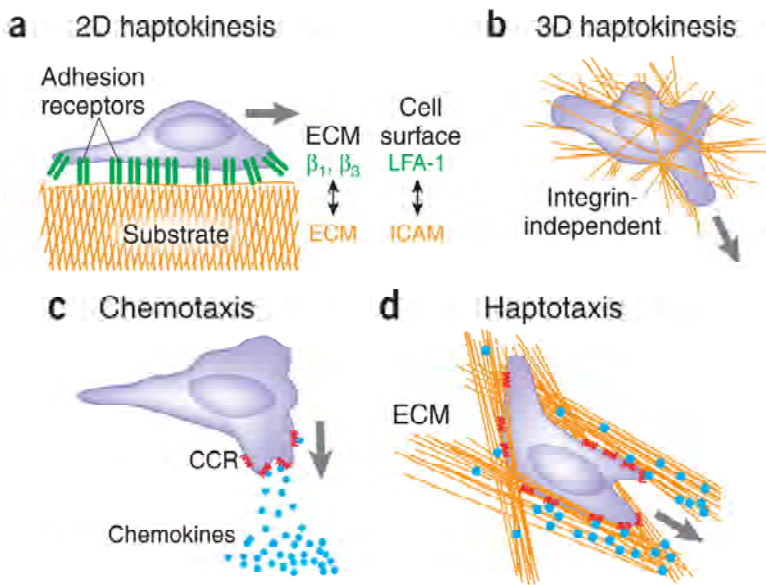


Figure 2. Principles of leukocyte–substrate interactions and guidance. **(a)** Haptokinetic, adhesion-dependent migration across a two-dimensional (2D) surface. Two-dimensional leukocyte migration requires integrin-mediated interaction with the substrate. *in vivo*, haptokinetic migration is present during leukocyte crawling across vascular endothelium or inner body surfaces, such as the peritoneum or the bronchial tract. **(b)** Three-dimensional (3D) haptokinesis and contact guidance results from shape change and the flow of anterior actin, but in leukocytes, lacks integrin-mediated adhesion requirements. In organized tissue, alignment of the cell body to nonrandom tissue structures leads to contact guidance. **(c)** Chemotaxis is induced by soluble, freely diffusing compounds that lead to preferential signaling and actin-rich protrusions at the leading edge. Chemotaxis adds a direction to 2D and 3D haptokinetic migration. **(d)** Haptotaxis is the directed migration toward chemoattractants that are immobilized on tissue structures, such as interstitial collagens or a stromal cell network.

Pericellular proteolysis

The degradation of ECM is a key mechanism supporting cell migration through physically constraining tissue regions⁴³. The penetration of the very dense meshwork of basement membranes likely requires proteolytic activity, at least during the initial phase of leukocyte influx^{6,44,45}. Whether interstitial leukocyte migration *in vivo* depends upon similar proteolytic ECM degradation is unclear, as controversial results have been reported¹⁰. Better dissection of the *in vivo* requirements for proteolytic ECM processing in different phases of leukocyte trafficking will require knowledge of ECM structure and composition before and after trafficking and consideration of other protease functions that may affect migration rates through diverse mechanisms, including the processing of surface receptors, cytokines, and growth factors^{46,47}. In defined *in vitro* environments, such as fibrillar three-dimensional collagen matrices of known pore diameter (averaging 3 to 6 μm), lymphocytes and myeloid cells migrate in the absence of collagen degradation or proteolytic track generation¹⁰. As a mechanism, nonproteolytic amoeboid migration results from marked shape change, propulsion and squeezing through narrow tissue regions (Fig. 2b), similar to leukocyte movement through interstitial tissue with minimum collateral damage during nondestructive inflammation^{10,41,48}. Because the physical structure of interstitial human and mouse tissues *in vivo* is quite heterogeneous, ranging from loose fibrillar regions of spacing similar to that of three-dimensional collagen lattices to compact dense connective tissue with submicron spacing (K. Wolf and P.F., unpublished data), it is likely that leukocytes adapt to tissue geometry and follow paths of least resistance, a process known as contact guidance.

Migration programs in different leukocytes subsets

The basic amoeboid migration program is retained in most, if not all, leukocytes as well as lymphoma cells⁴⁹. Whereas granulocytes and lymphocytes maintain the typical ‘hand-mirror’ shape reminiscent of Dictyostelium, monocytes contain more cytoplasm and often lack a bona fide uropod, but otherwise follow amoeboid principles of shape change and squeezing¹⁰. In dendritic cells (DCs), the leading edge consists of multiple dendrites that intercalate between tissue structures, but the cell body and uropod are retained^{37,50}. As perhaps the only exception, tissue-resident macrophages and macrophage-derived epithelioid cells adopt adhesive fibroblast-like morphology⁵¹, are poorly motile and show upregulated $\beta 1$, $\beta 2$ and $\beta 3$ integrins, together with matrix metalloproteases (MMPs)^{52,53}. Whereas the principles of amoeboid movement, including basic adhesion, protease and signaling requirements, seem to apply to all rapidly moving leukocytes, their peak velocities *in vitro* and *in vivo* differ for neutrophils (up to 30 $\mu\text{m}/\text{min}$), lymphocytes (up to 25 $\mu\text{m}/\text{min}$), B cells (15 $\mu\text{m}/\text{min}$), DCs (10 $\mu\text{m}/\text{min}$) and monocytes (5 $\mu\text{m}/\text{min}$). The

maximum migration velocity is likely proportional to myosin II activity and the deformability of the nucleus, as suggested by impaired migration rates *in vitro* because of nuclear entrapment at ECM structures after myosin II inhibition³⁷. Further, the repertoire of expressed chemoattractant and adhesion receptors mediating migration and attachment diverge, providing cell type-specific recruitment and positioning in tissues^{1,8,26,31}.

Leukocyte trafficking into tissues and initial migration

For immigration of circulating leukocytes into tissues (Fig. 3), transmigration through the vascular endothelial layer is the rate-limiting step, involving two independently regulated events, binding to vessel endothelium followed by diapedesis^{1,54}. The basement membrane underlying all normal vessels represents the first postendothelial tissue structure and barrier to cells undergoing diapedesis (Fig. 3a). The known mechanistic steps of vascular basement membrane penetration include adhesion to the substrate via integrin $\alpha 6 \beta 1$, the principal laminin receptor on leukocytes⁵⁵. For passage through vessel basement membrane in interstitial tissue, locally confined cleavage of the structural proteins laminin-10 and type IV collagen occurs by secreted or membrane-anchored MMPs and serine proteases^{44,56}. Cell body deformation is coupled to cytoplasmic propulsion and streaming through preexisting or newly formed pores. In acute inflammation *in vivo*, early neutrophil diapedesis occurs preferentially through basement membrane regions having decreased density of laminin-10, collagen IV and nidogen-2, suggestive of anatomic zones of least resistance between the pericytes⁴⁵. As leukocyte influx and proteolytic ECM degradation proceed, these regions further lose basement membrane components and develop into inflammation-induced preferred entry points for other leukocytes^{6,45}. In brain vessels, proteolytic basement membrane remodeling is essential for immune cell diapedesis^{57,58}, but it remains unresolved whether proteolytic breakdown is indispensable or rather auxiliary for diapedesis through other basement membranes^{44,45,59}. The deformation capability of leukocytes is considerable, reaching submicron constrictions in neutrophils⁶⁰; thus, proteolytic and nonproteolytic mechanisms may synergize. In transendothelial migration models *in vitro*, the engagement of CD31 and likely of integrin $\beta 2$ in neutrophils and activated lymphocytes leads to the upregulation of integrin $\alpha 6 \beta 1$ and $\alpha 4 \beta 1$, thus initiating a tissue phenotype that supports interstitial and cell-guided crawling^{55,61,62}. Upon leukocyte diapedesis, while the uropod is still engaged with the vessel wall, the leading edge reaches the perivascular loose connective tissue, consisting of filamentous collagen fibers and elongated gap-like tracks that facilitate cell alignment and migration (Fig. 3a). Such

perivascular tracks are present in virtually all organs and provide preferential cell migration routes to distal regions of the tissue⁴¹.

With inflammation, these tracks become further widened by hydrostatic pressure from vascular leakage and edema, likely facilitating cell trafficking⁴¹. In inflamed tissue, freely diffusing chemoattractants, such as bacterial peptides, provide short-lived or pulsatile directional information (Fig. 2c), in addition to the longer-lived cues provided by constitutive or induced tissue-bound chemoattractants (Fig. 2d)²⁶. Thus, besides chemotaxis, haptotaxis and contact guidance synergize to direct early steps of interstitial trafficking.

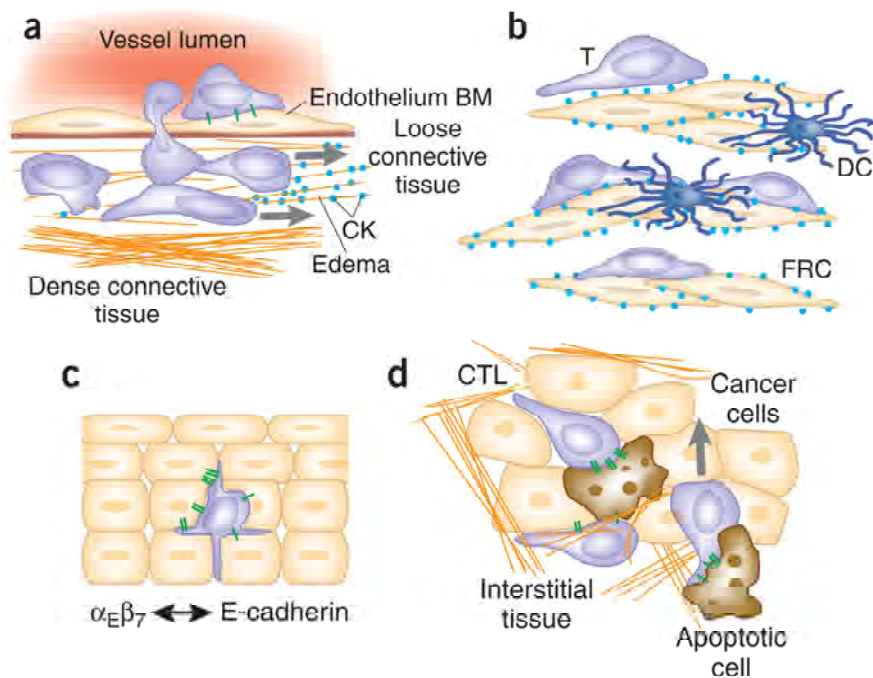


Figure 3. Leukocyte migration in different environments in vivo. **(a)** Interstitial leukocyte migration in loose connective tissue. Such preformed tracks of least resistance are present along most basement membranes (BMs), including those lining blood vessels and below epithelia that are particularly receptive to edematous swelling and enlargement of ECM gaps and tracks⁴¹. **(b)** Migration along cellular networks in lymphoid organs, such as fibroblastic reticular cells⁶³ (FRCs) or DC networks⁶⁴ in the T cell zone in lymph nodes. **(c)** Intraepithelial migration and positioning. After reverse transmigration through the basement membrane, leukocytes migrate briefly along cell–cell junctions until stable positioning is reached. In epidermis, integrin $\alpha E\beta 7$ in lymphocytes is the counterpart receptor for epithelial E-cadherin. **(d)** Intratumoral migration guided by cell–matrix and cell–cell contacts. CK, cytokine.

Migration along cell scaffolds

In contrast to epithelial and mesenchymal cells, leukocytes are particularly prone to use other cell surfaces for guided migration, recognition and arrest as part of their immune surveillance function (Table 1). In uninflamed lymph nodes, T and B lymphocytes immigrate through high endothelial venules and predominantly migrate along the cellular network of fibroblastic reticular cells (FRCs), DCs and follicular dendritic cells, as shown by intravital microscopy in living lymph nodes (Fig. 3b)^{63,64}. FRCs in particular provide a structural scaffold, with cell-surface ICAM-1 as a counter-ligand to leukocyte LFA-1 and also with decoration with chemokines⁶³. T cell positioning is dependent on CCR7 and its ligands CCL21 and CCL19, expressed by and bound at the surfaces of FRCs and DCs⁶³. Mice lacking CCR7 or its chemokine ligands fail to generate proper T and B cell regions^{65,66}; thus, both lymphocyte positioning and the anatomy of the T and B cell zones largely depend upon chemokine guidance. The migration pattern up and down the FRC network corresponds to a persistent random walk²⁻⁴, suggesting haptokinesis and/or contact guidance^{2,63,67}. Besides promoting migration, chemokine signals submit latent preactivation that increases T cell sensitivity to subsequent activation, such as TCR triggering⁶⁸.

Despite their importance for cell-cell interactions and migration across surfaces¹⁶, no active role for LFA-1–ICAM-1 interaction in the intranodal migration of T cells, B cells and DC has been detected^{37,69}. Other mechanisms providing translocation along cell scaffolds may include weak adhesion by chemokine-chemokine receptor interaction or non-adhesive shape change^{37,69}. Given cell scaffold-mediated migration strategies in lymph nodes, it is likely that leukocytes in peripheral tissues move along stromal cells as part of their surveillance function⁶¹.

Balancing adhesion and migration

Trafficking leukocytes often reduce their migration speed, pause and polarize toward the bound cell or tissue structure to execute crucial functions, including phagocytosis, cell-to-cell signaling and activation, and the release of cytokines or toxic factors toward a cell encountered. In vivo studies using histological end points cannot differentiate interstitial leukocyte accumulation by chemotaxis from random migration coupled to local arrest of migration and so provide only indirect insight into positioning mechanisms. Because of the current lack of data from live-cell imaging in peripheral tissues, little is known about the steady-state proportion of moving and sessile infiltrating cells during acute and chronic inflammation. Therefore, most knowledge of positioning stems from dynamic imaging in three-dimensional in vitro models and in lymph nodes in vivo. At least three basic kinetic states govern leukocyte positioning in tissues, including fast migration (5 to

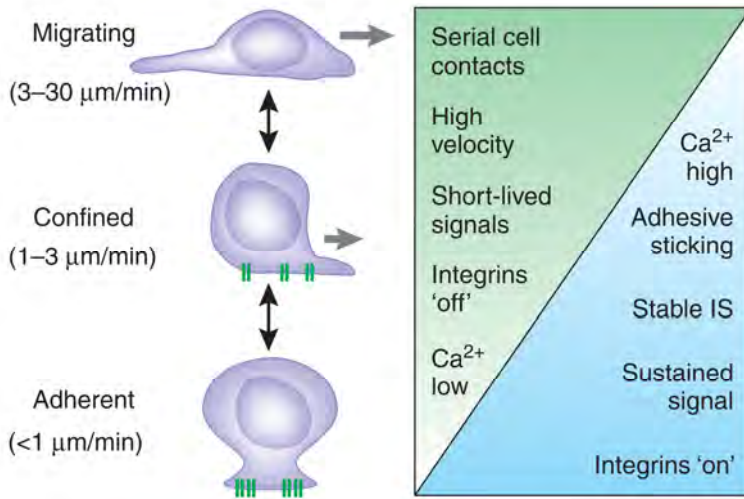


Figure 4. A balance between amoeboid migration, adhesive arrest and intermediate states. Moving leukocytes are able to slow down and completely cease migration within seconds to minutes and vice versa. High-velocity movement occurs by actin flow and shape change but without integrin-mediated adhesion and high calcium currents. Conversely, adhesive arrest is mediated by integrin engagement, accompanied by calcium oscillations and loss of amoeboid polarization. Because promigratory and antimigratory signals are gradual, rather than discrete, intermediate states may be adopted, resulting in slow migration in a confined region, often on the surface of a single cell. IS, immunological synapse.

25 μm/min), slow and often locally confined movement (2 to 5 μm), and adhesive arrest; and these rapidly interconvert (Fig. 4).

Based on these kinetic states, leukocyte accumulation in tissues occurs through at least three distinct mechanisms. Local engagement of adhesion receptors causes individual leukocytes to stick and become immobilized at a specific spot. The degradation of promigratory ‘go’ signals causes cell populations to slow down or stop movement. And the loss of exit signals confines cells to a local microenvironment despite ongoing migration. Complete migration arrest is mediated by activation of adhesion receptors on the moving cell followed by attachment to counter-receptors on other cells or ECM structures, leading to an immobilized cell (Table 1)⁷⁰. Within seconds, adhesion overrides ongoing promigratory signals; this is followed by cytoskeletal polarization toward the bound cell or ECM structure^{70,71}. Despite the promigratory lymph node environment, antigenic signaling prompts T and B cells to cease migration through LFA-1–ICAM-1 interaction⁷⁰ followed by the formation of a stable immunological synapse⁷². Under conditions of strong antigenic signaling, T cells contacting DCs undergo a rapid and strong adherence response to the antigen-presenting DC for signal exchange^{73–75}.

Activated B cells after antigen uptake attach to follicular stromal cells through LFA-1–ICAM and integrin $\alpha 4\beta 1$ –VCAM interactions and receive survival signals⁷⁶. Besides cell–cell signaling, such stable binding further supports the polarized release of cytokines into the cell–cell junction, as in helper T cells bound to B cells⁷⁷. By contrast, local confinement despite ongoing motility occurs by local adhesion coupled to slow migration ‘on the spot’⁷². Here, integrin-mediated arrest is coupled to polarized cytoskeletal dynamics and movement across the surface of the counterpart cell; this movement is thought to support receptor turnover and scanning of the cell surface^{3–5,14,74,78}. In both cases, the immobilization response is proportional to, and probably caused by, transient elevation of intracellular calcium in the T cell that confines migration by enhanced adhesion (Fig. 4)^{5,74}. The adhesive contact structures mediating arrest vary. In T cells, the immunological synapse is mediated by an adhesion plane enriched in filamentous actin, LFA-1, TCR and costimulatory molecules⁷². In monocytes and immature dendritic cells, adhesive arrest to ECM substrate is mediated by podosomes composed of multiple actin-rich focal adhesion zones of 1 to 3 μm in diameter and 10 to 30 min duration, formed underneath cells adhering to two-dimensional ECM substrate⁷⁹. Compared to migrating cells, both immunological synapses and podosomes are relatively stable and thus slow migration down or confer adhesive arrest for a limited duration, ranging from minutes to hours. Thus, whereas arrest mechanisms and underlying signals and adhesion structures vary in a cell- and context-dependent manner, migration confinement is a graded response proportional to proadhesive signal strength.

Long-lived confinement and tissue residency

Under homeostatic conditions, long-lasting tissue residency (for days and weeks) of leukocytes supports sentinel and surveillance function at epithelial interfaces to the outside world or at inner surfaces that filter blood or lymph for pathogens⁸⁰. Whereas the tissue lifespan of neutrophils until death is estimated at a few hours and that of interstitial T cells until egress is estimated at 1 d, resident macrophages, DCs or $\gamma\delta$ T cells may survive months to years until egress or death. In the skin, intraepidermal $\gamma\delta$ T cells integrate between keratinocytes and use integrin $\alpha\text{E}\beta 7$ for binding to epidermal E-cadherin (Fig. 3c)⁸¹. Likewise, intraepithelial leukocytes in the gut are dependent on $\alpha\text{E}\beta 7$ binding to E-cadherin⁸². For other tissue-resident leukocytes, such as interstitial DCs or macrophages, the retention mechanisms are unknown.

Relocation

After immigration and migration arrest, the re-onset of migration prompts leukocyte relocation toward regions nearby⁵⁴. The lymph node is the best-studied organ for

relocation; here, T and B cells change subregions in the course of their activation and differentiation program. After antigen capture, B cells located within the B cell follicle become activated, upregulate CCR7 and migrate chemotactically along a CCL21 gradient toward the follicle boundary, where they contact activated CD4⁺ helper T cells⁸³. Conversely, initially activated CD8⁺ T cells expressing CCR5 are directed by CCL3 and CCL4 to reach the region of ongoing interaction between CD4⁺ T cells and DCs, where they receive T cell help⁸⁴. In lymphoid organs relocation connects particular leukocyte functions to sequentially occur in different anatomic regions; however, repositioning programs in peripheral tissues remain elusive. Relocation further serves to allow lymphocytes to accumulate short-lived activation signals. Naive T cells migrate at high velocity across the surface of DCs presenting noncognate or very weak antigen and receive weak, homeostatic signals^{2,74} (J. Storim and P.F., unpublished data). If antigenic strength is moderate, naive T cells slow down after engaging with the DCs, detach again within minutes and engage with neighboring DCs, where they receive TCR triggering signals⁷⁵. Here, serial interactions with different DCs are mediated by relocation and provide pulsatile cognate TCR-mediated signals until early activation is reached, mediating T cell arrest and commitment to a single DC^{4,75,85}. A special type of relocation during stable cell–cell adhesion is the ‘carried translocation’ of T cells bound to a moving DC86, a resting B cell pushed by a moving T cell⁷¹ and the guidance of T cells by an activated migrating B cell⁸³. Because of their stability, these conjugates provide antigenic signaling and passive translocation of immobile cells to another tissue region, yet the function of these interactions remains unclear. Thus, both active and passive cell movements contribute to leukocyte relocation.

Counter-regulation of interstitial leukocyte trafficking

Beyond adhesive migration arrest, the local reduction of promigratory signals is achieved by the down-modulation of chemoattractant receptors, receptor desensitization and ligand competition, whereas termination of chemoattractant activity occurs through capture by neutralizing chemoattractant receptors and/or proteolytic degradation. After ligation, chemoattractant receptors become internalized and either recycled to the leading edge or stored in vesicles in the uropod, thus limiting the availability of both the chemoattractant and its receptor²⁰. In T cells, the activation-induced downregulation of S1P1 is the best-studied example of how chemoattractant signaling is tuned (see below)⁸⁷. Migration-inducing agonists can further be competed away from the receptor by endogenous antagonists. Resolvin E1 acts as a competitive antagonist of LTB4 by binding to and desensitizing BLT1⁸⁸. Resolvins are found in high concentrations in inflammatory tissue fluids, where they counteract the influx of neutrophils by limiting

LTB₄-mediated chemotaxis and enhance the resolution of dermal inflammation, peritonitis and colitis in mouse disease models⁸⁹. Local chemokine availability is reduced by binding to chemokine receptors on bystander cells ('sink function'). Erythrocytes and endothelial cells express silent chemokine receptors, including DARC (Duffy antigen receptor for chemokines), which capture interleukin (IL)-8, CCL5 and others, thereby limiting their bioavailability in tissues²⁶. Further, chemoattractants are drained by the lymph fluid or blood. Lastly, chemokine degradation occurs through MMP2, MMP9 and other MMPs released by resident and infiltrate cells⁴⁶. These proteases cleave many, if not all, chemokines, including CCL2, CCL7, CCL8, CCL13 and CXCL12, into either inactive or even antagonistic forms (reviewed in ref. 90). This function of MMPs downscales inflammatory infiltrates in a timely fashion and prevents tissue damage⁴⁶. How these different mechanisms act together or synergize to limit interstitial leukocyte trafficking is unclear.

Exit control from tissues

Emigration from tissues and organs is confined to lymphocytes and DCs; it does not occur for granulocytes and macrophages. Exit of lymphocytes and DCs from lymph nodes provides peripheral tissues with activated effector cells for host defense⁹¹. In peripheral tissues, efflux delivers peripheral T cells and antigen-presenting cells (APCs) to the lymph node. Efflux further limits and resolves an inflammatory response. In both lymph nodes and interstitial tissues, a monolayer of lymphatic endothelial cells (LECs) needs to be crossed, likely by a process of reverse diapedesis. In peripheral tissues, exit also may occur through gaps and blunt ends of terminal lymph vessels⁹². In the lymph node, exit routes are the paracortical and medullary sinuses. After 12–24 h of intranodal migration, T cells reach the sinus epithelium, which releases S1P into predominantly the afferent lymphatic vessel, thus likely creating a chemotactic gradient. In the absence of activation signals, passenger T and B cells express S1P receptors and require the S1P signal to cross the epithelium for exit⁹¹. However, once T cells receive TCR triggering and early activation signal by APCs leading to the upregulation of CD69, S1P1 becomes downregulated for 2–3 d and the cells are prevented from exiting the lymph node⁹³. Thus, down-modulation of a chemoattractant receptor that does not participate in maintaining baseline motility limits egress and confines mobile T cells to the lymph node until activation is complete. In peripheral tissues, exit occurs into afferent lymph capillaries located parallel to blood vessels by a chemoattractant- and adhesion receptor-dependent process rather than by passive entry⁹⁴. In T cells, experimental S1P1 agonism causes migration arrest at the basal surface of the lymphatic endothelium through adhesion mediated by LFA-1–ICAM-1 and VLA4–VCAM-1 interactions⁹⁵.

Therefore, high S1P concentrations in inflamed tissue may support tissue retention of effector cells⁹⁵. The egress of DCs from peripheral tissues is promoted mostly by chemokines. In epidermal Langerhans cells, signals induced by irritants or pathogens downregulate E-cadherin but upregulate CCR7^{92,96}, which allows Langerhans cells to leave the epidermis, follow CCL21 constitutively produced by and decorating dermal LECs, and diapedese into lymphatic vessels of the upper dermis⁹⁶. Thus, active reverse diapedesis rather than passive transport of lymphocytes and DCs mediates egress into afferent lymphatics⁹⁵. At their basal surface LECs express macrophage mannose receptor and CLEVER-1, which have been implicated as counter-receptors for leukocyte adhesion to LECs and migration to lymph nodes^{92,97,98}. The counter-receptors on leukocytes likely are not integrins, because integrin-deficient dermal DCs efficiently travel through afferent lymph vessels into lymph nodes³⁷. In blood vessels of the liver sinus, monocytes use LFA-1 binding to ICAM-1 to migrate along the intraluminal endothelium of the vessel wall^{99,100}, but it remains to be shown where leukocytes use such haptokinetic mechanisms to move along the inner LEC walls and where passive transport occurs.

Migration during interstitial inflammation

Any acute or chronic inflammation in the tissue in response to damage, tumor growth or viral infection or in autoimmune disease and allograft rejection prompts tissue infiltration by effector cells, including neutrophils, monocytes, T cells and, in chronic states, B cells. Often, chronic inflammation causes de novo, tertiary lymphoid tissue formation, dependent upon a multistep developmental program of cell migration and positioning. Initially small and unstructured T cell infiltrates eventually segregate into a T cell area with DC networks, high endothelial venules and adjacent B cell follicles with germinal centers¹⁰¹. This process is initiated by lymphotoxin $\alpha 1\beta 2$ released from activated B and T cells, which activates stromal cells to release lymphoid homeostatic chemokines (CCL19, CCL21, CXCL12 and CXCL13)^{101,102}. How the spatial separation into T and B cell areas occurs is unknown but, in reminiscence of secondary lymphoid organs, guidance and adhesion likely direct the temporary assembly of peripheral lymph follicles. If persistent for weeks and months, chronic inflammation may eventually trigger the remodeling of tissue structures within and adjacent to connective tissues. In mouse models of rheumatoid arthritis, a progressive influx of granulocytes followed by T cells is observed preceding destruction¹⁰³. Immigrated T cells of the CD4⁺ memory phenotype reach the synovial membrane; secrete IL-2, interferon- γ and IL-17; and thereby activate monocytes, tissue macrophages, fibroblasts and the synoviocytes to produce ECM-degrading enzymes and fibrosis-inducing transforming growth factor- β , IL-13 and platelet-derived growth factor^{104,105}. In later stages, B cells may infiltrate the synovium

and form tertiary lymphoid tissue. Experimental arthritis in mouse models is reduced or abrogated by interfering with PI(3)K- γ ¹⁰⁶ and LT β ¹⁰⁷ signaling, which link interstitial trafficking, particularly of neutrophils, to disease outcome.

Migration in cytotoxic effector response

Cytotoxic T lymphocytes (CTLs) infiltrate solid tumors by moving along the tumor–matrix interface and along junctions between target cells (Fig. 3d)^{108,109}. LFA-1–ICAM interactions have been implicated in CTLs crawling along tumor cell strands *in vitro*¹¹⁰, but the *in vivo* mechanisms are unclear. In experimental tumors, activated CTLs reach their target site after a phase of movement through the adjacent stroma rather than from vessels inside the tumor¹⁰⁸. Chemokines produced by tumor cells, tumor-associated macrophages¹¹¹ or fibroblasts^{112,113}, including CXCL12 (through CXCR4)^{114,115}, CXCL10 (CXCR3)^{114,115} and CCL2 (CCR4)¹¹⁶, are important in attracting effector T cells into the tumor tissue. Likewise, monocytes are recruited *de novo* and activated by CCL3, CCL4 and CCL5 released by tumor-infiltrating T cells¹¹⁷. Effector cells migrate through interstitial spaces and across the surface of stromal and tumor cells and scan for expressed cognate antigen (Fig. 3d). This ‘search function’ follows the rules of a persistent random walk, similarly to T cells in the lymph node cortex, as shown by *in vivo* microscopy^{118,119}. With antigenic peptide present, fast scanning by CTLs converts to migration arrest and prolonged engagement with individual target cells in both virally infected or tumor cells^{108,109,118,119}. An effector synapse polarizes TCR and LFA-1 to the target cell *in vitro*¹¹⁹, which results in migration arrest until target cell apoptosis *in vivo*^{108,109} and regression of the lesion^{108,109,118,119}. Integrin α E β 7 engagement on CTLs supports polarized binding to target cells and enhances exocytosis of cytolytic granules¹²⁰, consistent with a function in adhesive costimulation. Other adhesion-promoting and costimulatory molecules, including Mac-1, LFA-1 and VLA-4, support CD8+ effector T cell function in viral disease, but whether transendothelial migration, local positioning or both are favored remains unclear¹²¹. Tumors may also counteract the migration of infiltrating leukocytes. By unresolved mechanisms, stop signals can arrest the movement of tumor-infiltrating lymphocytes¹²², and they represent a potential escape strategy. Further, the sequence of cells encountered before the target cells affects effector function. If nearby regulatory T cells suppress effector functions, target cell killing but not migration or conjugation may be impaired by a transforming growth factor- β –sensitive mechanism¹²³. Thus, effector function is critically dependent on both efficient immigration of CTLs into the tumor and killing of it, and interference with either process supports target cell survival.

Migration during liver inflammation

Immune surveillance in the liver is provided by both resident and blood-borne 'passenger' lymphocytes and macrophages. In liver sinusoids, passenger lymphocytes scan endothelium and - without leaving the bloodstream, but rather through endothelial fenestrations - hepatocytes for antigenic peptide¹²⁴⁻¹²⁶. Likewise, natural killer (NK) T cells and monocytes crawl along and patrol the lumen of liver sinusoids¹⁰⁰ through binding of LFA-1 and chemokine receptor CX3CR1 to their respective ligands ICAM-1 and CX3CL1 (also known as fractalkine) on liver endothelium⁹⁹. During liver inflammation, such as viral hepatitis, NK, $\gamma\delta$ T, NK T and CD8⁺ effector cells become further recruited to cross the endothelium, move between hepatocytes and diffusely infiltrate the liver^{127,128}. This recruitment requires CCR5 and CXCR3 expression on leukocytes and CCL3, CCL4, CCL5, CXCL9 and CXCL10 produced by hepatocytes and sinus endothelial cells¹²⁸. Recruitment of CD8⁺ T cells into liver parenchyma and elimination of virally infected hepatocytes both depend upon CXCL9 and CXCL10¹²⁹. Instead of recirculating, most infiltrate cells in the liver die within hours to days¹²⁷; thus, little is known about exit mechanisms. During chronic colonization of liver cells with intracellular bacteria, including *Mycobacterium tuberculosis*, migration and positioning of infiltrate cells leads to granuloma formation to locally confine and eliminate the infection¹³⁰. Pathogen-infected macrophages recruit other macrophages and blood-derived monocytes to accumulate and form a dense cellular scaffold around the pathogen-infected region. This monocyte-derived convolute serves as track system for effector cells, including CD4⁺, CD8⁺, $\gamma\delta$ and CD1-restricted T lymphocytes, which rapidly enter the macrophage network and engage in dynamic as well as sustained macrophage-T lymphocyte interactions¹³¹. Effector CD4⁺ T lymphocytes secrete TH1-type cytokines, such as interferon- γ , which activate macrophages and CD8⁺ effector cells to eliminate intracellular pathogen and infected cells, respectively¹³⁰. Thus, recruited macrophages form a structural barrier that hosts mobile T cells, conditioning the microenvironment with cytokines and effector molecules. Dynamic imaging data are not yet available for other inflammatory disorders, including glomerulonephritis, atherosclerosis, acute and chronic lung inflammation, and thyroiditis, which likely comprise similar recruitment and resolution mechanisms.

Therapeutic targeting of leukocyte trafficking in tissues

Many new anti-inflammatory drugs aim at interfering with transendothelial migration by antagonizing surface integrins, selectins or chemokines involved in leukocyte homing⁸. Because of its contribution in virtually every step of inflammation, interstitial leukocyte migration is another target function to modulate immune cell function in tissues (Supplementary Table 1 online). In clinical use since the early twentieth century to blunt

acute inflammation, colchicine prevents microtubule assembly by binding to tubulin, which inhibits chemotactic migration of neutrophils and monocytes into and within interstitial tissue¹³². More recently developed strategies to interfere with chemoattractant signaling show strong promise in reducing tissue damage in chronic inflammation⁸. Likewise, competitive inhibitors of the LTB₄ receptor BLT1 reduce inflammation in models of rheumatoid arthritis and atherosclerosis^{107,133}. FTY-720, an agonist of S1P1, leads to short-term receptor activation followed by internalization and degradation and, thereby, suppresses S1P signaling. The FTY-720–induced inhibition of T and B cell egress from lymphoid and peripheral organs causes secondary lymphopenia and blunts T cell–dependent tissue inflammation¹³⁴. Inhibition of PI(3)K- γ strongly reduces the infiltration of neutrophils and T cells in mouse models of chronic destructive inflammation, including rheumatoid arthritis and lupus-like syndrome^{106,135}. To improve effector function, such as in established cancers, proinflammatory strategies aim at enhancing tissue infiltration by CTLs and cytolytic killing. Small molecule agonists of Toll-like receptors 7 and 8 activate cutaneous dendritic cells and macrophages. They release proinflammatory cytokines, including interferon- γ , tumor necrosis factor and the chemokines CCL3, CCL4 and CCL2, that attract CTLs and support CTL-mediated eradication of skin tumors in small-animal models and humans^{136,137}.

Conclusions

With increased kinetic information on different disease models, many interference strategies are likely to show effects on interstitial trafficking and signal exchange between cells. Because of their role in navigation control, chemokines and their downstream signaling pathways show promise as therapeutic targets, at both the vascular and interstitial tissue levels. Because diseases that often are not immediately fatal will be targeted, issues of safety will increase. To avoid unwanted chronic immunosuppression, fine-tuning of dosing and meaningful combination therapy will be needed. Targeting interstitial migration will need to aim at particular contexts and specific leukocyte subsets to modulate migration and positioning; this promises to complement interference with cell cycle progression (cytostatic drugs) or transendothelial migration (for example, integrin antagonists). Interstitial leukocyte migration is regarded not only as means to change position from one place to another but as integral to immune cell surveillance and molecular recognition, including the search for APCs and target cells, the scanning of receptors expressed at the cell surfaces encountered and the accumulation of signals during migration and over time. Because of their amoeboid features, moving T cells act as bipolar sensory cells that integrate discrete signals over time until thresholds are reached and result in a cellular reaction,

not unlike a mobile, position-changing neural cell. Whether myeloid cells collect signals in a similar, migratory manner is not known. In conclusion, live-cell microscopy has shifted our conceptions of immune processes from an abstract, imagined appreciation of leukocyte trafficking into a visual and more detailed understanding of how, when, where and in which sequence immune cells get together, exchange information and eliminate pathogens and tumor cells.

Note: Supplementary information is available on the Nature Immunology website.

ACKNOWLEDGMENTS

Supported by Deutsche Forschungsgemeinschaft grant FR1155/6-3 (P.F.).

Published online at <http://www.nature.com/natureimmunology/>

Reprints and permissions information is available online at <http://npg.nature.com/reprintsandpermissions/>

Table 1 Haptokinetic and adhesive cell-cell interactions in interstitial leukocyte trafficking

Cellular scaffold	Ligand contacted	Leukocyte	Receptor	Outcome	Ref.
Fibroblast, synovioocyte	LFA-1	All	ICAM-1	Slowing, arrest	6
	FN	All	$\alpha_5\beta_1$, $\alpha_4\beta_1$	Slowing, arrest	138
	VCAM-1	All	$\alpha_4\beta_1$	Slowing, arrest	6
	CD40	T	CD40L	Costimulation	139
DC	ICAM-1	CD4 ⁺ , CD8 ⁺	LFA-1	Slowing, arrest	70
	CCL21	CD4 ⁺ , CD8 ⁺	CCR7	Costimulation, arrest	63
MZ stromal cell	ICAM-1	MZ B	LFA-1	Arrest	76
	VCAM-1	MZ B	$\alpha_4\beta_1$	Arrest	76
FDC	CXCL13	B	CXCR5	Haptotaxis	66
LEC (lymph node)	S1P	T, B	S1P ₁	Emigration from lymph node	91
Afferent LEC	ICAM-1	T, DC	LFA-1	Arrest, impaired tissue egress	95
	VCAM-1	T, DC	$\alpha_4\beta_1$	Arrest, impaired tissue egress	95
	CLEVER-1	T, DCs	?	Tissue egress	98
	Macrophage mannose receptor-1	T, DCs	?	Tissue egress	97
FRC	ICAM-1	T, B	LFA-1	Arrest	140
	CCL19, CCL21	T, B, DC	CCD7	Haptotaxis, costimulation	63
	ER-TR7 epitope	T, B, DC	?	Haptotaxis?	141
Target cell	Peptide-MHC I, ICAM	CTL	TCR, LFA-1	Arrest, effector function	108-110
Epidermis	E-cadherin	CTL	$\alpha_5\beta_7$	Arrest, polarization, killing	120
	E-cadherin	$\gamma\delta$ T	$\alpha_5\beta_7$	Adhesion, long-lived integration	81

MZ, splenic marginal zone.

References

1. von Andrian, U.H. & Mackay, C.R. T-cell function and migration. Two sides of the same coin. *n. engl. J. Med.* 343, 1020–1034 (2000).
2. Miller, M.J., Hejazi, A.S., wei, S.H., Cahalan, M.D. & Parker, I. T cell repertoire scanning is promoted by dynamic dendritic cell behavior and random T cell motility in the lymph node. *Proc. natl. acad. Sci. uSa* 101, 998–1003 (2004).
3. Miller, M.J., Safrina, O., Parker, I. & Cahalan, M.D. Imaging the single cell dynamics of CD4+ T cell activation by dendritic cells in lymph nodes. *J. exp. Med.* 200, 847–856 (2004).
4. Mempel, T.R., Henrickson, S.E. & Von Andrian, U.H. T-cell priming by dendritic cells in lymph nodes occurs in three distinct phases. *nature* 427, 154–159 (2004).
5. Bhakta, N.R., Oh, D.Y. & Lewis, R.S. Calcium oscillations regulate thymocyte motility during positive selection in the three-dimensional thymic environment. *nat. immunol.* 6, 143–151 (2005).
6. Ley, K., Laudanna, C., Cybulsky, M.I. & Nourshargh, S. Getting to the site of inflammation: the leukocyte adhesion cascade updated. *nat. rev. immunol.* 7, 678–689 (2007).
7. Heit, B. et al. PTEN functions to ‘prioritize’ chemotactic cues and prevent ‘distraction’ in migrating neutrophils. *nat. immunol.* 9, 743–752 (2008).
8. Mackay, C.R. Moving targets: cell migration inhibitors as new anti-inflammatory therapies. *nat immunol.* 9, 988–998 (2008). 9. Friedl, P. Prespecification and plasticity: shifting mechanisms of cell migration. *curr. opin. cell Biol.* 16, 14–23 (2004).
10. Wolf, K., Muller, R., Borgmann, S., Broucker, E.B. & Friedl, P. Amoeboid shape change and contact guidance: T-lymphocyte crawling through fibrillar collagen is independent of matrix remodeling by MMPs and other proteases. *Blood* 102, 3262–3269 (2003).
11. Wolf, K. et al. Multi-step pericellular proteolysis controls the transition from individual to collective cancer cell invasion. *nat. cell Biol.* 9, 893–904 (2007).
12. Friedl, P. et al. Migration of coordinated cell clusters in mesenchymal and epithelial cancer explants in vitro. *cancer res.* 55, 4557–4560 (1995).
13. Friedl, P., Hegerfeldt, Y. & Tusch, M. Collective cell migration in morphogenesis and cancer. *int. J. Dev. Biol.* 48, 441–449 (2004).
14. Friedl, P. & Broucker, E.B. TCR triggering on the move: diversity of T-cell interactions with antigen-presenting cells. *immunol. rev.* 186, 83–89 (2002). 15. wei, X., Tromberg, B.J. & Cahalan, M.D. Mapping the sensitivity of T cells with an optical trap: polarity and minimal number of receptors for Ca²⁺ signaling. *Proc. natl. acad. Sci. uSa* 96, 8471–8476 (1999).
16. Stanley, P. et al. Intermediate-affinity LFA-1 binds alpha-actinin-1 to control migration at the leading edge of the T cell. *eMBO J.* 27, 62–75 (2008). 17. Negulescu, P.A., Krasieva, T.B., Khan, A., Kerschbaum, H.H. & Cahalan, M.D. Polarity of T cell shape, motility, and sensitivity to antigen. *immunity* 4, 421–430 (1996).
18. Beemiller, P., Hoppe, A.D. & Swanson, J.A. A phosphatidylinositol-3-kinase-dependent signal transition regulates ARF1 and ARF6 during Fcγ receptor-mediated phagocytosis. *PLoS Biol.* 4, e162 (2006).
19. Pytowski, B., Maxfield, F.R. & Michl, J. Fc and C3bi receptors and the differentiation antigen BH2-Ag are randomly distributed in the plasma membrane of locomoting neutrophils. *J. cell Biol.* 110, 661–668 (1990).
20. Servant, G., weiner, O.D., Neptune, E.R., Sedat, J.w. & Bourne, H.R. Dynamics of a chemoattractant receptor in living neutrophils during chemotaxis. *Mol. Biol. cell* 10, 1163–1178 (1999).
21. Fernandez-Segura, E., Garcia, J.M. & Campos, A. Topographic distribution of CD18 integrin on human neutrophils as related to shape changes and movement induced by chemotactic peptide and phorbol esters. *cell. immunol.* 171, 120–125 (1996).
22. Friedl, P., Entschladen, F., Conrad, C., Niggemann, B. & Zanker, K.S. CD4+ T lymphocytes migrating in three-dimensional collagen lattices lack focal adhesions and utilize beta1 integrin-independent strategies for polarization, interaction with collagen fibers and locomotion. *eur. J. immunol.* 28, 2331–2343 (1998).

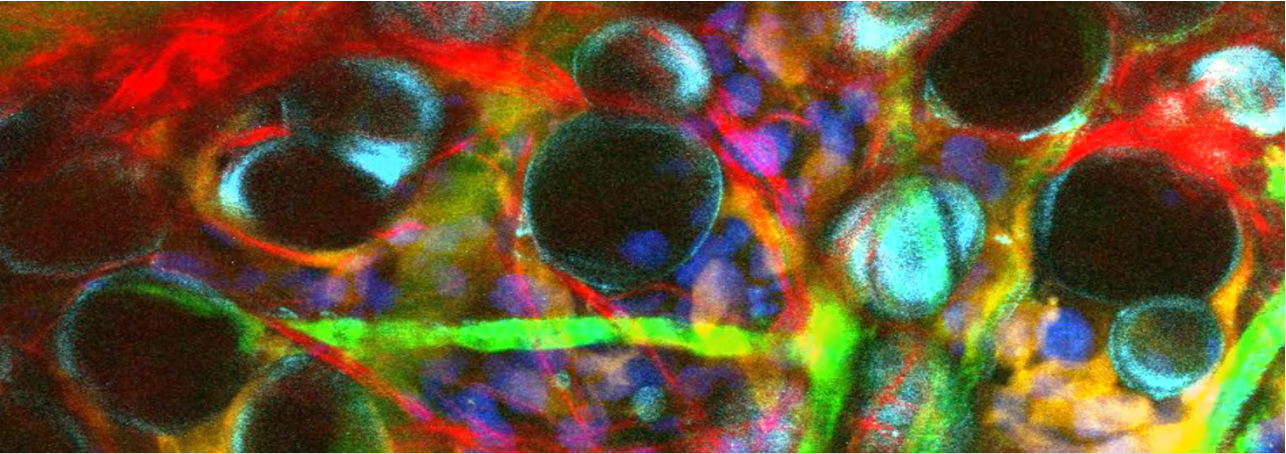
23. Laskin, D.L., Kimura, T., Sakakibara, S., Riley, D.J. & Berg, R.A. Chemotactic activity of collagen-like polypeptides for human peripheral blood neutrophils. *J. leukoc. Biol.* 39, 255–266 (1986).
24. Senior, R.M., Gresham, H.D., Griffin, G.L., Brown, E.J. & Chung, A.E. Entactin stimulates neutrophil adhesion and chemotaxis through interactions between its Arg-Gly-Asp (RGD) domain and the leukocyte response integrin. *J. clin. invest.* 90, 2251–2257 (1992).
25. Adair-Kirk, T.L. et al. A site on laminin alpha 5, AQARSAASKVKVSMKF, induces inflammatory cell production of matrix metalloproteinase-9 and chemotaxis. *J. immunol.* 171, 398–406 (2003).
26. Thelen, M. & Stein, J.V. How chemokines invite leukocytes to dance. *nat immunol.* 9, 953–959 (2008).
27. Marone, R., Cmiljanovic, V., Giese, B. & Wymann, M.P. Targeting phosphoinositide 3-kinase: moving towards therapy. *Biochim. Biophys. Acta* 1784, 159–185 (2008).
28. Stambolic, V. & Woodgett, J.R. Functional distinctions of protein kinase B/Akt isoforms defined by their influence on cell migration. *trends cell Biol.* 16, 461–466 (2006).
29. Enomoto, A. et al. Akt/PKB regulates actin organization and cell motility via Girdin/APE. *Dev. cell* 9, 389–402 (2005).
30. Rommel, C., Camps, M. & Ji, H. PI3K δ and PI3K γ : partners in crime in inflammation in rheumatoid arthritis and beyond? *nat. rev. immunol.* 7, 191–201 (2007).
31. Nombela-Arrieta, C. et al. Differential requirements for DOCK2 and phosphoinositide-3-kinase gamma during T and B lymphocyte homing. *immunity* 21, 429–441 (2004).
32. Ibarra, N., Pollitt, A. & Insall, R.H. Regulation of actin assembly by SCAR/WAVE proteins. *Biochem. Soc. trans.* 33, 1243–1246 (2005).
33. Machesky, L.M. et al. Scar, a WASP-related protein, activates nucleation of actin filaments by the Arp2/3 complex. *Proc. natl. acad. Sci. USA* 96, 3739–3744 (1999).
34. Charest, P.G. & Firtel, R.A. Feedback signaling controls leading-edge formation during chemotaxis. *curr. opin. genet. Dev.* 16, 339–347 (2006).
35. Bendix, P.M. et al. A quantitative analysis of contractility in active cytoskeletal protein networks. *Biophys. J.* 94, 3126–3136 (2008).
36. Eddy, R.J., Pierini, L.M. & Maxfield, F.R. Microtubule asymmetry during neutrophil polarization and migration. *Mol. Biol. cell* 13, 4470–4483 (2002).
37. Lammermann, T. et al. Rapid leukocyte migration by integrin-independent flowing and squeezing. *nature* 453, 51–55 (2008).
38. Ferguson, G.J. et al. PI(3)K γ has an important context-dependent role in neutrophil chemokinesis. *nat. cell Biol.* 9, 86–91 (2007).
39. Li, Z. et al. Regulation of PTEN by Rho small GTPases. *nat. cell Biol.* 7, 399–404 (2005).
40. Campello, S. et al. Orchestration of lymphocyte chemotaxis by mitochondrial dynamics. *J. exp. Med.* 203, 2879–2886 (2006).
41. Friedl, P. & Brocker, E.B. T cell migration in three-dimensional extracellular matrix: guidance by polarity and sensations. *Dev. immunol.* 7, 249–266 (2000).
42. Mandeville, J.T., Lawson, M.A. & Maxfield, F.R. Dynamic imaging of neutrophil migration in three dimensions: mechanical interactions between cells and matrix. *J. leukoc. Biol.* 61, 188–200 (1997).
43. Wolf, K. & Friedl, P. Mapping proteolytic cancer cell-extracellular matrix interfaces. *clin. exp. Metastasis* published online, doi: 10.1007/s10585-008-9190-2 (4 July 2008).
44. Leppert, D., Waubant, E., Galardy, R., Bunnett, N.W. & Hauser, S.L. T cell gelatinases mediate basement membrane transmigration in vitro. *J. immunol.* 154, 4379–4389 (1995).
45. Wang, S. et al. Venular basement membranes contain specific matrix protein low expression regions that act as exit points for emigrating neutrophils. *J. exp. Med.* 203, 1519–1532 (2006).
46. McQuibban, G.A. et al. Inflammation dampened by gelatinase A cleavage of monocyte chemoattractant protein-3. *Science* 289, 1202–1206 (2000).
47. Murphy, G., Murthy, A. & Khokha, R. Clipping, shedding and RIPPING keep immunity on cue. *trends immunol.* 29, 75–82 (2008).
48. Friedl, P. & Wolf, K. Proteolytic and non-proteolytic migration in tumor cells and leukocytes. *Biochem. Soc. Symp.* 70 277–285 (2003).

49. Pals, S.T., de Gorter, D.J. & Spaargaren, M. Lymphoma dissemination: the other face of lymphocyte homing. *Blood* 110, 3102–3111 (2007).
50. Gunzer, M., Kampgen, E., Brouck, E.B., Zanker, K.S. & Friedl, P. Migration of dendritic cells in 3D-collagen lattices. Visualisation of dynamic interactions with the substratum and the distribution of surface structures via a novel confocal reflection imaging technique. *adv. exp. Med. Biol.* 417, 97–103 (1997).
51. De Nichilo, M.O. & Burns, G.F. Granulocyte-macrophage and macrophage colony-stimulating factors differentially regulate alpha v integrin expression on cultured human macrophages. *Proc. natl. acad. Sci. uSa* 90, 2517–2521 (1993).
52. McNally, A.K. & Anderson, J.M. $\beta 1$ and $\beta 2$ integrins mediate adhesion during macrophage fusion and multinucleated foreign body giant cell formation. *am. J. Pathol.* 160, 621–630 (2002).
53. Chung, A., Gao, Q. & Kao, w.J. Macrophage matrix metalloproteinase-2/-9 gene and protein expression following adhesion to ECM-derived multifunctional matrices via integrin complexation. *Biomaterials* 28, 285–298 (2007).
54. Bromley, S.K., Mempel, T.R. & Luster, A.D. Orchestrating the orchestrators: chemokine control of T cell trafficking. *nat. immunol.* 9, 970–980 (2008).
55. Dangerfield, J., Larbi, K.Y., Huang, M.T., Dewar, A. & Nourshargh, S. PECAM-1 (CD31) homophilic interaction up-regulates $\alpha 6\beta 1$ on transmigrated neutrophils in vivo and plays a functional role in the ability of $\alpha 6$ integrins to mediate leukocyte migration through the perivascular basement membrane. *J. exp. Med.* 196, 1201–1211 (2002).
56. Young, R.E., Voisin, M.B., wang, S., Dangerfield, J. & Nourshargh, S. Role of neutrophil elastase in LTB4-induced neutrophil transmigration in vivo assessed with a specific inhibitor and neutrophil elastase deficient mice. *Br. J. Pharmacol.* 151, 628–637 (2007).
57. El-Shabrawi, Y., walch, A., Hermann, J., Egger, G. & Foster, C.S. Inhibition of MMP-dependent chemotaxis and amelioration of experimental autoimmune uveitis with a selective metalloproteinase-2 and -9 inhibitor. *J. neuroimmunol.* 155, 13–20 (2004).
58. Agrawal, S. et al. Dystroglycan is selectively cleaved at the parenchymal basement membrane at sites of leukocyte extravasation in experimental autoimmune encephalomyelitis. *J. exp. Med.* 203, 1007–1019 (2006).
59. Steadman, R. et al. Human neutrophils do not degrade major basement membrane components during chemotactic migration. *int. J. Biochem. cell Biol.* 29, 993–1004 (1997).
60. Thureson-Klein, A., Hedqvist, P. & Lindbom, L. Leukocyte diapedesis and plasma extravasation after leukotriene B4: lack of structural injury to the endothelium. *tissue cell* 18, 1–12 (1986).
61. Roussel, E. & Gingras, M.C. Transendothelial migration induces rapid expression on neutrophils of granule-release VLA6 used for tissue infiltration. *J. leukoc. Biol.* 62, 356–362 (1997).
62. Berg, L.P. et al. Functional consequences of noncognate interactions between CD4+ memory T lymphocytes and the endothelium. *J. immunol.* 168, 3227–3234 (2002).
63. Bajenoff, M. et al. Stromal cell networks regulate lymphocyte entry, migration, and territoriality in lymph nodes. *immunity* 25, 989–1001 (2006).
64. Lindquist, R.L. et al. Visualizing dendritic cell networks in vivo. *Nat. Immunol.* 5, 1243–1250 (2004).
65. Forster, R. et al. CCR7 coordinates the primary immune response by establishing functional microenvironments in secondary lymphoid organs. *Cell* 99, 23–33 (1999).
66. Ansel, K.M. et al. A chemokine-driven positive feedback loop organizes lymphoid follicles. *Nature* 406, 309–314 (2000).
67. Mempel, T.R., Scimone, M.L., Mora, J.R. & von Andrian, U.H. In vivo imaging of leukocyte trafficking in blood vessels and tissues. *Curr. Opin. Immunol.* 16, 406–417 (2004).
68. Friedman, R.S., Jacobelli, J. & Krummel, M.F. Surface-bound chemokines capture and prime T cells for synapse formation. *Nat. Immunol.* 7, 1101–1108 (2006).
69. woolf, E. et al. Lymph node chemokines promote sustained T lymphocyte motility without triggering stable integrin adhesiveness in the absence of shear forces. *Nat. Immunol.* 8, 1076–1085 (2007).
70. Dustin, M.L., Bromley, S.K., Kan, Z., Peterson, D.A. & Unanue, E.R. Antigen receptor engagement delivers a stop signal to migrating T lymphocytes. *Proc. Natl. Acad. Sci. USA* 94, 3909–3913 (1997).

71. Gunzer, M. et al. A spectrum of biophysical interaction modes between T cells and different antigen-presenting cells during priming in 3-D collagen and in vivo. *Blood* 104, 2801–2809 (2004).
72. Friedl, P., den Boer, A.T. & Gunzer, M. Tuning immune responses: diversity and adaptation of the immunological synapse. *Nat. Rev. Immunol.* 5, 532–545 (2005).
73. Shakhar, G. et al. Stable T cell-dendritic cell interactions precede the development of both tolerance and immunity in vivo. *Nat. Immunol.* 6, 707–714 (2005).
74. wei, S.H. et al. Ca²⁺ signals in CD4⁺ T cells during early contacts with antigen-bearing dendritic cells in lymph node. *J. Immunol.* 179, 1586–1594 (2007).
75. Henrickson, S.E. et al. T cell sensing of antigen dose governs interactive behavior with dendritic cells and sets a threshold for T cell activation. *Nat. Immunol.* 9, 282–291 (2008).
76. Lu, T.T. & Cyster, J.G. Integrin-mediated long-term B cell retention in the splenic marginal zone. *Science* 297, 409–412 (2002).
77. Huse, M., Lillemeier, B.F., Kuhns, M.S., Chen, D.S. & Davis, M.M. T cells use two directionally distinct pathways for cytokine secretion. *Nat. Immunol.* 7, 247–255 (2006).
78. Sims, T.N. et al. Opposing effects of PKC θ and wA Sp on symmetry breaking and relocation of the immunological synapse. *Cell* 129, 773–785 (2007).
79. Nobile, C. et al. Cognate CD4⁺ T-cell-dendritic cell interactions induce migration of immature dendritic cells through dissolution of their podosomes. *Blood* 111, 3579–3590 (2008).
80. Chieppa, M., Rescigno, M., Huang, A.Y. & Germain, R.N. Dynamic imaging of dendritic cell extension into the small bowel lumen in response to epithelial cell TLR engagement. *J. Exp. Med.* 203, 2841–2852 (2006).
81. Schon, M.P., Schon, M., Parker, C.M. & Williams, I.R. Dendritic epidermal T cells (DETC) are diminished in integrin αE (CD103)-deficient mice. *J. Invest. Dermatol.* 119, 190–193 (2002).
82. Cepek, K.L. et al. Adhesion between epithelial cells and T lymphocytes mediated by E-cadherin and the αE β7 integrin. *Nature* 372, 190–193 (1994).
83. Okada, T. et al. Antigen-engaged B cells undergo chemotaxis toward the T zone and form motile conjugates with helper T cells. *PLoS Biol.* 3, e150 (2005).
84. Castellino, F. et al. Chemokines enhance immunity by guiding naive CD8⁺ T cells to sites of CD4⁺ T cell-dendritic cell interaction. *Nature* 440, 890–895 (2006).
85. Gunzer, M. et al. Antigen presentation in extracellular matrix: interactions of T cells with dendritic cells are dynamic, short lived, and sequential. *Immunity* 13, 323–332 (2000).
86. Cahalan, M.D. & Parker, I. Choreography of cell motility and interaction dynamics imaged by two-photon microscopy in lymphoid organs. *Annu. Rev. Immunol.* 26, 585–626 (2008).
87. Pham, T.H., Okada, T., Matloubian, M., Lo, C.G. & Cyster, J.G. S1P1 receptor signaling overrides retention mediated by G αi -coupled receptors to promote T cell egress. *Immunity* 28, 122–133 (2008).
88. Arita, M. et al. Resolvin E1 selectively interacts with leukotriene B4 receptor BLT1 and ChemR23 to regulate inflammation. *J. Immunol.* 178, 3912–3917 (2007).
89. Schwab, J.M., Chiang, N., Arita, M. & Serhan, C.N. Resolvin E1 and protectin D1 activate inflammation-resolution programmes. *Nature* 447, 869–874 (2007).
90. Van Lint, P. & Libert, C. Chemokine and cytokine processing by matrix metalloproteinases and its effect on leukocyte migration and inflammation. *J. Leukoc. Biol.* 82, 1375–1381 (2007).
91. Cyster, J.G. Chemokines, sphingosine-1-phosphate, and cell migration in secondary lymphoid organs. *Annu. Rev. Immunol.* 23, 127–159 (2005).
92. Stoitzner, P., Pfaller, K., Stossel, H. & Romani, N. A close-up view of migrating Langerhans cells in the skin. *J. Invest. Dermatol.* 118, 117–125 (2002).
93. Cinamon, G. et al. Sphingosine 1-phosphate receptor 1 promotes B cell localization in the splenic marginal zone. *Nat. Immunol.* 5, 713–720 (2004).
94. Debes, G.F. et al. Chemokine receptor CCR7 required for T lymphocyte exit from peripheral tissues. *Nat. Immunol.* 6, 889–894 (2005).
95. Ledgerwood, L.G. et al. The sphingosine 1-phosphate receptor 1 causes tissue retention by inhibiting the entry of peripheral tissue T lymphocytes into afferent lymphatics. *Nat. Immunol.* 9, 42–53 (2008).

96. Martín-Fontecha, A. et al. Regulation of dendritic cell migration to the draining lymph node: impact on T lymphocyte traffic and priming. *J. Exp. Med.* 198, 615–621 (2003).
97. Marttila-Ichihara, F. et al. Macrophage mannose receptor on lymphatics controls cell trafficking. *Blood* 112, 64–72 (2008).
98. Salmi, M., Koskinen, K., Henttinen, T., Elima, K. & Jalkanen, S. CLEVER-1 mediates lymphocyte transmigration through vascular and lymphatic endothelium. *Blood* 104, 3849–3857 (2004).
99. Auffray, C. et al. Monitoring of blood vessels and tissues by a population of monocytes with patrolling behavior. *Science* 317, 666–670 (2007).
100. Geissmann, F. et al. Intravascular immune surveillance by CXCR6+ NKT cells patrolling liver sinusoids. *PLoS Biol.* 3, e113 (2005).
101. Aloisi, F. & Pujol-Borrell, R. Lymphoid neogenesis in chronic inflammatory diseases. *nat. Rev. Immunol.* 6, 205–217 (2006).
102. Kratz, A., Campos-Neto, A., Hanson, M.S. & Ruddle, N.H. Chronic inflammation caused by lymphotoxin is lymphoid neogenesis. *J. Exp. Med.* 183, 1461–1472 (1996).
103. Gal, I. et al. Visualization and in situ analysis of leukocyte trafficking into the ankle joint in a systemic murine model of rheumatoid arthritis. *Arthritis Rheum.* 52, 3269–3278 (2005).
104. Firestein, G.S. Evolving concepts of rheumatoid arthritis. *nature* 423, 356–361 (2003).
105. Gressner, A.M. & Weiskirchen, R. Modern pathogenetic concepts of liver fibrosis suggest stellate cells and TGF-beta as major players and therapeutic targets. *J. Cell. Mol. Med.* 10, 76–99 (2006).
106. Camps, M. et al. Blockade of PI3Kγ suppresses joint inflammation and damage in mouse models of rheumatoid arthritis. *Nat. Med.* 11, 936–943 (2005).
107. Mathis, S., Jala, V.R. & Haribabu, B. Role of leukotriene B4 receptors in rheumatoid arthritis. *Autoimmun. Rev.* 7, 12–17 (2007).
108. Boissonnas, A., Fetler, L., Zeelenberg, I.S., Hugues, S. & Amigorena, S. In vivo imaging of cytotoxic T cell infiltration and elimination of a solid tumor. *J. Exp. Med.* 204, 345–356 (2007).
109. Breart, B., Lemaitre, F., Celli, S. & Bousso, P. Two-photon imaging of intratumoral CD8 T cell cytotoxic activity during adoptive T cell therapy in mice. *J. Clin. Invest.* 118, 1390–1397 (2008).
110. Jaaskelainen, J. et al. Migration of recombinant IL-2-activated T and natural killer cells in the intercellular space of human H-2 glioma spheroids in vitro. A study on adhesion molecules involved. *J. Immunol.* 149, 260–268 (1992).
111. O’Hayre, M., Salanga, C.L., Handel, T.M. & Allen, S.J. Chemokines and cancer: migration, intracellular signalling and intercellular communication in the microenvironment. *Biochem. J.* 409, 635–649 (2008).
112. Silzle, T. et al. Tumor-associated fibroblasts recruit blood monocytes into tumor tissue. *eur. J. Immunol.* 33, 1311–1320 (2003).
113. Orimo, A. et al. Stromal fibroblasts present in invasive human breast carcinomas promote tumor growth and angiogenesis through elevated SDF-1/CXCL12 secretion. *Cell* 121, 335–348 (2005).
114. Zhang, T. et al. CXC chemokine ligand 12 (stromal cell-derived factor 1 alpha) and CXCR4-dependent migration of CTLs toward melanoma cells in organotypic culture. *J. Immunol.* 174, 5856–5863 (2005).
115. Zhang, B., Chan, Y.K., Lu, B., Diamond, M.S. & Klein, R.S. CXCR3 mediates region-specific antiviral T cell trafficking within the central nervous system during west Nile virus encephalitis. *J. Immunol.* 180, 2641–2649 (2008).
116. Brown, C.E. et al. Tumor-derived chemokine MCP-1/CCL2 is sufficient for mediating tumor tropism of adoptively transferred T cells. *J. Immunol.* 179, 3332–3341 (2007).
117. Winter, H. et al. Therapeutic T cells induce tumor-directed chemotaxis of innate immune cells through tumor-specific secretion of chemokines and stimulation of B16BL6 melanoma to secrete chemokines. *J. Transl. Med.* 5, 56 (2007).
118. Mrass, P. et al. Random migration precedes stable target cell interactions of tumor-infiltrating T cells. *J. Exp. Med.* 203, 2749–2761 (2006).
119. Kawakami, N. et al. Live imaging of effector cell trafficking and autoantigen recognition within the unfolding autoimmune encephalomyelitis lesion. *J. Exp. Med.* 201, 1805–1814 (2005).

120. Le Floc'h, A. et al. $\alpha\text{E}\beta 7$ integrin interaction with E-cadherin promotes antitumor CTL activity by triggering lytic granule polarization and exocytosis. *J. Exp. Med.* 204, 559–570 (2007).
121. Thomsen, A.R., Nansen, A., Madsen, A.N., Bartholdy, C. & Christensen, J.P. Regulation of T cell migration during viral infection: role of adhesion molecules and chemokines. *Immunol. Lett.* 85, 119–127 (2003).
122. Applegate, K.G., Balch, C.M. & Pellis, N.R. In vitro migration of lymphocytes through collagen matrix: arrested locomotion in tumor-infiltrating lymphocytes. *Cancer Res.* 50, 7153–7158 (1990).
123. Mempel, T.R. et al. Regulatory T cells reversibly suppress cytotoxic T cell function independent of effector differentiation. *Immunity* 25, 129–141 (2006).
124. Lalor, P.F. & Adams, D.H. Adhesion of lymphocytes to hepatic endothelium. *Mol. Pathol.* 52, 214–219 (1999).
125. Warren, A. et al. T lymphocytes interact with hepatocytes through fenestrations in murine liver sinusoidal endothelial cells. *Hepatology* 44, 1182–1190 (2006).
126. Xu, X.D. et al. Trafficking of recirculating lymphocytes in the rat liver: rapid transmigration into the portal area and then to the hepatic lymph. *Liver Int.* 28, 319–330 (2008).
127. Valiante, N.M. et al. Life, activation and death of intrahepatic lymphocytes in chronic hepatitis C. *Immunol. Rev.* 174, 77–89 (2000).
128. Zeremski, M., Petrovic, L.M. & Talal, A.H. The role of chemokines as inflammatory mediators in chronic hepatitis C virus infection. *J. Viral Hepat.* 14, 675–687 (2007).
129. Hokeness, K.L. et al. CXCR3-dependent recruitment of antigen-specific T lymphocytes to the liver during murine cytomegalovirus infection. *J. Virol.* 81, 1241–1250 (2007).
130. Saunders, B.M. & Britton, w.J. Life and death in the granuloma: immunopathology of tuberculosis. *Immunol. Cell Biol.* 85, 103–111 (2007).
131. Egen, J.G. et al. Macrophage and T cell dynamics during the development and disintegration of mycobacterial granulomas. *Immunity* 28, 271–284 (2008).
132. Ben-Chetrit, E., Bergmann, S. & Sood, R. Mechanism of the anti-inflammatory effect of colchicine in rheumatic diseases: a possible new outlook through microarray analysis. *Rheumatology (Oxford)* 45, 274–282 (2006).
133. Aiello, R.J. et al. Leukotriene B4 receptor antagonism reduces monocytic foam cells in mice. *arterioscler. thromb. Vasc. Biol.* 22, 443–449 (2002).
134. Chiba, K. FTY720, a new class of immunomodulator, inhibits lymphocyte egress from secondary lymphoid tissues and thymus by agonistic activity at sphingosine 1-phosphate receptors. *Pharmacol. Ther.* 108, 308–319 (2005).
135. Barber, D.F. et al. PI3K inhibition blocks glomerulonephritis and extends lifespan in a mouse model of systemic lupus. *nat. Med.* 11, 933–935 (2005).
136. Wenzel, J., Uerlich, M., Haller, O., Bieber, T. & Tueting, T. Enhanced type I interferon signaling and recruitment of chemokine receptor CXCR3-expressing lymphocytes into the skin following treatment with the TLR7-agonist imiquimod. *J. Cutan. Pathol.* 32, 257–262 (2005).
137. Schon, M.P. & Schon, M. TLR7 and TLR8 as targets in cancer therapy. *Oncogene* 27, 190–199 (2008).
138. Hauzenberger, D., Klominek, J. & Sundqvist, K.G. Functional specialization of fibronectin-binding beta 1-integrins in T lymphocyte migration. *J. Immunol.* 153, 960–971 (1994).
139. Nemoto, E., Tada, H. & Shimauchi, H. Disruption of CD40/CD40 ligand interaction with cleavage of CD40 on human gingival fibroblasts by human leukocyte elastase resulting in down-regulation of chemokine production. *J. Leukoc. Biol.* 72, 538–545 (2002).
140. Pasvolsky, R. et al. RhoA is involved in LFA-1 extension triggered by CXCL12 but not in a novel outside-in LFA-1 activation facilitated by CXCL9. *J. Immunol.* 180, 2815–2823 (2008).
141. Van Vliet, E., Melis, M., Foidart, J.M. & Van Ewijk, w. Reticular fibroblasts in peripheral lymphoid organs identified by a monoclonal antibody. *J. Histochem. Cytochem.* 34, 883–890 (1986).



CHAPTER 3

Intravital Third Harmonic Generation Microscopy of Collective Melanoma Cell Invasion: Principles of Interface Guidance and Microvesicle Dynamics

Weigelin B¹, Bakker GJ¹ & Friedl P^{1,2}

IntraVital 2012; 1:9-20.

¹ Department of Cell Biology, Radboud University Nijmegen Medical Centre,
The Netherlands

² David H. Koch Center for Applied Research of Genitourinary Cancers, Department of
Genitourinary Medical Oncology, The University of Texas MD Anderson Cancer Center,
Houston, USA

Abstract

Cancer cell invasion is an adaptive process based on cell-intrinsic properties to migrate individually or collectively, and their adaptation to encountered tissue structure acting as barrier or providing guidance. Whereas molecular and physical mechanisms of cancer invasion are well-studied in 3D *in vitro* models, their topographic relevance, classification and validation toward interstitial tissue organization *in vivo* remain incomplete. Using combined intravital third and second harmonic generation (THG, SHG), and three-channel fluorescence microscopy in live tumors, we here map B16F10 melanoma invasion into the dermis with up to 600 μm penetration depth and reconstruct both invasion mode and tissue tracks to establish invasion routes and outcome. B16F10 cells preferentially develop adaptive invasion patterns along preformed tracks of complex, multi-interface topography, combining single-cell and collective migration modes, without immediate anatomic tissue remodeling or destruction. The data suggest that the dimensionality (1D, 2D and 3D) of tissue interfaces determines the microanatomy exploited by invading tumor cells, emphasizing non-destructive migration along microchannels coupled to contact guidance as key invasion mechanisms. THG imaging further detected the presence and interstitial dynamics of tumor-associated microparticles with submicron resolution, revealing tumor-imposed conditioning of the microenvironment. These topographic findings establish combined THG, SHG and fluorescence microscopy in intravital tumor biology and provide a template for rational *in vitro* model development and context-dependent molecular classification of invasion modes and routes.

Introduction

Tumor cell invasion into adjacent tissues is a key step of cancer cell dissemination towards locoregional and systemic metastasis^{1,2}. Invasive migration of individual cells through 3D connective tissue depends upon a sequence of physicochemical steps that generate polarized cell interaction with the tissue substrate and force transmission. Actin-driven protrusion of the leading edge is followed by focalized cell-matrix adhesion, proteolysis of extracellular matrix constraints and actomyosin mediated contractions of the cell body, which together mediate a cycle of forward protrusion and rear retraction.³ Besides individual cell migration, collective invasion of multiple cells occurs when moving cells maintain functional cell-cell adhesion, leading to a “supracellular” organization of the actin cytoskeleton and multicellular polarity, protrusion and traction force generation.⁴ Single-cell and collective invasion are interconvertible, dependent on the up- or downregulation of cell-cell junctions and supracellular coordination; consequently, in cancer lesions invasion patterns range from broad multicellular masses with intact

cell-cell connections to small multicellular files and fully individualized cells.⁵ The cellular and molecular mechanisms driving different types of cancer invasion are commonly studied *in vitro* using reconstituted 2D or 3D environments with relatively uniform but controllable structural pattern and composition.^{6,7} In connective tissue *in vivo*, tumor cells however face more complex and structurally heterogeneous 3D tissue architecture consisting of molecular and physical interfaces of different composition, length scale and stiffness, that provide space and guidance or act as a physical barrier and restrict cell motility.^{8,9} Thereby, multiple cell and ECM parameters are integrated by migrating cells to determine type, direction, efficiency and protease-dependence of migration.^{5,8} Traditionally, the guidance mechanisms of cancer cell invasion are deduced from histological tissue samples or defined *in vitro* environments, resulting in the concepts of barrier function of connective tissue as well as its guidance principles.^{5,10} *In vitro* models have allowed to establish the mechanisms of contact guidance, chemotaxis, guidance by gradients of adhesive substrates (haptotaxis) and substrate rigidity (durotaxis), and the *de novo* track generation by proteolytic remodeling of tissue structures.^{3,11,12} *In vivo*, deduced from histopathological analysis of tumor samples, cancer invasion preferentially occurs along tracks of least resistance such as perineural, perimuscular and perivascular invasion,⁹ however the relative contribution of molecular and biophysical guidance mechanisms, such as matrix guidance vs. barrier function, remain to be determined. As complement to histological studies which provide a static and two-dimensional view on a dynamic and three-dimensional biological process and further suffers from structural artifacts due to tissue fixation and processing, intravital microscopy provides direct access to the three-dimensional cell and tissue morphology and function at cellular resolution and over time. Thereby, multiphoton-excited second and third harmonic imaging allows the visualization of 3D topography of tissue structures^{13,14} and delivers comprehensive insight into cell invasion and topographic guidance by tissues.^{10,15-17} Second harmonic generation (SHG) results from the near-simultaneous arrival of two photons at dense, non-centrosymmetric structures to be combined into one emitted photon of half the wavelength.^{14,18} In interstitial tissues, SHG is elicited by collagen fibers and striated muscle myosin,¹⁸ detecting tumor-associated remodeling of collagen-rich ECM.^{10,19} Third harmonic generation (THG) is sensitive to local differences in third-order nonlinear susceptibility, refractive index and dispersion, resulting in unification of three near-simultaneously arriving photons to one emitted photon of triple frequency.²⁰ In tissues, third harmonic signals are particularly generated by water-lipid or water-protein scaffold interfaces and media of optical heterogeneity, including lipid bodies, fat cells, nerve fibers as well as cell membranes and intracellular vesicles.²¹⁻²³ Similar to SHG, THG is a predominantly forward scattering signal, the optimized detection of which requires

excitation by a strong pulsed infrared laser and forward detection, amenable to transparent samples or organisms including embryos of Zebrafish, *Drosophila*, *C. elegans* or mouse.²⁴⁻²⁷ As caveat of THG imaging in thick and optically challenging samples, such as collagen-rich connective tissue and tumors, the high laser intensities required for backward detection of scattered signal may introduce phototoxicity and compromise cell and tissue function. Consequently, examples for backward THG in interstitial tissues are rare, except for imaging of thin or poorly absorbing samples, such as the mouse cremaster muscle,²² lung surface²⁸ and mouse spinal cord²³ or brain tissue.²⁹ Thus, the potential of THG imaging in thick and scattering tissues and disease states, such as progressing tumors, remains uncertain. Using infrared multiphoton microscopy (MPM),³⁰ we establish the efficacy and tolerability of backward THG compared with SHG and fluorescence detection in tumor-free and B16F10 melanoma-bearing tissue in live mice. The data establish THG as important complement to SHG and fluorescence imaging for the longitudinal monitoring of cancer biology in living tissue and the detection of migration-enhancing and -impeding tissue structures, particularly to tumor invasion routes, secondary tissue remodeling and microenvironment conditioning by microparticles.

Results

Model set up for backward third harmonic generation (THG) microscopy.

A tandem near-infrared and infrared MPM set-up was used for simultaneous excitation of THG, SHG, and fluorophores GFP, E2-Crimson and AlexaFluor750 for both, forward and backward detection (Fig. 1A and B). To optimize THG efficacy, 3D collagen lattices containing homogeneously distributed single cells were used to detect backward and forward THG and SHG emission from collagen fibers and cells at increasing excitation power (Fig. 1B, left). THG and SHG emission were significantly stronger in forward compared with backward direction (SHG: ~5 times, THG: ~25 times) and showed respective third- and second order dependence (Fig. 1C), as described.^{20,22} To determine an optimized wavelength for simultaneous THG and SHG, excitation spectra were obtained by intravital imaging of mouse dermis at constant laser power (80 mW under the objective) and the backscatter of both signals was collected by rearward detection, showing peak efficacies at excitation with 1190 nm and 1130 nm wavelengths, respectively (Fig. 1D). The poor THG efficiency at emission wavelengths below 390 nm (corresponding to THG excitation wavelength of 1170 nm) is consistent with the limited UV transmission of barium fluoride glass components in the beam path. Because weak THG signals are rate-limiting in the backward direction, 1180 nm excitation for highest THG efficacy was used subsequently. Signal selectivity and separation were verified by

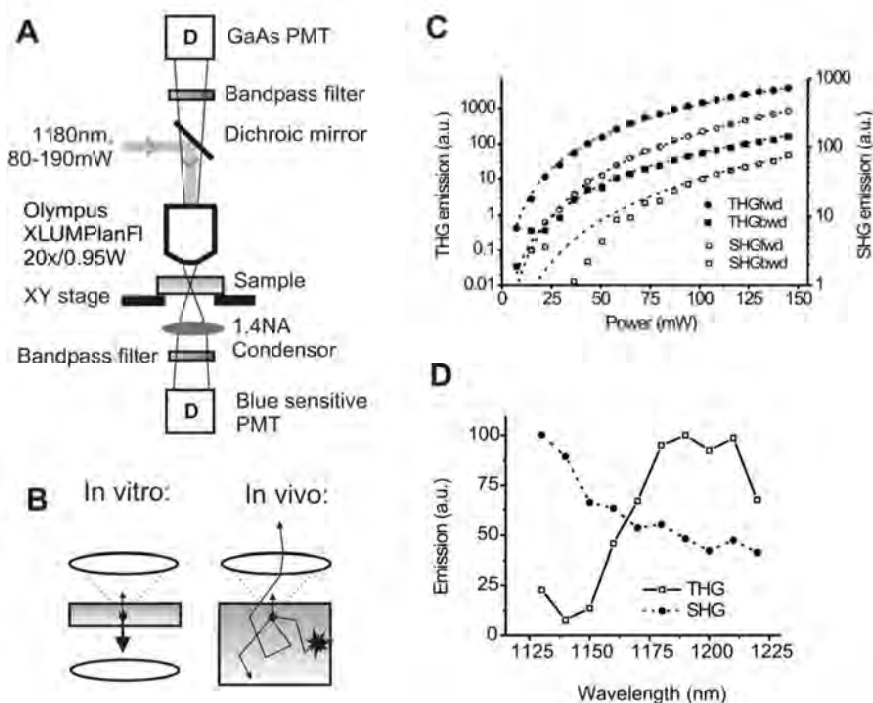


Figure 1. Beam path and efficiency of forward and backward third- and second-harmonic generation. (A) Beam path and main components of the multiphoton microscope including detectors (D) and numerical aperture (NA). **(B)** Detection of THG and backward scattered emission from thick light-absorbing in vivo samples (right), compared with THG detection of most in vitro or thin ex vivo samples (left). **(C)** THG and SHG emission from mouse fibrosarcoma (MCA-101) cells embedded in collagen matrix, as a function of excitation power. Emission was detected in the forward (fwd) and backward (bwd) direction. To separate emission from the background, images were background subtracted and thresholded before the average intensity was calculated in regions of interest containing SHG or THG emitting structures (collagen, intracellular vesicles). THG emission showed best fit with a model function dependent on the third-order of the excitation power (reduced-chi-sqr = 5 and 52 for forward and backward detection, respectively; dashed lines; 5% relative error in excitation power), whereas SHG emission showed best fit with second-order excitation (chi-sqr = 0.58 and 360 for forward and backward detection, respectively). **(D)** THG and SHG excitation spectra of the structures of the mouse dermis in backward direction (compare to Fig. 3). Images were acquired using a custom python script, controlling OPO wavelength, attenuator and tube lens settings to maintain constant excitation power (100 mW) and focal plane over the scanned wavelength range (1,130–1,220 nm). Curves were normalized to take fluctuations of the laser power into account.

the narrow filter bandwidth (FF01 395/8 (THG) and FF01 593/11 (SHG) and by the type and topography of emitting structures (Fig. 1C; Vid. S1).

Backward THG imaging in vivo: tissue penetration and phototoxicity.

The invasion of B16F10 melanoma cells was monitored using the dorsal skin-fold chamber model for multiphoton-excited THG, SHG and fluorescence intensity detection in backward direction in established tumors.¹⁶ Because surgery is performed only prior to tumor implantation but not required at the day of imaging, this model allows live-tumor observations without surgery-imposed disturbance of tissue anatomy including perfusion, cell viability and motility, and thus provides sufficient tissue stability for high-resolution time-lapse studies and particle-tracking. To establish the depth efficacy of backward THG compared with SHG and NIR fluorescence (AlexaFluor750) detection in the mouse dermis, the respective intensities retrieved with increasing imaging depth were estimated from a deep z-stack reaching 870 μm into the dermis. THG was retrieved for a significant tissue volume, ranging from deep to mid dermis with peak intensities caused by dense collagen and a fat cell layer located at 500 to 600 μm and sufficient THG signal-to-noise ratio reached to 650 μm in depth (Fig. 2A; Vid. S1). Likewise, SHG and NIR fluorescence were retrieved with similar profile and maximum depths of up to 650 μm (Fig. 2A). Thus, despite its emission in the blue range which shows higher absorption by tissue structures compared with red signal, the sensitive setup allowed to detect backward THG at depths beyond 600 μm . Because of the high laser power required to obtain THG in backward direction (100 to 150 mW under the objective), we addressed the risk of laser-induced tissue damage using continuous exposure and time-lapse monitoring of potentially sensitive tissue structures, such as highly absorbing fat cells and capillaries. Using a typical time-lapse setting with 60 sec time interval between individual z-scans, tissue integrity remained unperturbed for a 3.8 h observation period (230 frames), including normal morphology of fat cells, collagen fibers and striated myofibers, as well as regular erythrocyte flow indicating lack of heat-induced blood clotting with erythrocyte stasis (Fig. 2B, Vid. S2). To test the toxicity limits of time-lapse THG microscopy, a small scan field was exposed to continuous scanning of the same focal plane (130 mW laser power under the objective; frame rate 1.1/ sec). Regular erythrocyte flow persisted for 60 sec (60 frames), but with doubling of the frame rate (0.6/sec) tissue damage including swelling of fat cells (Fig. 2C, asterisk), intra-vascular coagulation and perturbed erythrocyte flow (Fig. 2C, arrowheads) were rapidly induced. Thus, with sufficient time intervals between individual imaging scans, even high infrared laser intensities required for generating backward THG are well tolerated by dermal tissues, whereas conditions requiring small imaging fields and continuous or high-speed exposure may be challenged by photodamage.

Interfaces of the tumor-free deep dermis.

THG is an interface signal particularly suited to detect cell membranes and tissue discontinuities.^{14,22} In the deep dermis of tumor-free mice, backward THG was generated by interfaces of cells and ECM while SHG was confined to fibrillar collagen and actomyosin structures, similar to mouse cremaster tissue.²² With progressing imaging depth, tissue structures eliciting THG included the loose connective tissue of the deep dermis (Fig. 2A; Vid. S2), a muscle layer, perfused blood vessels and nerves of the mid-dermis (Fig. 3A) and adipocytes with adjacent collagen bundles of the upper mid-dermis (Fig. 3B). Strongest THG was elicited by thick collagen bundles (Fig. 3C and D), peripheral nerves (Fig. 3D), adipocytes (Fig. 3E), striated muscle fibers (Fig. 3F) and perfused blood vessels (Fig. 3F). Combined with SHG and fluorescence signal, THG delivered quantitative information on the 3D anatomy of connective tissue, including pre-existing tissue tracks and barriers that may impact tumor cell invasion. Collagen networks were heterogeneous in organization, including randomly organized loose collagen networks (Fig. 3C; space diameter up to 30 μm) and aligned and more densely structured collagen bundles bordered by longitudinal, fissure-like tracks (Fig. 3D; 5–10 μm diameter). Spaces between fat cells included interspersed collagen bundles and showed heterogeneous widths, ranging from narrow clefts (1–2 μm) to wider gaps (up to 10 μm in cross-section) (Fig. 3E). Perineural tracks defined by nerve strands eliciting strong THG and adjacent collagen bundles generating both SHG and THG were linear in shape with 2–5 μm in diameter (Fig. 3D). Similar longitudinal interface signals were present along and between myofibers, revealing narrow tracks (up to 5 μm in cross-section) or imposing as interface signal without apparent track lumen (Fig. 3F, dotted lines). Thus, complementary THG/SHG imaging allows detailed 3D reconstructions of anatomic tissue structures and interfaces, suggesting a constitutive range of collapsed and non-collapsed tracks.

Interfaces guiding invasion of B16F10 melanoma cells.

B16F10 melanoma tumors expressing a mixture of H2B-eGFP single and H2B-eGFP/E2-Crimson double positive cells (Fig. S1A) were implanted in the dorsal skin-fold chamber and growth and invasion dynamics were monitored over up to 13 d. The growth curve of the main tumor, after an initial lag phase of 2 to 3 d, showed exponential growth starting day 4–5 (Fig. 1A), as described for other tumor types.¹⁶ The onset of invasion was observed in most tumors 1 to 4 d after implantation, resulting by day 8 in multicellular elongated strands of up to 120 densely arranged cells with several hundred micrometer in length (Fig. 4B). Dependent on the guiding tissue structures, two types of collective invasion were observed, (1) linear multicellular files headed by one or two leading tip

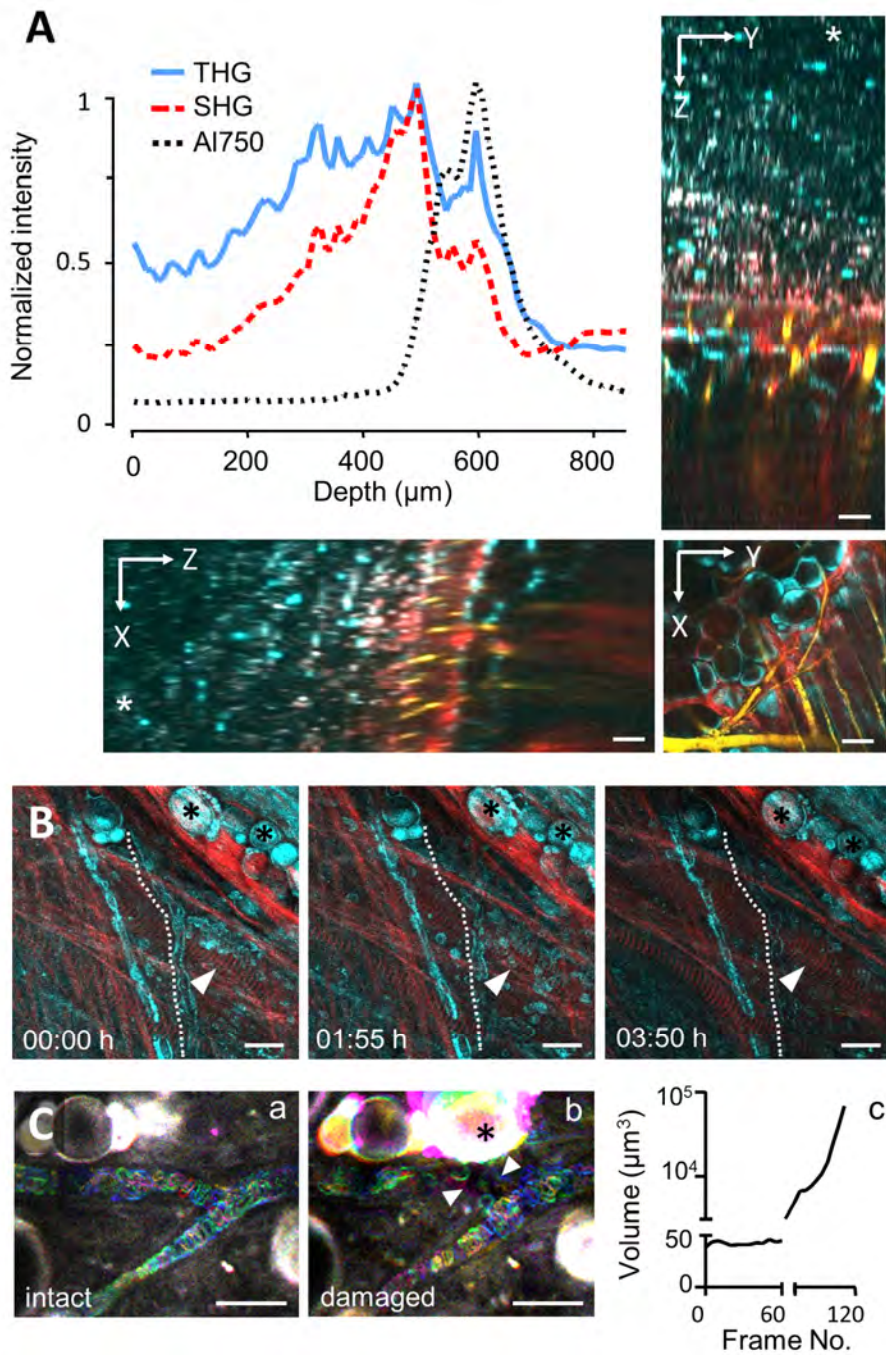


Figure 2. See next page.

Figure 2. Depth efficiency and phototoxicity of backward THG. (A) THG, SHG and AlexaFluor750 signal intensity as function of depth obtained from a 870 μm deep z-stack into the mouse dermis (*, level of the cover glass above the tissue). Images were acquired with a z-resolution of 10 μm , excitation wavelength of 1,180 nm and an excitation power of 150 mW under the objective. Images were background subtracted and average intensity of THG/SHG or AlexaFluor750 signals over the z-profile was plotted. THG (cyan) was detected up to 650 μm , similarly to SHG (red) and Alexa-Fluor750 (yellow). (B) Representative time points of THG (cyan) and SHG (red) during time-lapse recording of dermal tissue [λ (excitation) = 1,180 nm; 110 mW excitation power under the objective]. Z-scans of 80 μm tissue volume were acquired with z-steps of 5 μm and frame intervals of 60 sec (230 frames; 3.8 h observation period). Unperturbed tissue structures, including fat cells (asterisks), muscle fibers (arrow heads) and erythrocyte flow in capillaries (dotted line). (C) erythrocyte flow (temporal color coded) morphology of adipocytes (asterisk). (a) continuous exposure of small (60 μm \times 70 μm) scan field for 60 frames (frame rate: 1.1/sec) at 1,180 nm excitation and 130 mW excitation intensity. (b and c) Doubling of the frame rate (0.6/sec) followed by tissue damage, detected by swelling of adipocytes (asterisk) and intravascular coagulation and perturbed erythrocyte flow (arrowheads). Scale bars, 20 μm .

cells (Fig. 4A–D), and (2) broad collective invasion zones lead by multiple tip cells (Fig. 4E). Linear invasion strands were composed of coherent, tightly organized cell strains of uniform 3–5 cells in diameter, consistent with collective invasion,¹⁶ and detachment of single cells or small cell files was observed at the tips of a subset of invasion strands (Fig. 4B, inset).

Despite their compact organization, time-lapse recording and single-cell tracking revealed high intra-strand dynamics of individual B16F10 cells within multicellular strands maintaining median velocities of 0.25 $\mu\text{m}/\text{min}$ in forward and, occasionally, rearward direction (Fig. 4C; Vid. S3). Thereby, linear invasion strands recapitulated the orientation of confined 3D spaces present in the tissue, particularly aligned muscle fibers, small blood vessels, and perineural tracks detected by THG/SHG (Fig. 4D). Perimuscular invasion followed the outline of myofibers precisely, often accompanied by tumor cell deformation to adapt to the given narrow tracks between adjacent myofibers or myofiber and blood vessel (Fig. 5A). Occasionally, invading tumor strands entirely wrapped around the complete circumference of the myofiber with the nuclei in outward direction and inward-oriented cell extensions, consistent with cell polarization toward the myofiber interface (Fig. 4F; Fig. S2B). Remarkably, melanoma-cell containing paths were thereby widened to a caliber of 1 to 3 cells without apparent destruction of muscle integrity (Fig. 4D and F). Likewise, perineural space guided linear tumor cell strands with tumor cells oriented between lining collagen bundles and the nerve fiber, resulting in thin files (Fig. 4G, dotted line). Diffuse collective invasion into the irregular spaces of fat tissue and collagen networks consisted of two morphological zones. First, multiple “leader” cells formed an invasive front infiltrating with thin lamella-like protrusions along the interfaces between adipocyte surfaces and adipocyte and collagen bundles (Fig. 4H, arrowheads). This invasion front was followed by a broad multicellular mass which

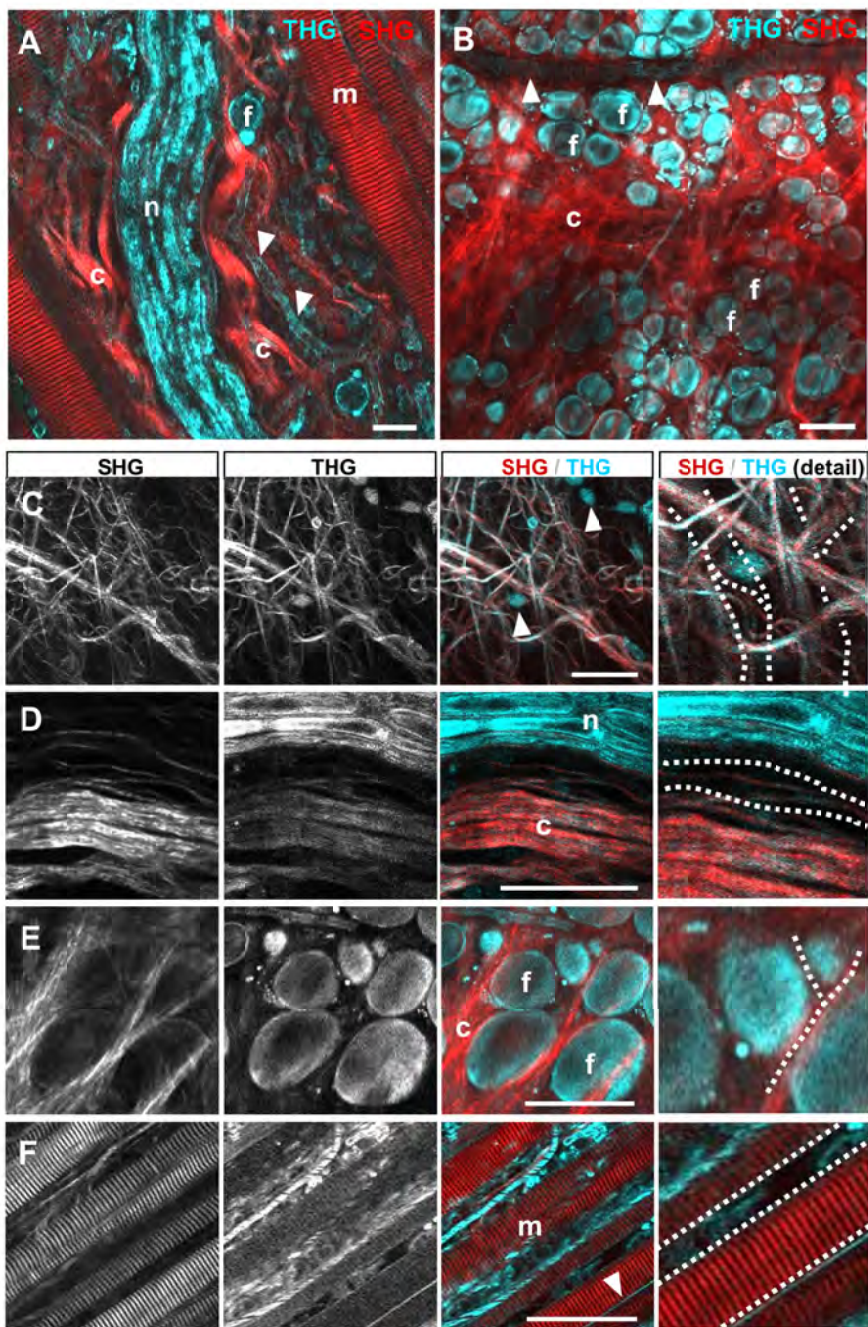


Figure 3. See next page.

Figure 3. THG/SHG 3D reconstruction of tissue interfaces in native dermis. Backward THG/SHG were acquired at 1180nm excitation and 100-130mW laser intensity under the objective. THG was generated by cellular interfaces of fat cells (**A-B, E**); flowing erythrocytes labeling perfused blood vessels (**A-B**; arrowheads); cell bodies interspersed in loose connective tissue (**C**; arrowheads); matrix interfaces including collagen fiber bundles (**C-D**); peripheral nerves (**A, D**); striated muscles (**F**) and outer membranes of myofibers (**F**; arrowhead). SHG was confined to collagen bundles (**A-B, D**) and striated muscle fibers (**A, F**). Combined THG/SHG revealed tissue tracks and spaces available for tumor cell invasion (examples highlighted in C-F as dotted lines). Scale bars, 50 μ m. Abbreviations: f, fat cells; m, myofiber; n, nerve; c, collagen.

surrounded adipocytes and concomitantly widened existing spaces without obvious adipocyte destruction, but the SHG signal of collagen bundles between adipocytes somewhat weakened (Fig. 4E). A similar diffuse invasion with often single-cell or loosely connected multicellular pattern occurred along and into collagen networks, characterized by a broad, loosely interconnected leading edge of multiple tip cells followed by a multicellular group, aligned parallel to collagen fibers (Fig. 4L; Fig. S2). When encountering narrow pores in the collagen network, cells deformed and adapted their shape to the given trail diameters (Fig. 4L). To estimate the reciprocal adaptation of tumor cells and tissue tracks and obtain insight into the extent of tissue remodeling secondary to invasion, track widths in tumor-free tissues, i.e., before invasion, were compared with the diameter of invading B16F10 cells, as measured for the space consumed between tissue boundaries (Fig. 5A). Near-identical constitutive track widths and diameters of infiltrating tumor cell bodies were found for collagen networks, perineural and adipose tissue invasion, suggesting lack of microscopic tissue deformation or degeneration at leading fronts of invasion (Fig. 5B). In contrast, track widening by 5–10 μ m was detected for perimuscular invasion, suggesting either proteolytic degradation of boundaries or non-proteolytic track widening by passive by outward pushing and space expansion. Cell diameters were largely unaltered in loose collagen tissue, besides occasional cell bodies squeezing through narrow matrix pores resulting in localized cell deformation (Fig. 4L, arrowhead; 2–5 μ m in cross-section).

Likewise, perimuscular, perineural, and fat tissue invasion resulted in similar deformation of cell bodies with diameters of cell bodies ranging from 3–10 μ m (Fig. 5B). Thus, SHG/THG imaging of tissue scaffolds, together with fluorescence detection of cell body and nucleus allow to establish a quantitative map of constitutive tissue tracks before and during cell invasion. The data suggest that the leader cells of collective tumor invasion preferentially exploit pre-existing tissue tracks and adapt their shape to the space available; thereby perimuscular tracks receive minor and other tracks no widening, without evidence for large-scale de-novo track generation or tissue destruction.

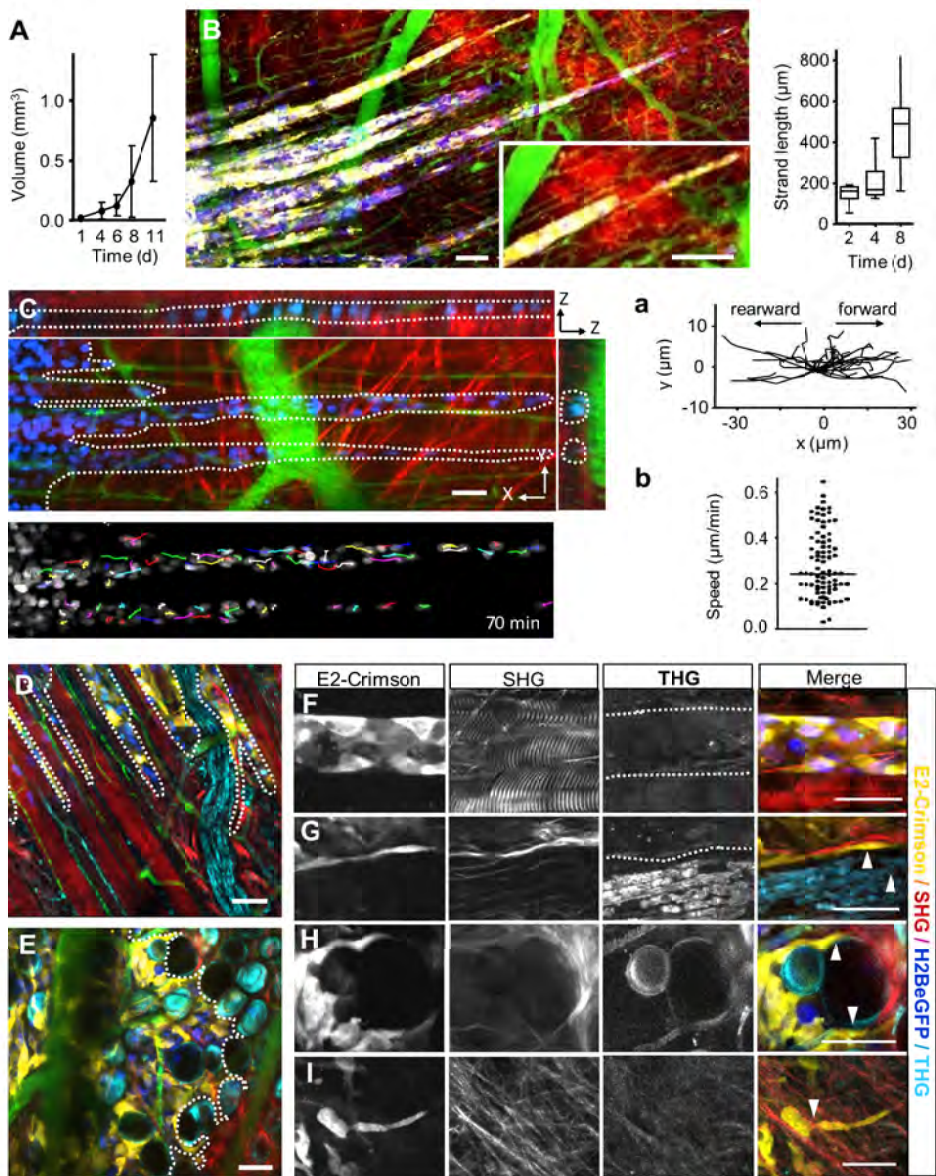


Figure 4. B16F10 melanoma invasion along dermal tissue interfaces. (A) B16F10 tumor volume growth over time. Error bars, mean \pm SD (n=8). (B) File-like collective invasion of mosaic tumors (compare Supplementary Fig. 2A) into the deep dermis. Invasion strands progressed on average 70 $\mu\text{m}/\text{day}$ (b) and appeared as coherent and tightly organized cell strains of near-constant diameter, except for occasional detachment of single cells or small cell files at the tip of the strands (B, inset). (C) Time-lapse microscopy and single-nuclei tracking show high intra-strand dynamics in rearward and forward direction (a) with median velocities of 0.25 $\mu\text{m}/\text{min}$ (b). During migration individual tumor cells remained within the 3D spaces defined by tissue interfaces (C, dotted lines) with leading edges strongly adapted to tissue confinement (D, E; dotted lines). Linear, aligned tracks along muscle fibers and nerves guiding file-like collective invasion (D), while irregular shaped spaces within fat tissue supported broad and diffusely organized collective invasion patterns (E). Invading tip cells preferentially moved along tissue interfaces such as linear perimuscular (F; dotted lines) and perineural (G; dotted lines) tracks, and irregular trails consisting of adipocyte interfaces (H) or collagen fiber networks (I). Cell body adapting to existing matrix spaces (F-I; arrowheads). Backward THG/SHG, E2-Crimson and AlexaFluor750 were excited with 1180nm (100-130 mW), eGFP was excited with 910nm (20-40 mW). Color scale: yellow, E2-Crimson (tumor cytoplasm); blue, histone-2B/eGFP (tumor nuclei); green, AlexaFluor750 (blood vessels); red, SHG; cyan, THG. Scale bars, 50 μm .

Conditioning of the tumor microenvironment by microparticles.

Whereas little immediate remodeling of tissue structures was noted during invasion, THG revealed altered tissue composition via strongly THG-positive tumor-associated microvesicles or microparticles. Using THG as measure, the size of microparticles ranged from below 1 μm in diameter (corresponding to 1–2 pixels in lateral diameter) to larger particles of up to 8 μm in diameter (Fig. 6A and B). In the B16/F10 live-cell models *in vitro* and *in vivo*, microparticles commonly lacked cytosolic fluorescence of E2-Crimson, in contrast to intact cells, larger macroaggregates and cell debris (Figs. S3, S4 and Vid. S6). Microvesicles are shed from a variety of cells including tumor cells during invasion³¹ (data not shown), and have been implicated in intercellular communication, with variable function depending on the cellular origin and cargo contained.³² To monitor the kinetics of microparticles *in vivo*, time-lapse microscopy was performed and the diffusion dynamics of THG-positive particles were compared with marker regions of the SHG-positive collagen network (Fig. 6A). Tracking of microparticle mobility showed at last three distinct subsets, including non-moving, randomly moving and directionally moving particles (Fig. 6C). The velocity and diffusion constant distributions of mobile THG-positive particles (filled bars) exceeded the dynamics of collagen reference points (open bars) reaching velocities of 9 $\mu\text{m}/\text{h}$, whereas a subset of particles showed overlapping velocity and diffusion constants consistent with immobilization (Fig. 6C and D). These observations suggest that the majority of THG-positive microparticles are mobile and independent of small tissue drifts which are intrinsic to live-tissue dynamics during intravital microscopy.

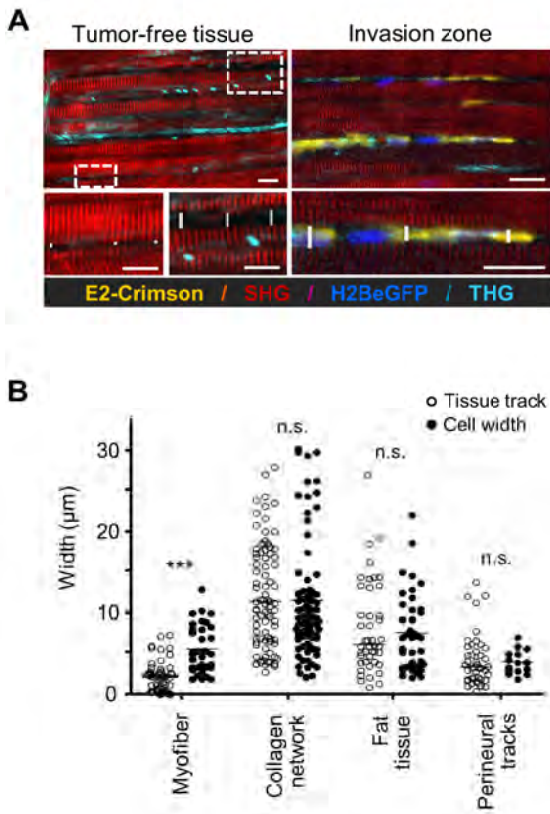


Figure 5. Quantification of native tissue spaces and tumor cell adaptation to pre-existing tissue tracks. (A) The diameter of tumor-free tissue tracks quantified from SHG and THG imaging (left) was compared with the diameter of invading cells, visualized by fluorescence of the cytoplasm and/or the nucleus. As example, perimuscular invasion is shown. Scale bar: 20µm. **(B)** Diameters of THG-/SHG-negative spaces and tracks in native, tumor-free tissue, compared with the diameter of tumor cell bodies during invasion. Tracks along myofibers were significantly widened by tumor cell infiltration (two-tailed Mann-Whitney test; *** = $p < 0.0001$), while all other tissue tracks maintained their original dimensions and required tumor cell adaptation (n.s., not significant). For each condition, at least 3 independent tissue samples were quantified.

These mobility characteristics of THG-positive particles showed regional variability suggesting that either random or directional movement, or immobilization depend upon properties of tissue micro-regions (Fig. 6A and C), the diverging nature of which remain to be identified. Thus, THG is suited to visualize the dynamics of tumor-associated microparticles *in vivo*, including locally tethered and slowly drifting subsets.

Discussion

Multimodal multiphoton microscopy combining THG, SHG and fluorescence intensity detection allows structure-function studies of cancer cell invasion in non-processed, live tissue with high penetration depth, submicron resolution and acceptable toxicity. Thereby, SHG excited by non-centrosymmetric structures, including collagen and striated actomyosin, and THG elicited by cell and tissue interfaces, including adipocytes, nerve fibers, perfused blood vessels, collagen fiber bundles and cell-derived particles deliver complementary read-out of the native tissue anatomy and function.

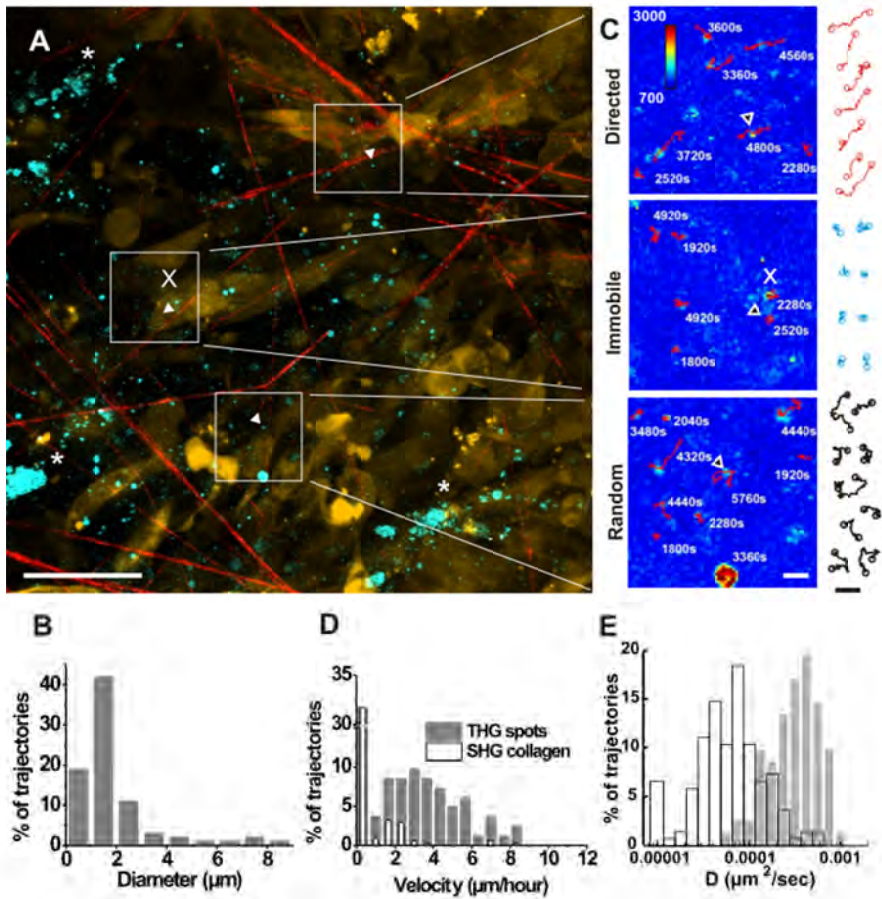


Figure 6. In vivo detection of microparticle location and dynamics. (A) Overview of THG emitting randomly distributed microparticles (white arrow-heads) and aggregated, likely intracellular vesicles (asterisks) detected at the border of a B16F10 tumor (d13) nearby collagen fiber-containing stroma. (B) The distribution of particle sizes determined from the cross-section of the THG signal. (C) Representative tracks of individual microparticles over 49 frames (98 min) showed subpopulations of immobilization (x, immobilized on cells or on collagen fibers), or random or directed diffusion kinetics. (D) Distribution of microparticle velocities (gray bars, 82 trajectories) relative to the distribution of velocities of individually tracked marker regions on collagen fibers (empty bars, 137 trajectories). (E) Logarithmic distribution of diffusion constants of individual trajectories from microparticles (gray bars) and second harmonic generating spots on collagen fibers (empty bars). Bars, 50 μm (left image) or 5 μm (right images and trajectories).

While THG was previously used in thin transparent samples and organisms,²² we show here the strengths of backward THG in collagen-rich, optically dense and scattering tissue reaching detection depths similar to SHG and NIR fluorescence. Combined THG/SHG/fluorescence imaging provides yet unprecedented 3D insight into the tissue

structures guiding tumor-cell invasion and the kinetics of tumor-cell derived microparticles. Cancer invasion into interstitial tissue is thought to require proteolytic degeneration of tissue barriers and to ultimately cause tissue destruction, consistent with upregulation of MMPs and extensive tissue remodeling detected upon histopathological analysis of advanced lesions.³³ The concept of de novo trail formation during invasion is strengthened by in vitro models showing proteolytic micro- and macro-patterning of dense 3D invasion models for tumor cells or fibroblasts.^{8,34,35} Using THG/SHG/fluorescence detection of both 3D tissue anatomy and invading cells, comparison of tumor-free and tumor-cell invaded tissue strongly suggests that invading cells follow pre-existing tracks bordered by cell or ECM interfaces and, rather than generating neo-trails, show remarkable adaptation of cell shape and invasion mode in response to tissue organization. Two topographic types of track systems were identified, (1) discontinuous, loosely confined spaces within fibrillar collagen networks (Fig. 7A and B) and (2) irregular- or linear-shaped tracks confined by 2D interfaces (Fig. 7C and D). The trails composed of fibrillar collagen networks consist of small fibrils or thicker fiber bundles bordering discontinuous spaces of 5–30 μm in diameter in random or aligned order, which support the invasion of individual or loosely connected cells oriented in parallel to the matrix structure (Fig. 7A and B). Irregular microtracks identified by THG/SHG imaging in fat tissue are composed of neighboring adipocytes, with occasional interspersed collagen bundles, forming irregular-shaped 3D clefts of 2–10 μm in diameter and polygonal, random organization (Fig. 7C). These tracks support multiple tip cells leading diffuse, irregularly shaped collective invasion as broad amorphous mass. Conversely, regular-shaped, aligned trails between myofibers, nerves and blood vessels are linear in organization, uniform in width and promote directionally persistent file-like collective invasion led by one or two tip cells (Fig. 7D). In tumor-free tissue, such aligned tracks either show a constitutive diameter range of 2 to 5 μm , as along nerves and myofibers or between myofibers and blood vessels. Alternatively, linear tracks are detectable as singular interphase along myofibers, possibly representing collapsed but preexisting space, which becomes moderately expanded by invading cells without apparent change of tissue structure, similar to cell-imposed but non-proteolytic widening of experimental microtracks in 3D collagen scaffolds.³⁶ Using mosaic-type tumors to visualize leading edges of invasion within a complex tumor mass, combined THG/SHG/fluorescence imaging allows to categorize tissue geometry and its impact on the mode of migration. Invasion into collagen-rich interstitial tissue occurs along fibrillar meshworks of collagen fibers bordering discontinuous, heterogeneous spaces, thus representing migration in 1D when cells move predominantly along a singular fiber,¹¹ 3D when three-dimensionally surrounded and touched by multiple fibers,³ and 1D/3D

	Fibrillar collagen	Micro- / Macrotracks
Random	<p>A</p> <p>1D 1D 3D Tumor cell Collagen fiber</p>	<p>C</p> <p>Counter-scaffold: adipocyte, collagen fiber, other tumor cell</p> <p>Adipocyte Basement membrane Scaffold: adipocyte surface</p>
Aligned	<p>B</p> <p>1D 3D 3D</p>	<p>D</p> <p>Counter-scaffold: myofiber, collagen bundle, blood / lymph vessel</p> <p>Scaffold: myofiber, nerve track</p>
Scaffold components	Collagen fibrils with interfibril gaps	Basement membrane, adjacent cell surfaces or collagen bundles bordering gap-like track
Type of topography	1D / 3D	2D / 3D
Mode of invasion	Individual, multicellular streaming (collective)	Collective
Frequency of occurrence	low	high

Figure 7. Classification of in vivo scaffold organization and corresponding migration modes in the B16F10 model. Both, connective tissue composed of predominantly fibrillar collagen or surrounding cell structures may show random or aligned organization, with impact on the invasion mode of B16F10 cells. Blue, THG-/SHG-positive scaffold; red, basement membrane, not detected by MPM of native tissue structures; yellow, tumor cells. 3D topography corresponds to either 1D (migration along a single fiber) or 2D (migration along a surface), when the cell body faces additional tissue structures apically or laterally, thus generating confinement.

combinations depending of alternating ECM porosity and alignment (Fig. 7A and B). By contrast, confined tracks consist of often simple-shaped 2D interfaces, such as the linear surface of myofibers or nerve strands, or the curved but nonetheless 2D surfaces of adipocytes. Because migrating cells engage with one interface scaffold and, with their apical pole, touch the counter-scaffold, here the adjacent myofiber, vessel, or collagen bundle, the tissue topography combines elements of 2D and 3D migration (Fig. 7C and D), similar to the continuous 3D environment that confines individual cells migrating between opposing 2D interfaces (“chimneying”).³⁷ Myofibers, peripheral nerves and adipocytes are covered by a basement membrane consisting of type IV collagen, laminin, nidogen/entactin, and perlecan,³⁸ and collagen fibers and bundles consist of fibrillar collagens, predominantly collagen type I and III; thus each invasion routes provides a variety of 1D fibrils, 2D surfaces of basement membrane and/ or bundled collagen, and complex fibrillar and multi-surface 3D geometries in close vicinity which are employed by cells in a versatile, adaptive and often simultaneous manner. In 2D models, surfaces coated with both basement membrane components and fibrillar collagens provide bona-fide substrate for cell polarization along the surface, engagement of integrins for mechanosensing and -transduction for haptokinetic migration.^{39,40} Likewise, B16F10 cells during 1D, 2D and/or 3D migration show preferential orientation along the preexisting tissue topography, consistent with contact guidance of *in vivo* invasion.¹¹ Similar ECM-directed guidance of tumor-cell invasion occurs along radially aligned collagen fiber bundles surrounding breast tumors in perpendicular orientation.^{11,12,19} Besides tissue topography and spaces of least resistance, the stiffness of such 2D/3D tissue scaffolds may support directional cell migration by reinforcing cell protrusions, formation of focal adhesions, and high-traction force for elongated cell movement.^{41,42} The stiffness of skin tissue components varies between deformable collagen networks (elastic modulus 1–3 kPa),⁴³ more rigid muscle fibers (elastic modulus ~12 kPa)⁴⁴ and fat tissue (elastic modulus 5–25 kPa),⁴⁵ thus providing different mechanical strengths for haptotactic and durotactic guidance cues in conjunction with 1D, 2D and 3D topography. Collective invasion is a multicellular migration mode dependent on cell-cell cohesion, supracellular organization, and the capacity to proteolytically degrade ECM and generate tracks.^{34,35} THG/SHG/fluorescence imaging further suggests that the shape, extend and speed of collective invasion is strongly impacted by the type and shape of encountered tissue. Linear microtracks, such as along muscle fibers, support fast (70 $\mu\text{m}/\text{d}$), directionally persistent and laterally confined collective invasion in B16F10 cells. Conversely, irregularly shaped, discontinuous tracks within fat tissues result in comparably slow, poorly organized multicellular mass invasion with multiple tip cells advancing slowly (estimated speed 10 to 15 $\mu\text{m}/\text{d}$; data not shown). Thus, besides cell-intrinsic features,

the topography and composition of connective tissue strongly impact the shape, distribution and efficacy of collective invasion with preference for tissue topography matching 2D/3D organization along flat and relatively rigid surfaces. As unexpected finding, THG imaging visualized (sub) micrometer sized tumor-associated particles in the tumor microenvironment and allowed estimations of size distribution, location and dynamics. Tumor microparticles are detectable using fluorescence labeling from *in vitro* or *ex vivo* samples,⁴⁶ but have not been visualized yet in native state *in vivo*. THG thus facilitates the visualization of native microvesicles in live tissue without fluorescence labeling requirement or tissue processing which delivers robust microparticle signal, in contrast to intra-vesicle fluorescence which may be degraded or leak out through membrane defects. As important technical limitation, due to the diffraction limit of infrared excited multiphoton excitation (lateral point-spread function above 650 nm³⁰) the size of very small particles is either overestimated (toward the micron range) or particles below 200 nm in diameter may remain undetected.⁴⁷ Tumor cells produce a heterogeneous mixture of small vesicular structures of submicrometer size which are implicated in cancer progression, by a dual mechanistic function. Microparticles may enhance progression by mediating intercellular communication and oncogenic conditioning of local and systemic microenvironmental niches and thereby promote tumor invasion and metastasis, angiogenesis and drug resistance.^{32,48} Conversely, microparticles serve as antigen carriers and after uptake by antigen-presenting cells may enhance anti-tumor immune reactions.⁴⁹ Time-lapse THG imaging shows distinct subsets of immobilized as well as randomly or directionally moving particles, likely in response to respective immobilization at collagen fibers or convection with interstitial fluid drifts.⁵⁰ Thus, THG may serve as supportive approach to monitor particle dynamics *in vivo* under physiological conditions and disease states.

Materials and Methods

Cells and cell culture. B16F10 mouse melanoma cells were cultured in RPMI1640 medium (GIBCO, 21875) supplemented with 10% FCS (SIGMA, F7524), 1% sodium pyruvate (GIBCO, 11360) and 1% penicillin and streptomycin (PA A, P11–010). Dual color cell lines were generated using the following constructs: pLenti6.2/V5-DEST™ Gateway® (Invitrogen, V36820) containing histone2B/eGFP and pCMV-E2-Crimson (Clontech, 632556).⁵⁶ Stable histone-2B/eGFP expressing cell lines were obtained by lentiviral transduction and blasticidin selection (10 µg/ml). Subsequently, stable dual color lines expressing histone-2B/eGFP and cytoplasmic E2-Crimson were created by electroporation followed by G418 selection (100 µg/ml) and fluorescence activated cell sorting of the double positive population.

Tumor implantation and intravital monitoring. Dorsal skin-fold chambers were transplanted on 8 to 14-week-old male C57/Bl6 J mice (Charles River), as described.¹⁶ The dorsal skin-fold chamber is mounted on a skin-flap to cover the deep dermis after surgically removing the opposite side of the skin, as described.⁵¹ One day post-surgery, two small tumors per chamber were implanted by injecting a cell pellet of histone-2B/eGFP and E2-Crimson expressing B16F10 cells (5×10^4 – 2×10^5 cells) with a 30 G needle into the dermis nearby the deep dermal vascular plexus.¹⁶ Tumor growth was then monitored for up to 13 d by epifluorescence and multi-photon microscopy. For intravital microscopy, mice were anesthetized with isoflurane (1–3 % in oxygen) and the skin-fold chamber was stably mounted on the temperature-controlled stage (37°C). Blood vessels were visualized by intravenous injection of AlexaFluor®750 labeled 70kDa-dextran (2 mg/mouse).

All animal experiments were approved by the Ethical Committee on Animal Experiments and performed in the Central Animal Laboratory of the Radboud University, Nijmegen, in accordance with the Dutch Animal Experimentation Act and the European FELASA protocol (www.felasa.eu/guidelines.php).

Two-photon system setup and image acquisition. Imaging was performed on a customized multiphoton microscope (TriMScope-II, LaVision BioTec), equipped with three tunable Ti:Sa (Coherent Ultra II Titanium:Sapphire) lasers and an Optical Parametric Oscillator (OPO PP Automatic equipped with a PP800 crystal; Coherent APE ; typical pulse width 200 fs, repetition rate 80 MHz; peak output power of 500– 650 mW at 1180 nm). THG imaging was performed with an Olympus XLUMPlanFI 206/0.95 W objective at a wavelength of 1180 nm resulting in a maximum intensity of 190 mW below the objective, which for imaging living tissue was commonly attenuated to 100–130 mW in the sample. During in vivo measurements, emission was backward detected by 4 PMTs in standard position (blue/THG, FF417/60 or FF01 395/8; green, ET525/50; red ET620/60,

FF01 593/11 or FF01 593/40 and far-red FF01 675/67, ET710/75x or ET810/90 FF filters: Semrock, Inc., ET filters: Chroma Technology Inc.). For high-sensitivity in vitro measurements, emission was also collected in the forward direction using a 1.4NA condenser and two detection channels (FF417/60 or FF01 395/8; and FF01 593/11 respectively). Ultrasensitive gallium arsenide phosphide, blue and red sensitive PMTs (Hamamatsu, H7422-40, H6780-01 and H6780-20 respectively) were used for backward detection using an ultrasensitive port directly adjacent to the objective. For THG forward detection, blue and red sensitive PMTs were used.

Image processing, single particle tracking and analysis. Images were processed using Fiji (<http://pacific.mpi-cbg.de/wiki/index.php/Fiji>). Mosaic images were stitched using the Fiji 2D/3D stitching plugin⁵² and drifts in time-lapse recordings were corrected using the StackReg plugin.⁵³ Quantitative analysis of tumor microvesicle dynamics was performed by single particle tracking, as described.⁵⁴ Two-dimensional trajectories in the plane of focus were reconstructed using IDL-based colloidal particle tracking software⁵⁵ which has been translated to MATLAB (Daniel Blair and Eric Dufresne, <http://physics.georgetown.edu/matlab>) and modified for tracing of heterogeneously distributed, low-intensity fluorescent spots. During tracking a maximum frame-to-frame displacement of 3 or 2 pixels (1.5 and 1 μm) was allowed for THG and SHG reference spots, respectively. The cross section of a tracked particle has been calculated by determination of the radius of gyration, around its local intensity maximum, in the first frame of the trajectory. Mean square displacement (MSD) curves were generated for each trajectory with a minimum length of 21 frames, and the short time lag diffusion coefficient D used in the histogram of Figure 6D was retrieved by linear fitting of the first four points of the MSD plot. To generate histograms of microvesicle velocity distribution, the first 1/4th of the points of the MSD plot of individual trajectories was fitted with a model function for directed diffusion: $\langle r(t)^2 \rangle = 4Dt + (Vt)^2$ where $\langle r(t)^2 \rangle$ is the mean square displacement for time lag t and V equals the velocity component.

Colocalization analysis was performed using the Colocalization Highlighter plugin of ImageJ software (NIH, Bethesda, MD). Images were background corrected, thresholded using automatically settings of the threshold tool, and ratio of intensity was set at 50%. Two points were considered as colocalized when their respective intensities were above threshold and the ratio of their intensities above 0.5.

Disclosure of Potential Conflicts of Interest

No potential conflicts of interest were disclosed.

Acknowledgments

We acknowledge Esther Wagena for outstanding assistance and technical support. This work was supported by the Dutch Cancer Foundation (KWF 2008-4031), the FP7 of the European Union (ENCITE HEALTH TH-15-2008-208142) and the Netherlands Science Organization (NWO-VICI 918.11.626).

Supplemental Materials

Supplemental materials may be found here: www.landesbioscience.com/journals/intravital/article/21223

References

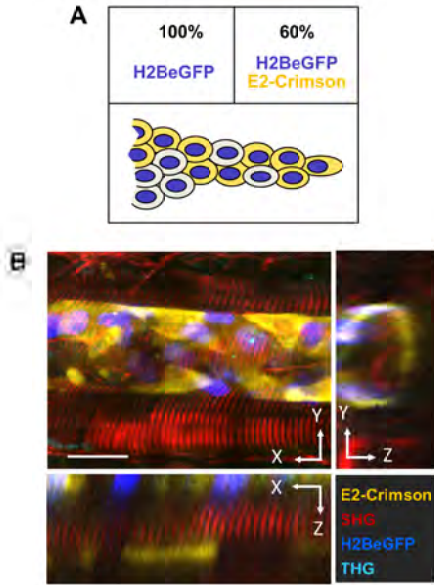
1. Sahai E. Illuminating the metastatic process. *Nat Rev Cancer* 2007; 7:737-49.
2. Bravo-Cordero JJ, Hodgson L, Condeelis J. Directed cell invasion and migration during metastasis. *Curr Opin Cell Biol* 2012; 24:277-83.
3. Wolf K, Mazo I, Leung H, Engelke K, von Andrian UH, Deryugina EI, et al. Compensation mechanism in tumor cell migration: mesenchymal-amoeboid transition after blocking of pericellular proteolysis. *J Cell Biol* 2003; 160:267-77.
4. Friedl P, Gilmour D. Collective cell migration in morphogenesis, regeneration and cancer. *Nat Rev Mol Cell Biol* 2009; 10:445-57.
5. Friedl P, Wolf K. Plasticity of cell migration: a multiscale tuning model. *J Cell Biol* 2010; 188:11-9.
6. Carey SP, Kraning-Rush CM, Williams RM, Reinhart-King CA. Biophysical control of invasive tumor cell behavior by extracellular matrix microarchitecture. *Biomaterials* 2012; 33:4157-65.
7. Wolf K, Friedl P. Extracellular matrix determinants of proteolytic and non-proteolytic cell migration. *Trends Cell Biol* 2011; 21:736-44.
8. Sabeh F, Shimizu-Hirota R, Weiss SJ. Protease-dependent versus -independent cancer cell invasion programs: three-dimensional amoeboid movement revisited. *J Cell Biol* 2009; 185:11-9.
9. Gritsenko PG, Iliina O, Friedl P. Interstitial guidance of cancer invasion. *J Pathol* 2012; 226:185-99.
10. Goetz JG, Minguet S, Navarro-Lérida I, Lazcano JJ, Samaniego R, Calvo E, et al. Biomechanical remodeling of the microenvironment by stromal caveolin-1 favors tumor invasion and metastasis. *Cell* 2011; 146:148-63.
11. Petrie RJ, Doyle AD, Yamada KM. Random versus directionally persistent cell migration. *Nat Rev Mol Cell Biol* 2009; 10:538-49.
12. Provenzano PP, Inman DR, Eliceiri KW, Knittel JG, Yan L, Rueden CT, et al. Collagen density promotes mammary tumor initiation and progression. *BMC Med* 2008; 6:11.
13. Oheim M, Michael DJ, Geisbauer M, Madsen D, Chow RH. Principles of two-photon excitation fluorescence microscopy and other nonlinear imaging approaches. *Adv Drug Deliv Rev* 2006; 58:788-808.
14. Friedl P, Wolf K, von Andrian UH, Harms G. Biological second and third harmonic generation microscopy. *Curr Protoc Cell Biol* 2007; Chapter 4:Unit 4.15.
15. Provenzano PP, Inman DR, Eliceiri KW, Trier SM, Keely PJ. Contact guidance mediated three-dimensional cell migration is regulated by Rho/ROCK-dependent matrix reorganization. *Biophys J* 2008; 95:5374-84.
16. Alexander S, Koehl GE, Hirschberg M, Geissler EK, Friedl P. Dynamic imaging of cancer growth and invasion: a modified skin-fold chamber model. *Histochem Cell Biol* 2008; 130:1147-54.
17. Condeelis J, Segall JE. Intravital imaging of cell movement in tumours. *Nat Rev Cancer* 2003; 3:921-30.
18. Bianchini P, Diaspro A. Three-dimensional (3D) backward and forward second harmonic generation (SHG) microscopy of biological tissues. *J Biophotonics* 2008; 1:443-50.
19. Provenzano PP, Eliceiri KW, Campbell JM, Inman DR, White JG, Keely PJ. Collagen reorganization at the tumor-stromal interface facilitates local invasion. *BMC Med* 2006; 4:38.

20. Débarre D, Beaufepaire E. Quantitative characterization of biological liquids for third-harmonic generation microscopy. *Biophys J* 2007; 92:603-12.
21. Débarre D, Supatto W, Pena A-M, Fabre A, Tordjmann T, Combettes L, et al. Imaging lipid bodies in cells and tissues using third-harmonic generation microscopy. *Nat Methods* 2006; 3:47-53.
22. Rehberg M, Krombach F, Pohl U, Dietzel S. Label-free 3D visualization of cellular and tissue structures in intact muscle with second and third harmonic generation microscopy. *PLoS One* 2011; 6:e28237.
23. Farrar MJ, Wise FW, Fetcho JR, Schaffer CB. In vivo imaging of myelin in the vertebrate central nervous system using third harmonic generation microscopy. *Biophys J* 2011; 100:1362-71.
24. Olivier N, Luengo-Oroz MA, Duloquin L, Faure E, Savy T, Veilleux I, et al. Cell lineage reconstruction of early zebrafish embryos using label-free nonlinear microscopy. *Science* 2010; 329:967-71.
25. Supatto W, Débarre D, Moulia B, Brouzés E, Martin J-L, Farge E, et al. In vivo modulation of morphogenetic movements in *Drosophila* embryos with femtosecond laser pulses. *Proc Natl Acad Sci U S A* 2005; 102:1047-52.
26. Tserevelakis GJ, Filippidis G, Megalou EV, Fotakis C, Tavernarakis N. Cell tracking in live *Caenorhabditis elegans* embryos via third harmonic generation imaging microscopy measurements. *J Biomed Opt* 2011; 16:046019.
27. Watanabe T, Thayil A, Jesacher A, Grieve K, Debarre D, Wilson T, et al. Characterisation of the dynamic behaviour of lipid droplets in the early mouse embryo using adaptive harmonic generation microscopy. *BMC Cell Biol* 2010; 11:38.
28. Lee W-J, Yu C-H, Tai S-P, Huang H-Y, Sun S-K. Acetic Acid as a Cell Nucleus Contrast Agent in Third-harmonic Generation Microscopy. *Journal of Medical and Biological Engineering* 2007; 27:161-4.
29. Witte S, Negrean A, Lodder JC, de Kock CPJ, Testa Silva G, Mansvelder HD, et al. Label-free live brain imaging and targeted patching with third-harmonic generation microscopy. *Proc Natl Acad Sci U S A* 2011; 108:5970-5.
30. Andresen V, Alexander S, Heupel W-M, Hirschberg M, Hoffman RM, Friedl P. Infrared multiphoton microscopy: subcellular-resolved deep tissue imaging. *Curr Opin Biotechnol* 2009; 20:54-62.
31. Mayer C, Maaser K, Daryab N, Zänker KS, Bröcker EB, Friedl P. Release of cell fragments by invading melanoma cells. *Eur J Cell Biol* 2004; 83:709-15.
32. Muralidharan-Chari V, Clancy JW, Sedgwick A, D'Souza-Schorey C. Microvesicles: mediators of extracellular communication during cancer progression. *J Cell Sci* 2010; 123:1603-11.
33. Hofmann UB, Westphal JR, Waas ET, Zendman AJ, Cornelissen IM, Ruitter DJ, et al. Matrix metalloproteinases in human melanoma cell lines and xenografts: increased expression of activated matrix metalloproteinase-2 (MMP-2) correlates with melanoma progression. *Br J Cancer* 1999; 81:774-82.
34. Wolf K, Wu YI, Liu Y, Geiger J, Tam E, Overall C, et al. Multi-step pericellular proteolysis controls the transition from individual to collective cancer cell invasion. *Nat Cell Biol* 2007; 9:893-904.
35. Gaggioli C, Hooper S, Hidalgo-Carcedo C, Grosse R, Marshall JF, Harrington K, et al. Fibroblast-led collective invasion of carcinoma cells with differing roles for RhoGTPases in leading and following cells. *Nat Cell Biol* 2007; 9:1392-400.

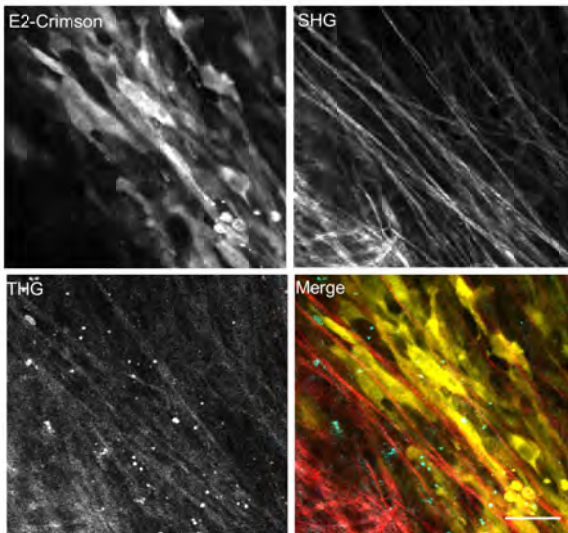
36. Iliina O, Bakker G-J, Vasaturo A, Hofmann RM, Friedl P. Two-photon laser-generated microtracks in 3D collagen lattices: principles of MMP-dependent and -independent collective cancer cell invasion. *Phys Biol* 2011; 8:015010.
37. Malawista SE, de Boisfleury Chevance A. Random locomotion and chemotaxis of human blood poly-morphonuclear leukocytes (PMN) in the presence of EDTA: PMN in close quarters require neither leukocyte integrins nor external divalent cations. *Proc Natl Acad Sci U S A* 1997; 94:11577-82.
38. LeBleu VS, Macdonald B, Kalluri R. Structure and function of basement membranes. *Exp Biol Med (Maywood)* 2007; 232:1121-9.
39. Lugassy C, Barnhill RL. Angiotropic melanoma and extravascular migratory metastasis: a review. *Adv Anat Pathol* 2007; 14:195-201.
40. Sroka IC, Anderson TA, McDaniel KM, Nagle RB, Gretzer MB, Cress AE. The laminin binding integrin alpha6beta1 in prostate cancer perineural invasion. *J Cell Physiol* 2010; 224:283-8.
41. Ulrich TA, de Juan Pardo EM, Kumar S. The mechanical rigidity of the extracellular matrix regulates the structure, motility, and proliferation of glioma cells. *Cancer Res* 2009; 69:4167-74.
42. Peyton SR, Kim PD, Ghajar CM, Seliktar D, Putnam AJ. The effects of matrix stiffness and RhoA on the phenotypic plasticity of smooth muscle cells in a 3-D biosynthetic hydrogel system. *Biomaterials* 2008; 29:2597-607.
43. Hadjipanayi E, Mudera V, Brown RA. Guiding cell migration in 3D: a collagen matrix with graded directional stiffness. *Cell Motil Cytoskeleton* 2009; 66:121-8.
44. Engler AJ, Griffin MA, Sen S, Bönnemann CG, Sweeney HL, Discher DE. Myotubes differentiate optimally on substrates with tissue-like stiffness: pathological implications for soft or stiff microenvironments. *J Cell Biol* 2004; 166:877-87.
45. Van Houten EEW, Dooley MM, Kennedy FE, Weaver JB, Paulsen KD. Initial in vivo experience with steady-state subzone-based MR elastography of the human breast. *J Magn Reson Imaging* 2003; 17:72-85.
46. Hood JL, San RS, Wickline SA. Exosomes released by melanoma cells prepare sentinel lymph nodes for tumor metastasis. *Cancer Res* 2011; 71:3792-801.
47. Débarre D, Supatto W, Beaurepaire E. Structure sensitivity in third-harmonic generation microscopy. *Opt Lett* 2005; 30:2134-6.
48. Lee TH, D'Asti E, Magnus N, Al-Nedawi K, Meehan B, Rak J. Microvesicles as mediators of intercellular communication in cancer--the emerging science of cellular 'debris'. *Semin Immunopathol* 2011; 33:455-67.
49. Zeelenberg IS, van Maren WWC, Boissonnas A, Van Hout-Kuijer MA, Den Brok MH, Wagenaars JA, et al. Antigen localization controls T cell-mediated tumor immunity. *J Immunol* 2011; 187:1281-8.
50. Shieh AC, Swartz MA. Regulation of tumor invasion by interstitial fluid flow. *Phys Biol* 2011; 8:015012.
51. Koehl GE, Gaumann A, Geissler EK. Intravital micro-copy of tumor angiogenesis and regression in the dorsal skin fold chamber: mechanistic insights and preclinical testing of therapeutic strategies. *Clin Exp Metastasis* 2009; 26:329-44.

52. Preibisch S, Saalfeld S, Tomancak P. Globally optimal stitching of tiled 3D microscopic image acquisitions. *Bioinformatics* 2009; 25:1463-5; PMID:19346324; <http://dx.doi.org/10.1093/bioinformatics/btp184>.
53. Thévenaz P, Ruttimann UE, Unser M. A pyramid approach to subpixel registration based on intensity. *IEEE Trans Image Process* 1998; 7:27-41.
54. Bakker GJ, Eich C, Torreno-Pina J a., Diez-Ahedo R, Perez-Samper G, van Zanten T S, et al. Lateral mobility of individual integrin nanoclusters orchestrates the onset for leukocyte adhesion. *Proceedings of the National Academy of Sciences* 2012;1-6.
55. Crocker, John C and Grier D G. *Methods of Digital Video Microscopy for Colloidal Studies*. *J Colloid Interface Sci* 1996; 310:298-310.
56. Strack RL, Hein B, Bhattacharyya D, Hell SW, Keenan RJ, Glick BS. A rapidly maturing far-red derivative of DsRed-Express2 for whole-cell labeling. *Biochemistry* 2009; 48:8279–81.

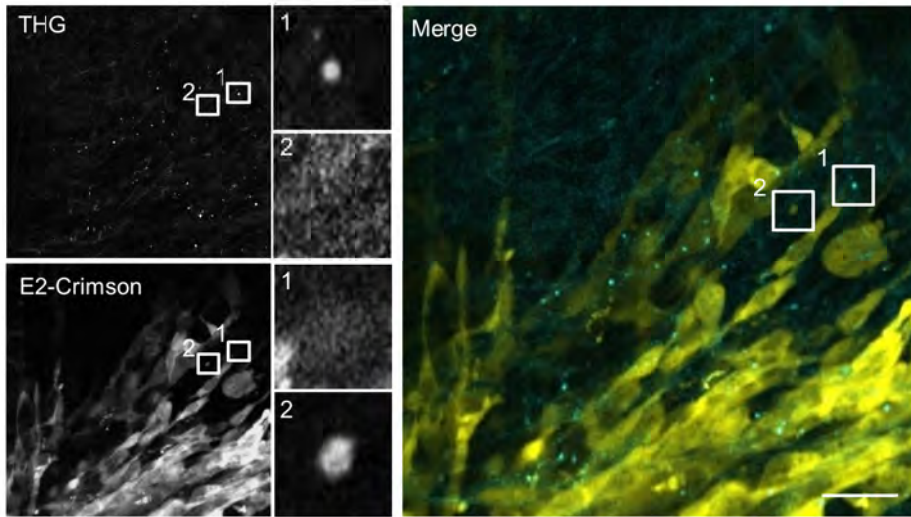
Supplementary Figures



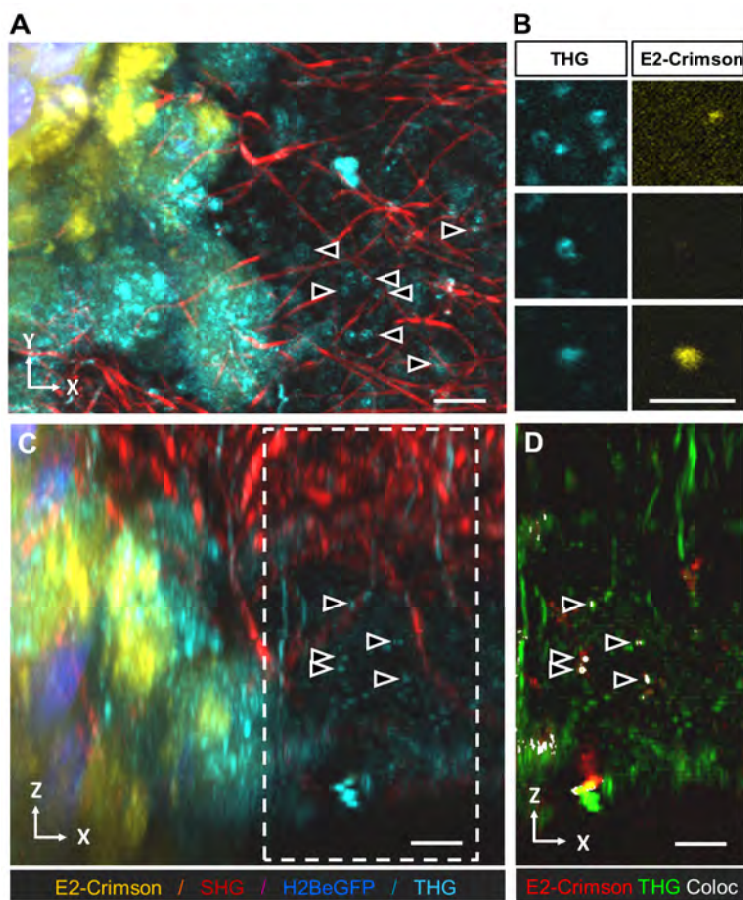
Supplementary Figure 1. Dual-color mosaic tumors (A) to quantify invasion routes (B). (A) Mosaic tumors consisting of 100% B16F10 cells with H2BeGFP (false-color blue) and 60% of the cells expressing additionally cytoplasmic E2-Crimson (false-color yellow). (B) Circumferent myofiber-guided invasion resulting in collective invasion strands wrapping as single-cell monolayer around individual myofibers without disintegration of either myofiber or surrounding tissue. Scale bar: 40 μm .



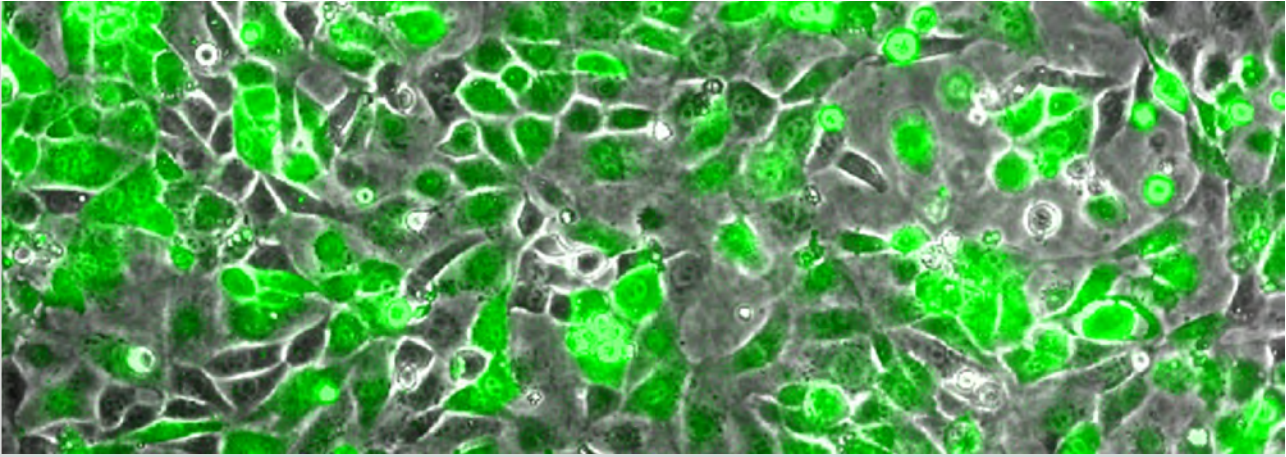
Supplementary Figure 2. Tumor cell invasion into aligned collagen fiber networks. Tumor cell bodies align in parallel to collagen fibers during invasion, recapitulating subjacent collagen fiber patterns. Backward THG/SHG and E2-Crimson were excited with 1180nm (100-130mW). Color scale: yellow, E2-Crimson (tumor cytoplasm); red, SHG (collagen fibers); cyan, THG (microparticles, collagen). Scale bars, 20 μm .



Supplementary Figure 3. Absence of cytoplasmic E2-Crimson signal in THG microparticles. THG microparticles are mostly negative for cytoplasmic E2-Crimson, in contrast to larger vesicles which contained cytoplasmic E2-Crimson but were mostly THG negative. Thus, exclusive THG-positivity may serve as marker for small tumor-derived particles. Color scale: yellow, E2-Crimson (tumor cytoplasm); cyan, THG (microparticles, collagen). Scale bars, 20 μm .



Supplementary Figure 4. In vitro characterization of cytoplasmic signals in THG microparticles released from live-cell culture. Multicellular spheroids of H2B/eGFP and E2-Crimson expressing B16F10 melanoma cells were incorporated into a 3D collagen matrix which was placed on top of a pre-polymerized matrigel to promote invasion along the collagen-matrigel interface. Extracellular mobile THG microparticles successively developed over a time-course of 3-4 days and remained in vicinity of the spheroid, particularly nearby regions of spontaneous cell death (compare supplementary Movie 6). **(A)** Maximum intensity z-projection of peripheral spheroid area. **(B)** Zoom in of individual particles. Similarly to the THG microparticles observed in tumors growing in the deep dermis, tumor cell derived THG microparticles in vitro were mostly negative for cytoplasmic E2-Crimson, despite a sensitive detection setup using gallium arsenide phosphide sensitive PMTs. **(C)** Maximum y-projection of A. **(D)** Colocalization of E2-Crimson and THG. Colocalized pixels were determined using the Colocalization Highlighter plug-in for ImageJ (white areas; red, E2-Crimson;— green, THG). E2-Crimson and THG/SHG (detected in forward direction) were simultaneously excited at 1180 nm (130 mW), and Histone-2B-eGFP was excited at 910 nm (40 mW) in a second, immediately subsequent scan. Color scale: yellow, E2-Crimson (tumor cytoplasm); blue, Histone-2B-eGFP (tumor nuclei), red, SHG (collagen fibers); cyan, THG (microparticles, collagen fibers). Scale bars, 10 μ m.



CHAPTER 4

A Three-Dimensional Organotypic Assay to Measure Target Cell Killing by Cytotoxic T Lymphocytes

Weigelin B & Friedl P

Biochem Pharmacol 2010; 80:2087–91.

Department of Cell Biology, RIMLS, Radboud University Medical Center
Nijmegen, The Netherlands and
Rudolf Virchow Center for Experimental Biomedicine and Department of Dermatology,
University of Würzburg, Germany

Abstract

Cytotoxic T lymphocytes (CTL) mediate antigen- and cell–cell contact dependent killing of target cells, such as cancer cells and virus-infected cells. In vivo, this process requires the active migration of CTL towards and away from target cells. We here describe an organotypic 3D collagen matrix assay to monitor CTL migration together with CTL-mediated killing of target cells. The assay supports both, time-lapse microscopy of killing dynamics as well as population analysis of killing after matrix digestion and flow cytometry. The assay was used to assess the detrimental effect of cyclosporine A (CsA) present during CTL activation, which caused an inhibition of CTL-target cell conjugation and strongly impaired CTL-mediated killing, particularly at low effector–target ratios. Thus, the organotypic assay is useful to monitor spatiotemporal control mechanisms of cytotoxic immune effector functions.

Introduction

Cytotoxic T lymphocytes (CTL) mediate the killing of target cells that express antigenic peptide in the context of the MHC complex and thereby eliminate virally infected and malignant cells. In the tissues, CTL-mediated cytotoxicity is a multi-step process which requires initial entry through the blood vasculature into the diseased tissue, migration towards and surface scanning of target cells followed by TCR triggering by cognate peptide/MHC complexes and stable conjugation. Specific TCR-induced signaling then mediates lytic granule release or the engagement of FasL death receptors with Fas on the target cell and subsequent apoptosis induction. As last step, mediated by the re-onset of migration, the CTL dissociates from the dying or already dead target cell for consecutive contacts [1]. Thus a complex series of migration, adhesive cell–cell interaction and signaling steps is integrated in a spatiotemporal manner.

Because of their ability to kill tumor cells effectively and specifically, adoptive transfer of ex vivo activated, autologous or heterologous CTL are used for anti-tumor immunotherapy. The current criteria for selection of T cells for adoptive immunotherapy include a high avidity for tumor-associated antigens, the capability to produce Th1 cytokines, and a potent tumor specific lytic capacity [2]. In the clinical practice however, in vitro measured anti-tumor reactivity often fails to correlate with the anti-tumor efficacy after adoptive transfer into the patient [2]. Thus, yet unidentified factors present in the tumor microenvironment counteract CTL function.

CTL mediated cytotoxicity is typically studied in two-dimensional liquid cocultures of target cells and CTL [3,4]. However, this approach does not sufficiently reflect the in vivo situation in solid tumors and likely leads to an inaccurate estimation of CTL efficiency. Therefore, in vitro assays that mimic the interstitial characteristics of the tumor

microenvironment are required to identify and routinely test additional parameters of an efficient CTL effector phase.

In the clinic, the immunosuppressive drug cyclosporine A (CsA) is used as standard treatment to reduce CTL effector function to cope with autoimmune diseases and unwanted graft rejection. By blocking the calcium calmodulin-dependent serine/threonine phosphatase calcineurin, CsA interferes with TCR mediated activation of the transcription factor NF-AT and subsequently with the transcription of genes required for T cell activation and proliferation (e.g., IL-2) [6]. Calcineurin signaling supports T cell effector functions including degranulation and formation of the immunological synapse [9,10]; consequently inhibition of this pathway was shown to inhibit CTL effector function in classical CTL-mediated killing assays which use passive co-sedimentation and, hence, bypass the active phase of CTL conjugation with the target cell [8–10].

We here describe an organotypic collagen matrix-based three-dimensional assay for measuring CTL effector function against antigenic target cells that can be used for monitoring single-cell dynamics and killing as well as population analysis of killing efficiency. To avoid the potential bias towards forced conjugation and lytic interaction introduced by passive sedimentation present in other CTL function assays we here re-assessed CsA effects on CTL functions.

Material and methods

Target cells.

C57BL/6 mouse embryonic fibroblast-like cells transfected with B7.1 and a minigene encoding the OVA-derived CTL epitope SIINFEKL (MEC/OVAp) or the adenovirus type 5 E1A-derived CTL epitope SGPSNTPPEI (MEC/E1Ap) coupled to a signal-sequence which directs epitope expression to the endoplasmic reticulum were used as target cells [5]. The cells were cultured in RPMI1640 medium (GIBCO, 21875) supplemented with 10% FCS (SIGMA, F7524), 10 mM HEPES (GIBCO, 15630), 500 mM 2-mercaptopyethanol, 1% penicillin and streptomycin (PAA, P11-010), 1% sodium pyruvate (GIBCO, 11360), and 0.1 mM non-essential amino acids (GIBCO, 11140).

Isolation and activation of primary OT1 CD8⁺ T lymphocytes.

Splenocytes from OT1 mice were isolated and erythrocytes were depleted by ammonium chloride (0.83% NH₄Cl, 0.1% KHCO₃, 0.37% Na₂EDTA) treatment. For the expansion of antigen-specific CTL, splenocytes were cultured at a concentration of 2.5 x 10⁵/ml in the presence of 0.5 µg/ml SIINFEKL peptide in 24-well plates for 3 days. On day 3, IL-2 (100 U/ml), either alone or in combination with cyclosporine A (Sigma) in different concentrations was added to the cultures. Lymphocytes were incubated for further 48 h

and harvested on day 5 by a Ficoll gradient (AXIS-SHIELD PoC AS, Oslo, Norway) – with a purity of Valpha2⁺CD8⁺CD44^{hi} cells exceeding 96 %, determined by flow cytometry.

To determine the proliferation of CTL upon addition of IL-2 and CsA, CTL were labeled with 5 mM CFSE and proliferation was quantified as decreasing CFSE fluorescence following cell divisions.

Collagen-matrix based cytotoxicity assay.

A sandwich assay consisting of target cells adherent to the bottom to the culture dish overlaid with a polymerized 3D collagen lattice containing preactivated CTL was developed (Fig. 1A). Subconfluent MEC/OVAp target or MEC/E1Ap control cells were washed with phosphate-buffered saline (PBS), labeled with either low (0.4 mM, CFSE^{low}) or high (8 mM CFSE^{high}) concentrations of CFSE (5 min, RT) to generate differentially labeled target/control cells. Cells were then washed twice with PBS, detached with trypsin/EDTA and seeded in a 1:1 ratio into 96-flat bottom wells (final density of 2 10⁴/well). After 4 h of incubation and cell attachment to form a subconfluent target cell layer, collagen solution (PureCol1, Inamed BioMaterials; 75 ml/well; collagen concentration 1.7 mg/ml;) containing the CD8⁺ T lymphocytes was added on top. After polymerization for 30 min at 37 °C, the matrix was overlaid with growth medium (75 ml) and incubated for 16– 20 h (37 °C, 5% CO₂, humidified atmosphere).

To harvest surviving cells, the collagen was dissolved by collagenase I (40 U/well; 30 min; Sigma C0130) and the remaining adherent cells detached with trypsin/EDTA (5 min). Both cell fractions were unified, stained with propidium iodide (5 mg/ml, 5 min, RT) washed twice with PBS, fixed in 4 % PFA (30 min, RT) and analyzed by flow cytometry.

The specific killing efficiency was determined as the ratio of propidium iodide negative CFSE^{low} target to CFSE^{high} control cells and normalized to background cell death from the negative control cultured in the absence of CTL. The relative survival of CFSE^{low} target cells compared to CFSE^{high} control cells was calculated as follows: $1 - (\text{ratio CFSE}^{\text{low}}/\text{CFSE}^{\text{high}}_{\text{reference sample}})/(\text{ratio CFSE}^{\text{low}}/\text{CFSE}^{\text{high}}_{\text{CTL sample}}) = \% \text{ specific killing efficiency}$. At least 10,000 CFSE⁺ PI events were measured from each sample.

To compare CTL viability in different samples and treatment conditions, the ratio of viable CTL to surviving CFSE^{high} control cells was determined. At E:T ratios below 1:2 no unspecific bystander killing of CFSE^{high} labeled control cells was observed, which allowed their use as internal standard for cell counting given their presence in equal numbers in all samples. To quantify CTL-target cell conjugate formation, CTL were labeled with 4 mM CellTrackerTM Orange (CMTMR; Molecular Probes) before coculture and CTL-target cell conjugates were determined by flow cytometry as propidium iodide negative, CFSE/CMTMR double positive events.

Time-lapse bright-field and fluorescence microscopy.

Migration of CTL in the collagen matrix and scanning of CFSE labeled target cells was recorded by fluorescence time-lapse microscopy in a Microscope Stage Incubator (Oko-Lab, Italy), ensuring optimal culture conditions, using a Nikon DiaPhot equipped with a Hamamatsu C8484-05G digital camera. Images were taken with a 1 min frame interval for up to 24 h using the time-lapse software (Oko-Lab, version 2.7).

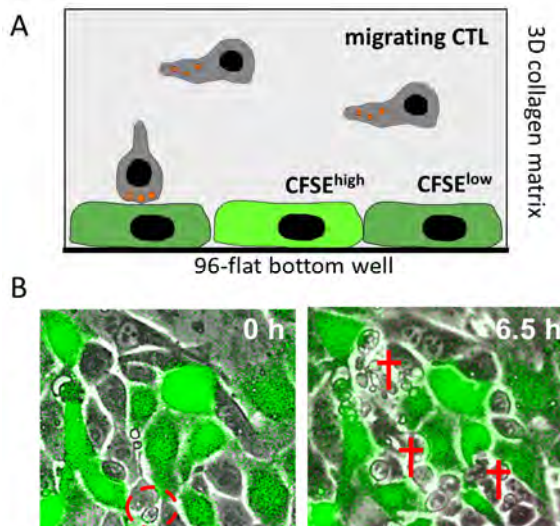


Figure 1. Visualization of CTL migration dynamics and target cell killing. (A) 3D collagen assay setup. Monolayers of CFSE^{low} target and CFSE^{high} control cells (in 1:1 ratio), were overlaid with a collagen matrix containing CTL. The three-dimensional matrix prevents passive aggregation of CTL and target cells and instead promotes the natural migration behavior of CTL. (B) CTL mediated killing of target cells, monitored by time-lapse epifluorescence and bright field microscopy. MEC/OVAp target cells (CFSE^{low}) and MEC/E1Ap control cells (CFSE^{high}) were cocultured with in vitro activated CTL from OT1 mice. Time-lapse movies were recorded for up to 24 h with a frame rate of 1/min. The combination of bright field and fluorescence microscopy allowed the detection of specific apoptosis induction in target cells (indicated by membrane blebbing) during or after CTL interactions and effector function. Areas of apoptotic target cells are indicated by red crosses.

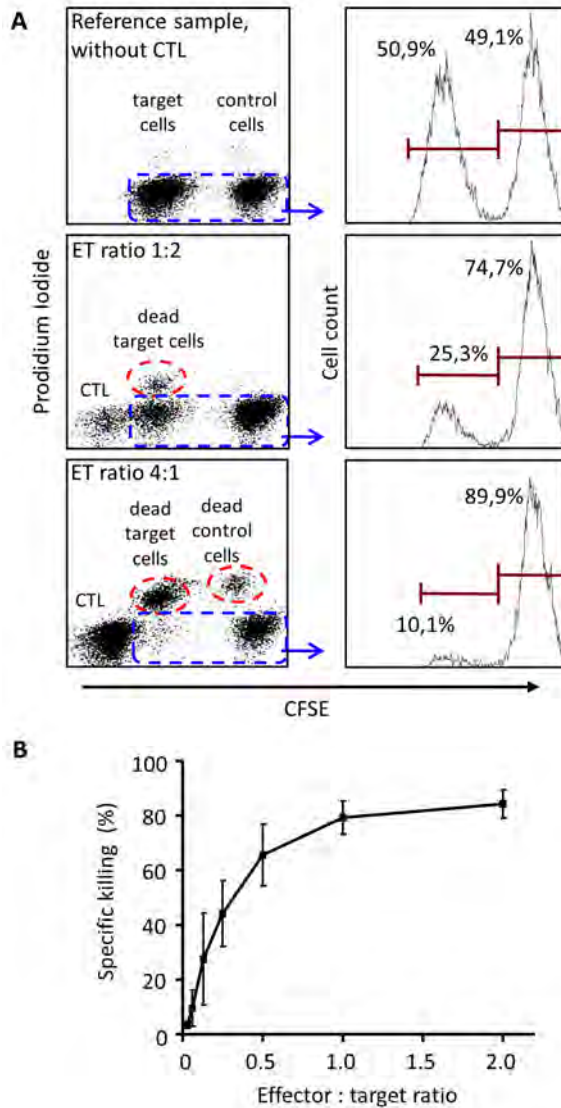


Figure 2. Quantification of antigen-specific target cell killing by flow cytometry. (A) Flow cytometric read out. Dot plots were gated on morphologically intact cells. The differentially CFSE labeled target and control cells were distinguished from CFSE negative CTL, with propidium iodide staining discriminating viable, intact from dead subpopulations. At E:T ratios above 1:1 unspecific cell death was observed in control cells through bystander effects. The histograms depict the viable CFSE positive target cell populations. The relative percentage of surviving CFSE^{low} target cells to CFSE^{high} control cells served to calculate the specific killing efficiency. **(B)** Dose-response curve. Increasing numbers of CTL were cocultured with stable numbers of target cells and harvested for analysis after 16 h of incubation. Data represent the means and standard deviation of at least 4 independent experiments.

Results

Principle of migration-based cytotoxicity assay

The organotypic killing assay consisted of a 3D fibrillar collagen matrix containing CTL and the interface between collagen and the culture dish containing subconfluent target cells (Fig. 1A). To address whether the design supports CTL effector function together with active movement before and after target cell killing, the interface was monitored by long-term time-lapse fluorescence microscopy. MEC/OVAp target cells (CFSE^{low}) and MEC/E1Ap control cells (CFSE^{high}) were equally well contacted by CTL which immigrated from the above collagen scaffold towards the collagen-target cell interface (Fig. 1B; Movie 1). Contacts of individual CTL with MEC/OVAp eventually led to target cell rounding, detachment and blebbing, followed by structural disintegration, consistent with apoptosis induction (Fig. 1B; arrowheads) supplementary information, movie 1. Compared with MEC/E1Ap control cells which only occasionally showed unspecific cell death, MEC/OVAp cells were preferentially contacted and killed within the 24 h observation period (Fig. 1B). Thus, the assay supports migration-dependent interaction of CTL with target cells followed by apoptosis induction in target cells in an antigen-dependent manner.

Quantification of CTL mediated specific killing by flow cytometry

To achieve sufficient throughput for pharmacological and other screenings, the 3D culture system was combined with a flow cytometry read out. At the end of the incubation time the collagen matrix was dissolved using collagenase and surviving adherent target cells were detached and combined with the supernatant containing CTL and dead target cells for flow cytometric analysis. The differential CFSE^{high/low} label in combination with propidium iodide staining allowed to distinguish several discrete cell populations (Fig. 2A). Intact, viable CFSE^{low} MEC/OVAp target and CFSE^{high} MEC/ E1Ap control cells formed two distinct propidium iodide-negative populations which were separate from CFSE^{negative} but weakly autofluorescent CTL (Fig. 2A). Propidium iodide-positive cells retained the initial CFSE intensity prior to structural disintegration (Fig. 2A, lower panel). The relative percentage of surviving CFSE^{low} MEC/OVAp target cells compared to CFSE^{high} MEC/E1Ap control cells was used to calculate the specific killing efficiency. Thereby, the ratio of viable CFSE^{high} to CFSE^{low} target cells at the endpoint of the assay was compared to the ratio of viable CFSE^{high} to CFSE^{low} target cells in a reference sample without CTL.

To analyze the dose effect of CTL mediated cytotoxicity, effector and target cells were incubated in various ratios and harvested for analysis after 16 h of incubation.

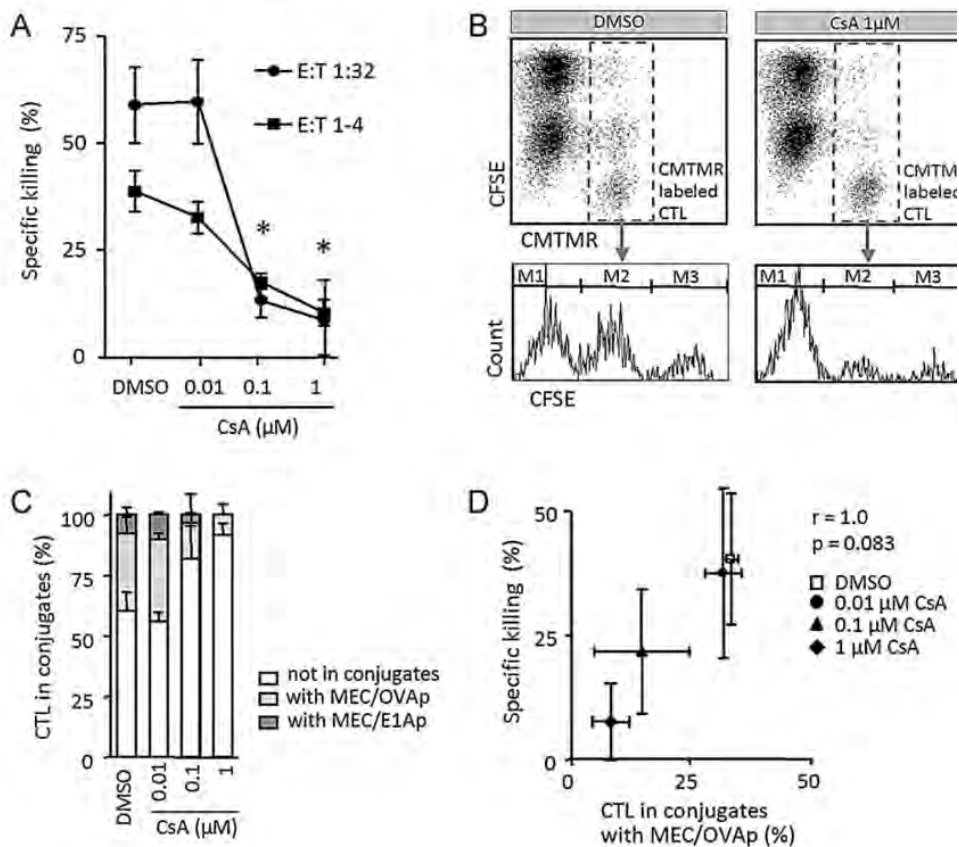


Figure 3. Cyclosporine A (CsA) reduces CTL-target cell conjugation and killing in the organotypic assay. Activated CTL were cultured for 48 h with IL-2 and CsA at different concentration and tested for killing efficiency in the organotypic assay. **(A)** Dose-dependent inhibition of specific killing in the presence of CsA. CsA concentrations of 0.1 mM and 1 mM resulted in significantly reduced CTL killing efficiencies after 16 h of coculture with target cells and in presence of CsA. For improved sensitivity at low effector:target (E:T) ratios (1:32 and below) the duration of coculture was 40 h and otherwise 16 h. Data represent the means and SEM of at least 3 independent experiments. Asterisks, $p < 0.05$ (two-tailed Mann Whitney test). **(B)** Flow-cytometric detection of CTL–target cell conjugate formation in the absence (DMSO solvent) or presence of CsA. Gating of CMTMR labelled CTL (dashed box) either as CMTMR single-positive cells without conjugation (M1) or as CFSE/CMTMR double positive CTL–target cell conjugates with MEC/OVAp target cells (M2) or MEC/E1Ap control cells (M3). **(C)** Ratio of conjugated and unconjugated CTL with MEC/OVAp target or MEC/E1Ap control cells (3 independent experiments). **(D)** Correlation (r) of CTL conjugation with target cells and killing efficiency (Spearman’s correlation test). **(C and D)** Frequency of conjugates and killing efficiency are shown as means SD from 3 independent experiments.

Specific killing efficiency was reliably obtained for a minimum E:T ratio of 1:128 and above. At an ET ratio of 1:1 a plateau of killing efficiency (85%) was reached. Higher E:T ratios induced substantial unspecific collateral damage and thereby decreased the target cell number in non-cognate control cultures which served as internal reference to calculate the specific killing efficiency. The combination of the sensitive single cell read out and incubation times of up to 40 h (data not shown) allow the sensitive quantification of CTL effector pathways at low effector: target ratios.

Cyclosporine A impairs CTL effector function by reducing the ability of CTL to form stable interactions with target cells

To address the effect of CsA on in vitro activated CTL effector function, CTL during pre-activation were cultured in the absence or presence of CsA at concentrations reached in patients' blood samples [7], together with IL-2. Even at high concentrations (1 mM), CsA did not affect CTL proliferation or the expression levels of CD25 during pOVA-induced CTL priming (data not shown). However, in the organotypic effector function assay, CsA impaired CTL mediated target cell lysis significantly at concentrations of 0.1 mM and above (Fig. 3) which led to near-complete abrogation of killing even at intermediate and low E:T ratio. CsA had no effect on CTL viability (data not shown) but strongly inhibited adhesive interaction of CTL with target cells. Using CTL labeled with red-fluorescent CMTMR confronted with green-fluorescent CFSE-labeled target cells, a strong reduction of CFSE/CMTMR double positive CTL-target cell conjugates was obtained by flow cytometry (Fig. 3B, dashed lines). The conjugation defect was dose-dependent and near-complete at high CsA concentration for both, pOVA expressing target cells and non-cognate control cells (Fig. 3C). Using time-lapse microscopy in parallel, no difference in basic migration in the collagen lattice and towards target cells was detected for CsA treated and control CTL, excluding that CsA causes a migration deficit (supplementary information, Movie 2). Consequently, impaired killing efficiency was a linear function of impaired CTL adhesion to target cells in the presence of CsA (Fig. 3D).

Discussion

The 3D matrix environment of the organotypic killing assay mimics the tumor matrix interface and depends upon an active migration phase of CTL to reach and interact with target cells. Consequently, passive aggregation of CTL with target cells, which is integral to established cell-suspension based killing assays, is avoided. Further, the dense accumulation of CTL in conventional killing assays may promote unspecific killing through high local concentrations of effector molecules. In addition, the absence of fibrillar extracellular matrix structures or stable cellular networks hinders active migration and

scanning of cell surfaces by CTL. In contrast, the novel migration-based system promotes the natural dynamic behavior of CTL thereby providing improved biologically relevant information on CTL effector function. In contrast to a recently developed 3D matrix-based spheroid model to monitor CTL function which does not support microscopic monitoring of live-cell interactions and target cell apoptosis [11], the organotypic assay allows to monitor all substeps of CTL mediated killing, including migration through the interstitial matrix, active conjugation with target cells including a stop-signal, and detachment from the target cell.

The assay was validated using CsA present during the activation of effector CTL, which mimics CsA effects under steady-state conditions in patients [7]. The used doses match CsA plasma levels reached under clinical conditions with an average of 0.2 mM and peak concentrations up to 1.8 mM [7]. In the ^{51}Cr release assay subtotal (80%) inhibition of target cell lysis was described after CsA exposure for a dose-range up to 1 mM [8], which was fully reproduced here using the 3D organotypic assay. As main difference, in contrast to the passive aggregation used in conventional CTL-mediated killing assays which preclude meaningful assessment of CTL-target cell conjugation, the 3D collagen environment requires CTL to migrate towards and actively approach, and detach from, target cells. Thus the natural conjugation phases are recapitulated and an overestimation of killing efficiency caused by artificial aggregation is avoided. Further, unlike the conventional ^{51}Cr release assay which is limited to 4–8 h, the organotypic assay supports observation periods of up to 40 h which facilitates the sensitive detection of weak or delayed effector mechanisms at low effector-to-target ratios and thereby better reflects the sequence of conjugation steps during CTL effector function. This new topographic element allows the meaningful combination of measuring killing efficiency with associated functions, including conjugation measured by flow cytometry and CTL migration monitored by time-lapse microscopy. This combined approach provides mechanistic insight into CTL effector function beyond the capabilities of cell-suspension based killing assays. Treatment of CTL with CsA in the presence of IL-2 leaves CTL proliferation and migration capabilities intact, however near-completely ablates stable conjugation with target cells and, consequently cytotoxic outcome. This finding complements previous observations of a CsA mediated reduction of CD3/TCR relocalization to the T cell– target cell interface [9] and is consistent with an impaired timely formation of the cytolytic effector synapse [12].

Because of its tissue-based organization, this assay will be amenable to further mechanistic studies on effector CTL functions, including the detection of cell surface markers to characterize surviving target cell subpopulations; intracellular staining of cytokine expression profiles of the immune effector cells; and to determine the cell cycle

stage of surviving target cells based on propidium iodide labeling. If combined with fixation and antibody staining in parallel cultures, additional information of cell–cell conjugation and the immunological synapse can be retrieved (own unpublished observations) providing additional information on effector–target cell conjugation and the mechanisms of CTL mediated apoptosis induction. This will allow screening for factors modulating CTL efficiency, including factors that affect dynamic CTL migration and antigen- and costimulation dependent cell–cell adhesion with adequate throughput. Thus, the organotypic CTL function assay will be useful to establish and monitor optimized tumor-reactive CTL for adoptive immunotherapy as well as for pharmacological screenings in the development of efficient and selective immunosuppressive or –activating drugs.

Acknowledgements

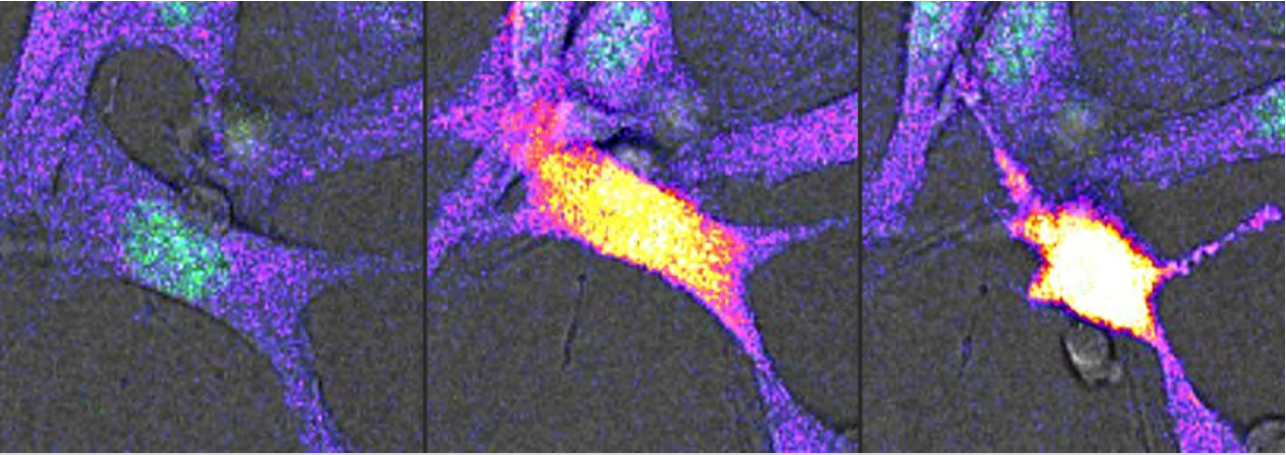
This work was supported by grants from the DFG (FR1155/6-3) and the EU (FP7, ENCITE HEALTH TH-15-2008-208142).

Appendix A. Supplementary data

Supplementary data associated with this article can be found, in the online version, at doi:10.1016/j.bcp.2010.09.004.

References

- [1] Friedl P, Weigelin B. Interstitial leukocyte migration and immune function. *Nat Immunol* 2008;9:960–9.
- [2] Gattinoni L, Powell Jr DJ, Rosenberg SA, Restifo NP. Adoptive immunotherapy for cancer: building on success. *Nat Rev Immunol* 2006;6:383–93.
- [3] Jedema I, van der Werff NM, Barge RM, Willemze R, Falkenburg JH. New CFSE-based assay to determine susceptibility to lysis by cytotoxic T cells of leukemic precursor cells within a heterogeneous target cell population. *Blood* 2004;103: 2677–2682.
- [4] Brunner KT, Mauel J, Cerottini JC, Chapuis B. Quantitative assay of the lytic action of immune lymphoid cells on 51-Cr-labelled allogeneic target cells in vitro; inhibition by isoantibody and by drugs. *Immunology* 1968;14:181–96.
- [5] Schoenberger SP, Jonges LE, Mooijaart RJ, Hartgers F, Toes RE, Kast WM, et al. Efficient direct priming of tumor-specific cytotoxic T lymphocyte in vivo by an engineered APC. *Cancer Res* 1998;58:3094–100.
- [6] Ho S, Clipstone N, Timmermann L, Northrop J, Graef I, Fiorentino D, et al. The mechanism of action of cyclosporine A and FK506. *Clin Immunol Immunopathol* 1996;80:40–4.
- [7] Halloran PF, Helms LM, Kung L, Noujaim J. The temporal profile of calcineurin inhibition by cyclosporine in vivo. *Transplantation* 1999;68:1356–61.
- [8] Zhan X, Brown B, Slobod KS, Hurwitz JL. Inhibition of ex vivo-expanded cytotoxic T-lymphocyte function by high-dose cyclosporine. *Transplantation* 2003;76:739–40.
- [9] Zeyda M, Geyeregger R, Poglitsch M, Weichhart T, Zlabinger GJ, Koyasu S, et al. Impairment of T cell interactions with antigen-presenting cells by immuno-suppressive drugs reveals involvement of calcineurin and NF-kappaB in immunological synapse formation. *J Leukoc Biol* 2007;81:319–27.
- [10] Dutz JP, Fruman DA, Burakoff SJ, Bierer BE. A role for calcineurin in degranulation of murine cytotoxic T lymphocytes. *J Immunol* 1993;150:2591–8.
- [11] Budhu S, Loike JD, Pandolfi A, Han S, Catalano G, Constantinescu A, Clynes R, Silverstein SC. CD8+ T cell concentration determines their efficiency in killing cognate antigen-expressing syngeneic mammalian cells in vitro and in mouse tissues. *J Exp Med* 2010;207:223–35.
- [12] Friedl P, Storim J. Diversity in immune-cell interactions: states and functions of the immunological synapse. *Trends Cell Biol* 2004;14:557–67.



CHAPTER 5

Cytotoxic T lymphocyte Migration and Effector Function in the Tumor Microenvironment

Weigelin B, Krause M & Friedl P

Immunol Lett 2011; 138:19–21.

Department of Cell Biology, RIMLS, Radboud University Medical Center,
Nijmegen, The Netherlands

Abstract

Immunological control of cancer lesions requires local uptake of tumor-specific antigen followed by the activation and expansion of tumor specific cytotoxic T-lymphocytes (CTL). An efficient effector phase further depends upon the entry of activated CTL into the tumor microenvironment and scanning of tumor tissue, which leads to direct interaction of the CTL with target cells followed by apoptosis induction and shrinkage of the tumor lesion [1,2]. Whereas the antigens and pathways that lead to efficient activation of tumor-specific CTL are well established, the local mechanisms that enable efficient – or deficient – CTL function in the tumor tissue are poorly understood. Firstly, effector T lymphocytes need to be mobile to reach the tumor lesion. Next, they must physically interact with and scan tumor cells for antigenic MHC/peptide complexes. Lastly, CTLs must undergo activation and functional conjugation with target cells to induce apoptosis either by the release of perforins or the engagement of Fas/FasL [3]. All these steps of effector function are interdependent and require the amoeboid migration of CTL through tissue to reach, engage with and leave encountered cells [4].

Amoeboid migration and tissue surveillance by cytotoxic T lymphocytes

With the onset of amoeboid migration, leukocytes adopt a typical ‘hand-mirror’ shape, consisting of a leading edge where short-lived pseudopods form and engage with the tissue substrate, a more rigid mid-region including the nucleus, and a posterior tail, termed uropod, that contains actin filaments, microtubules and organelles [5]. The force that drives amoeboid locomotion is generated by the actin-mediated forward flow of the leading edge, including pseudopods and lamellipods, followed by actomyosin-mediated contraction of the mid region and uropod [6]. In contrast to other migration modes, amoeboid cell locomotion does not depend on integrin mediated adhesion [6,7]. Due to the low adhesion coupled to rapid turn-over of cell–matrix interaction amoeboid moving cells are the fastest mammalian cells in tissues (up to 30 $\mu\text{m}/\text{min}$) with the ability to rapidly change directions, enter and pass through tissues, and engage with other cells [4]. Consistent with short-lived, poorly adhesive cell–substrate interactions, migrating lymphocytes deform tissue structures only temporarily and do not degrade or reorganize the extracellular matrix but rather slip through and along existing tissue gaps and trails [8], thereby preserving tissue integrity despite locally high lymphocyte infiltration [9].

Besides its function in T cell trafficking, the amoeboid polarization contributes to T cell functions by enhancing the cells’ capability to sense and respond to signals received from the extracellular environment. Leading edge and uropod are both required for cell and tissue scanning during the effector phase. The dynamic leading edge shows an increased sensitivity to TCR triggering by peptide/MHC complexes and chemokine signals

[10]. Conversely, the trailing uropod contains increased levels of adhesion receptors, including intercellular adhesion molecule (ICAM)-1, integrins and the highly glycosylated surface receptors CD43 and CD44 [11]; which likely regulate attachment to cell surfaces and extracellular matrix (ECM) during migration [12]. The uropod is important in maintaining polarity during migration. Interfering with a cytoplasmic domain of CD44 in CTL affects polarity and migration as well as scanning of target cells needed for an efficient anti-tumor immune reaction *in vivo* [13].

Contact acquisition and killing of target cells

During scanning of encountered cells, CTL engage the TCR to probe counterpart peptide/MHC complexes. Initial scanning of tumor cells occurs randomly along the tumor-stroma border until cognate peptide–MHC (pMHC) complexes on target cells result in TCR triggering and delivery of a “stop-signal” [14]. Initial adhesion with B cell target cells results from integrin engagement, such as LFA-1/ICAM-1 and/or CD2/CD58 so that T cell motility slows down and a stable immunological synapse is being formed [15]. Consistently, when monitored by intravital microscopy *in vivo*, CTL tend to slow down migration in tumors expressing cognate antigen, engage with individual tumor cells for at least half an hour, and are able to induce cytotoxic killing and eradication of the lesion [16,17].

The induction of apoptosis in target cells is a sensitive and fast process (Fig. 1). CTLs detect single pMHC complexes on the cell surface and interaction with only few pMHC complexes can induce a cytolytic response [18]. If B cells are the target, few minutes of contact can lead to apoptotic cell death [15]. Yet, *in vivo*, CTL contacts to target cells in solid tumors occur in the range of several hours until killing is achieved [17].

Two often synergistic pathways lead to target cell killing, the ligation of death receptors (Fas–FasL) and the release of lytic granules. The Fas pathway is important in eliminating activated immune cells in the termination of immune responses and further contributes to anti-tumor responses in Fas expressing tumors [19]. A different route to target cell death induction is degranulation of lytic granules that contain the pore-forming protein perforin and a set of proteases, including Granzyme A and B, which enter the target cell, activate intracellular caspases, and thereby induce apoptosis. During binding to target cells, granules move via microtubules towards the cell–cell contact, and release their content towards the target cell [15]. Whereas stop signal, MHC density and contact times *in vitro* occur under usually optimized conditions, their contribution to *in vivo* killing in the tumor microenvironment likely differs in both mechanism and efficiency [17].

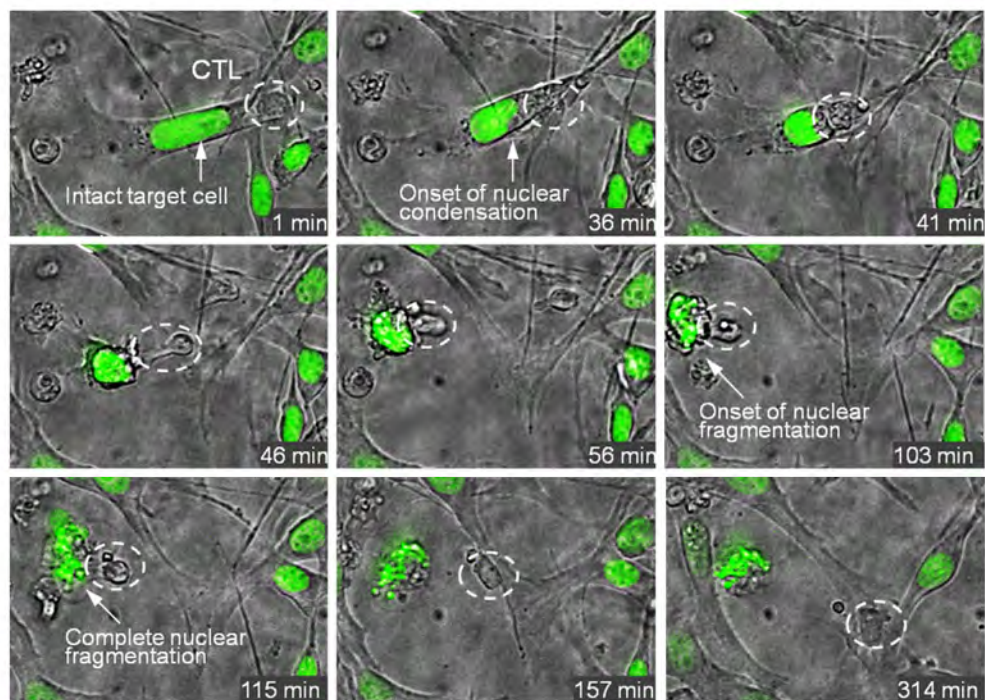


Figure 1. Dynamics of cytotoxic T cell induced apoptosis in a target cell. Murine B16F10 melanoma cells endogenously expressing ovalbumin (OVA) peptide (SIINFEKL) and histone 2B–eGFP were cocultured with *in vitro* activated CTL from OT1 mice. Time-lapse movies were recorded for up to 24 h with a frame rate of 1/min. The combination of bright field and fluorescence microscopy allowed the detection of apoptosis induction (indicated by membrane blebbing and change of nuclear histone 2B–eGFP pattern) during CTL binding and effector function. The phases of nuclear condensation, fragmentation and terminal aggregation are indicated. Notably, membrane blebbing occurred near-simultaneously to nuclear condensation. Time (min) after contact initiation is indicated (right lower corner).

Determinants of killing efficiency

The mechanisms that modulate CTL–target cell interactions *in vivo* are incompletely understood; they comprise the molecular plasticity of tumor cells to evade CTL-induced killing and cytokines and chemokines released by the tumor microenvironment. Consequently, immunologic evasion of tumor cells occurs via downregulation of peptide/MHC, Fas and/or accessory adhesion receptors at the cell surface.

The strength of TCR signaling depends on the duration of the interaction and the avidity of the TCR for its peptide/MHC ligand. Consequently, higher peptide avidity or higher peptide density both support exocytosis of granule content and target cell killing [20]. The presence of cognate antigen further induces CTL migration deeply into the tumor. In model tumors, CTL initially accumulate in the periphery of the tumor by an

antigen-independent process, however their infiltration towards the center is only observed in antigen expressing tumors [16,17].

Likewise altered availability of accessory molecules modulates effector function. LFA-1 and CD2 initiate and stabilize cell–cell binding which, together with costimulating CD28 signaling, enhances effector function [21]. On the other hand, compromising contact duration and/or polarization are thought to lower killing efficiency by interfering with the focusing or the release of lytic granules towards the target cell. Accordingly, interference with contact stability by blocking LFA-1 receptors reduces CTL mediated killing [22].

Besides their established promigratory function, chemokines (e.g. CXCL12) in high concentration can induce a paradox negative chemotactic signal in CTLs and thereby prevent sufficient infiltration into the tumor [23]. By a different mechanism chemokines (e.g. CXCL10) may further impair CTL effector function by overruling the antigen-driven stop signal [24]. Conversely, IL-12 appears to promote immunological synapse formation and enhance CTL efficiency [25]. Thus, the balance of both positive and negative regulators in a given microenvironment determines local CTL efficiency.

Conclusions

In vitro assays for CTL function poorly mimic the tumor microenvironment and may provide an over-optimistic view on when and how efficient target cell killing occurs *in vivo*. Therefore they likely fail to recapitulate thus far unknown factors and rules present in the tumor microenvironment that support or inhibit target cell killing. As key denominators, the balance of CTL migration towards and less mobile positioning within the tumor lesion to generate precise- and long-enough antigen-dependent polarization towards the target cell are regulated by diverse factors of the tumor microenvironment. The positive or negative outcome may be greatly context dependent. Therefore, not only achieving sufficient CTL density and an even distribution in the tumor but also the local control of migration versus adhesion are critical determinants of efficient immunotherapy.

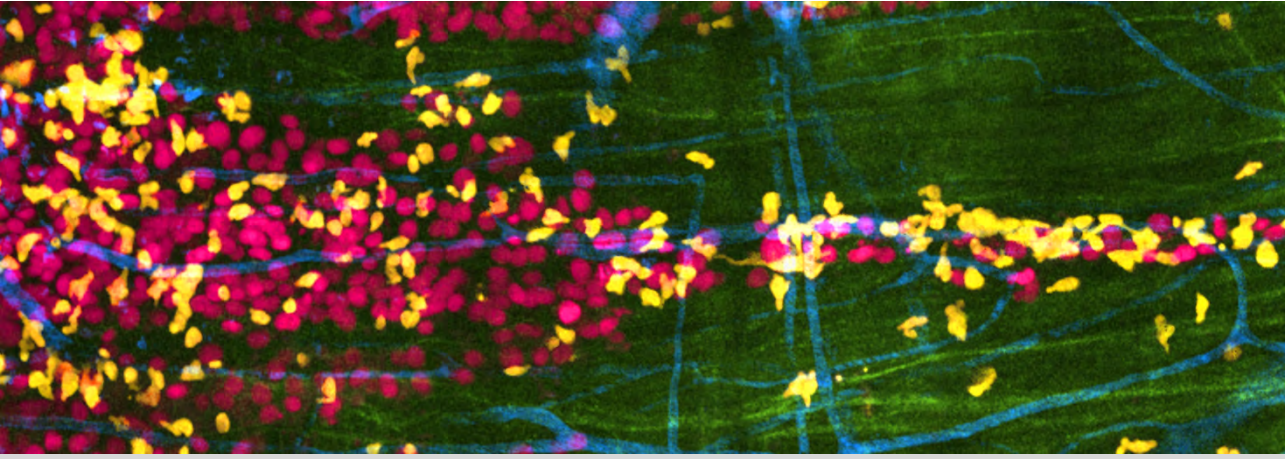
Acknowledgments

Supported by grants from the DFG (FR1155/7-3) and KWF (2008-4031).

References

- [1] Mempel TR, Bauer CA. Intravital imaging of CD8⁺ T cell function in cancer. *Clinical & Experimental Metastasis* 2009;26:311–27.
- [2] Ng LG, Mrass P, Kinjyo I, Reiner SL, Weninger W. Two-photon imaging of effector T-cell behavior: lessons from a tumor model. *Immunological Reviews* 2008;221:147–62.
- [3] Barry M, Bleackley RC. Cytotoxic T lymphocytes: all roads lead to death. *Nature Reviews Immunology* 2002;2:401–9.
- [4] Friedl P, Weigelin B. Interstitial leukocyte migration and immune function. *Nature Immunology* 2008;9:960–9.
- [5] Friedl P, Bröcker EB. T cell migration in three-dimensional extracellular matrix: guidance by polarity and sensations. *Developmental Immunology* 2000;7:249–66.
- [6] Lämmermann T, Sixt M. Mechanical modes of ‘amoeboid’ cell migration. *Current Opinion in Cell Biology* 2009;21:636–44.
- [7] Friedl P, Wolf K. Plasticity of cell migration: a multiscale tuning model. *The Journal of Cell Biology* 2010;188:11–9.
- [8] Wolf K, Müller R, Borgmann S, Bröcker E-B, Friedl P. Amoeboid shape change and contact guidance: T-lymphocyte crawling through fibrillar collagen is independent of matrix remodeling by MMPs and other proteases. *Blood* 2003;102:3262–9.
- [9] Friedl P, Wolf K. Proteolytic and non-proteolytic migration of tumour cells and leucocytes. *Biochemical Society Symposium* 2003;277–285.
- [10] Wei X, Tromberg BJ, Cahalan MD. Mapping the sensitivity of T cells with an optical trap: polarity and minimal number of receptors for Ca²⁺ signaling. *Proceedings of the National Academy of Sciences of the United States of America* 1999;96:8471–6.
- [11] Sánchez-Madrid F, Serrador JM. Bringing up the rear: defining the roles of the uropod. *Nature Reviews Molecular Cell Biology* 2009;10:353–9.
- [12] Smith A, Bracke M, Leitinger B, Porter JC, Hogg N. LFA-1-induced T cell migration on ICAM-1 involves regulation of MLCK-mediated attachment and ROCK-dependent detachment. *Journal of Cell Science* 2003;116:3123–33.
- [13] Mrass P, Kinjyo I, Ng LG, Reiner SL, Puré E, Weninger W. CD44 mediates successful interstitial navigation by killer T cells and enables efficient antitumor immunity. *Immunity* 2008;29:971–85.
- [14] Dustin ML, Bromley SK, Kan Z, Peterson DA, Unanue ER. Antigen receptor engagement delivers a stop signal to migrating T lymphocytes. *Proceedings of the National Academy of Sciences of the United States of America* 1997;94:3909–13.
- [15] Stinchcombe JC, Bossi G, Booth S, Griffiths GM. The immunological synapse of CTL contains a secretory domain and membrane bridges. *Immunity* 2001;15:751–61.
- [16] Boissonnas A, Fetler L, Zeelenberg IS, Hugues S, Amigorena S. In vivo imaging of cytotoxic T cell infiltration and elimination of a solid tumor. *The Journal of Experimental Medicine* 2007;204:345–56.
- [17] Breart B, Lemaître F, Celli S, Bousso P. Two-photon imaging of intratumoral CD8⁺ T cell cytotoxic activity during adoptive T cell therapy in mice. *The Journal of Clinical Investigation* 2008;118:1390–7.
- [18] Purbhoo MA, Irvine DJ, Huppa JB, Davis MM. T cell killing does not require the formation of a stable mature immunological synapse. *Nature Immunology* 2004;5:524–30.

- [19] Caldwell SA, Ryan MH, McDuffie E, Abrams SI. The Fas/Fas ligand pathway is important for optimal tumor regression in a mouse model of CTL adoptive immunotherapy of experimental CMS4 lung metastases. *Journal of Immunology* (Baltimore, MD: 1950) 2003;171:2402–12.
- [20] Jenkins MR, La Gruta NL, Doherty PC, Trapani JA, Turner SJ, Waterhouse NJ. Visualizing CTL activity for different CD8+ effector T cells supports the idea that lower TCR/epitope avidity may be advantageous for target cell killing. *Cell Death and Differentiation* 2009;16:537–42.
- [21] Andersen MH, Schrama D, Thor Straten P, Becker JC. Cytotoxic T cells. *The Journal of Investigative Dermatology* 2006;126:32–41.
- [22] Beal AM, Anikeeva N, Varma R, Cameron TO, Norris PJ, Dustin ML, et al. Protein kinase C theta regulates stability of the peripheral adhesion ring junction and contributes to the sensitivity of target cell lysis by CTL. *Journal of Immunology* (Baltimore, MD: 1950) 2008;181:4815–24.
- [23] Vianello F, Papeta N, Chen T, Kraft P, White N, Hart WK, et al. Murine B16 melanomas expressing high levels of the chemokine stromal-derived factor-1/CXCL12 induce tumor-specific T cell chemorepulsion and escape from immune control. *Journal of Immunology* (Baltimore, MD: 1950) 2006;176:2902–14.
- [24] Bromley SK, Peterson DA, Gunn MD, Dustin ML. Cutting edge: hierarchy of chemokine receptor and TCR signals regulating T cell migration and proliferation. *Journal of Immunology* (Baltimore, MD: 1950) 2000;165:15–9.
- [25] Markiewicz MA, Wise EL, Buchwald ZS, Cheney EE, Hansen TH, Suri A, et al. IL-12 enhances CTL synapse formation and induces self-reactivity. *Journal of Immunology* (Baltimore, MD: 1950) 2009;182:1351–61.



CHAPTER 6

Cytotoxic T cell Cooperation is Required for Serial Killing of Cancer Cells

Weigelin B¹, Wagena E¹, den Boer A², Broen K³, de Boer R⁴, Dolstra H³,
Figdor CG⁵, Textor J⁴, & Friedl P^{1,6,7}

In revision.

¹Department of Cell Biology, RIMLS, Radboud University Medical Center,
Nijmegen, The Netherlands

²Department of Internal Medicine, Maastricht University,
Maastricht, The Netherlands

³Department of Laboratory Medicine – Laboratory of Hematology, Radboud
University Medical Center, Nijmegen, The Netherlands

⁴Theoretical Biology & Bioinformatics, Utrecht University,
Utrecht, The Netherlands

⁵Department of Tumor Immunology, RIMLS, Radboud University Medical Centre,
Nijmegen, The Netherlands

⁶David H. Koch Center for Applied Research of Genitourinary Cancers, Department of
Genitourinary Medical Oncology, The University of Texas MD Anderson Cancer Center,
Houston, USA

⁷Cancer Genomics Centre Netherlands (CGC.nl)

Abstract

Cytotoxic T lymphocytes (CTL) eliminate tumor target cells in an antigen and cell-contact dependent manner, both spontaneously and when activated by immunotherapy. Lethal hit delivery is considered to be a rapid and binary “yes/no” process under conditions of high immunogenicity¹⁻³, and killing enhancement may result from sequential conjugation of one CTL with multiple target cells, termed “serial killing”^{4,5}. Despite its potential significance in amplifying anti-tumor immune responses, the principles of serial killing and its contribution to effector function in established tumors remain unclear^{6,7}. Here we show that elimination of cancer cells results from a cooperative process executed by multiple CTL engaging sequentially with the same target cell. Long-term time-lapse microscopy of three distinct tumor models supported by statistical modeling revealed that migrating CTL transit between target cells and cooperate to initiate apoptosis by a series of sublethal interactions (additive cytotoxicity), whereas individual conjugations rarely reached thresholds to induce apoptosis. Consequently, in invading B16F10 melanoma tumors treated with adoptive T cell therapy *in vivo*, serial engagements and tumor-cell apoptosis induction were confined to regions with high CTL density, which supported CTL accumulation and additive cytotoxicity. Highest rates of serial engagements followed by tumor eradication were reached in the invasive tumor front where moving tumor cells and CTL collided within the same pro-migratory tissue compartment, suggesting invading tumor cells as target for immunotherapy. Thus, additive cytotoxicity requires CTL cooperation and serial engagements with target cells to deliver cumulative sublethal events and successfully eradicate solid tumor cells. The need for additive “hits” has implications for topographic mechanisms of immune evasion of tumor cells as well as immune intervention to enhance CTL accumulation and cooperation.

CTL can bind to and attack more than one target cell simultaneously⁸ and retain detectable levels of granzyme, an effector molecule required for apoptosis induction, after killing target cells⁹. Consistently, mathematical modeling suggests that CTL are capable of eliminating multiple target cells expressing viral antigen *in vitro* and *in vivo* (ranging from 1 up to 20 kills per CTL and day in bulk killing assays)^{10,11}. Quantitative time-lapse analysis of target cell killing by NK cells identifies sequential or simultaneous kills of up to 14 adjacent tumor cells within 6 hours, with target cell elimination occurring in spatio-temporally confined clusters (burst-kinetics)¹². Whereas the concept of multiple kills per effector cell is emerging, the underlying kinetics and efficacy thresholds of serial killing at the single-cell level, and how these interactions impact immune control of subregions within solid tumors, remains unclear.

To quantitatively establish serial killing of target cells by single CTL in solid tumor models, we used a 3D collagen-matrix based, organotypic assay to enable CTL movements along a tumor-stroma interface monitored by long-term time-lapse microscopy (Fig. 1a). *In vitro* activated OVA-specific OT1 CTLs were confronted with transformed mouse embryonic fibroblasts expressing the OVA peptide (MEC-1/OVA) and the co-stimulatory molecule B7.1¹³ (Extended Data Fig. 1a-c). In contrast to *in vivo* generated tumor cell lines, this engineered model lacks natural immune escape modifications (e.g. down regulation of MHC-I or apoptosis resistance) and, thus, represents an idealized model for maximized CTL efficacy at a single cell level. After 24 h of co-culture, killing efficacy was near 100% at high effector-target (ET) ratios and reached background level below ET ratios of 1:128 (Fig. 1b). At moderate ET ratio (1:32), the daily killing efficiency per CTL amounted to 17 killed target cells (Fig. 1b), consolidating that individual CTL can kill multiple target cells in a serial or simultaneous manner. At the end-point, Lamp-1, a cytotoxic vesicle-associated transmembrane protein which appears on the CTL surface after lytic vesicle exocytosis, is upregulated in 85% of CTL (Fig. 1c), indicating cytolytic engagement of nearly the complete CTL population.

To assess the killing efficacy at single CTL level, we analyzed singular CTL-target cell interactions and outcome by excluding conjugations of multiple other CTL with the same target cell. After contact initiation, the duration of individual CTL-target cell interactions was variable until detachment, lasting few minutes for non-specific interactions (median 7.8 ± 1.9) and several minutes to hours in antigen-specific interactions (Extended Data Fig. 1d; median 19.2 ± 6.5 min). With the onset of apoptosis, target cells underwent cell rounding and membrane blebbing simultaneously with condensation and fragmentation of the nucleus, both markers of irreversible apoptotic cell death (Extended Data Fig. 1e). The median lag phase from contact initiation to target cell blebbing was 1.8 ± 1.5 h with a range of, again, minutes to hours (Extended Data Fig. 1f), often followed by ongoing CTL engagement with the dead cell body (Fig. 1d; “necrophilic phase”).

This extended lag phase until apoptosis differs from those obtained for CTL-mediated killing of target cells from leukocyte lineages, including P815 mastocytoma (<5 min)¹, B cell lymphoma (<15 min)³ and peptide-pulsed B cells (<25 min)². As control, excluding compromised CTL movement or cytotoxic conjugation ability caused by the interface assay (Fig. 1a), the lag phase to apoptosis of target cells distributed in interface-free 3D collagen matrices yielded equal variability ranging from few minutes to hours after initial contact (median 90 min) (Extended Data Fig. 2; Movie 1). Thus, the induction time to apoptosis was highly variable, ranging from several minutes to hours.

When monitored in regions of low local CTL density, the repetition of contact acquisition, death induction and detachment resulted in the serial killing of multiple

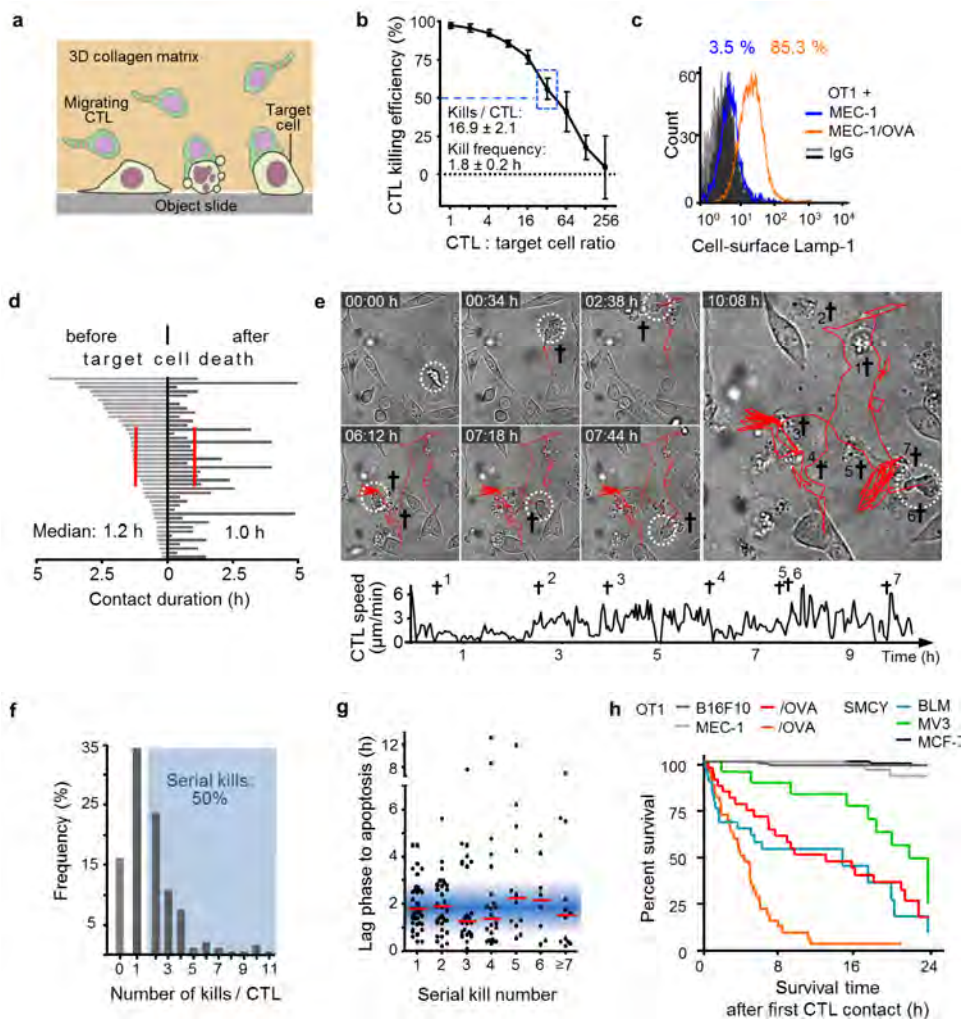


Figure 1. Serial killing. **a**, 3D collagen-target cell interface assay to monitor serial cytotoxicity. **b**, Killing of MEC-1/OVA targets by OT1 CTL at different ET ratios, determined by flow cytometry after 24 h of co-culture. Error bars, means \pm SD (3 independent experiments). **c**, Lamp-1 expression at the surface of OT1 CTL after 24h coculture with MEC-1/OVA cells. **d**, Duration of CTL-target cell contacts before and after the onset of target cell apoptosis. Red bars, median. **e**, Time-lapse sequence and migration track of one OT1 CTL killing 7 MEC-1/OVA target cells sequentially within 11 h. Circles, CTL; cross, apoptotic target cell. **f**, Frequency of serial kills and **(g)** lag-phase until apoptosis of consecutive kills by the same CTL (43 CTL from 8 independent experiments). Red bars, median. **h**, Population survival of 4 distinct antigen-dependent target cell and 3 control models. Quantifications stem from \geq 3 independent experiments.

neighboring target cells by a single CTL (Fig. 1e; Movie 2). Population-wise, 50% of the CTL acted as serial killers (maximum of 11 killed target cells/24 h), whereas a small CTL subset (15%), repeatedly contacted target cells but failed to induce apoptosis (Fig. 1f) despite a largely homogeneous activation status of the CTL population (Material and methods section). The lag phase to apoptosis was neither compromised nor accelerated over consecutive killing events (Fig. 1g), which resulted in a median eradication frequency of 1 kill every 2 hours (Extended Data Fig. 1g). Thus, for eliminating highly immunogenic target cells, serial killing is a non-exhaustive process.

To validate serial killing for solid tumor cells which typically retain resistance to CTL mediated killing, OT1 CTL were confronted with mouse melanoma B16F10 cells expressing the OVA peptide (B16F10/OVA) (Extended Data Fig. 3a). As second model, IL-2 activated human SMCY.A2 CTL¹⁴, which recognize an HLA-A2 restricted antigen encoded on the y chromosome, were confronted with male human melanoma cell lines BLM and MV3 (Extended Data Fig. 4a, b). Compared to the MEC-1/OVA cells, these three melanoma models show moderately delayed, but ultimately equally complete, target cell elimination at the end-point after 24 hours (Fig. 1h), whereas OVA-negative B16F10 and female MCF-7 cells survived. Thus, both murine and human models for probing CTL effector function in 3D culture show similar overall kinetics and efficacy to target cell elimination.

CTL killing efficiency depends on multiple parameters, such as the CTL killing mechanism (perforin/granzyme exocytosis or engagement of death receptors Fas-FasL), pMHC-I expression levels on the target cell surface and the engagement of costimulatory molecules (e.g. molecules from the B7 family)¹⁵. The mild difference in killing kinetics between MEC-1 and B16/F10-OVA cells could not be explained by differential Fas or B7.1 expression and function (Extended Data Fig. 1b, 3e, f), nor the surface levels of pOVA (Extended Data Fig. 3g), indicating additional cell-intrinsic mechanisms for divergent half-maximum survival rates (Fig. 1h). Consequently, consistent with pronounced surface induction of Lamp-1 on OT1 cells (Fig. 1c), these findings suggest a perforin-mediated elimination program in both models.

Comparing contact kinetics at single-cell level, all melanoma models confirmed the serial interaction concept, including extended lag phases until target cell apoptosis with broad variance from min to hours (Extended Data Fig. 3c, d and 4c-e, Movie 3,4) and an extended necrophilic phase (Extended Data Fig. 1d; 3d, 4e). Thus, dynamic serial conjugations with multiple target cells characterize CTL effector function across target cell types and species.

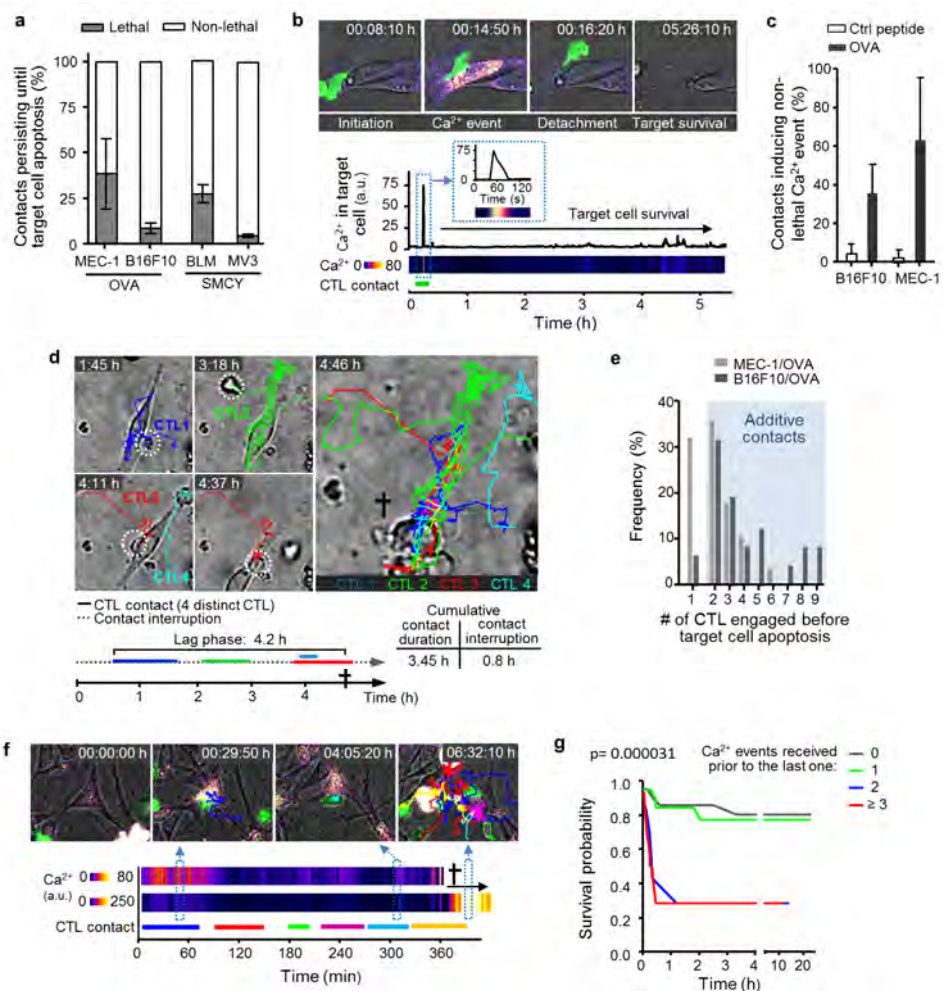


Figure 2. Additive cytotoxicity. **a**, Inefficiency of individual CTL contacts in OT-1 and SMCY.A2 CTL models. Error bars, mean \pm SD (≥ 100 contacts from ≥ 3 independent experiments per model). **b**, Time-lapse sequence of CTL-associated intracellular Ca²⁺ event in B16F10/OVA cell and subsequent target cell survival. Ca²⁺ intensity was measured in the target cell cytosol and plotted over time. Green, OT1 CTL (GFP); Fire LUT, Ca²⁺ intensity (GCaMP6s). **c**, Percentage of CTL contacts that induce Ca²⁺ events. Error bars, mean \pm SD (n=3 independent experiments). **d**, Time-lapse sequence of multiple CTL sequentially engaging with 1 target cell followed by apoptosis. Circles, CTL; crosses, apoptotic target cells. **e**, Frequency of multiple contacts preceding apoptosis. **f**, Time-lapse sequence and intensity plot of multiple Ca²⁺ events followed by target cell apoptosis. Green fluorescence, OT1 CTL (dsRed); Fire LUT, Ca²⁺ intensity (GCaMP6s). Cross, target cell death. **g**, Survival probability of B16F10/OVA cells having received increasing numbers of Ca²⁺ events prior to the last event preceding apoptosis. P value, log rank test comparing all groups.

We next tested whether apoptosis induction is a stochastic event of individual contacts or caused by cooperation of multiple CTL. Consistent across models, only a minority of individual CTL-target cell contacts induced apoptosis at first encounter (Fig. 2a). Conversely, 60-70% (MEC-1/OVA, BLM) or >90% (B16F10/OVA, MV3) of individual conjugations were unsuccessful, followed by target cell survival (Fig. 2a; Extended Data Fig. 1d, Movie 5). CTL degranulation mediates transient, reversible perforin-mediated pores in the target cell membrane, which elicits diffusion of extracellular factors into the target cell cytosol, including CTL-derived granzymes and extracellular calcium¹⁶. To discriminate sublethal cytotoxic hits from functionally inert interactions, MEC-1/OVA and B16F10/OVA cells were engineered to express the calcium sensor GCaMP6s¹⁷, to measure transient Ca²⁺ influx through perforin pores during CTL engagement. OT1 CTL contacts were associated with single or repetitive Ca²⁺ events occurring after a variable lag phase of few minutes to several hours after contact acquisition (Fig. 2b; Extended Data Fig. 5a-g, Movie 6). A substantial fraction of antigen-specific but non-lethal CTL-target cell contacts showed CTL associated intracellular Ca²⁺ events in B16F10/OVA (40%) and MEC-1/OVA (60%), whereas target cell death without prior Ca²⁺ events was rare (Extended Data Fig. 5i) and OVA-negative control cells lacked such Ca²⁺ events (Fig. 2c). Single CTL contacts predominantly induced singular and less frequently repetitive Ca²⁺ events at intervals of several minutes, with higher number and frequency for contacts with MEC-1/OVA fibroblasts compared to B16F10/OVA melanoma cells (Extended Data Fig. 5e, f). Surviving B16F10 melanoma cells could tolerate multiple serial Ca²⁺ events, triggered by one or multiple, serially or simultaneously engaging CTL (Extended Data Fig. 5j, 6a). Thus, despite effective high-affinity peptide/MHC conditions single OT1 CTL conjugations with tumor cells often remain sublethal, consistent with serial but sub-threshold cytotoxicity.

By gating on successful kills together with Ca²⁺ events, two kinetic apoptosis induction mechanisms were identified. The longer uninterrupted single contacts persisted, the more likely apoptosis was achieved in the absence of conjugation by additional CTL (Extended Data Fig. 1d, 3b, 4c). Alternatively, sequential or simultaneous contacts by the same or multiple CTL with the same target cell resulted in multiple sequential calcium events and lethal outcome (Fig. 2d, Extended Data Fig. 1d, 3b, 4c). On average, successful kills were preceded by conjugations of 2-9 independent CTL (Fig. 2d, e; Movie 7, 8), and the probability for apoptosis induction increased with the number of Ca²⁺ events (Extended Data Fig. 5i). Thus, apoptosis induction by CTL may occur through a sequence of sublethal cytotoxic hits which accumulate over time.

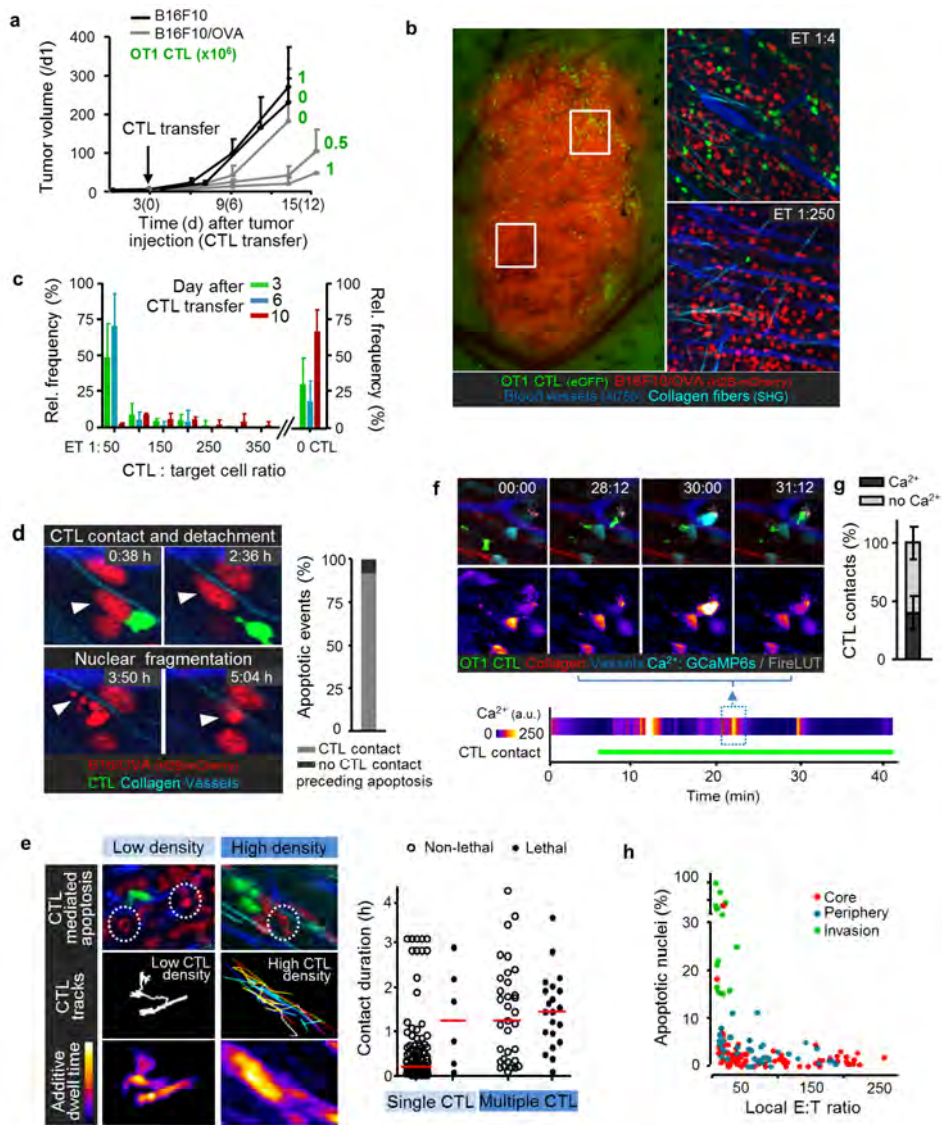


Figure 3. CTL cooperation in live tumors. **a**, Time-dependent impact of adoptive CTL transfer on B16F10 tumor volume. Error bars, mean \pm SD (5 independent tumors). **b**, Multi-photon 3D reconstruction of B16F10/OVA lesion 3 days after transfer of OT1 CTL. **c**, Subregional ET ratios over time (8 independent tumors). **d**, Intravital time-lapse detection (left) and frequency (right) of CTL-mediated tumor cell apoptosis using H2B/mCherry. Arrow heads, nuclear condensation/fragmentation. Data represent 32 apoptotic events from \sim 150 h of time-lapse imaging. **e**, Contact duration and outcome of single or multiple CTL contacting B16F10/OVA cells. Fire LUT, CTL dwell time. **f**, Repetitive intracellular Ca^{2+} events (GCaMP6s) in B16F10/OVA cell during CTL engagement. Green, OT1 CTL; Cyan, GCaMP6s in B16F10/OVA; Lower panel: Fire LUT, Ca^{2+} intensity (GCaMP6s). **g**, Frequency of CTL-target cell contacts which induced one or more Ca^{2+} events (45 contacts from 4 independent tumors). **h**, Correlation of CTL density and apoptotic frequency in tumor subregions (8 independent tumors).

To discriminate whether apoptosis induction occurred stochastically from individual hits within a series of Ca^{2+} events, or as an additive process from a consecutive series of hits we probed the stochastic killing hypothesis using time-lapse monitoring over 18-24h and survival analysis (Supporting Methods). The survival probability of B16F10/OVA target cells after the last received Ca^{2+} event was plotted, classifying cells according to the total number of preceding Ca^{2+} events received prior to the last event before apoptosis (Fig. 2g). Both the lag time to apoptosis after the last Ca^{2+} event and the survival probability significantly depended on the number of preceding Ca^{2+} events, with 80% survival probability after none or a single Ca^{2+} event and strongly increased death rate after 2 and more prior Ca^{2+} events (Fig. 2g). This contradicts apoptosis induction as stochastic process. Simulations assuming stochastic apoptosis induction by single hits resulted in the loss of the correlation between the number of prior Ca^{2+} events and the probability to survive (Extended Data Fig. 6c), which fails to replicate the actual survival data (Fig. 2g, Extended Data Fig. 6a, b). Hence, apoptosis induction results from additive CTL-mediated cytotoxic events which individually remain sublethal but, when occurring as series over time, achieve target cell damage.

The significance of apoptosis induction by sequential versus individual interactions by CTL was further tested by varying CTL density. At high CTL density (ET 1:2) target cell death was frequent and predominantly resulted from contacts by multiple CTL, whereas at low CTL density (ET 1:16) apoptosis was rare and followed near-exclusively single-contact engagements (Extended data Fig. 5j). Thus, both the predominant CTL conjugation type and killing efficiency are functions of CTL density. Serial conjugation and efficient apoptosis induction require high CTL density (“swarming”, “crowding”), whereas killing at low CTL density must rely on single encounters with low overall efficacy.

To address whether and in which tumor subregions CTL-mediated serial killing occurs *in vivo*, activated OT1 CTL were adoptively transferred into C57BL/6 J mice bearing intradermally invading B16F10 melanoma lesions and monitored longitudinally by intravital microscopy through a skin window (Extended Data Fig. 7a, b). A single application of OT1 CTL caused a dose-dependent growth delay of the OVA antigen-expressing but not of control tumors (Fig. 3a, Extended Data Fig. 7c), indicating efficient but transient anti-tumor activity. Topographic volume analysis of entire tumors (Fig. 3b) showed that intra-tumor CTL density varied time-dependently and locally with peak numbers at days 3-6 after transfer (Extended Data Fig. 7c). Peak densities along the tumor-stroma interface reached local ET ratios of 1:1 contrasting poor CTL infiltration in the tumor core with ET ratios below 1:250 (Fig. 3b, h) between day 3 and 6 after CTL transfer (Fig. 3c). Individual CTL-tumor cell interactions were mapped by time-lapse

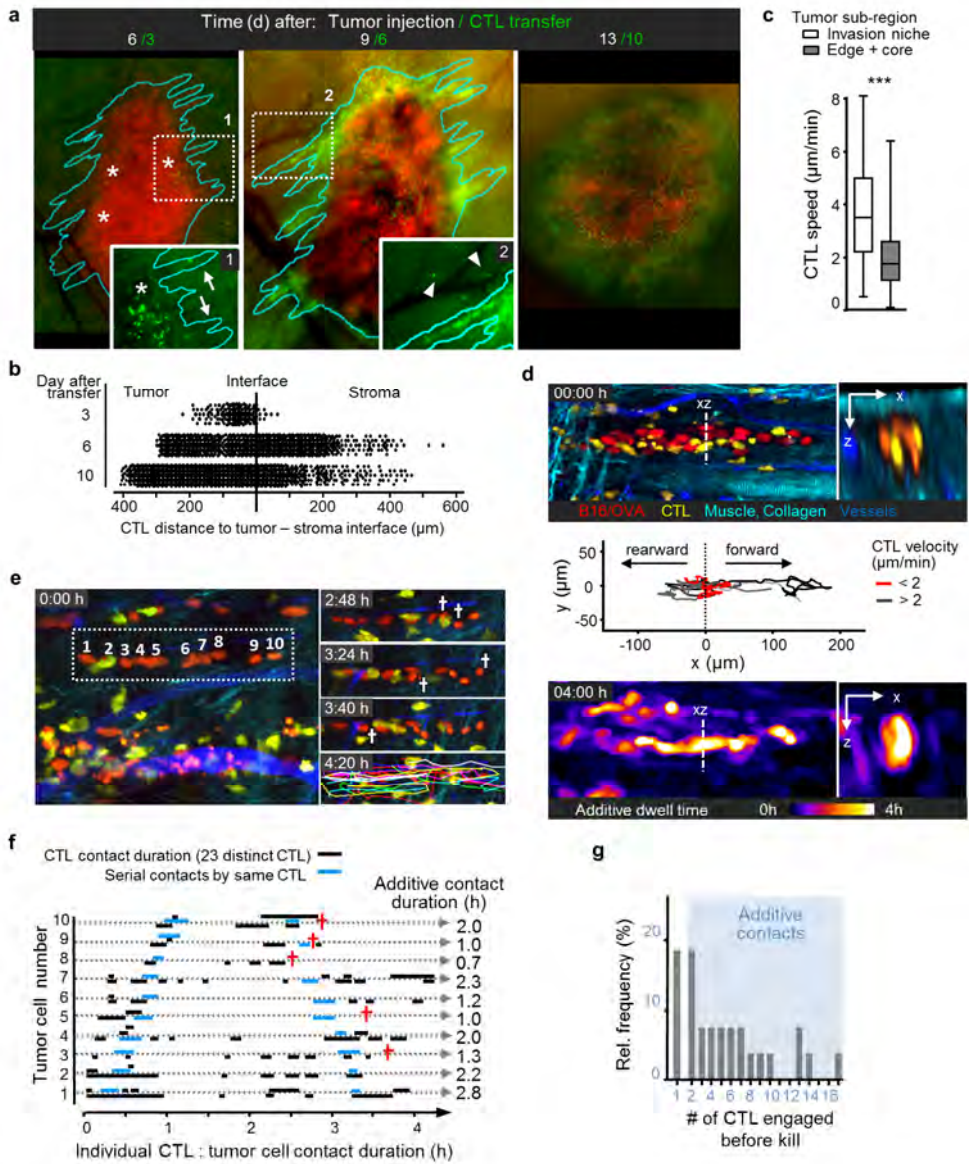


Figure 4. Preferential elimination of invading tumor cells. **a, b**, Time-dependent CTL accumulation along the tumor-stroma interface. Red, nuclei B16F10/OVA cells; green: OT1 CTL. **c**, CTL migration speed within tumor main mass and invasion zones. **d**, Distribution (top), migration tracks (middle) and dwell-time (bottom) after 4 h time-lapse recording (bottom) of CTL (yellow) between tumor cells (red) along channel-like invasion niche confined by collagen bundles (cyan) and blood vessels (blue). **e, f**, Time-lapse sequence (**e**) and plot (**f**) of serial engagements of multiple CTL with B16F10/OVA cells and outcome. **g**, Apoptosis of B16F10/OVA cells after one single or multiple contacts by CTL (30 apoptotic events from 150 h of movies, 20 independent tumors).

microscopy over 4–8h at non-toxic imaging conditions (Extended Data Fig. 7 f-h). Apoptosis induction in B16F10/OVA cells was registered by the histone-2B/mCherry (H2B/mCherry) signal which reliably discriminates intact from condensed or fragmented nuclei (Fig. 3d) and detects apoptosis with similar temporal precision as phosphatidylserine staining (Extended Data Fig. 8a-c). OT1 CTL efficiently migrated between tumor cells with intermittently reduced migration speed and migration arrest during interaction with B16F10/OVA cells (Extended Data Fig. 8d), but maintained non-confined high-speed migration in OVA-negative tumors (Extended Data Fig. 8d, e). This indicates decreased CTL mobility upon OVA-mediated recognition and effector function¹⁸.

Whereas most contacts were transient in duration (median 15 min) and non-lethal (Fig. 3e), rare individual CTL-target cell interactions were sustained enough to induce apoptosis followed by sequential conjugation of adjacent tumor cells (Fig 3e, Movie 9). Individual productive but sublethal interactions *in vivo* were confirmed by Ca²⁺ imaging in target cells during CTL engagement, with kinetics and efficacy rates similar to those obtained *in vitro* (Fig 3f,g, Movie 10). In regions of low CTL density and consistent with their short duration (median 15 min), individual CTL-target cell contacts typically lacked repeated Ca²⁺ events during 3-4 h observation periods, with target cell survival as consequence (Fig. 3e). Conversely, regions with high CTL density reached higher cumulative contact times per target cell by several CTL (Fig. 3e, median 1.5 h) and high frequency of apoptosis (Fig. 3h). Thus, high CTL density favors serial interactions and apoptosis induction whereas individual short-lived contacts typically lack efficacy.

As key progression event of established melanoma, B16F10 cells invade the skin as coherent multi-cellular strands¹⁹. Concomitantly, CTL first accumulated in the tumor periphery from where they redistributed preferentially towards the invasive tumor front (Fig. 4a, b). As consequence, quantified by high-resolution 3D mapping of tumor subregions, high apoptosis rates occurred in this invasion niche, while central tumor regions with overall low CTL density harbored negligible apoptosis rates (Fig. 3h). To identify how preferential eradication of invading tumor cells was achieved, we co-registered CTL kinetics and apoptosis induction over time. In the invasion niche, median CTL speed was nearly doubled compared to the main tumor mass (Fig. 4c), with consistent orientation of CTL migration tracks along the invasion zone and its microanatomy, particularly myofibers, blood vessels and collagen bundles (Extended Data Fig. 8f, Movie 11). Whereas most individual CTL-target cell contacts were, again, dynamic and short-lived (median 15 min), local CTL accumulation combined with confined migration along the tissue structures supported consecutive engagements with tumor cells and high cumulative contact duration (Fig. 4d-f; median 2.2 h). Despite generally short-lived and non-productive individual engagements, this niche supported

serial additive conjugation and eradication of invading melanoma cells (Fig. 4e, Movie 12, 4g). Thus, *in vivo* eradication of tumor regions by CTL is a primary function of CTL migration and cumulative contact duration in the context of particular tissue niches.

Compared with the deterministic and reliable elimination of B cells¹⁻³, CTL effector function against solid tumor cells is an inefficient process with a high failure rate which is rarely completed by a single CTL interaction, but requires a sequence of sublethal hits. Apoptosis induction is, thus, not a binary event but instead implies the accumulation of a death signal within the target cell over time (“additive cytotoxicity”), not unlike the accumulation of activation signal in naïve T cells by successive encounters with APCs *in vitro* and *in vivo*²⁰⁻²³. Because additive cytotoxicity is rarely delivered by repetitive contacts from the same CTL (Extended Data Fig. 5e) but typically requires cooperation of multiple CTL (compare Movies 7, 12), CTL density control may provide a filter limiting accidental cell damage by single, miss-targeted CTL. Conversely, high CTL density provides effector redundancy as fail-safe mechanism to maintain effector function under adverse conditions, such as in immunosuppressive environments. Lethal hit delivery by serial CTL engagements, as gradual, tunable process, may further respond to microenvironmental and therapeutic immunomodulation, including stabilization of CTL-target cell contacts^{24,25}, activation of immunostimulatory pathways²⁶ and/or blockade of immune checkpoints²⁷. In conclusion, serial interaction of CTL with target cells and additive induction of death signal define the efficacy of CTL effector function which can be exploited by targeted therapy to increase both single contact efficacy and CTL cooperativity.

Methods summary

Organotypic three-dimensional cytotoxicity assay and time lapse microscopy.

Sub-confluent target cell monolayers were overlaid with 3D fibrillar collagen (PureCol, concentration: 1.7 mg/ml) containing *in vitro* activated OT1 CTL (cell models and activation protocols described in the Methods section). CTL migration, interactions with target cells and apoptosis induction was monitored by time-lapse bright-field microscopy frame intervals of 30 sec for 12 h followed by cell manual tracking and quantitative population analysis.

CTL induced calcium events in target cells.

Target cells were lentivirally transduced to stably express the calcium sensor GCaMP6¹⁷. DsRed OT1 CTL-target cell conjugation and consecutive intracellular Ca²⁺ events were coregistered by confocal 3D time-lapse microscopy (Leica SP8 SMD) at 488 nm and 561 nm excitation (both 0.05 mW) at frame intervals of 8-12 sec for up to 12 h. CTL position and Ca²⁺ intensity analysis were obtained by manual image segmentation and quantification.

Intravital multiphoton microscopy.

Histone-2B/mCherry expressing B16F10/OVA melanoma cells (1×10^5) were injected into the deep dermis of C57/B16 J mice (Charles River) carrying a dorsal skin-fold chamber and were repeatedly monitored for up to 15 days²⁸. With the onset of tumor invasion and angiogenesis at day 3 after implantation, *in vitro* activated eGFP or dsRed OT1 CTLs ($0.5-1 \times 10^6$) were injected intravenously. Multi-parameter intravital multiphoton microscopy was performed on anesthetized mice (1-3 % isoflurane in oxygen) on a temperature-controlled stage (37°C) recording up to 5 channels simultaneously to visualize blood vasculature (70kD dextran/ AlexaFluor750) and peri-tumor stroma (SHG).

Statistical modeling.

Survival curves of target cells receiving serial Ca²⁺ events were computed in GNU R using the 'survival' and 'rms' packages.

Statistical analysis.

Unpaired student's t-tests or Mann-Whitney U-tests, as appropriate, were applied using GraphPad Prism 5.

References

1. Stinchcombe, J. C., Bossi, G., Booth, S. & Griffiths, G. M. The immunological synapse of CTL contains a secretory domain and membrane bridges. *Immunity* **15**, 751–61 (2001).
2. Mempel, T. R. *et al.* Regulatory T cells reversibly suppress cytotoxic T cell function independent of effector differentiation. *Immunity* **25**, 129–41 (2006).
3. Purbhoo, M. a, Irvine, D. J., Huppa, J. B. & Davis, M. M. T cell killing does not require the formation of a stable mature immunological synapse. *Nat. Immunol.* **5**, 524–30 (2004).
4. Rothstein, T. L., Mage, M., Jones, G. & McHugh, L. L. Cytotoxic T lymphocyte sequential killing of immobilized allogeneic tumor target cells measured by time-lapse microcinematography. *J. Immunol.* **121**, 1652–6 (1978).
5. Martz, E. Multiple target cell killing by the cytolytic T lymphocyte and the mechanism of cytotoxicity. *Transplantation* **21**, 5–11 (1976).
6. Caramalho, I., Faroudi, M., Padovan, E., Müller, S. & Valitutti, S. Visualizing CTL/melanoma cell interactions: multiple hits must be delivered for tumour cell annihilation. *J. Cell. Mol. Med.* **13**, 3834–46 (2009).
7. Breart, B., Lemaître, F., Celli, S. & Bousso, P. Two-photon imaging of intratumoral CD8+ T cell cytotoxic activity during adoptive T cell therapy in mice. *J. Clin. Invest.* **118**, 1390–7 (2008).
8. Wiedemann, A., Depoil, D., Faroudi, M. & Valitutti, S. Cytotoxic T lymphocytes kill multiple targets simultaneously via spatiotemporal uncoupling of lytic and stimulatory synapses. *Proc. Natl. Acad. Sci. U. S. A.* **103**, 10985–90 (2006).
9. Isaaz, S., Baetz, K., Olsen, K., Podack, E. & Griffiths, G. M. Serial killing by cytotoxic T lymphocytes: T cell receptor triggers degranulation, re-filling of the lytic granules and secretion of lytic proteins via a non-granule pathway. *Eur. J. Immunol.* **25**, 1071–9 (1995).
10. Regoes, R. R., Yates, A. & Antia, R. Mathematical models of cytotoxic T-lymphocyte killing. *Immunol. Cell Biol.* **85**, 274–9 (2007).
11. Ganusov, V. V & De Boer, R. J. Estimating in vivo death rates of targets due to CD8 T-cell-mediated killing. *J. Virol.* **82**, 11749–57 (2008).
12. Choi, P. J. & Mitchison, T. J. Imaging burst kinetics and spatial coordination during serial killing by single natural killer cells. **2013**, (2013).
13. Schoenberger, S. P. *et al.* Efficient Direct Priming of Tumor-specific Cytotoxic T Lymphocyte in Vivo by an Engineered APC Efficient Direct Priming of Tumor-specific Engineered APC1. 3094–3100 (1998).
14. Broen, K. *et al.* A polymorphism in the splice donor site of ZNF419 results in the novel renal cell carcinoma-associated minor histocompatibility antigen ZAPHIR. *PLoS One* **6**, e21699 (2011).
15. Barry, M. & Bleackley, R. C. Cytotoxic T lymphocytes: all roads lead to death. *Nat. Rev. Immunol.* **2**, 401–9 (2002).
16. Lopez, J. a. *et al.* Perforin forms transient pores on the target cell plasma membrane to facilitate rapid access of granzymes during killer cell attack. *Blood* **121**, 2659–68 (2013).
17. Chen, T.-W. *et al.* Ultrasensitive fluorescent proteins for imaging neuronal activity. *Nature* **499**, 295–300 (2013).
18. Boissonnas, A., Fetler, L., Zeelenberg, I. S., Hugues, S. & Amigorena, S. In vivo imaging of cytotoxic T cell infiltration and elimination of a solid tumor. *J. Exp. Med.* **204**, 345–56 (2007).

19. Weigel, B., Bakker, G.-J. & Friedl, P. Intravital third harmonic generation microscopy of collective melanoma cell invasion: Principles of interface guidance and microvesicle dynamics. *IntraVital* **1**, 9–20 (2012).
20. Friedl, P. & Gunzer, M. Interaction of T cells with APCs: the serial encounter model. *Trends Immunol.* **22**, 187–91 (2001).
21. Marangoni, F. *et al.* The Transcription Factor NFAT Exhibits Signal Memory during Serial T Cell Interactions with Antigen-Presenting Cells. *Immunity* **38**, 237–49 (2013).
22. Lodygin, D. *et al.* A combination of fluorescent NFAT and H2B sensors uncovers dynamics of T cell activation in real time during CNS autoimmunity. *Nat. Med.* **19**, 784–90 (2013).
23. Moreau, H. D. & Bousso, P. Visualizing how T cells collect activation signals in vivo. *Curr. Opin. Immunol.* **26**, 56–62 (2014).
24. Hoffmann, P. *et al.* Serial killing of tumor cells by cytotoxic T cells redirected with a CD19-/CD3-bispecific single-chain antibody construct. *Int. J. Cancer* **115**, 98–104 (2005).
25. Baeuerle, P. a. & Reinhardt, C. Bispecific T-cell engaging antibodies for cancer therapy. *Cancer Res.* **69**, 4941–4 (2009).
26. Melero, I., Grimaldi, A. M., Perez-Gracia, J. L. & Ascierto, P. A. Clinical development of immunostimulatory monoclonal antibodies and opportunities for combination. *Clin. Cancer Res.* **19**, 997–1008 (2013).
27. Pardoll, D. M. The blockade of immune checkpoints in cancer immunotherapy. *Nat. Rev. Cancer* **12**, 252–64 (2012).
28. Alexander, S., Koehl, G. E., Hirschberg, M., Geissler, E. K. & Friedl, P. Dynamic imaging of cancer growth and invasion: a modified skin-fold chamber model. *Histochem. Cell Biol.* **130**, 1147–54 (2008).

Supplementary Information is linked to the online version of the paper at www.nature.com/nature.

Acknowledgements

This work was supported by the Dutch Cancer Foundation (KWF 2008-4031) to C.G.F. and P.F., a personal KWF grant to AdB), the FP7 of the European Union (ENCITE HEALTH TH-15-2008-208142), NWO-VICI (918.11.626) and the Cancer Genomics Cancer, The Netherlands to P.F.. We thank Stephen P. Schoenberger for providing the MEC-1/OVA cell line.

Author contributions

B.W., P.F. designed the experiments, interpreted the data and wrote the paper. A.d.B. designed and performed experiments, B.W., E.W., performed experiments and quantitatively analyzed the data, K.B. isolated, characterized and cultured the human SMCY.A2 CTL, J.T. and R.d.B performed mathematical analyses, H.D. and C.F. contributed to data interpretation. All authors read and corrected the manuscript.

Author Information

Reprints and permissions information is available at www.nature.com/reprints. The authors declare no competing financial interests. Correspondence and requests for materials should be addressed to peter.friedl@radboudumc.nl.

Methods section

Cell lines and primary cell culture.

C57BL/6 mouse embryonic fibroblast-like cells (MEC-1) expressed B7.1 and the OVA-derived CTL epitope SIINFEKL (MEC-1/OVA) or the adenovirus type 5 E1A-derived CTL epitope SGPSNTPPEI (MEC-1/E1A) coupled to a signal-sequence which directs epitope expression to the endoplasmic reticulum¹. The cells were cultured in RPMI 1640 medium (GIBCO, 21875-034) supplemented with 10% FCS (SIGMA, F7524), 10 mM HEPES (GIBCO, 15630-056), 500 mM 2-mercaptoethanol, 1% penicillin and streptomycin (PAA, P11-010), 1% sodium pyruvate (GIBCO, 11360-039), and 0.1 mM non-essential amino acids (GIBCO, 11140-035).

B16F10 mouse melanoma cells expressing the OVA-derived CTL epitope SIINFEKL (B16F10/OVA) were transduced to express histone-2B/mCherry as described². A low-pigmented subline was derived by sequential passaging and validated for unchanged growth, invasion ability, antigenicity and apoptosis resistance *in vitro* and *in vivo*. The cells were cultured in RPMI 1640 medium (GIBCO, 21875-034) supplemented with 10% FCS (SIGMA, F7524), 1% sodium pyruvate (GIBCO, 13360-039) and 1% penicillin and streptomycin (PAA, P11-010). Prior to experiments, cells were stimulated with 200 U/ml murine IFN γ (PEPROTECH, 315-05) for 48h.

MV3 and BLM male HLA-A2 expressing human melanoma cells were cultured in DMEM medium (GIBCO, 10938-025) supplemented with 10% FCS (SIGMA, F7524), glutamine (LONZA, BE17-605), 1% sodium pyruvate (GIBCO, 13360-039) and 1% penicillin and streptomycin (PAA, P11-010). Prior to experiments, cells were stimulated with 200 U/ml human IFN γ (SIGMA, I3265) for 48h.

Mice.

C57BL/6 J mice (4-6 weeks of age) were purchased at Charles River Laboratories. Transgenic mice expressing eGFP under the human ubiquitin C promoter (Jackson Laboratories, stock number: 004353) and transgenic mice expressing dsRed under the chicken beta-actin promoter (Jackson Laboratories, stock number: 006051) were crossed to OT-I TCR transgenic mice (Jackson Laboratories, stock number: 003831). Double transgenic eGFP/OT-1 and dsRed/OT-1 were bred in the Central Animal Laboratory of the Radboud University Nijmegen, The Netherlands.

Isolation and activation of primary CD8⁺ OT1 CTL.

OT1 CTL were activated as described³. In short, splenocytes from OT1 or double-transgenic eGFP/OT1 or dsRed/OT1 mice were isolated and erythrocytes were depleted by ammonium chloride (0.83% NH₄Cl, 0.1% KHCO₃, 0.37% Na₂ EDTA). For the expansion of antigen-specific CTL, splenocytes were cultured at a concentration of 2.5 x10⁵ /ml in the presence of 0.5 μ g/ml SIINFEKL peptide in 24-well plates for 3 days. On day 3, IL-2

(100 U/ml) (ABD SEROTEC, PMP-38) was added to the cultures. Lymphocytes were incubated for further 24-48 h and harvested on days 4-5 by a Ficoll gradient (AXIS-SHIELD PoC AS, Oslo, Norway). Purity was determined by flow cytometry and typically exceeded 96% of $V\alpha 2^+CD8^+CD62L^{low}CD44^{hi}$ cells.

To determine the surface expression of Lamp-1 after 24h of coculture with target cells in the 3D cytotoxicity assay, CTL and surviving target cells were harvested by dissolving the collagen with collagenase I (40 U / 96-well; 30 min; SIGMA C0130) and detaching the remaining adherent cells with trypsin/EDTA (5 min). Both cell fractions were combined, washed in PBS, stained with AlexaFluor488-conjugated anti-Lamp-1 rat-IgG (BIOLEGEND, 121608) and detected after signal enhancement by donkey anti-rat/Alexa488 (LIFE TECHNOLOGIES, A21208). CTL were gated on intact morphology, viability by propidium iodide exclusion and dsRed expression using De Novo FCS Express 4. Percentages of positive events were calculated using the build-in FCS Express function for histogram subtraction.

Activation and culture of primary human SMCY.A2 CTL.

The $CD8^+$ SMCY CTL line was isolated and cultured as described previously⁴. In short, $CD8^+$ CTL were isolated from PBMC obtained from a renal cell carcinoma patient who received allogeneic stem cell transplantation (SCT) and donor lymphocyte infusions (DLI). This patient has given informed consent to the prospective collection of peripheral blood samples for investigational use, which was approved by the Radboud University Medical Centre (RUMC) Institutional Review Board. $CD8^+$ T cells were expanded by weekly stimulation with PBMC obtained before SCT in Iscove's modified Dulbecco's medium (IMDM; INVITROGEN, Carlsbad, CA) supplemented with 10% human serum (HS; Sanquin blood bank, Nijmegen, the Netherlands). After initial stimulation, CTL (0.5×10^6) were cultured in IMDM/10% HS containing irradiated (80 Gy) recipient EBV-LCL (0.5×10^6) and irradiated (60 Gy) allogeneic PBMC (0.5×10^6) from two donors, together with IL-2 (100 IU/ml; Chiron, Emeryville, CA) and PHA-M (1 mg/ml; Boehringer, Alkmaar, the Netherlands). A greater than 95% pure population of SMCY.A2 specific CTL was isolated by FACS sorting (tetramer staining of HLA-A2-restricted SMCY.A2 epitope FIDSYICQV). Specificity of SMCY.A2 CTL was further confirmed by lack of cytotoxicity against female HLA-A2 expressing breast carcinoma cell (MCF-7) as target cells (Fig. 1h).

Three-dimensional cytotoxicity assay and time-lapse microscopy.

A sub-confluent monolayer of target cells was overlaid with a 3D collagen gel (PureCol, concentration: 1.7 mg/ml) containing pre-activated CTL in a customized imaging chamber, allowed to polymerize (30 min, 37°C) and filled with undiluted CTL growth medium. CTL dynamics were recorded by time-lapse bright-field microscopy with a 30 sec frame interval for 24-48 h.

CTL-target cell interactions were quantified by manual analysis. CTLs in contact with target cells slowed migration speed and spread on the target cell surface, which was used as morphological marker to distinguish irrelevant passenger CTL. For quantification of the frequency of serial killing events, only CTLs which could be followed for >12 h were included in the statistical analysis. CTL-target cell interactions were classified as non-lethal after survival of the target cell for > 3 h after CTL detachment. The > 3 h follow-up period is based on statistics of the lag time between last CTL induced Ca^{2+} event and target cell death which predominantly remained below 1 h in MEC-1/OVA and 1-2 h in B16F10/OVA (Extended Data Fig. 5h).

Monitoring CTL induced calcium events in target cells.

Target cells were lentivirally transduced to stably express the calcium sensor GCaMP6s⁵ by selection with blasticidin (10 $\mu\text{g}/\text{ml}$; Life Technologies, R210-01) and FACS sorting on GCaMP6s background expression. CTL-target cell conjugation and associated intracellular Ca^{2+} events were obtained by coregistering GCaMP6 and dsRed OT1 CTL as single scans at frame intervals of 8-12 sec for up to 12 h on a Leica SP8 SMD confocal scanner using 0.05 mW for each excitation line (488, 561 nm). Viability of CTL and target cells during long-term imaging was controlled by verifying constant CTL migration speed and viability over time as well as lack of laser induced cell death and unperturbed proliferation compared to bright-field imaging in target cell cultures without CTL. CTL-associated Ca^{2+} events were identified by manual image segmentation and intensity analysis and displayed for cell populations of multiple independent experiments.

Intravital multiphoton microscopy.

All intravital imaging experiments were approved by the Ethical Committee on Animal Experiments and performed in the Central Animal Laboratory of the Radboud University, Nijmegen (RU-DEC 2009-174, 2011-298), in accordance with the Dutch Animal Experimentation Act and the European FELASA protocol (www.felasa.eu/guidelines.php).

Histone-2B/mCherry expressing tumor cells (1×10^5) were injected into the deep dermis of C57/B16 J mice (Charles River) carrying a dorsal skin-fold chamber and were repeatedly monitored for up to 15 days⁶. Three days after tumor implantation, *in vitro* activated eGFP or dsRed OT1 CTLs ($0.5\text{--}1 \times 10^6$) were injected intravenously. Multiparameter intravital multiphoton microscopy was performed on anesthetized mice (1-3 % isoflurane in oxygen) on a temperature-controlled stage (37°C). Blood vessels were contrasted by intravenous injection of AlexaFluor750-labeled 70kD dextran (2 mg/mouse; Invitrogen).

Tumor volume was reconstructed from epifluorescence overview images recorded at sequential time points. Tumor volume (V) was calculated as $(\text{tumor width})^2 \times (\text{tumor length}) \times \pi/6$.

Imaging was performed on a customized near-infrared/infrared multiphoton microscope (TriMScope-II, LaVision BioTec, Bielefeld, Germany), equipped with three tunable Ti:Sa (Coherent Ultra II Titanium:Sapphire) lasers and an Optical Parametric Oscillator (OPO). 4D time-lapse recordings were acquired by sequential scanning with 910 nm (eGFP and Alexa750, 20-30 mW) and 1090 nm (mCherry and SHG, 30-60 mW) with a sampling rate of 1 frame / 2min over periods of 4-8 h or for visualization of intracellular Ca^{2+} dynamics with a sampling rate of 1 frame / 10-15 sec over periods of 1-2 h.

Image processing and quantification.

Images were processed using Fiji/ImageJ (<http://pacific.mpi-cbg.de/wiki/index.php/Fiji>). Mosaic images were stitched using the Stitch Grid/Collection plugin⁷ and drifts in time-lapse recordings were corrected using the StackReg plugin⁸ and the Correct 3D Drift plugin. For presentation of time-lapse recordings, 4D stacks were adjusted for bleaching using the Bleach Correction plugin (Histogram normalization). If necessary background noise was filtered using the Remove Outliners plugin and images were scaled and adjusted for brightness and contrast to enhance visualization. For image quantifications the raw, unmodified images were used.

Intact vs. apoptotic states of tumor nuclei and CTL ratios were quantified from individual slices of multiple 3D stacks of 350 x 350 μm , acquired with 7 μm z-resolution until imaging depths of up to 300 μm . To avoid repeated counting of the same cell, every 3rd slice per stack was analyzed. Nuclei and CTL were segmented by applying a Gaussian Blur filtering followed by automated thresholding (Li algorithm) and separation of touching objects using Watershed. Using the Analyze Particles command of FIJI, segmented objects were filtered for size (Nuclei: $\geq 60 \mu\text{m}^2$; CTL: $\geq 50 \mu\text{m}^2$) and counted per slice. To determine subregional apoptosis and mitosis rates, apoptotic and mitotic nuclei were counted manually and calculated as percentage of total nuclei per slice.

Statistical modeling.

The analysis of target cell survival, Ca^{2+} events and the resulting survival probability curves were computed in GNU R using the 'survival' and 'rms' packages. In a subset of analyses, redundant Ca^{2+} -positive "hits" which may bias the analysis by concealing the already occurred lethal hit and being misleadingly interpreted as prior, additive hits were removed, based on the following considerations. The "stochastic killing" hypothesis predicts that each Ca^{2+} event has the same likelihood to induce apoptosis and, consequently, the number of Ca^{2+} events received prior to the last event preceding apoptosis should not impact target cell survival. However, redundant Ca^{2+} events induced by the same or other CTL, which are dispensable for apoptosis, may occur after target cells received the lethal hit, and result on an overestimation of required hits. We

used the following approach to identify and remove such redundant events. Waiting times to apoptosis following the last lethal event were assumed to be exponentially distributed, and the mean waiting time best describing the data was fitted using the maximum likelihood method. For each target cell, the Ca^{2+} event whose likelihood of being the terminal event was largest, given the fitted distribution, was determined. This event was defined as the terminal event for the given cell, and all subsequent Ca^{2+} events were considered redundant (Extended Data Fig. 6a). Despite the removal of redundant contacts, survival probability and lag times to apoptosis remained significantly dependent on prior Ca^{2+} events ($p=0.00032$ with removal, $p=0.00003$ without), in agreement with additive cytotoxicity of serial Ca^{2+} events (Extended Data Fig. 6b).

To simulate purely stochastic killing, the time between serial Ca^{2+} events and the lag time between Ca^{2+} events to apoptosis were randomly permuted. Assuming stochastic killing, these permutations should not affect target cell survival probability after the last contact. However, the permuted data revealed significantly enhanced killing efficiency compared to the actual killing efficiency derived from live-cell measurements whereby the amount of prior Ca^{2+} events lacked impact on survival probability after the last Ca^{2+} event (Extended Data Fig. 6c). Thus, stochastic apoptosis induction by individual hits is incompatible with the experimentally observed killing kinetics.

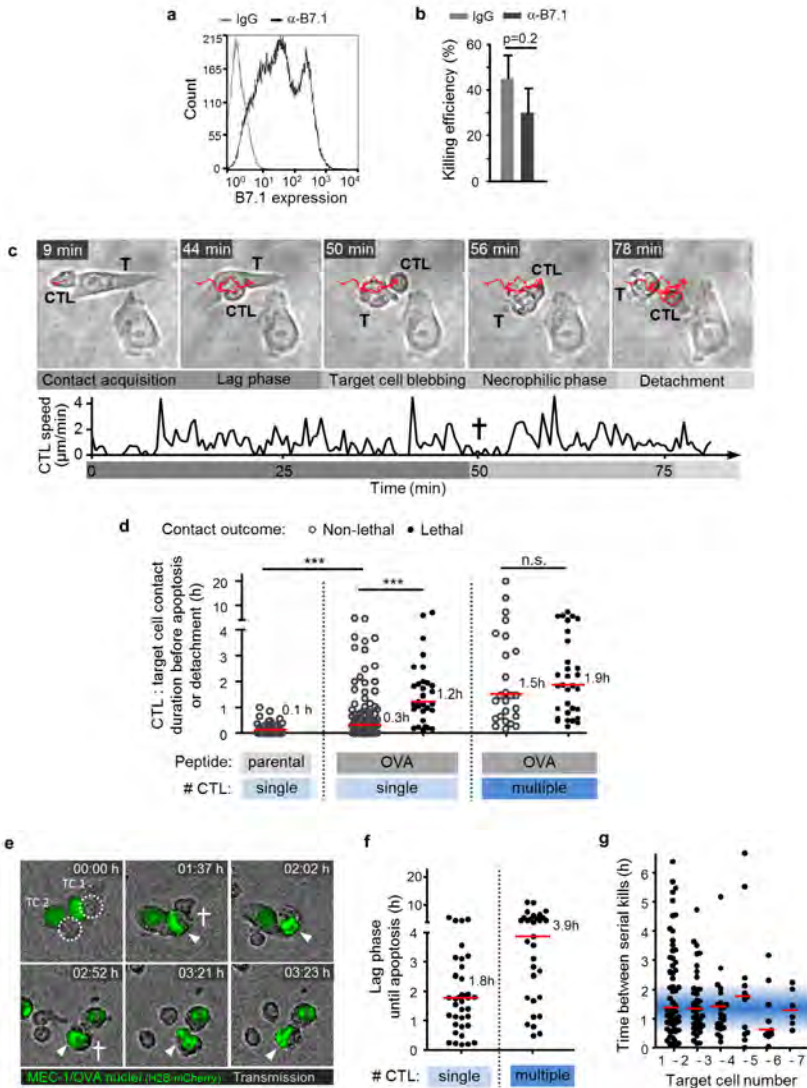
Statistical analysis.

Unpaired student's t-tests or Mann-Whitney U-tests, as appropriate, were applied using GraphPad Prism 5.

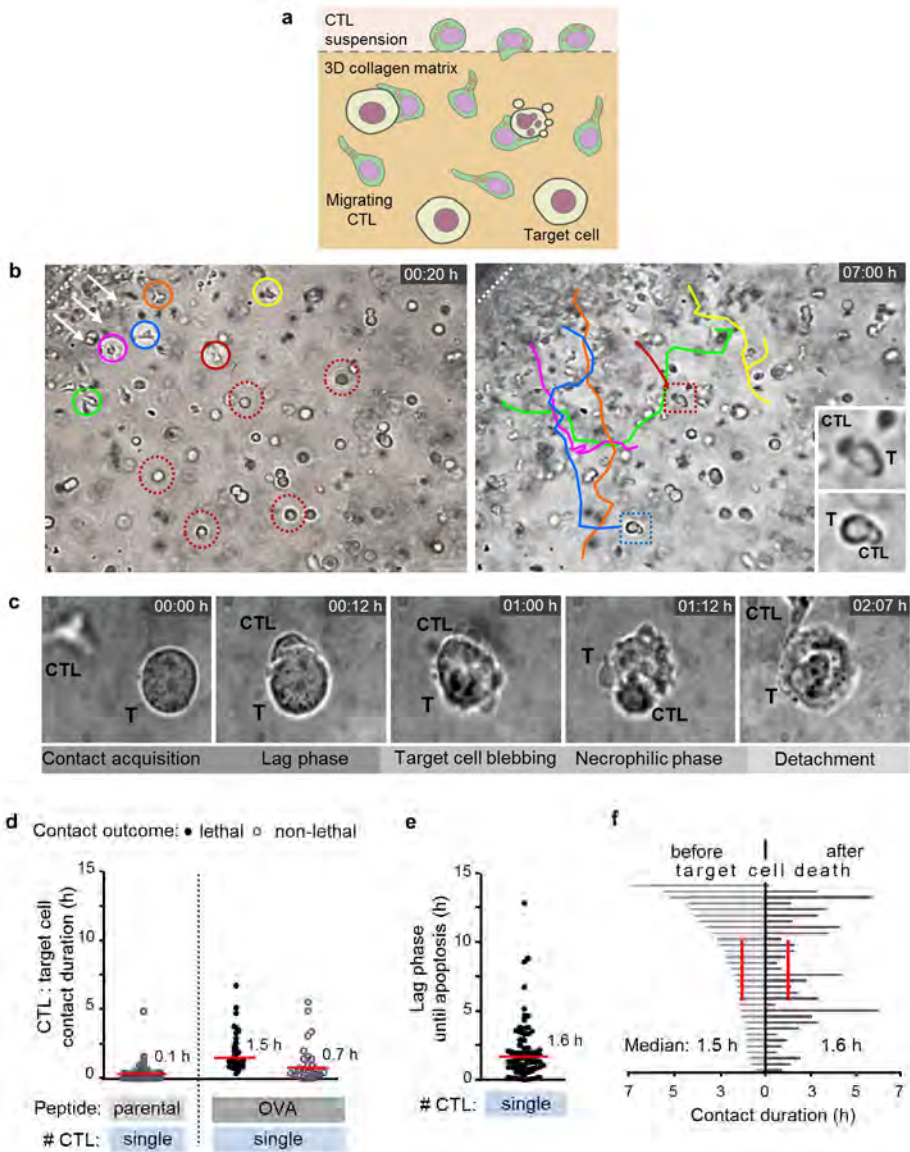
References Methods Section

29. Schoenberger, S. P. *et al.* Efficient Direct Priming of Tumor-specific Cytotoxic T Lymphocyte in Vivo by an Engineered APC Efficient Direct Priming of Tumor-specific Engineered APC1. 3094–3100 (1998).
30. Weigelin, B., Bakker, G.-J. & Friedl, P. Intravital third harmonic generation microscopy of collective melanoma cell invasion: Principles of interface guidance and microvesicle dynamics. *IntraVital* **1**, 9–20 (2012).
31. Weigelin, B. & Friedl, P. A three-dimensional organotypic assay to measure target cell killing by cytotoxic T lymphocytes. *Biochem. Pharmacol.* **80**, 2087–91 (2010).
32. Broen, K. *et al.* A polymorphism in the splice donor site of ZNF419 results in the novel renal cell carcinoma-associated minor histocompatibility antigen ZAPHIR. *PLoS One* **6**, e21699 (2011).
33. Chen, T.-W. *et al.* Ultrasensitive fluorescent proteins for imaging neuronal activity. *Nature* **499**, 295–300 (2013).
34. Alexander, S., Koehl, G. E., Hirschberg, M., Geissler, E. K. & Friedl, P. Dynamic imaging of cancer growth and invasion: a modified skin-fold chamber model. *Histochem. Cell Biol.* **130**, 1147–54 (2008).
35. Preibisch, S., Saalfeld, S. & Tomancak, P. Globally optimal stitching of tiled 3D microscopic image acquisitions. *Bioinformatics* **25**, 1463–5 (2009).
36. Thévenaz, P., Ruttimann, U. E. & Unser, M. A pyramid approach to subpixel registration based on intensity. *IEEE Trans. Image Process.* **7**, 27–41 (1998).

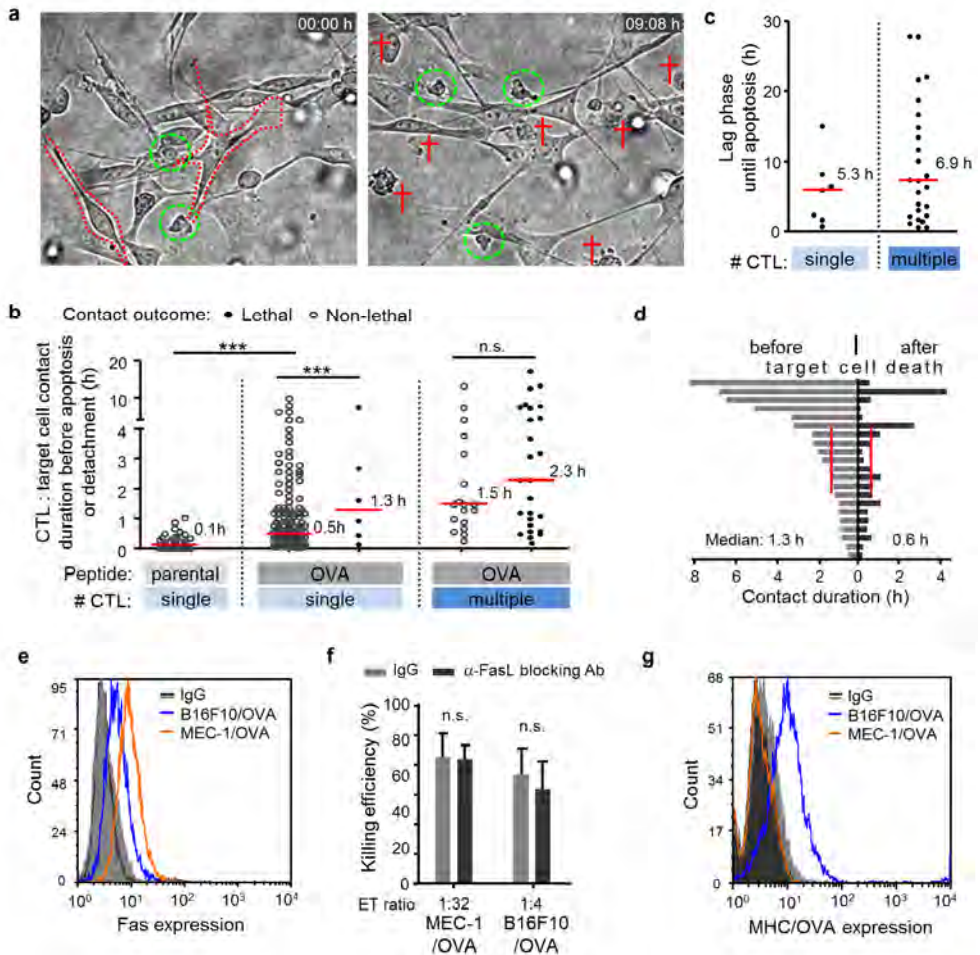
Supplementary Figures



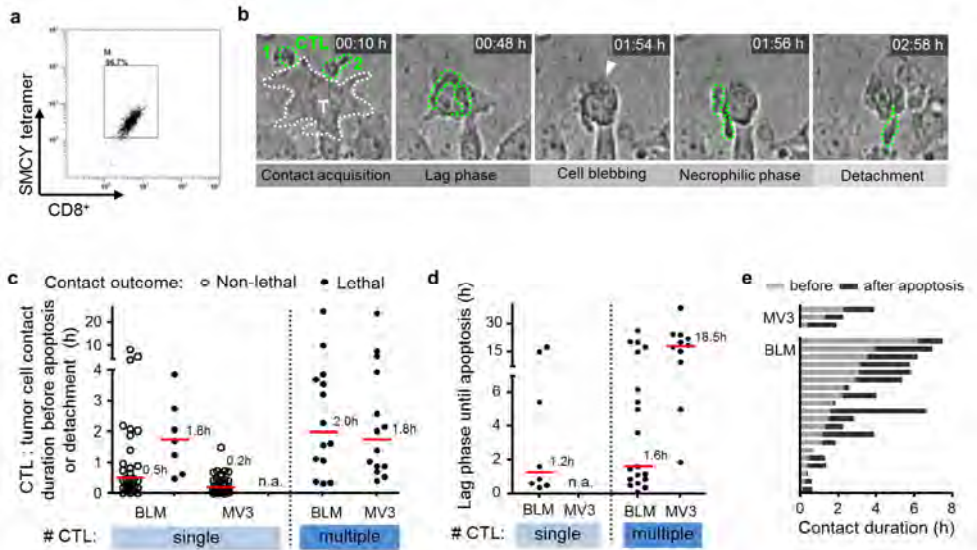
Extended data figure 1. CTL contact phases, types and duration in MEC-1/OVA model. a, Expression level of B7.1 on MEC-1/OVA target cells. **b**, Efficiency of killing by OT1 CTL after blocking B7.1 with α -B7.1 Ab (15 $\mu\text{g}/\text{ml}$) in 3D cytotoxicity assay. **c**, Contact phases and speed of individual OT1 CTL during contact. **d**, CTL-target cell contact durations and contact outcome. **e**, Live detection of apoptosis by target cell morphology (blebbing) and nuclear condensation/fragmentation, using H2B/eGFP as label. Image sequence shows two MEC-1/OVA target cells (TC) killed by two OT1 CTL. Circles: OT1 CTL; Cross: target cell apoptosis; Arrow heads: nuclear condensation and fragmentation. **f**, Lag phase until apoptosis of targets induced by single or multiple CTL. **g**, Time between serial killing events mediated by the same CTL. *** $p < 0.001$; n.s., not significant (two-tailed Mann-Whitney U-test). Red bars, median. Pooled data (**d,f,g**) from 9 independent experiments.



Extended data figure 2. Validation of CTL contacts by interphase-free 3D invasion assay. **a**, 3D collagen-based invasion assay. **b**, Early and late CTL immigration into 3D collagen matrix containing individually dispersed MEC-1/OVA target cells. Dotted white line, medium-collagen matrix interface overlaid with CTLs. Colored circles and colored lines denote CTLs and migration paths. Dotted red circles, target cells. Insets, CTL-target cell conjugates. **c**, Phases of OT1 CTL engaging with target cell in 3D collagen (time-lapse sequence). **d**, CTL-target cell contact durations and outcome. **e**, Lag phase until apoptosis induced by single CTL-target cell contact. **f**, CTL contact durations with the same target cell before and after target cell blebbing. Individual CTL contacts and target cell fate were manually tracked and quantified. *** $p < 0.001$ (two-tailed Mann-Whitney U-test). Red bars, median. Pooled data from 3 independent experiments.

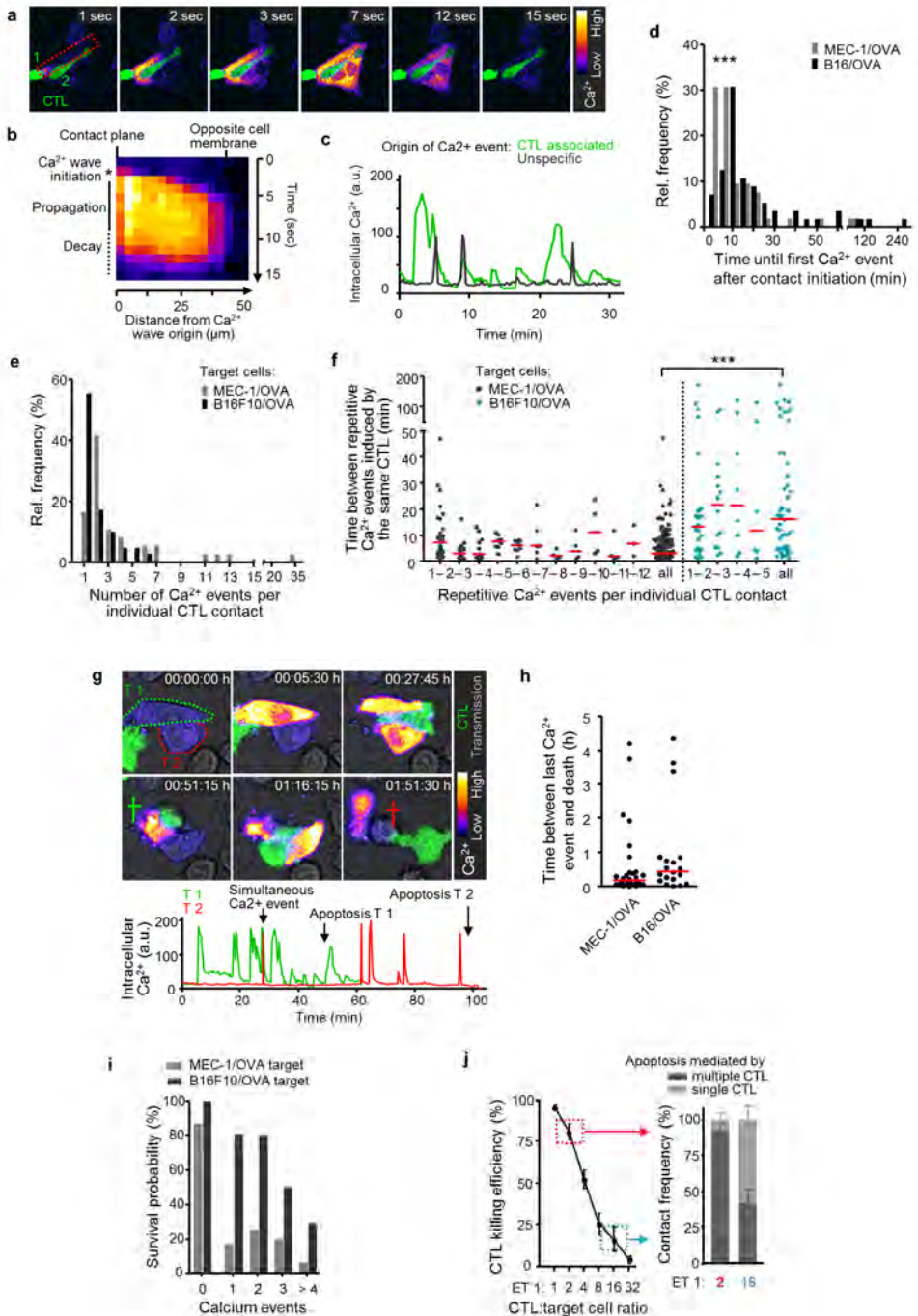


Extended data figure 3. Validation of CTL effector function against mouse B16F10 melanoma cells. **a**, Overview image of sub-confluent monolayer of B16F10/OVA with CTL in the 3D collagen matrix interface assay at consecutive time points. Green circles, CTL; Red cross, apoptotic target cell. **b**, Duration of contacts between individual and multiple CTL with B16F10/OVA target cells until apoptosis induction. **c**, Lag phase until apoptosis induced by contacts from single or multiple, sequentially engaged CTL. **d**, Duration of contact phases between individual CTL with target cell before and after target cell blebbing, obtained by manual tracking. Red lines, median. **e**, Fas expression levels on MEC-1/OVA and B16F10/OVA target cells. Histograms representative for 2 independent experiments. **f**, CTL killing efficiency upon blocking FasL by α -FasL Ab (MFL4) (10 μ g/ml). Error bars, mean \pm SD (n=3). n.s., non-significant (two-tailed Mann-Whitney U-test). **g**, MHC/OVA expression levels on MEC-1/OVA and B16F10/OVA. Histograms representative for 3 independent experiments.

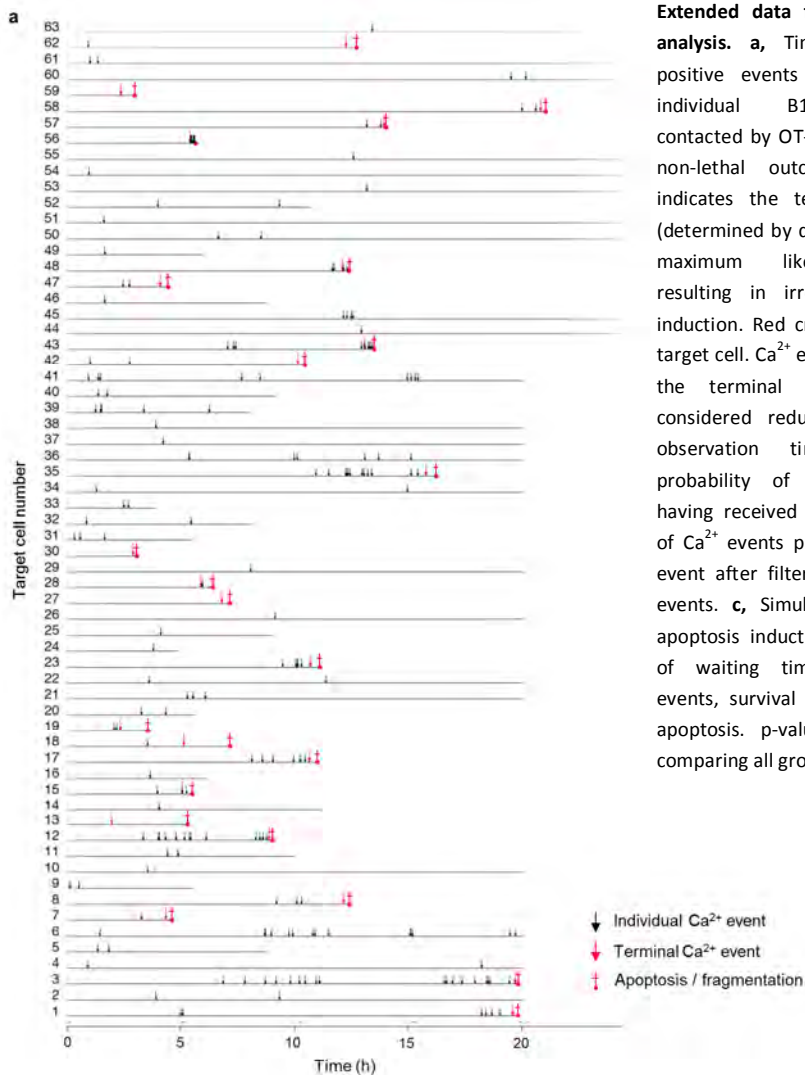


Extended data figure 4. Validation of CTL effector phases in human SMCY.A2 model. **a**, SMCY.A2 tetramer / CD8 double staining confirming CTL specificity and purity of > 95%. **b**, Time-lapse sequence of two simultaneously engaging CTL with human BLM melanoma target cell followed by target-cell apoptosis. **c**, SMCY.A2 CTL contact durations with BLM and MV3 melanoma targets and contact outcome. N.a., not applicable. **d**, Lag phase until apoptosis induced by single or multiple CTL. **e**, CTL contact duration with the same target cell before and after target cell blebbing. Red bars, median. Pooled data from 3 (MV3) and 4 (BLM) independent experiments.

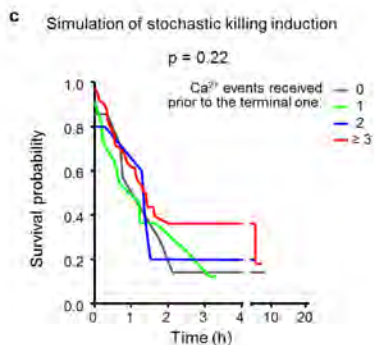
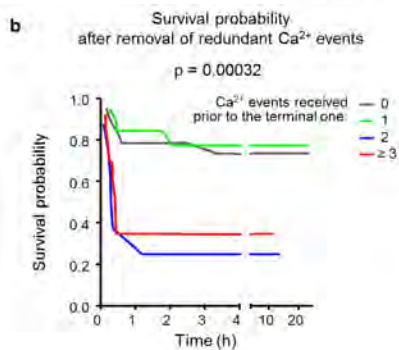
Extended data figure 5. (see next page) CTL induced intracellular Ca^{2+} events in target cells. **a**, Time-lapse sequence of OT1 CTL (green) associated Ca^{2+} event (Fire LUT) in MEC-1/OVA target cell. Frame rate: 1 sec. **b**, Ca^{2+} influx originating at the CTL-target cell contact plane and propagating through the target cell cytoplasm at 20 $\mu\text{m}/\text{sec}$ velocity. **c**, Amplitude and duration of CTL-associated calcium events compared with spontaneous intracellular calcium fluctuations in the absence of CTL. **d**, Lag phase until first Ca^{2+} event after contact initiation. **e**, Number of Ca^{2+} events associated with the same CTL in MEC-1/OVA and B16F10/OVA cells. **f**, Intervals between repetitive Ca^{2+} events induced by the same CTL during one contact, ranging from seconds to hours with medians of 4 min (MEC-1/OVA) and 18 min (B16F10/OVA). **g**, Time-lapse sequence and intensity plot of simultaneous Ca^{2+} events (Fire LUT, GCaMP6s) in 2 neighboring target cells contacted by the same CTL (green). TC, target cell. **h**, Lag phase between last Ca^{2+} event and target cell apoptosis. *** $p < 0.0001$ (two-tailed Mann-Whitney U-test). Red line, median. Pooled data from 2 (MEC-1/OVA) and 3 (B16F10/OVA) independent experiments. **i**, Survival probability as percentage of target cells that survived increasing numbers of CTL-associated Ca^{2+} events. **j**, Absolute killing efficacy of B16F10/OVA cells and frequency of apoptosis induction by single or multiple CTL in dependence of ET ratio. Killing efficiency, $n=3$ cytotoxicity assays. Contact frequency, 110 contacts from 4 independent movies per ET ratio.

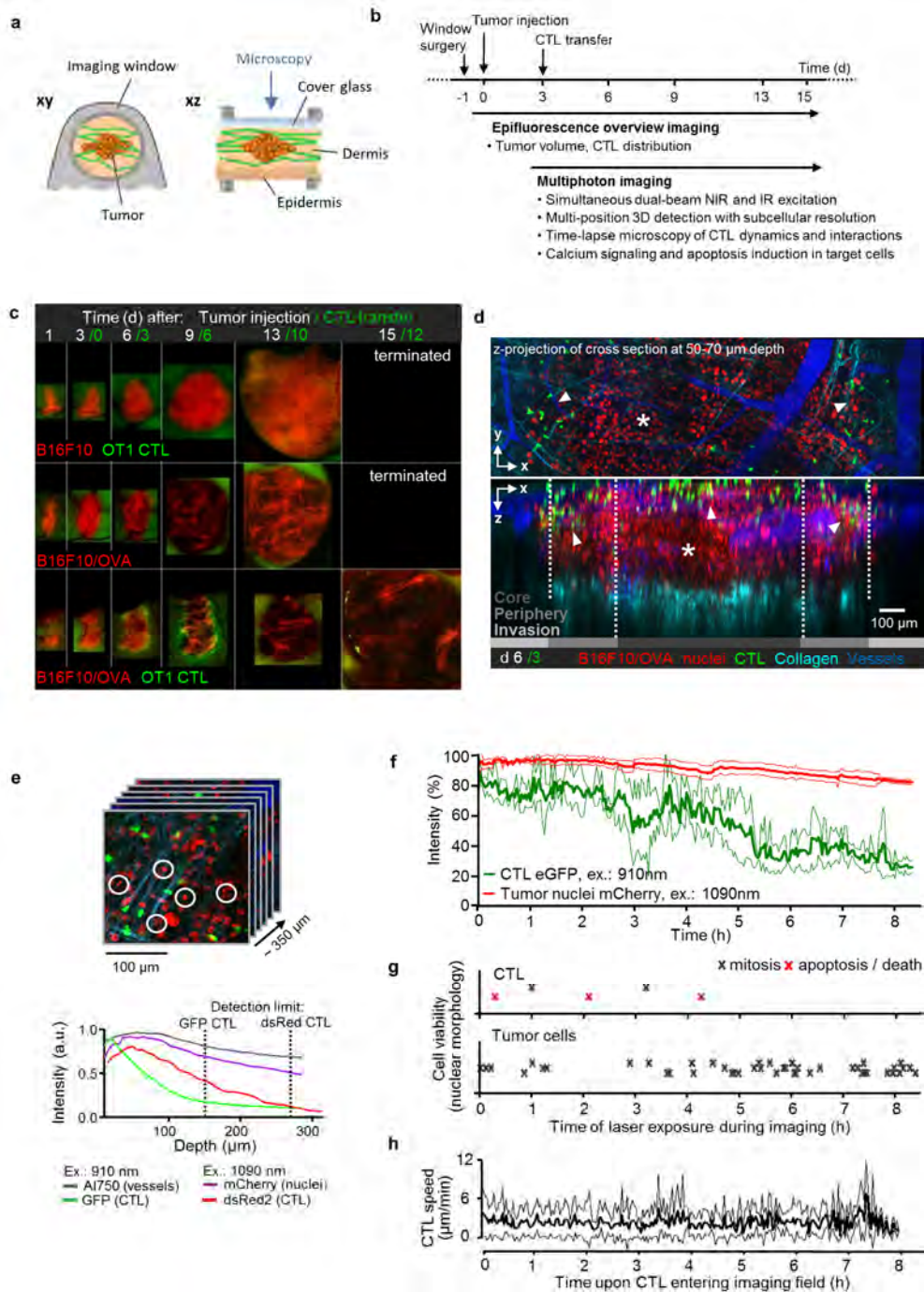


Extended data figure 5. See previous page.



Extended data figure 6. Statistical analysis. **a**, Time-points of Ca^{2+} -positive events (black arrows) in individual B16F10/OVA cells contacted by OT-1 CTL and lethal or non-lethal outcome. Red arrow indicates the terminal Ca^{2+} event (determined by data fitting using the maximum likelihood method) resulting in irreversible apoptosis induction. Red crosses, apoptosis of target cell. Ca^{2+} events subsequent to the terminal Ca^{2+} event were considered redundant. Gray lines, observation time. **b**, Survival probability of B16F10/OVA cells having received increasing numbers of Ca^{2+} events prior to the terminal event after filtering redundant Ca^{2+} events. **c**, Simulation of stochastic apoptosis induction by permutation of waiting times between Ca^{2+} events, survival and lag times until apoptosis. p-values, log rank test comparing all groups.

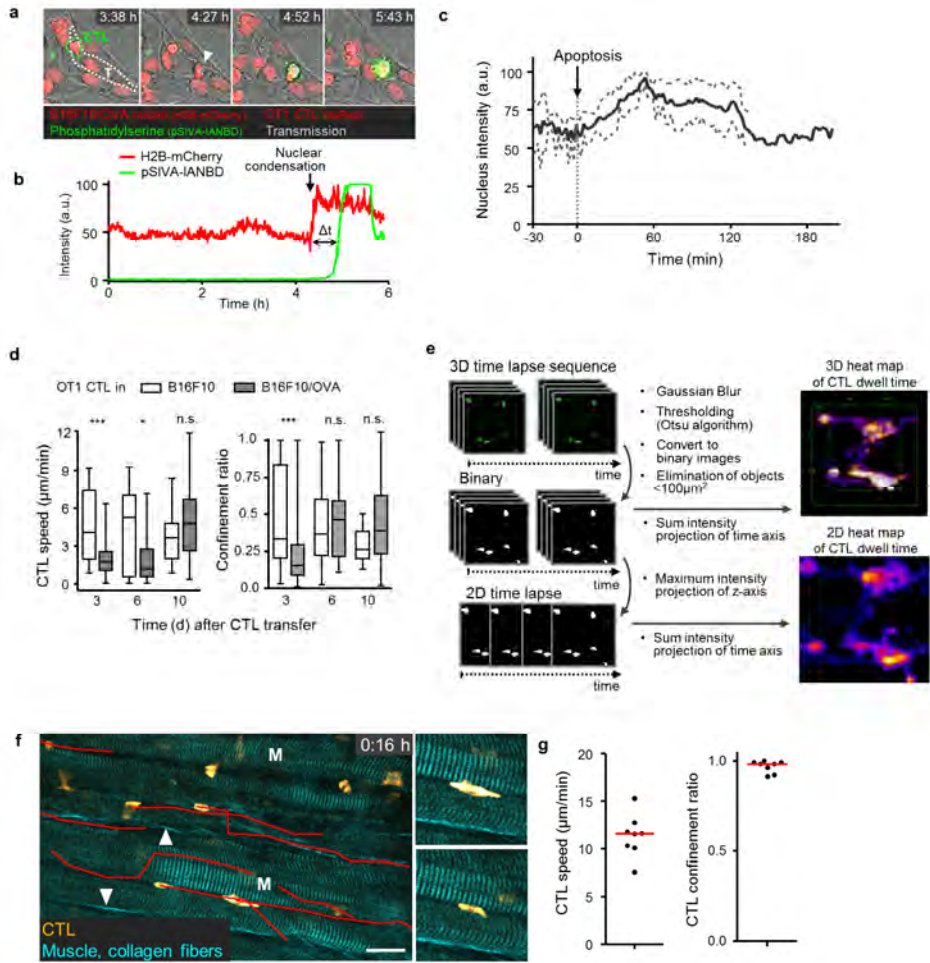




Extended data figure 7. See next page.

Extended data figure 7. (see previous page) Intravital microscopy of target cell killing: experimental model and data analysis. Established B16F10/OVA melanoma tumors received adoptive OT1 CTL therapy (day 3) followed by CTL arrival in the lesion (day5-6). **a**, Dorsal skin-fold chamber setup and tumor model. **b**, Setup and time line, including cell application, intravital monitoring and parameter extraction. **c**, Time-dependent tumor morphology and distribution of CTL monitored by epifluorescence detection through the skin window. Red fluorescence, B16F10 nuclei (histone-2B/mCherry); strong green, OT1 CTL (eGFP); weak green, background autofluorescence. **d**, 3D multi-photon microscopy image stacks obtained from multiple positions in the same tumor. Image dimensions: 350 x 350 μm with 5-7 μm z-resolution and total depth of $\sim 350 \mu\text{m}$. Red, tumor nuclei (histone-2B/mCherry); green, OT1 CTL (eGFP); cyan, collagen fibers (SHG); blue, blood vessels (70kDa-dextran/Alexa750). Images were acquired as sequential scans of 910nm (GFP, A1750) and 1090nm (mCherry, SHG) with a linear laser power increase in z ranging from 20-75 mW (910nm) and 30-100 mW (1090nm). **e**, Loss of fluorescence intensity as function of imaging depth. As consequence, the detection limit for CTL expressing GFP was $\sim 150 \mu\text{m}$ and $\sim 280 \mu\text{m}$ for dsRed. **f-h**, Lack of phototoxicity in long-term time-lapse recordings. Imaging conditions: z resolution, 5 μm ; frame rate, 2 min; imaging duration, 8h; laser power, 25 mW (910nm) and ~ 40 mW (1090nm). **f**, Bleaching of GFP (CTL) and mCherry (tumor nuclei). **g**, Unperturbed mitosis or apoptosis rates in CTL and tumor cells. **h**, Unperturbed average migration speed of CTLs. Error bars: mean \pm SD.

Extended data figure 8 (see next page). Visualization of target cell apoptosis, CTL dwell time and migration dynamics along guiding tissue structures. **a**, Time-lapse detection of apoptosis in B16F10/OVA cell by nuclear condensation (red: nuclei, histone-2B/mCherry) and phosphatidyl serine exposure (green: pSIVA-IANBD) on the cell surface upon CTL contact (red: dsRed CTL). Arrowhead, onset of nuclear condensation. **b**, Intensity increase of H2B/mCherry coincides with nuclear condensation during apoptosis and is followed by an increase of pSIVA-IANBD signal. Representative example for >15 cells from 3 independent experiments. The time difference (Δt) between the onset of detected nuclear condensation or fragmentation and cell blebbing and subsequent onset of phosphatidyl serine signal was 23.3 ± 6.1 min (Δt until maximum PS signal: 36.6 ± 12.6 min). **c**, Duration of increased fluorescence intensity in nuclei during/after apoptosis induction. Arrow, duration of signal increase (average 2-3 h). **d**, CTL migration speed and confinement ratio over time. **e**, Image processing routine to display 3D and 2D CTL dwell time heat maps. **f**, CTL migration tracks in tumor-free deep dermis (perimuscular niche). CTL tracks align with guiding structures of the tissue. Zoom: CTL shape change and alignment along perimuscular space. Arrowheads, collagen fibrils. Bar, 20 μm . **g**, CTL migration speed (left) and directionality during intradermal migration. Red bars: median.



Extended data figure 8. See previous page.



CHAPTER 7

Focusing and Sustaining the anti-Tumor CTL Response by Agonist α CD137 mAb

Weigelin B^{*1}, Bolaños-Mateo E^{*2}, Teijeira A², Martínez-Forero I²,
Labiano S², Azpilicueta A², Morales-Kastresana A², Quetglas JI²,
Wagena E¹, Rodríguez A², Chen L³, Friedl P⁺¹ & Melero I⁺²

Proc Natl Acad Sci 2015; 112(24):7551–7556

(/+ contributed equally)*

¹ Department of Cell Biology, Radboud University Nijmegen Medical Center, 6525 GA Nijmegen, The Netherlands

² Centro de Investigación Médica Aplicada (CIMA) and Clínica Universidad de Navarra, Pamplona, Spain

³ Department of Immunobiology, Yale University School of Medicine, New Haven, USA

Abstract

Cancer immunotherapy is undergoing significant progress due to recent clinical success of refined adoptive T-cell transfer and immunostimulatory monoclonal Ab (mAbs). B16F10-derived OVA-expressing mouse melanomas resist curative immunotherapy with either adoptive transfer of activated anti-OVA OT1 CTLs or agonist anti-CD137 (4-1BB) mAb. However, when acting in synergistic combination, these treatments consistently achieve tumor eradication. Tumor-infiltrating lymphocytes that accomplish tumor rejection exhibit enhanced effector functions in both transferred OT-1 and endogenous cytotoxic T lymphocytes (CTLs). This is consistent with higher levels of expression of eomesodermin in transferred and endogenous CTLs and with intravital live-cell two-photon microscopy evidence for more efficacious CTL-mediated tumor cell killing. Anti-CD137 mAb treatment resulted in prolonged intratumor persistence of the OT1 CTL-effector cells and improved function with focused and confined interaction kinetics of OT-1 CTL with target cells and increased apoptosis induction lasting up to six days post-adoptive transfer. The synergy of adoptive T-cell therapy and agonist anti-CD137 mAb thus results from *in vivo* enhancement and sustainment of effector functions.

Adoptive T-cell therapy is being developed following different approaches including infusion of expanded tumor infiltrating lymphocytes to preconditioned lympho-depleted hosts (1) and adoptive transfer of T cells genetically engineered to express tumor-specific T-cell receptors or chimeric antigen receptors (CARs) (2). The dazzling clinical success of CARs against leukemias (3, 4) is related to the fact that these chimeric receptors intracellularly include both signaling elements of the CD3-TCR (CD3 ζ) and of costimulatory molecules (3). The intracellular costimulatory signaling domain with best reported effects so far is that of CD137 (4-1BB) (5). CD137 (4-1BB) is a TNFR family costimulatory receptor (TNFRSF9) that is expressed on activated T (6) and NK cells (7) and mediates costimulation of both types of lymphocytes (8). On CD8⁺ T cells *ex vivo*, CD137 ligation with the agonist antibodies determines increased proliferation, survival, memory formation and stronger effector functions in terms of both cytotoxicity and cytokine production (9). *In vivo*, anti-CD137 mAb protects adoptively transferred CTLs from activation-induced cell death resulting in better antitumor efficacy in a mouse myeloma model (10). Significant therapeutic effects against transplanted tumor models (11) have provided the rationale for currently ongoing phase I and II clinical trials (NCT01471210; NCT01775631; NCT01307267) (8). NK cells up-regulate CD137 and ligation by anti-CD137 mAb enhances NK-mediated antibody-dependent cellular cytotoxicity functions resulting in synergistic effects with anti-CD20 (12), anti-HER2 (13)

and anti-EGFR (14) mAb. CD137 expression can also be induced on dendritic cells (15), tumor endothelial cells (16), B cells (17), and myeloid leukocytes (18) upon activation. Although positive effects of CD137 ligation for CD8⁺ T-cell memory generation are well explored (9, 19), its relevance for enhancing effector function in solid tumor lesions *in vivo* has not been established. In this study we show a synergy of adoptively transferred and endogenous CD8⁺ T cells against B16F10 melanoma that depends on the ability of both CTL populations to receive costimulation via CD137. Flow-cytometry of tumor-rejecting lymphocyte infiltrates and intravital microscopy of tumors provide evidence that anti-CD137 mAb therapy sustained the efficacy of more focused anti-tumor CTLs.

Results

B16F10-OVA tumors are amenable to eradication by combined adoptive transfer of OT-1 CTLs and CD137 costimulation.

The B16F10-OVA cell line is a stable transfectant derived from B16F10 melanoma that expresses chicken ovalbumin (20). In our hands, it is a difficult-to-treat transplantable tumor model, at least by means of immunotherapy (21). Adoptive transfer of 2×10^6 cognate peptide-activated OT-1 cells to mice s.c. inoculated with 5×10^5 tumor cells and given no antibody or control antibody showed rapid exponential tumor growth (Fig. 1A). Treatment on day 3 with 100 μ g of the agonist anti-CD137 mAb 1D8 (22) showed no therapeutic impact in this model (Fig. 1B). Likewise, infusion of polyclonal activated CD8⁺ T cells showed no efficacy, indicating that OVA-specificity was an absolute requirement (Fig. 1B). In striking contrast, combined treatment with activated OT1 CTL and anti-CD137 mAb accomplished complete regression of all tumors when treatment was instigated 3 days following tumor cell inoculation (Fig. 1C). However, if combination immuno-therapy was delayed until day +7, no therapeutic effects were retained, and mice developed lethal tumors that progressed consistently, albeit with a slight delay (Fig. 1D) compared with controls (Fig. 1A). A single dose of 1D8 anti-CD137 did not alter hepatic function parameters but increased the content of liver CD8⁺ T, NKT and NK cells (Fig. S1). CD4⁺ T-cell depletion experiments with a monoclonal antibody ruled out a role for CD4⁺ T cells in this therapeutic setting, because tumors in mice depleted of CD4⁺ T cells were rejected as in nondepleted controls (Fig. 1E). NK1.1+ NK lymphocytes were also dispensable because complete depletion did not hinder the therapeutic outcome of treatment with 1D8 and 2A, two different anti-CD137 mAb (Fig. S2). Mice cured with the combined therapy of anti-CD137 mAb 1D8 and adoptive OT1 transfer were able to reject an inoculum of B16F10-OVA given at day 90 posttreatment (Fig. S3, Left), showing effective memory state. OVA-negative B16F10 tumors progressed in all mice, irrespective

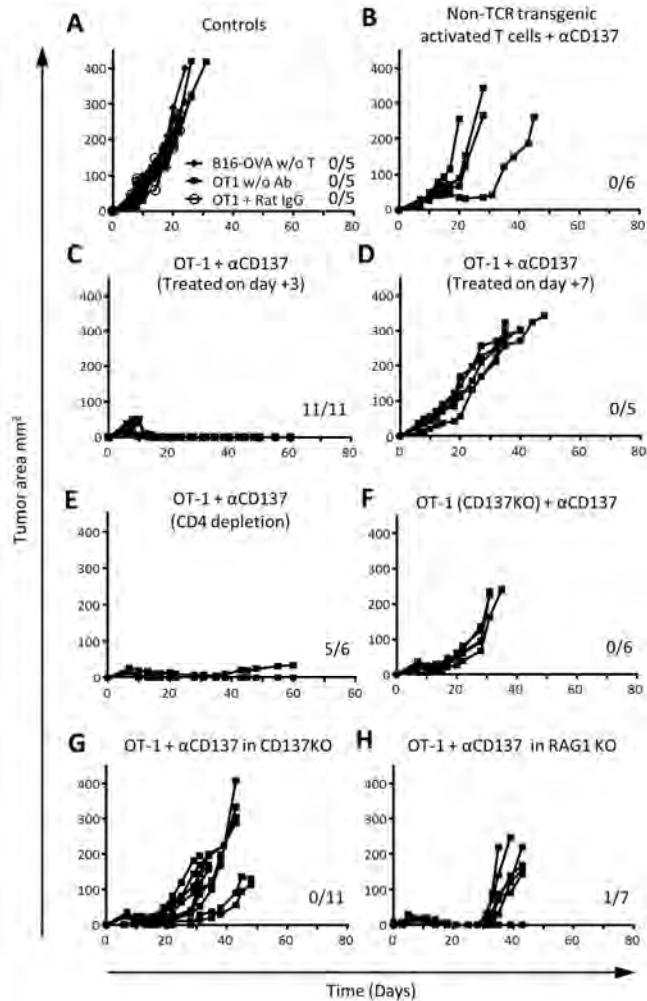


Figure 1. Synergistic combination of adoptive T-cell therapy and anti-CD137 mAb requires CD137 expression on both transferred OT-1 and endogenous CD8⁺ T lymphocytes. Mice were s.c. inoculated with 5×10^5 B16F10-OVA melanoma cells on day 0. Graphs represent individual follow-up of tumor size and the fraction of tumor-free mice at the end of the experiment. **(A)** Mice were left untreated or treated on day +3 with rat IgG or cognate peptide-activated OT-1 lymphocytes. **(B)** Mice were adoptively transferred with 2×10^6 polyclonally activated T cells from non-TCR-transgenic CD45.1 congenic mice and anti-CD137 mAb (1D8) on day +3. **(C)** Mice were adoptively transferred with activated OT-1 CD8⁺ T lymphocytes and 100 μ g of anti-CD137 mAb on day +3. **(D)** Mice were treated as in C but treatment was postponed to day +7 following tumor cell inoculation. **(E)** Mice were treated as in C but starting one day before treatment (day +2) mice received a depleting course of anti-CD4 mAb that was dosed every 5 d for up to four doses. **(F)** Mice were treated as in C, but OT-1 cells were harvested from OT-1 CD137- deficient mice. **(G)** B16F10-OVA-bearing CD137^{-/-} mice were treated as in C with CD137-sufficient OT-1 lymphocytes. **(H)** Tumor-bearing recipient mice were RAG1^{-/-} and were treated as in C. Experiments were repeated at least twice rendering comparable results with at least six animals per group.

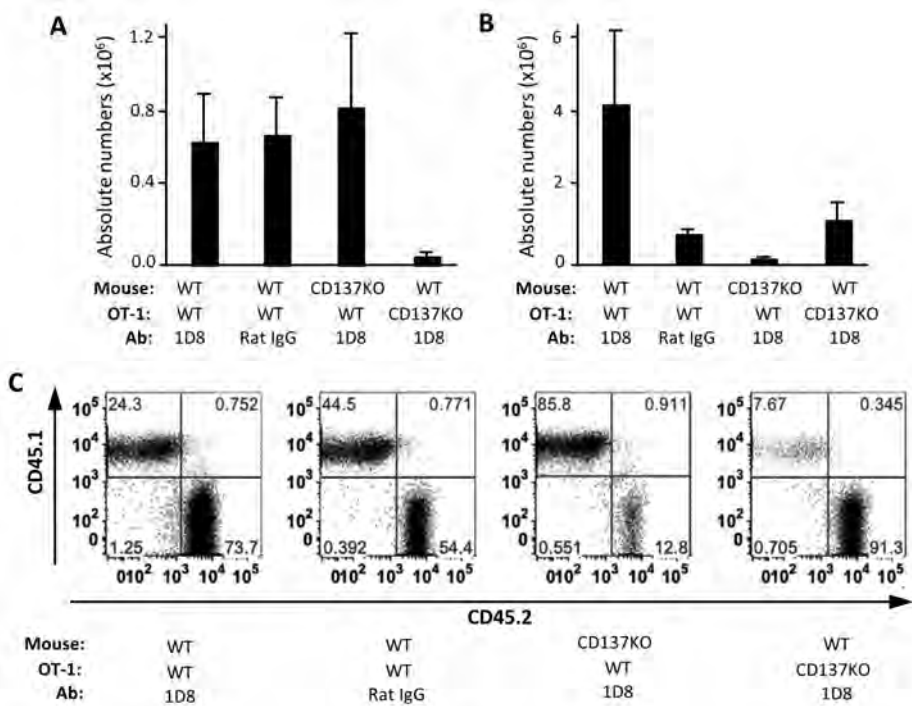


Figure 2. Combination with CD137 mAb does not result in increased numbers of transferred OT-1 lymphocytes in the tumor but enhances recruitment of endogenous T cells in a CD137-dependent manner. Absolute numbers of CD8⁺ T lymphocytes were counted in cell suspensions obtained from tumors (n = 6 per group) excised 7 d following treatment with OT-1 T lymphocytes and anti-CD137 on day 3 after tumor cell inoculation. Transferred CD45.1⁺ (A) and endogenous CD45.2⁺CD8⁺ T (B) cells were differentially counted using perfect count beads as internal standards. Recipient mice and OT-1 lymphocytes were WT or CD137^{-/-} as indicated in the figure. Treatment with antibodies (Ab): 1D8 or control rat antibody (Ab) as indicated. Two similar independent experiments were performed rendering similar results. Statistical differences were assessed by Student's t tests. (C) Representative dot plots are shown to indicate the relative abundance of endogenous (CD45.2) and transferred (CD45.1) CD8⁺ T lymphocyte in the tumor infiltrates. *P ≤ 0.01.

of prior treatments, even though mice that had undergone CD4⁺ T-cell depletion experienced faster tumor progression (Fig. S3, Right).

Combined adoptive T-Cell therapy and anti-CD137 mAb requires CD137 expression on transferred and endogenous T cells.

To study which lymphocyte subsets needed to express CD137 for efficacy, we performed experiments using CD137^{-/-} syngenic mice as tumor recipients and CD8⁺ T cells from double transgenic OT-1 CD137^{-/-} mice. Mice treated with peptide-activated CD137^{-/-} OT-

1 lymphocytes did not show activity upon combined treatment with anti-CD137 mAb, exhibiting only a transient delay in progression (Fig. 1F). Surprisingly, if recipient mice were CD137^{-/-} and treated with CD137-sufficient OT-1 cells, tumors also progressed in every case after a brief period of transient tumor control (Fig. 1G). To address whether endogenous T cells were indispensable, we performed similar experiments in RAG1^{-/-} deficient mice that lack T and B lymphocytes. Results in Fig. 1H indicate that dual-treatment with OT-1 cells and anti-CD137 mAb transiently controlled tumor growth even though all tumor lesions progressed after week three. Collectively, our results indicate that expression CD137 both on adoptively transferred T cells and on endogenous CD8⁺ T cells is mandatory to achieve complete tumor eradication upon combined immunotherapy.

Combined therapy results in tumor infiltrating CTLs with an enhanced effector phenotype.

To understand the mechanisms behind the therapeutic synergistic effects, we studied the CD8⁺ T lymphocytes present in the tumors on day 10 when the lesions start to shrink in size. Our first hypothesis was that a higher number of adoptively transferred T lymphocytes infiltrated the tumor lesion thus numerically explaining the synergistic effects. We performed quantitative experiments using WT or CD137^{-/-} mice as recipients and either CD137-sufficient or CD137^{-/-} OT1 cells. Adoptively transferred OT-1 T cells were CD45.1 in these experiments, which allowed their tracing and discrimination from the endogenous CD45.2 CD8⁺ T cells. Surprisingly, we observed that anti-CD137 mAb treatment did not increase the number of OT-1 T cells within the tumors in both wild-type and CD137^{-/-} recipient mice (Fig. 2 A and B). However, when CD137^{-/-} OT-1 were used, virtually none of these cells were present in the infiltrate (Fig. 2A). Dot plots in Fig. 2C provide a reference at a glance of the relative abundance of transferred (CD45.1⁺) and endogenous (CD45.2⁺) CD8⁺ T lymphocytes in the different experimental groups. When treatment was given on day +7, absolute OT1 CTL numbers in the tumor increased but normalization by tumor weight was consistent with decreased OT-1 CTL density (Fig. S4 A and B). Increased expression of VCAM on tumor endothelial cells induced by 1D8 treatment of B16F10-OVA tumors growing in RAG^{-/-} T-cell-deficient mice indicated an inflammatory phenotype induced by direct effects on endothelial cells (16). However, combined treatment did not alter transcription of CTL-attracting chemokines in WT mice compared with mice treated with OT-1 and control antibody (Fig. S5). Thus, rather than a mere numeric increase, these data implicate altered CTL function as the basis for improved therapeutic outcome. CD107a (Lamp-1) is a cytotoxic granule protein that reaches the plasma membrane when CTLs degranulate

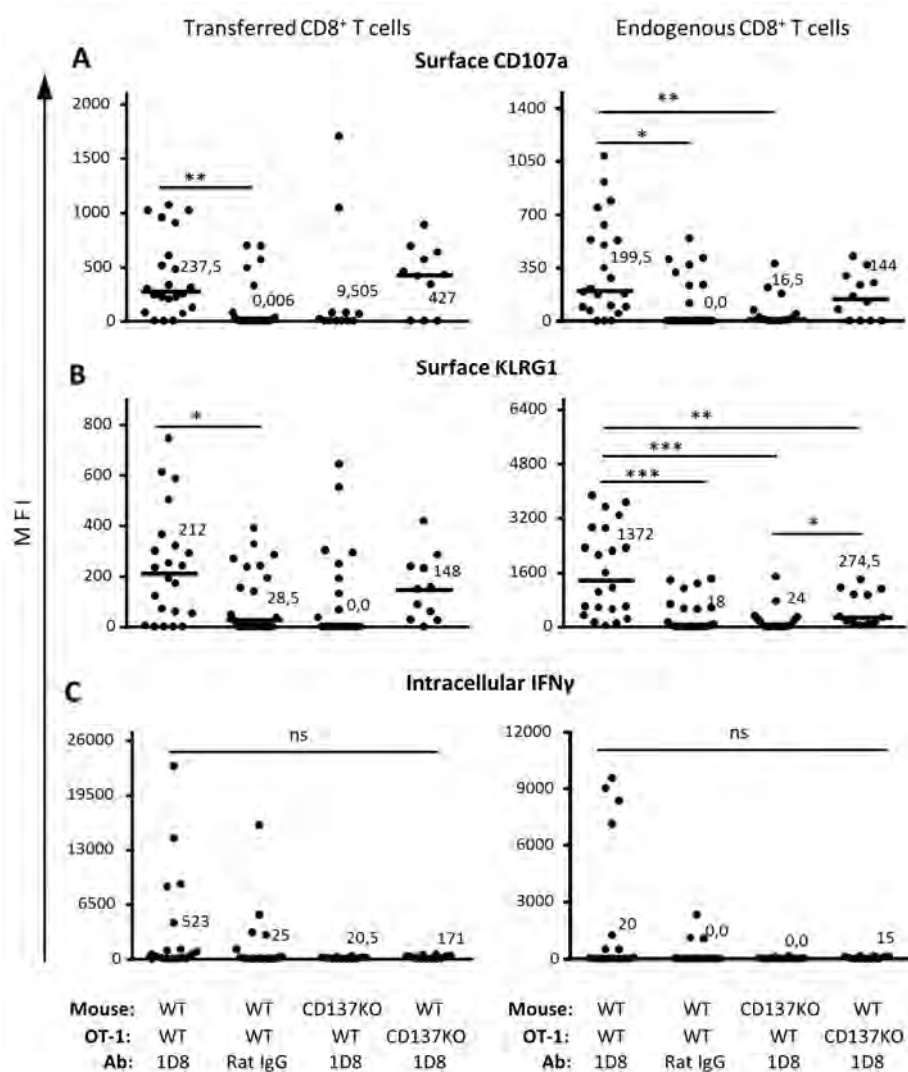


Figure 3. Combined treatment enhances the effector phenotype in both transferred and endogenous CD8⁺ TILs. Results from FACS analyses of cell suspensions retrieved on day 10 from tumors as those in Fig. 2 treated with OT-1 cells and anti-CD137 mAb (1D8). When indicated, recipient mice or transferred OT-1 lymphocytes were CD137^{-/-}. Transferred and endogenous lymphocytes were differentially gated as CD45.1⁺ or CD45.1⁻ CD8⁺ lymphocytes and analyzed for surface CD107a (**A**), KLRG1 (**B**), and intracellular IFN γ (**C**). Results are presented as the mean intensity of fluorescence for the indicated marker from individual mice including three pooled experiments. p represents Student's t test P values. Lines represent the median values. n.s., not significant; *P \leq 0.01; **P \leq 0.001; ***P \leq 0.0001. CD137KO, CD137^{-/-}; WT, wild type.

on target cells. Surface CD107a was increased after treatment with OT-1 and anti-CD137, compared with treatment with OT-1 and control antibody (Fig. 3A) in both transferred OT-1 CTL and, importantly, endogenous CD8⁺ T cells of unknown antigen specificity. Levels of surface CD107a on transferred cells were reduced when the recipient mouse was CD137^{-/-} but undiminished on transferred CD137^{-/-} OT-1 lymphocytes in WT mice. A similar picture emerged when surface KLRG1 was used as effector T-cell marker (Fig. 3B) and when immunostaining for intracellular IFN γ was carried out (Fig. 3C). Similarly, intracellular IFN γ expression in transferred OT1 and endogenous CTL tended to decrease when either transferred OT-1 cells or the recipient mouse were CD137^{-/-}, suggesting cooperation between exogenous and endogenous lymphocyte subsets. When CTLs were restimulated in vitro with SIINKFEL IFN γ levels were increased in OT-1 TILs treated with 1D8 compared with control antibody, whereas endogenous TILs did not respond to the immunodominant OVA epitope (Fig. S6). Tumor draining lymph nodes showed similar but less obvious changes of CTL effector markers (Fig. S7). Moreover, transferred OT-1 CTLs expressed PD-1 and TIM-3 but anti-CD137 treatment did not modify their level of expression, whereas anti-CD137 enhanced the expression on endogenous CD8⁺ CTLs (Fig. S8). Of note, tumors treated by the OT-1 + 1D8 combination tended to contain more CD4⁺ Foxp-3⁺ Treg cells. An interplay of transcription factors is involved in regulating the lymphocyte effector phenotype (23). Previous studies revealed a relation of eomesodermin and CD137 costimulation (24, 25). Eomes is involved in both favoring the expression of effector molecules (26) and favoring differentiation to memory T lymphocytes (27, 28). We stained for intracellular expression of EOMES in tumor infiltrating CD8⁺ T cells. Combined treatment induced higher levels of intracellular EOMES (Fig. 4A). This was much more evident among endogenous TILs than transferred OT-1 CTLs (Fig. 4A). More importantly, the induction of EOMES critically required the ability to express CD137 in the recipient mouse but not in the transferred OT-1 cells. Thus, transcriptional regulation of eomesodermin satisfactorily explains a more robust effector phenotype. Further evidence for a more pronounced effector phenotype was attained by detecting multiple CTL effector markers by quantitative RT-PCR on whole tumor mRNA comparing the effect of OT-1 + 1D8 over OT-1 + control antibody treatments, including increased expression of EOMES, Granzyme B, perforin, FAS-L, BLIMP-1, and CXCR3 (Fig. S5). Conversely, the homologous and functionally interrelated T-bet transcription factor was not induced by anti-CD137 mAb treatment, although the CD137 sufficiency of the receptor mouse favored higher T-bet expression in adoptively transferred and endogenous CD8⁺ T cells (Fig. 4B and Fig. S5). Despite a similar induction of effector markers (including TIM-3 and PD-1), tumors surpassed immune control when treatment start was delayed until day +7 after tumor inoculation (Fig. S4B).

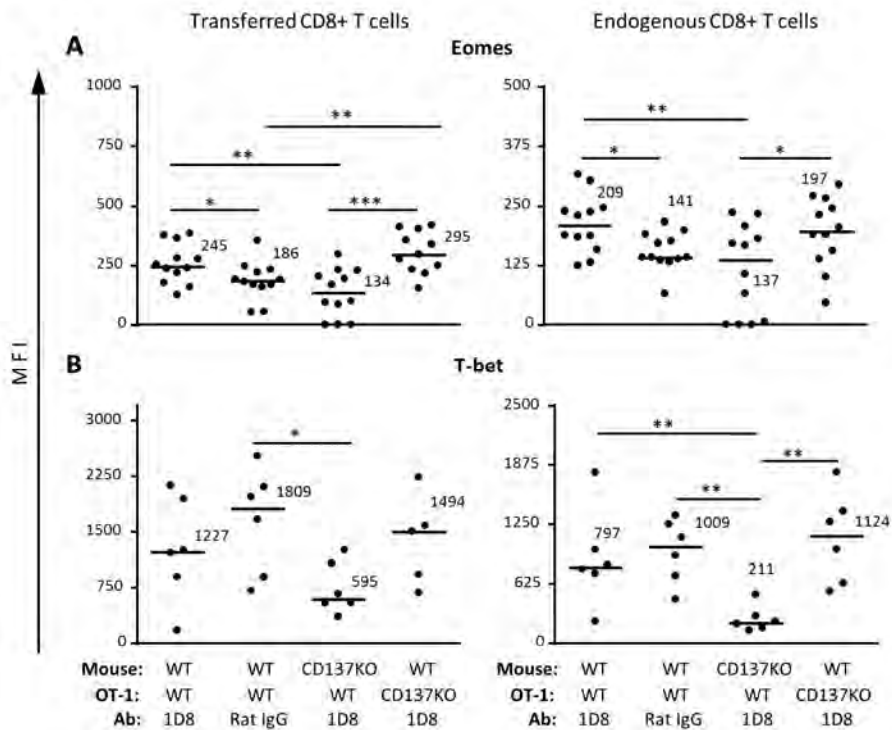


Figure 4. EOMES is induced in transferred and endogenous intratumor CTLs by anti-CD137 mAb treatment. FACS analyses experiments as in Fig. 3 with intracellular staining for the transcription factors EOMES (A) and T-bet (B) in CD8⁺ TILs from the indicated experimental groups. In each graph, the adoptively transferred cells, the recipient mouse, and the antibody treatment are provided in the horizontal axis [WT: wild type; CD137KO: CD137^{-/-}]. Results in A are from two pooled experiments performed identically. Statistical differences were assessed with Mann-Whitney u test. n.s., not significant, *P ≤ 0.01.

Evidence for more effective CTL activity in the microenvironment of B16F10-OVA tumors upon combined immunotherapy.

To address whether anti-CD137 mAb therapy enhances local antitumor CTL efficacy, frozen tumor sections were stained for CD8 and cleaved Caspase-3 to identify apoptotic cells. Tumors undergoing combined treatment revealed an increase of apoptotic tumor cells (Fig. S9) together with an increased total number and relative ratio of CTLs in direct contact with caspase-3–positive, dead, or dying tumor cells (Fig. S9 A–C). Thus, combined treatment increases tumoricidal events between CTL and tumor cells. Both CTL-tumor cell conjugates and cytotoxic efficacy observed upon combined treatment were partially reduced when recipient mice were CD137^{-/-} deficient (Fig. S9 C and D). Analysis of OT-1 CD137^{-/-} lymphocytes did not permit relevant observations due to the paucity of such T cells in the tumors.

Anti-CD137 mAb therapy prolongs in vivo efficacy of CTL effector function.

To dissect how anti-CD137 therapy improves CTL effector function and tumor growth control or regression, the intratumor migration, interactions, and viability of adoptively transferred dsRed2, OT1 CTL were directly monitored by intravital multiphoton microscopy in B16F10-OVA tumors expressing histone-2B/mCherry as readout for mitosis, apoptosis, or necrosis (Fig. S10A). In control mice, adoptively transferred OT1 CTL induced a transient growth delay with exponential regrowth of the tumor thereafter, whereas combined therapy of OT1 transfer + anti-CD137 mAb resulted in a significantly increased suppression of tumor growth (Fig. S10 A and B). To directly address whether individual CTL show enhanced effector function, we quantified CTL effector dynamics by long-term 4D time-lapse microscopy. Migrating OT1 CTL efficiently infiltrated the tumor margin with decreasing CTL densities towards the tumor core and with reduced migration speed of $2 \pm 1.7 \mu\text{m}/\text{min}$ in OVA expressing tumors compared with B16F10 parental tumors ($4 \pm 2.8 \mu\text{m}/\text{min}$) and increased confinement of migration (Fig. 5 A and B). This interaction pattern explains cognate antigen recognition and active effector function (29).

When combined with anti-CD137 mAb, tumor infiltrating CTL showed an even more focused effector phenotype, defined by further reduced migration speed ($1.5 \pm 1.2 \mu\text{m}/\text{min}$) during interactions with tumor cells resulting in prolonged dwell time per focus (Fig. 5 A–D and Movie S1). Quantification of OT1 CTL– tumor cell interactions and outcome showed that 75 % of tumor cell apoptosis were directly preceded by an OT1 contact, indicating cell-contact dependent cytotoxicity as major mechanism of apoptosis induction (Fig. 6A and Movies S2 and S3). Combined treatment of OT1 transfer and anti-CD137 mAb resulted in mildly enhanced frequency but substantially prolonged effector

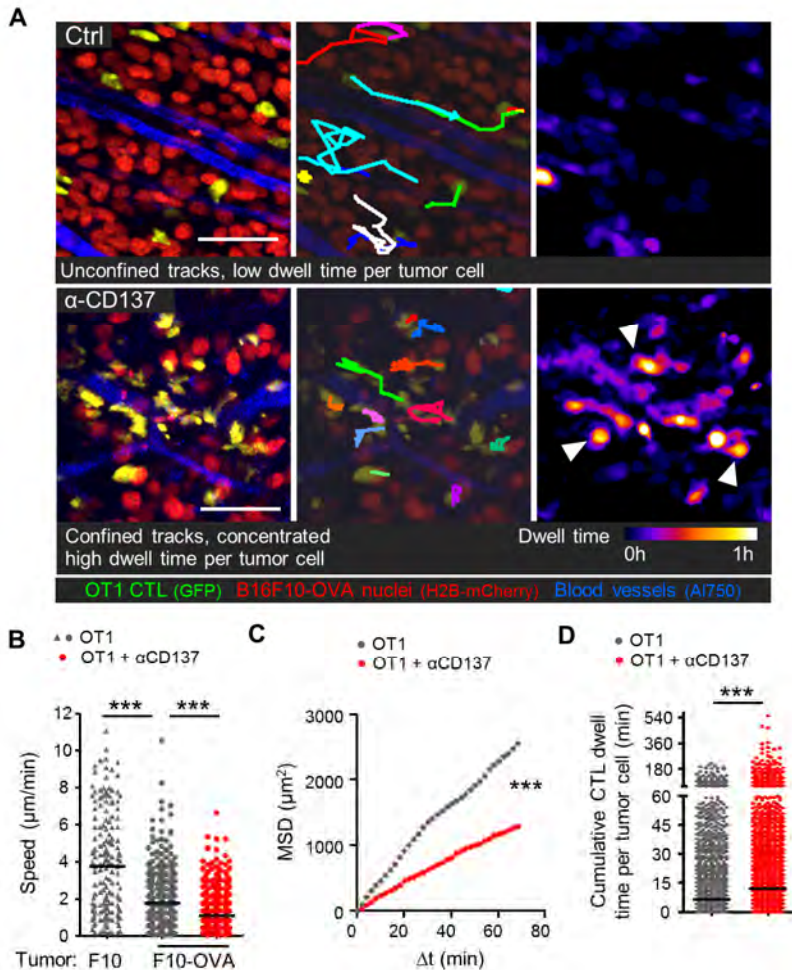


Figure 5. Intravital microscopy shows focused effector dynamics of adoptively transferred OT1 CTL. (A) OT1 CTL migration dynamics and pattern. Heat map of CTL dwell time shows confined CTL migration tracks (arrow heads) in CD137 cotreated tumors. **(B)** OT1 CTL migration speed in parental, OVA expressing and anti-CD137 mAb treated tumors. **(C)** The mean square displacement relates to the area covered by the migrating cells at increasing time intervals. For each time interval Δt , the mean squared displacement is plotted for tracks of OT1 CTL with and without anti-CD137 treatment. Significance test, two-way ANOVA. **(D)** Cumulative OT1 CTL–tumor cell interactions. Quantifications are based on at least three independent experiments with at least 180 CTL tracks of 75 min length analyzed per condition. Black lines indicate the median. Statistical differences were assessed using the Mann–Whitney u test; *** $P \leq 0.0001$. (Scale bars, 50 μ m.)

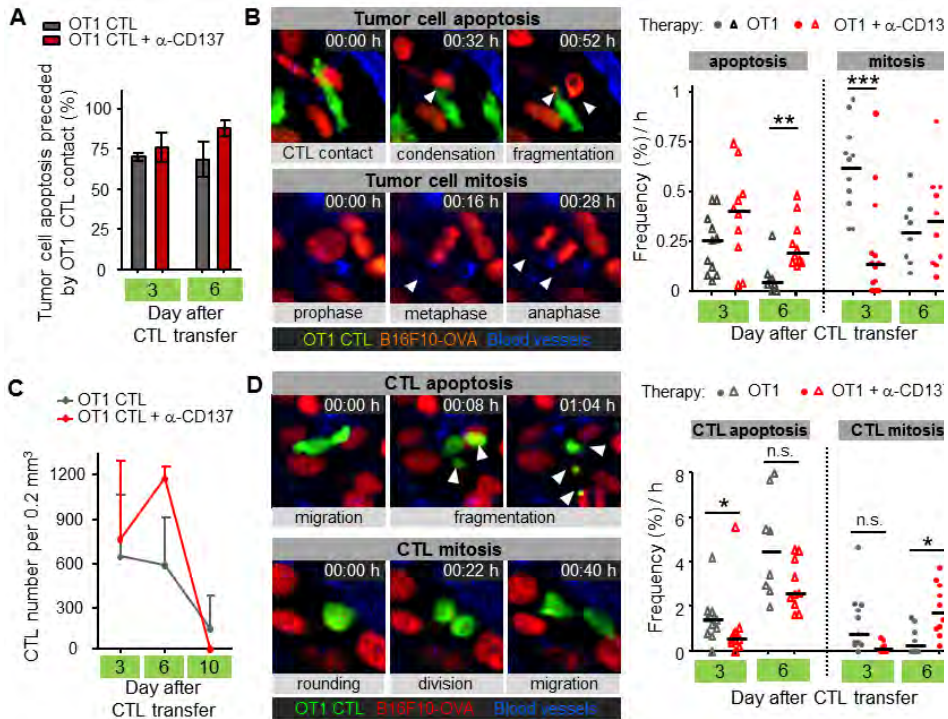


Figure 6. Intravital microscopy shows improved CTL viability and sustained effector function of adoptively transferred OT-1 T cells. (A) Percentage of tumor cell apoptosis events preceded by OT1 CTL contacts. Error bars, SD. **(B)** Image sequence of B16F10/OVA apoptosis and mitosis visualized by H2B-mCherry. Arrowheads point to nuclear fragmentation and mitotic nuclei, respectively. Dot plots: Quantification of tumor cell apoptosis and mitosis rates per hour. **(C)** OT1 CTL numbers in the tumor. Error bars, SD. **(D)** Image sequence of CTL mitosis and apoptosis in the tumor. Arrowheads indicate apoptotic fragmentation. Dot plots: Quantification of OT1 CTL apoptosis and mitosis rates per hour. Data were obtained from time lapse recordings of 350 × 350 × 100 μ m stacks scanned at 2-min frame rate and recorded at ≥ 3 independent positions per tumor. $n = 3$ independent tumors with total observation times of ≥ 20 h per condition and time point. Statistical differences were assessed using the Mann–Whitney u test; n.s., not significant, * $P \leq 0.01$, ** $P \leq 0.001$, *** $P \leq 0.0001$.

window of apoptosis induction by OT1 CTL (Fig. 6B). Concurrently, tumor cell proliferation was impaired (Fig. 6B), but OT1 CTL proliferation increased and apoptosis rates decreased, consistent with transiently increased CTL densities in the tumor under combined anti-CD137 mAb treatment (Fig. 6D). Thus, combining adoptive CD8⁺ T-cell therapy with anti-CD137 mAb induces a local effector phenotype with prolonged and more focused cytotoxic activity against tumor cells.

Discussion

In this study we observed effective synergism of CTL infusion combined with anti-CD137 mAb treatment, resulting in complete regression of s.c. and efficient growth control of intradermal B16F10-OVA melanoma tumors in a CD4 and NK cell independent fashion. However, when treatment is postponed to day +7, the therapy loses efficacy probably as a result of immunosuppressive mechanisms deployed by the larger tumor (30) and because the rapidly increasing tumor cell burden overwhelms the immunotherapeutic regimen despite transient increases in CTL tumor infiltration. The synergistic effects between adoptive CTL transfer and antibody-induced enhanced CD137 signaling could operate and be exploited at multiple levels: (i) CD137 ligation is known to promote proliferation (6) and prevent activation induced cell death (31) in T cells. (ii) CD137 is expressed on the endothelial cells of tumor vessels which, when stimulated in this location, enhances T-cell trafficking into tumors (16). In our case this mechanism appears dispensable for recruiting adoptively transferred T cells into tumors, but we observe higher numbers of endogenous CD8⁺ T cells, that are lost if the recipient mouse is CD137^{-/-}, indicating an effect of anti-CD137 therapy on endothelial cells and/or on the tumor homing capability of endogenous CD8⁺ T lymphocytes. Of note, endogenous CD8⁺ T cells outnumbered by about 8- to 10-fold those adoptively transferred and their function is crucial to sustain the complete response over time, as found in experiments with recipient RAG1^{-/-} mice deficient in T cells. Rather than increasing the peak activity in the lesion, here we show that exposure to the CD137 agonist results in prolonged CTL-mediated cytotoxicity as the basis for higher efficacy at killing tumor cells. These phenotypic changes were dependent on the ability of CD137 to be expressed both on endogenous cells of the recipient mouse and on adoptively transferred OT1 cells. This finding is consistent with the *in vivo* treatment efficacy that required the expression of CD137 on both endogenous and adoptively transferred cells. Our results are compatible with those on targeting hematologic malignancy using bone marrow chimeras (32) which showed that endogenous T cells were required for the efficacy of transferred memory-like CD8⁺ T cells and anti-CD137 mAb combined treatment against experimental immunogenic EG7 lymphomas. In this case of high CTL efficacy, the ability to express CD137 on endogenous or adoptively transferred cells was mutually dispensable, being required only in one of the subsets. The apparent discrepancy with our results indicates the different degree of immunogenicity of EG7-OVA lymphomas compared with the B16F10-OVA melanomas and, possibly, different efficacy of reactivated memory-like OT-1 lymphocytes (32) versus the recently activated OT-1 used here. Our observations using the very aggressive B16F10-OVA melanoma which shows poor immunogenicity toward endogenous effector cells strongly advocate for translational research of this

immunotherapy combination. Indeed, we have recently reported synergy against spontaneous liver cancer expressing transgenic OVA of a combination of anti-OVA OT-1 + OT-2 T cells in conjunction with a combination of immunostimulatory mAb (33). Our work is also consistent with previous reports on the critical role of EOMES as a transcription factor in the effects of CD137 costimulation (24, 25). EOMES up-regulates transcription of molecules that CTLs use for killing (26), and likely supports the overall enhanced performance of transferred and endogenous CTLs. However, the transcriptional and epigenetic control networks that would mediate the effects of CD137 costimulation are likely more complex (34) involving an interplay of transcription factors regulating CTL differentiation. Live-cell imaging of tumors undergoing rejection clearly showed that CTLs were associated with more tumor cell death that was correlated with more frequent and prolonged interaction of CTLs with target cells. The perforin-granzyme machinery represents the predominant tumor-killer effector mechanism upon anti-CD137 mAb treatment (35), which is consistent with more focused behavior of the OT-1 lymphocytes inside the tumor and strongly suggests enhanced stringency of CTL engagement with target cells, degranulation, and apoptosis induction. Previous intravital imaging studies indicated that long-lasting CTL-tumor cell interactions support tumor cell killing (36) and tumor immunotherapy models show that CTLs initiate relevant tumor regression few days after adoptive transfer. Besides initial activation, CTL are required to maintain a sustained effector phenotype within the tumor microenvironment (37) for prolonged time periods to efficiently eradicate tumors. Our data indicate that CD137 mAb therapy, besides directly stimulating cytotoxic function, prolongs the CTL effector phase and viability in the local tumor microenvironment, which sustains local cytotoxicity. The combination of adoptive T-cell therapy and anti-CD137 mAb is likely to involve various application possibilities. First, CD137 expression can be used for immunomagnetic selection of tumor reactive TILs (38), and subsequent culture of T cells in the presence of CD137 renders more efficacious phenotypic features (39, 40). Second, the effector performance (11), survival (10), and memory differentiation (41) can be enhanced by coadministration of the agonist antibody *in vivo*. Lastly, as shown here, anti-CD137 infusion may enhance adoptive immunotherapy by CTL by a dual mechanism, enhancing endogenous effector functions as well as focusing and prolonging the efficacy of therapeutically transferred lymphocytes.

Materials and Methods

See SI Materials and Methods. In brief, experimental designs were based on adoptive transfer of OT-1 TCR transgenic T cells. As needed, OT-1 donor mice were crossed to become CD137^{-/-} or double transgenic for green or red fluorescent proteins. Adoptively T-cell transferred mice were dosed anti-CD137 agonist antibodies (1D8 or 2A) or control antibodies to subsequently follow up tumor size, retrieve intratumoral lymphocytes for flow cytometry evaluation or to perform imaging experiments by intravital microscopy of tumors implanted in dorsal skin-fold chambers, using a customized multiphoton microscope (TriMScope-II, LaVision BioTec).

Acknowledgements

This work was supported by MICINN (SAF2008-03294, SAF2011-22831; to I.M.). I.M. was also funded by the Departamento de Educación del Gobierno de Navarra and Departamento de Salud del Gobierno de Navarra, Redes temáticas de investigación cooperativa RETIC (RD06/0020/0065), European commission 7th framework program (ENCITE and IACT), and “UTE for project FIMA.” P.F. was funded by the Dutch Cancer Foundation (KWF 2008-4031), the Cancer Genomics Center Netherlands and FP7 of the European Union (ENCITE HEALTH TH-15-2008-208142). This work was initiated as Proof-of-Concept project supported by EuroBioImaging. A.M.-K. and S.L. are recipients of predoctoral scholarships from Ministerio de Economía.

Author contributions

B.W., P.F., and I.M. designed research; B.W., E.B., A.T., I.M.-F., S.L., A.A., A.M.-K., J.I.Q., E.W., and A.R.S.-P. performed research; J.I.Q. and L.C. contributed new reagents/analytic tools; B.W., E.B., A.T., S.L., A.M.-K., E.W., A.R.S.-P., P.F., and I.M. analyzed data; and B.W., E.B., P.F., and I.M. wrote the paper.

Conflict of interest statement: I.M. is a consultant for: Bristol Myers Squibb, AstraZeneca, Roche Genentech, Boehringer Ingelheim, and Leadartis. Research grants were provided to I.M. from Pfizer and Bristol Myers Squibb.

This article contains supporting information online at www.pnas.org/lookup/suppl/doi:10.1073/pnas.1506357112/-/DCSupplemental.

References

1. Restifo NP, Dudley ME, Rosenberg SA (2012) Adoptive immunotherapy for cancer: Harnessing the T cell response. *Nat Rev Immunol* 12(4):269–281.
2. Darcy PK, Neeson P, Yong CS, Kershaw MH (2014) Manipulating immune cells for adoptive immunotherapy of cancer. *Curr Opin Immunol* 27:46–52.
3. Kalos M, et al. (2011) T cells with chimeric antigen receptors have potent antitumor effects and can establish memory in patients with advanced leukemia. *Sci Transl Med* 3(95):95ra73.
4. Porter DL, Levine BL, Kalos M, Bagg A, June CH (2011) Chimeric antigen receptor-modified T cells in chronic lymphoid leukemia. *N Engl J Med* 365(8):725–733.
5. Milone MC, et al. (2009) Chimeric receptors containing CD137 signal transduction domains mediate enhanced survival of T cells and increased antileukemic efficacy in vivo. *Mol Ther* 17(8):1453–1464.
6. Pollok KE, et al. (1993) Inducible T cell antigen 4-1BB. Analysis of expression and function. *J Immunol* 150(3):771–781.
7. Melero I, Johnston JV, Shufford WW, Mittler RS, Chen L (1998) NK1.1 cells express 4-1BB (CDw137) costimulatory molecule and are required for tumor immunity elicited by anti-4-1BB monoclonal antibodies. *Cell Immunol* 190(2):167–172.
8. Melero I, Hirschhorn-Cymerman D, Morales-Kastresana A, Sanmamed MF, Wolchok JD (2013) Agonist antibodies to TNFR molecules that costimulate T and NK cells. *Clin Cancer Res* 19(5):1044–1053.
9. Wortzman ME, Clouthier DL, McPherson AJ, Lin GH, Watts TH (2013) The contextual role of TNFR family members in CD8(+) T-cell control of viral infections. *Immunol Rev* 255(1):125–148.
10. May KF, Jr, Chen L, Zheng P, Liu Y (2002) Anti-4-1BB monoclonal antibody enhances rejection of large tumor burden by promoting survival but not clonal expansion of tumor-specific CD8+ T cells. *Cancer Res* 62(12):3459–3465.
11. Melero I, et al. (1997) Monoclonal antibodies against the 4-1BB T-cell activation molecule eradicate established tumors. *Nat Med* 3(6):682–685.
12. Kohrt HE, et al. (2011) CD137 stimulation enhances the antilymphoma activity of anti-CD20 antibodies. *Blood* 117(8):2423–2432.
13. Kohrt HE, et al. (2012) Stimulation of natural killer cells with a CD137-specific antibody enhances trastuzumab efficacy in xenotransplant models of breast cancer. *J Clin Invest* 122(3):1066–1075.
14. Kohrt HE, et al. (2014) Targeting CD137 enhances the efficacy of cetuximab. *J Clin Invest* 124(6):2668–2682.
15. Wilcox RA, et al. (2002) Cutting edge: Expression of functional CD137 receptor by dendritic cells. *J Immunol* 168(9):4262–4267.
16. Palazón A, et al. (2011) Agonist anti-CD137 mAb act on tumor endothelial cells to enhance recruitment of activated T lymphocytes. *Cancer Res* 71(3):801–811.
17. Zhang X, et al. (2010) CD137 promotes proliferation and survival of human B cells. *J Immunol* 184(2):787–795.
18. Lee SW, et al. (2008) Identification of regulatory functions for 4-1BB and 4-1BBL in myelopoiesis and the development of dendritic cells. *Nat Immunol* 9(8):917–926.

19. Lin GH, et al. (2012) Contribution of 4-1BBL on radioresistant cells in providing survival signals through 4-1BB expressed on CD8⁺ memory T cells in the bone marrow. *Eur J Immunol* 42(11):2861–2874.
20. Bellone M, et al. (2000) Relevance of the tumor antigen in the validation of three vaccination strategies for melanoma. *J Immunol* 165(5):2651–2656.
21. Quetglas JI, et al. (2012) Immunotherapeutic synergy between anti-CD137 mAb and intratumoral administration of a cytopathic Semliki Forest virus encoding IL-12. *Mol Ther* 20(9):1664–1675.
22. Shuford WW, et al. (1997) 4-1BB costimulatory signals preferentially induce CD8⁺ T cell proliferation and lead to the amplification in vivo of cytotoxic T cell responses. *J Exp Med* 186(1):47–55.
23. Kaech SM, Cui W (2012) Transcriptional control of effector and memory CD8⁺ T cell differentiation. *Nat Rev Immunol* 12(11):749–761.
24. Qui HZ, et al. (2011) CD134 plus CD137 dual costimulation induces Eomesodermin in CD4 T cells to program cytotoxic Th1 differentiation. *J Immunol* 187(7):3555–3564.
25. Curran MA, et al. (2013) Systemic 4-1BB activation induces a novel T cell phenotype driven by high expression of Eomesodermin. *J Exp Med* 210(4):743–755.
26. Pearce EL, et al. (2003) Control of effector CD8⁺ T cell function by the transcription factor Eomesodermin. *Science* 302(5647):1041–1043.
27. McLane LM, et al. (2013) Differential localization of T-bet and Eomes in CD8 T cell memory populations. *J Immunol* 190(7):3207–3215.
28. Li G, et al. (2013) T-Bet and Eomes Regulate the Balance between the Effector/Central Memory T Cells versus Memory Stem Like T Cells. *PLoS ONE* 8(6):e67401.
29. Boissonnas A, Fetler L, Zeelenberg IS, Hugues S, Amigorena S (2007) In vivo imaging of cytotoxic T cell infiltration and elimination of a solid tumor. *J Exp Med* 204(2): 345–356.
30. Rabinovich GA, Gabilovich D, Sotomayor EM (2007) Immunosuppressive strategies that are mediated by tumor cells. *Annu Rev Immunol* 25:267–296.
31. Hurtado JC, Kim YJ, Kwon BS (1997) Signals through 4-1BB are costimulatory to previously activated splenic T cells and inhibit activation-induced cell death. *J Immunol* 158(6):2600–2609.
32. Lin GH, et al. (2010) Evaluating the cellular targets of anti-4-1BB agonist antibody during immunotherapy of a pre-established tumor in mice. *PLoS ONE* 5(6):e11003.
33. Morales-Kastresana A, et al. (2013) Combined immunostimulatory monoclonal antibodies extend survival in an aggressive transgenic hepatocellular carcinoma mouse model. *Clin Cancer Res* 19(22):6151–6162.
34. Melero I, Murillo O, Dubrot J, Hervás-Stubbs S, Perez-Gracia JL (2008) Multi-layered action mechanisms of CD137 (4-1BB)-targeted immunotherapies. *Trends Pharmacol Sci* 29(8):383–390.
35. Morales-Kastresana A, et al. (2013) Essential complicity of perforin-granzyme and FAS-L mechanisms to achieve tumor rejection following treatment with anti-CD137 mAb. *J Immunother Cancer* 1:3.
36. Breart B, Lemaître F, Celli S, Bousso P (2008) Two-photon imaging of intratumoral CD8⁺ T cell cytotoxic activity during adoptive T cell therapy in mice. *J Clin Invest* 118(4):1390–1397.
37. Palazón A, et al. (2012) The HIF-1 α hypoxia response in tumor-infiltrating T lymphocytes induces functional CD137 (4-1BB) for immunotherapy. *Cancer Discov* 2(7): 608–623.

38. Wolf M, et al. (2007) Activation-induced expression of CD137 permits detection, isolation, and expansion of the full repertoire of CD8+ T cells responding to antigen without requiring knowledge of epitope specificities. *Blood* 110(1):201–210.
39. Hernandez-Chacon JA, et al. (2011) Costimulation through the CD137/4-1BB pathway protects human melanoma tumor-infiltrating lymphocytes from activation-induced cell death and enhances antitumor effector function. *J Immunother* 34(3):236–250.
40. Chacon JA, et al. (2013) Co-stimulation through 4-1BB/CD137 improves the expansion and function of CD8(+) melanoma tumor-infiltrating lymphocytes for adoptive T-cell therapy. *PLoS ONE* 8(4):e60031.
41. Hendriks J, et al. (2005) During viral infection of the respiratory tract, CD27, 4-1BB, and OX40 collectively determine formation of CD8+ memory T cells and their capacity for secondary expansion. *J Immunol* 175(3):1665–1676.

Supporting Information

SI Materials and Methods

Mice.

C57BL/6 J WT mice (5–6 wk old) were purchased from Harlan Laboratories. CD137^{-/-} [B6.Cg-Tnfrsf9tm1Byk] (1), OT-I/ CD45.1 [C57BL/6-Tg(TcraTcrb)1100Mjb/J (OT-1) crossing with B6.SJL-PtprcaPep3b/BoyJ (CD45.1)], CD137^{-/-}/OT-1/CD45.1 [C.129 × 1(B6)-Ptprc <tmlWeis > Tg(TcraTcrb) 1100 Mjb/J crossing with B6.Cg-Tnfrsf9tm1Byk] TCR transgenic mice harboring OVA-specific CD8⁺ T cells and Rag1^{-/-}[B6.129S7-Rag1tm1Mom/J], were bred in our animal facility under specific pathogen-free conditions (breeding protocol numbers 064/10, 026/09, 118/12, and 068/10). All animal procedures were conducted under institutional guidelines that comply with national laws and policies (study number 066/10).

Transgenic mice expressing dsRed under the chicken beta actin promoter (Jackson Laboratories, stock number: 006051) were crossed to OT-I TCR transgenic mice (Jackson Laboratories, stock number: 003831). Double transgenic dsRed/OT-1 were bred in the central animal facility (CDL) of the Radboud University Nijmegen, The Netherlands.

B16F10 OVA Tumors and Treatment.

5×10^5 B16F10-OVA (2) cells (mycoplasma free, tested by MycoAlert Mycoplasma Detection Kit from Lonza) were injected s.c. into the right flank of C57BL/6 syngenic mice (3). B16F10-OVA melanoma-derived cells are B16F10 cells transfected to express chicken ovalbumin (OVA) (2). On day 3 or 7 after tumor inoculation, mice were treated i.v. with 2×10^6 OT-1 lymphocytes, obtained from OT1-TCR transgenic mice spleens and activated for 48 h with 0.1 µg/mL of SIINFEKL cognate peptide, and 100 µg of anti-CD137 (4) (clone 1D8) or Rat IgG (Sigma-Aldrich) given intraperitoneally. At the indicating time point, tumors were excised and digested in collagenase (400 mandl)/DNase I (50 µg/mL) at 37 °C. After 15 min of incubation, collagenase/DNase were inactivated with 12 µL of EDTA per mL. Then tumors were mechanically disaggregated and passed by a 0.7-µm cell strainer. Cell suspensions were then immunostained and/or mixed with perfect-count beads (Cytognox) for cell counting according to manufacturer's instructions. For CD4⁺ T-cell depletion, tumor-bearing mice were injected with depleting anti-CD4 mAb (clone GK1.5) before anti-CD137 treatment. A total of 200 µg per dose of the depleting mAb were administered intraperitoneally every 5th day beginning 1 d before treatment onset. For NK depletion, NK1.1-specific mAb (200 µg per dose) was administered i.v. for 5 consecutive days, beginning 3 d before anti-CD137 treatment, and thereafter administration continued in 3-d intervals.

Flow Cytometry.

A single cell suspension was obtained from excised tumors and lymph nodes to be stained with the following fluorochrome-conjugated antibodies: anti-CD8-APC (clone 53- 6.7 from Pharmingen), anti-CD8-BV510 (clone 53-6.7 from Pharmingen), anti-CD8 β -APC (clone YTS156.7.7 from Biolegend), anti-CD4-BV421 (clone RM4-5 from Pharmingen), anti-CD4-PE (clone GK1.5 from e-Bioscience), anti-CD45.1-PrCPC5 (clone A20 from Pharmingen), anti-CD3-FITC (clone 145-2C11 from Pharmingen), anti-NK1.1-PrCPC5 (clone PK-136 from Pharmingen), anti-CD107a-FITC (clone 1D4B), anti-IFN γ -FITC (clone XMG1.2 from Biolegend), anti-EOMES-PE (clone 21Mags8 from eBioscience), anti-KLRG1-FITC (clone 2F1 from Santa Cruz), anti- T-bet-BV421(clone eBio4B10 from eBioscience), anti-PD1-FITC (clone 29F.1A12 from Biolegend), anti-Tim3-PE (clone RMT3-28 from life Technologies), Zombie NIR (from Biolegend). Perfect-count microspheres were purchased from Cytognos. For intracellular staining of IFN γ cells, suspensions were stimulated in 5 h cultures in the presence of GolgiPlug (Becton-Dickinson). Cells were acquired using a BD Biosciences FACSCanto II flow cytometer. Data were analyzed using FlowJo software (Tree Star). For intracellular stainings cells were permeabilized with Cytofix/cytoperm according to manufacturer instructions (BD-Biosciences).

Quantitative RT-PCR.

B16F10-OVA bearing mice treated on day 3 with 2×10^6 OT1 and 1D8 or control antibody were killed on day 10 and their tumors excised and disaggregated. RNA from cell suspensions was extracted by trizol-phenol-chlorophorm and was subjected retrotranscription (Invitrogen).

Quantitative PCR was made using CFX96 Real-Time PCR Detection System. Specific primer pairs for each gene were:

T-bet (5'AGCAAGG-ACGGCGAATGTT3'; 5'GGGTGGACATATAAGCGGTTCC3'),
Eomes (5'GGCCCTATGGCTCAAATTC3'; 5'GAACCAC-TTCCACGAAAACATTG3'),
Granzyme B (5'CCACTCTCGA-CCCTACATGG3'; 5'GGCCCCAAAGTGACATTTATT3'),
Perforin (5' TGCAGCTGAGAAGACCTATCA3'; 5'AGTC-AAGGTGGAGTGGAGGT3'),
FasL (5'TCCGTGAGTTCACC-AACCAA3'; 5'GGGGGTTCCCTGTAAATGGG3'),
BIM1 (5'CCCGGAGATACGGATTGCAC3'; 5'GCCTCGCGGTAA-TCATTTGC3'),
Bcl-xL (5'GACAAGGAGATGCAGGTATT-GG3'; 5'TCCCGTAGAGATCCACAAAAGT3'),
FOXO3 (5'CT-GGGGGAACCTGTCTATG3'; 5'TCATTCTGAACGCGCAT-GAAG3'),
Blimp1 (5'TTCTCTTGAAAAACGTGTGGG3'; 5'GGAGCCGGAGCTAGACTTG3'),
CXCR3 (5'TACCTTGAGG-TTAGTGAACGTCA3'; 5'CGCTCTGTTTTCCCATATC3'),
CXCL9 (5'GGAGTTCGAGGAACCCTAGTG3'; 5'GCACGA-TCCACTACAAATCCC3'),
CXCL10 (5'CCAAGTGCTGCCG-TCATTTTC3'; 5'GGCTCGCAGGGATGATTCAA3'),

RPLO (5'AACATCTCCCCCTTCTCT3'; 5'GAAGGCTTGACCTTT-TCAG3').

Results were normalized to RPLO and fold change of each gene was calculated by $2(\Delta\Delta Ct_{1D8} - \Delta\Delta Ct_{RatIgG})$.

Confocal Microscopy.

B16 tumor-bearing mice were killed at day 10 post tumor engraftment and tumors were excised, embedded in OCT, and frozen. Cryosections (10–12 μm) were treated for 20 min with 0.01 % Triton X-100 in 3 % BSA/PBS and treated with anti-CD8 (clone 53-6.7, Pharmingen) and anti-cleaved Caspase-3 (clone C92-605, Pharmingen) at 4 °C in BSA 3 %/PBS overnight. Cryosections were then incubated with anti-rat AlexaFluor488 antibody (Life technologies,). Ten micrometer confocal z-stack acquisitions were taken on a LSM-510 confocal microscope (Zeiss, Jena, Germany) with a 40 \times objective (N.A., 1.3). 10 CD8+ T-cell containing fields were imaged per condition. Data were obtained from three experiments. Maximum z-stack projections, linear contrast, and 3D reconstruction of images were performed with Imaris software (Bitplane). The number of cells positive for both markers and the contact between them was quantified manually.

Intravital Multiphoton Microscopy.

Dorsal skin-fold chambers were transplanted onto 8- to 14-wk-old male C57/Bl6 J mice (Charles River), as described (5). After one epidermal side of the skin flap was surgically removed, the chamber was mounted and a cover glass was added to shield the imaging field. One day post surgery, one or two small tumors per chamber were implanted into the deep dermis near the deep dermal vascular plexus by injecting a cell pellet of histone-2B/mCherry expressing B16F10/OVA (6) cells (5×10^4 to 2×10^5 cells) with a 30 G needle. Tumor growth was monitored for up to 15 d by epifluorescence and multiphoton microscopy. For intravital microscopy, mice were anesthetized with isoflurane (1–3 % in oxygen) and the skin-fold chamber was stably mounted on a temperature-controlled stage (37 °C). Blood vessels were visualized by i.v. injection of AlexaFluor750-labeled 70-kDa dextran (2 mg per mouse). Three days after tumor implantation, $0.5\text{--}1 \times 10^6$ in vitro activated eGFP OT1 CTL were i.v. administered.

All intravital imaging experiments were approved by the Ethical Committee on Animal Experiments and performed in the Central Animal Laboratory of the Radboud University, Nijmegen (protocol no. RU-DEC 2010–259), in accordance with the Dutch Animal Experimentation Act and the European FELASA protocol (www.felasa.eu/recommendations).

Multiphoton Microscopy and Image Processing.

Imaging was performed on a customized multiphoton microscope (TriMScope-II, LaVision BioTec), equipped with three tunable Ti:Sa (Coherent Ultra II Titanium:Sapphire) lasers and an Optical Parametric Oscillator (OPO) (PP Automatic equipped with a PP800

crystal; Coherent APE; typical pulse width, 200 fs; repetition rate, 80 MHz; peak output power of 500–650 mW at 1,180 nm). Three-dimensional time-lapse recordings were acquired by sequential scanning with 1,090 nm (mCherry and SHG) using 60 mW under the objective, and with 910 nm (eGFP and Alexa750) using 20 mW under the objective with a sampling rate of 1 frame/2 min over a maximum period of 4 h. Images were processed using Fiji (pacific.mpi-cbg.de/wiki/index.php/Fiji). Drifts in time-lapse recordings were corrected using the StackReg plugin (7), and CTL tracking was performed manually using the Manual Tracking plugin.

Statistics.

Prism software (Graph Pad Software V4.0) was used for statistical analysis by applying unpaired Student's t test or Mann-Whitney U tests, as appropriate. P values of < 0.05 were considered significant.

1. Zhu Y, Zhu G, Luo L, Flies AS, Chen L (2007) CD137 stimulation delivers an antigen-independent growth signal for T lymphocytes with memory phenotype. *Blood* 109(11):4882–4889.
2. Bellone M, et al. (2000) Relevance of the tumor antigen in the validation of three vaccination strategies for melanoma. *J Immunol* 165(5):2651–2656.
3. Quetglas JI, et al. (2012) Immunotherapeutic synergy between anti-CD137 mAb and intratumoral administration of a cytopathic Semliki Forest virus encoding IL-12. *Mol Ther* 20(9):1664–1675.
4. Shuford WW, et al. (1997) 4-1BB costimulatory signals preferentially induce CD8+ T cell proliferation and lead to the amplification in vivo of cytotoxic T cell responses. *J Exp Med* 186(1):47–55.
5. Alexander S, Koehl GE, Hirschberg M, Geissler EK, Friedl P (2008) Dynamic imaging of cancer growth and invasion: A modified skin-fold chamber model. *Histochem Cell Biol* 130(6):1147–1154.
6. Weigelin B, Krause M, Friedl P (2011) Cytotoxic T lymphocyte migration and effector function in the tumor microenvironment. *Immunol Lett* 138(1):19–21.
7. Thévenaz P, Ruttimann UE, Unser M (1998) A pyramid approach to subpixel registration based on intensity. *IEEE Trans Image Process* 7(1):27–41.

Supplementary figures

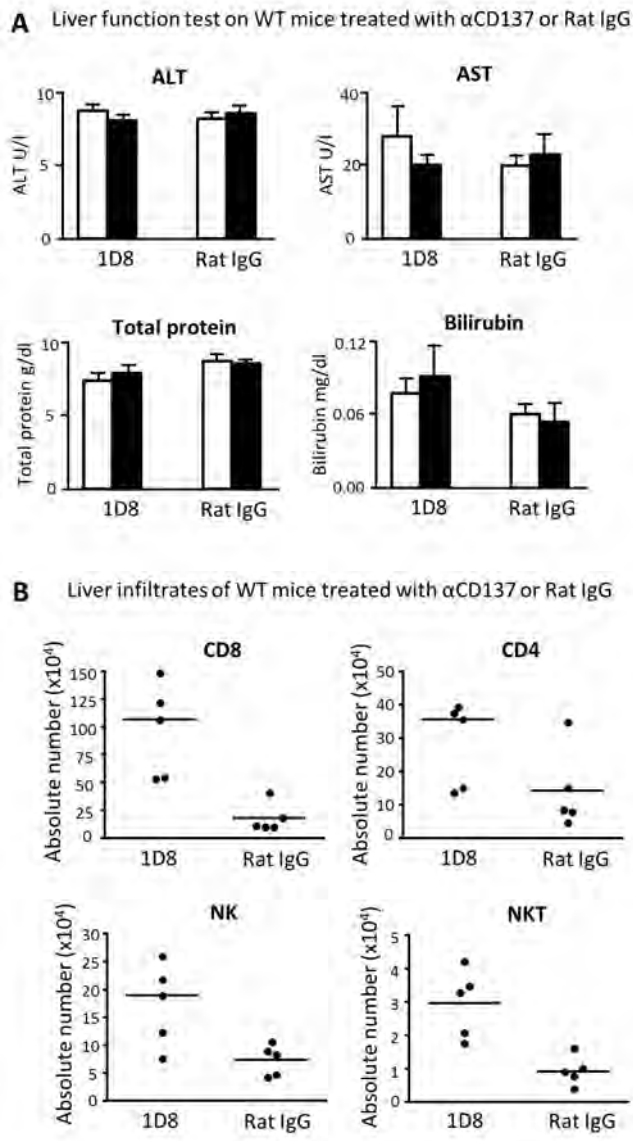


Figure S1. Liver safety of a single dose of 1D8 anti-CD137 mAb. C57BL/6 mice were treated with a single dose of 100 μ g of 1D8 or control antibody and killed 1 wk later after bleeding when livers were excised. **(A)** Liver function tests in treated mice ($n = 5$ per group) measuring transaminases, total serum protein and bilirubin as indicated. **(B)** Absolute lymphocyte numbers in the liver parenchyma of treated mice assessed by multicolor immunostaining with anti CD3, CD4, CD8, and NK1.1 monoclonal antibodies using flow cytometry and true-count beads. Results are from a single experiment with five mice per group.

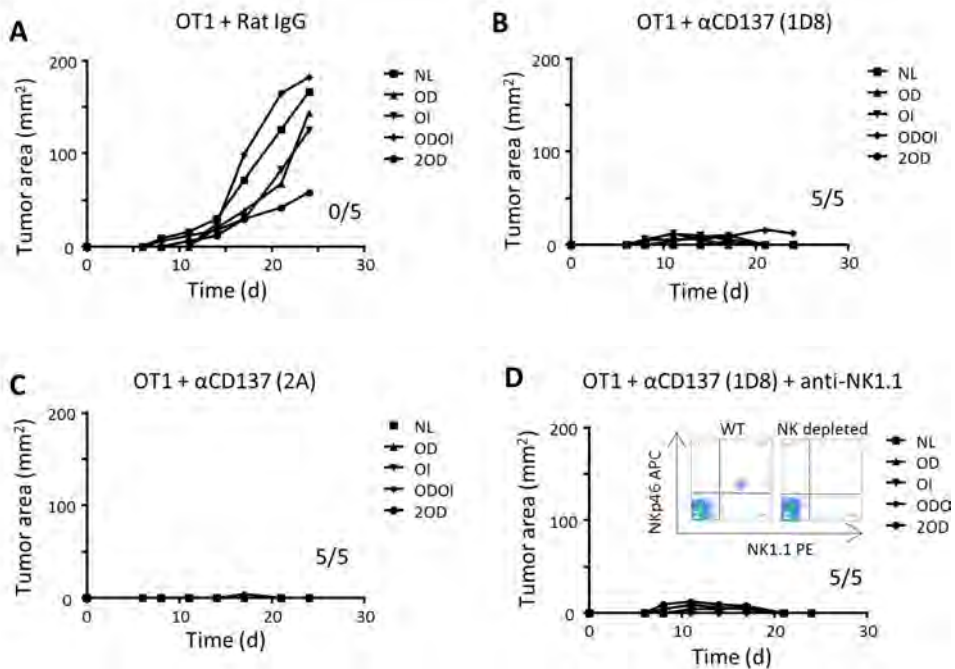


Figure S2. Therapeutic efficacy is elicited by anti-CD137 mAb binding different epitopes and is not dependent on NK cells. Experiments as in Fig. 1 in which B16F10-OVA bearing mice (for 3 d), were treated with adoptive transfer of OT-1 and the indicated anti-CD137 mAb or control antibody as in Fig. 1. Mice represented in the last panel were given NK and NKT depleting doses of anti-NK.1.1 mAb (dot plots representing the extent of depletion in peripheral blood on day 10 are included as Inset). Individual tumor size follow-ups of a single experiment are provided in each graph with the fraction of mice completely Fig. S2. Therapeutic efficacy is elicited by anti-CD137 mAb binding different epitopes and is not dependent on NK cells. Experiments as in Fig. 1 in which B16F10-OVA bearing mice (for 3 d), were treated with adoptive transfer of OT-1 and the indicated anti-CD137 mAb or control antibody as in Fig. 1. Mice represented in the last panel were given NK and NKT depleting doses of anti-NK.1.1 mAb (dot plots representing the extent of depletion in peripheral blood on day 10 are included as Inset). Individual tumor size follow-ups of a single experiment are provided in each graph with the fraction of mice completely rejecting their tumors. 1D8 and 2A mAbs bind to different noncompeting CD137 epitopes and 2A blocks CD137L binding, whereas 1D8 does not.

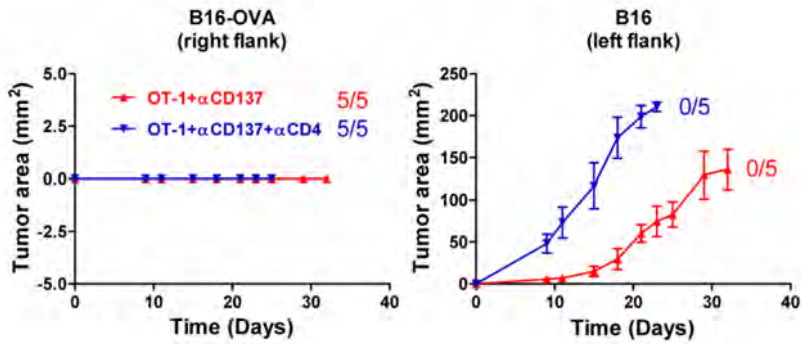


Figure S3. Mice cured by combined adoptive OT-1 lymphocytes + CD137 mAb treatment were rechallenged with B16F10-OVA (right flank) or B16F10 (left flank). When indicated mice had been depleted of CD4⁺ T cells during the primary tumor inoculation and combined therapy. Although B16F10-OVA rechallenges were rejected in every case, B16F10 grafted in all mice. However, engraftment took place with faster kinetics in mice that had been depleted of CD4⁺ cells during combined immunotherapy. Of note, these mice, which had been depleted of CD4⁺ lymphocytes, grafted the B16F10-derived tumors with the kinetics of tumor-naïve mice.

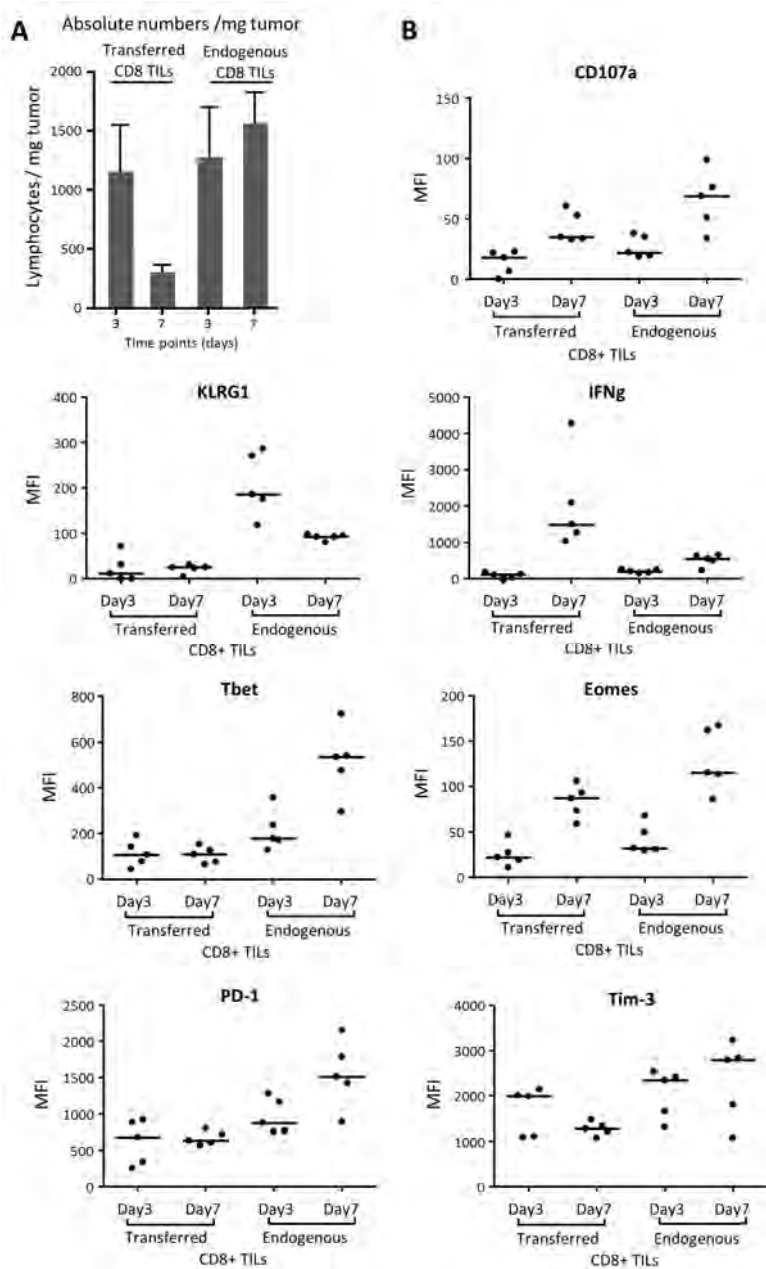


Figure S4. Comparison of tumor infiltrates of mice treated on day 3 or day 7 with the combination of activated OT-1 cells and anti-CD137 mAb. Mice treated as in Fig. 1 on day 3 or day 7, as indicated, were killed on day 10, and their tumors were excised. **(A)** Number of adoptively transferred and endogenous CD8⁺ T lymphocytes normalized by mg of tumor tissue and assessed with perfect-count beads. **(B)** Expression of the indicated markers as in Figs. 3 and 4. Results are from a single experiment with five mice per group.

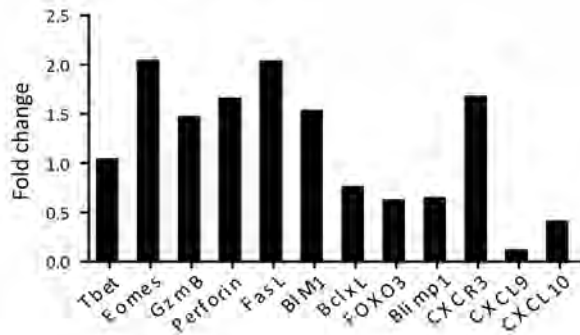


Figure S5. Comparative changes in mRNA expression in B16F10-OVA tumors from mice transferred with activated OT-1 lymphocytes that are dependent on cotreatment with anti-CD137 mAb or control antibody. Total mRNA extracted from excised tumors on day +7 following adoptive transfer and antibody treatment was subjected to quantitative RT-PCR analyses for the indicated genes using specific primers. Data are represented as the fold change in CD137 mAb-treated cases over the mean expression of mice treated with the control antibody that was normalized to one. Data were attained with the analyses of three independent tumors per treatment condition with less than 10% coefficient of variation.

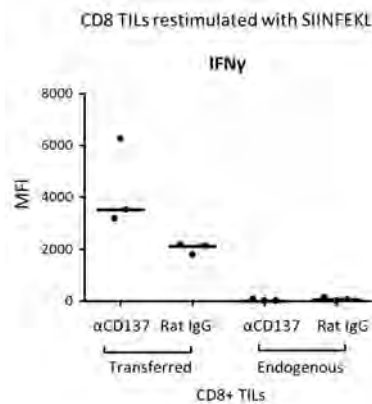


Figure S6. TIL restimulation with cognate peptide. TILs in tumor cell suspensions retrieved as in Figs. 3 and 4 were cultured in the presence of SIINFEKL or control peptide for 5 h, and gated transferred endogenous CD8⁺ T lymphocytes were stained for intracellular IFN γ . Data are represented as the MFI subtracting isotype-matched control staining. Results are from a single experiment with three mice per group.

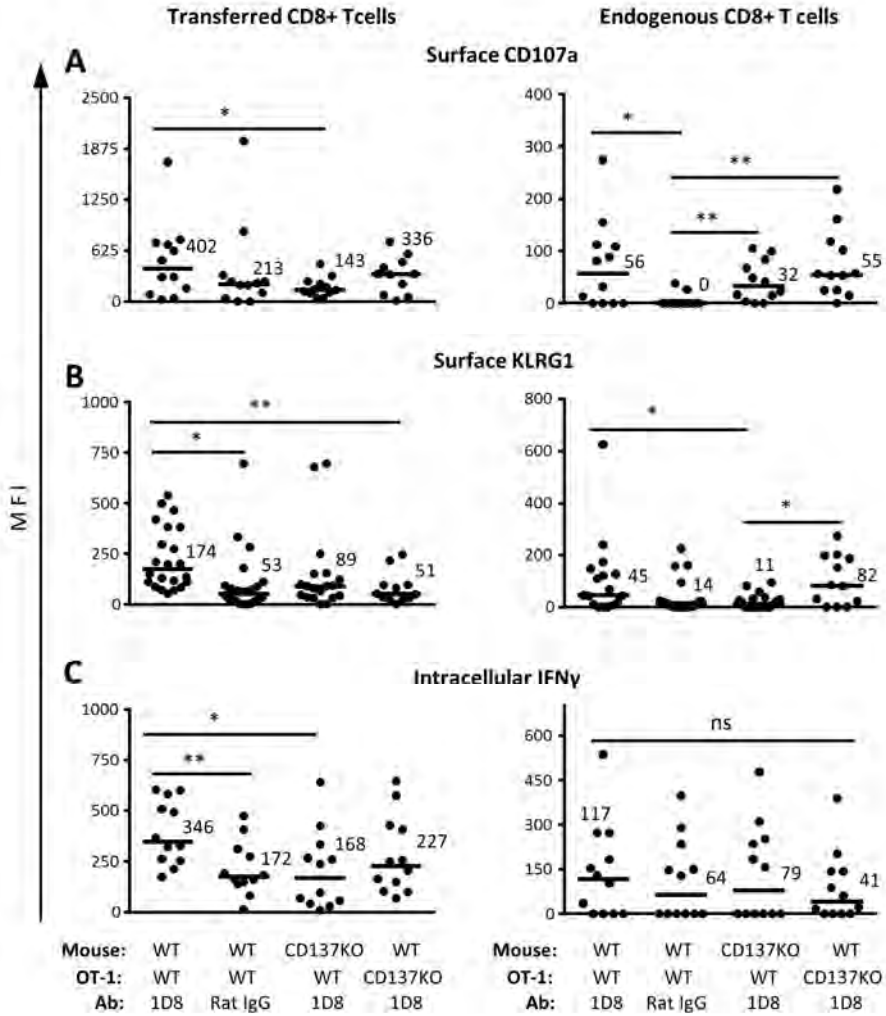


Figure S7. Lymph node CD8⁺ T cells from animals in Figs. 3 and 4 were analyzed by multicolor FACS analyses for the indicated markers. Data are presented as in Fig. 3 and 4 indicating the CD137 wt or CD137^{-/-} status of recipient mice or transferred OT-1 T cells. **(A)** shows CD107A surface staining, **(B)** shows surface KLRG1 staining, and **(C)** shows intracellular IFN- γ staining. Results show a similar tendency for a stronger effector phenotype upon CD137 mAb treatment, although less marked than in TILs. ns, not significant, * $P \leq 0.01$, ** $P \leq 0.001$.

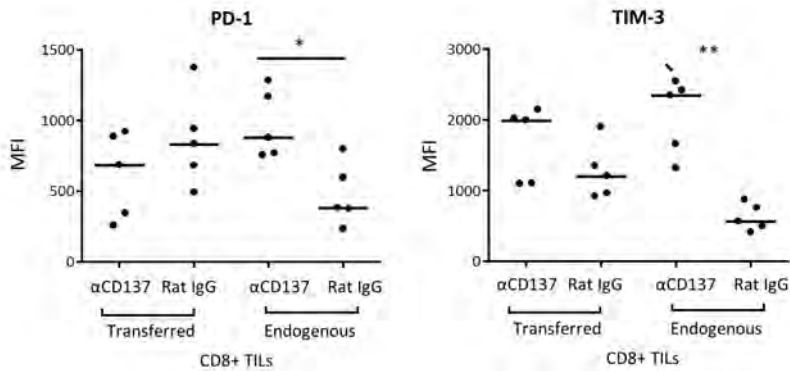


Figure S8. Experiment as those in Figs. 3 and 4 in which TILs were immunostained for surface expression of PD-1 and TIM-3. Results are presented as the MFI subtracting immunostaining by isotype-matched controls. Results are from a single experiment with five mice per group. * $P \leq 0.01$, ** $P \leq 0.001$.

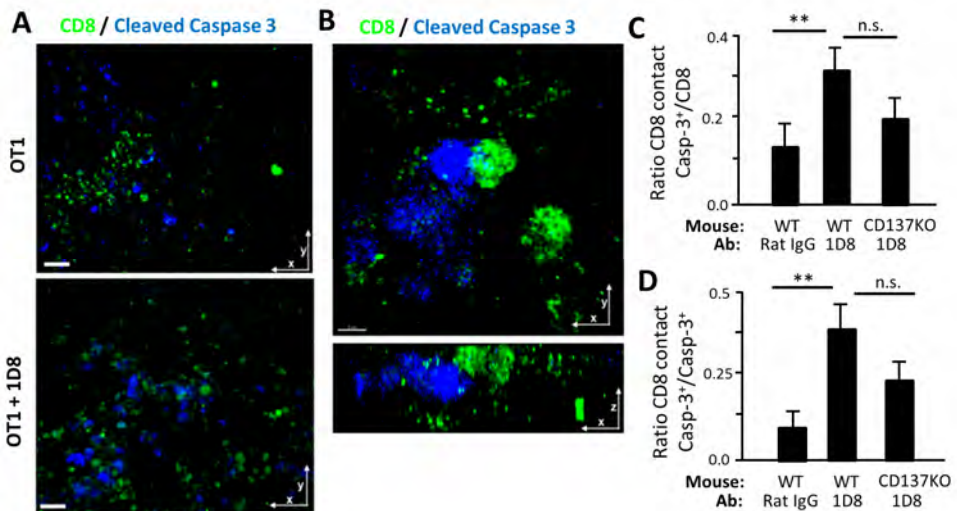


Figure S9. Combined treatment gives rise to more effective OT-1 CTLs in the tumor tissue microenvironment. B16F10-OVA-bearing mice were treated as in Fig. 1C with adoptive transfer of OT-1 T cells along with anti-CD137 or control antibody. Tumors excised on day 10 were analyzed by immunofluorescence and confocal microscopy for CD8 and cleaved caspase 3 as a marker of apoptosis in morphologically identified tumor cells. **(A)** Z-stack maximum projection of a representative field showing more apoptotic cells in contact to CD8⁺ T cells upon combined treatment. **(B)** A 3D reconstruction of a representative case XY (up) and XZ (down) maximum projection of Z-Stack. C and D represent the indicated ratios of events of 30 microscopy fields of images as in A from six tumors treated with OT-1 with or without CD137 mAb. CD137KO indicates when recipient mice were CD137^{-/-}. **(C)** and **(D)** The ratio of CD8⁺ T cells engaged with a dead or dying caspase 3⁺ B16F10-OVA cell **(C)** and the ratio of apoptotic B16F10-OVA cells that are in contact with a CD8 CTL **(D)**. n.s., not significant, ** $P \leq 0.001$.

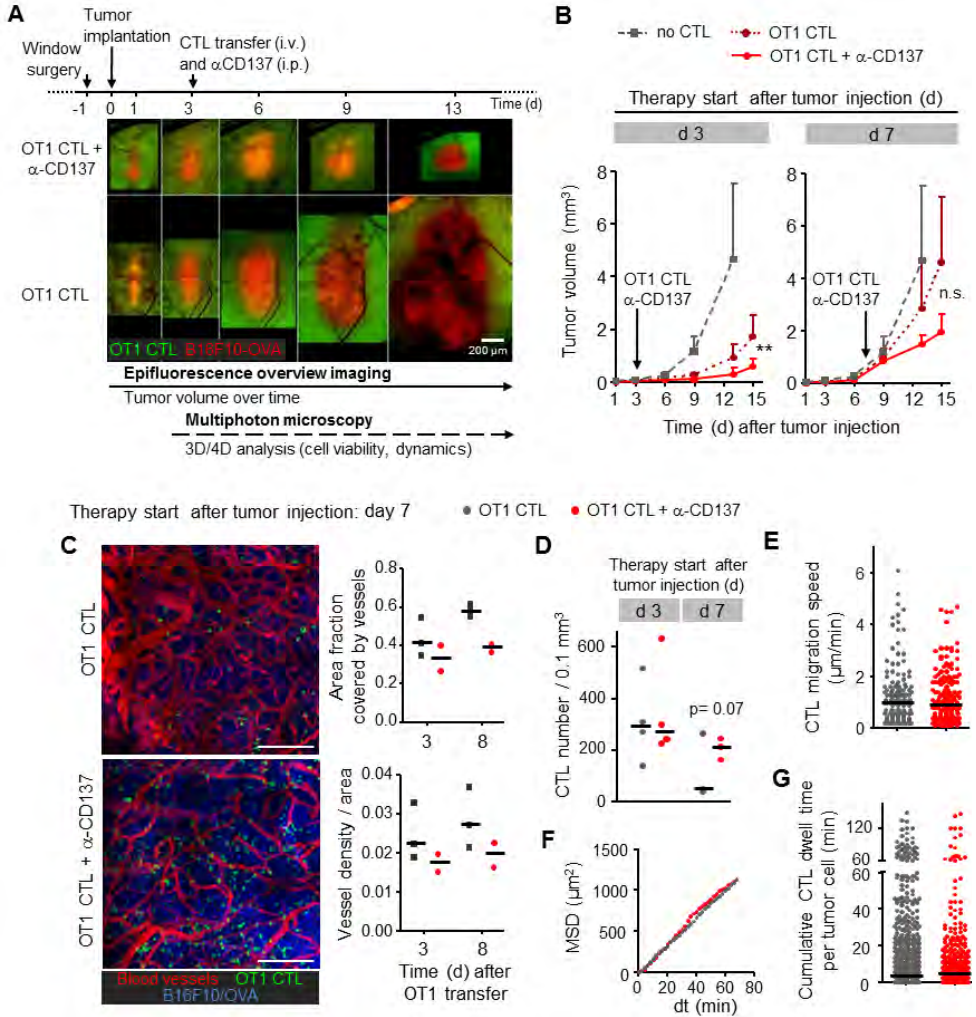
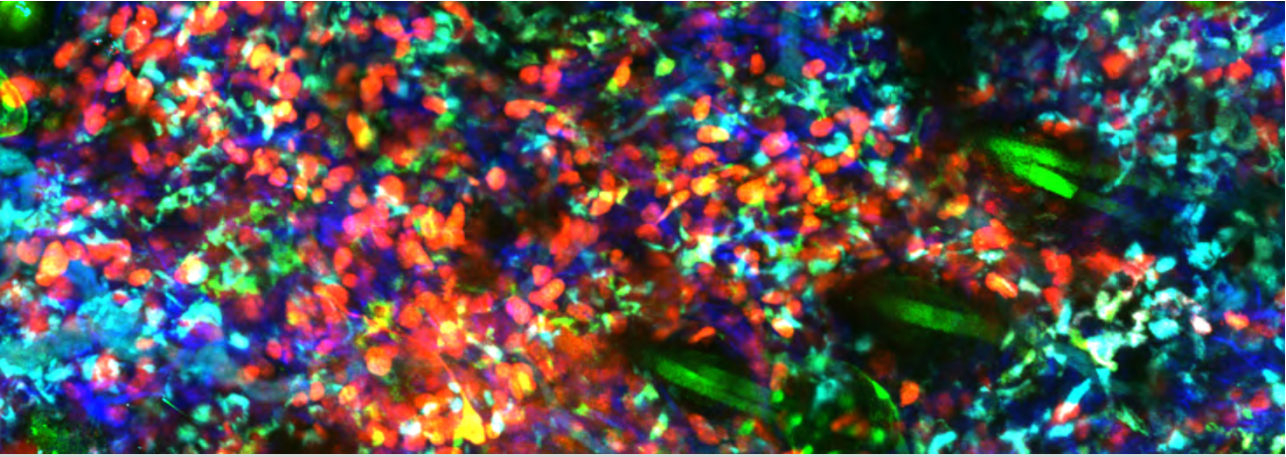


Figure S10. (A) Experimental setup for intravital imaging of CTL dynamics in the dorsal skin-fold chamber model to monitor tumor growth and regression. (B) Growth control by adoptively transferred CTL. A single dose of 1×10^6 OT1 CTL and anti-CD137 mAb was given either day 3 or 7 after tumor implantation and tumor volume was monitored over time. Significance test, two-Way ANOVA. n.s., not significant, $***P \leq 0.001$. (C) Overview image of vessel structures and CTL infiltration. On day 3 after OT1 CTL transfer and anti-CD137 mAb injection, a tissue volume of $1,000 \times 1,000 \times 160 \mu\text{m}$ was recorded with $7\text{-}\mu\text{m}$ z-steps. Maximum projections of the image volumes were analyzed for area covered by vessels and vessel density using the MATLAB based program RAVE. Anti-CD137 therapy decreased blood vessel diameter and density matching neovessel normalization phenotypes. (D) OT1 CTL numbers in the tumor (day 3 after CTL transfer) were increased with anti-CD137 therapy in late tumors (therapy start day 7 after tumor injection) while no effect on CTL numbers was detected in young tumors (therapy start day 3 after tumor injection). Data represent 3–5 independent mice. (Scale bars, $200 \mu\text{m}$.) (E–G) CTL migration speed (E), migration pattern (Mean Square Displacement) (F), and cumulative contact duration with tumor cells (G) were not affected by anti-CD137 mAb therapy in late tumors.



CHAPTER 8

Discussion and Implications

Partially published in modified form in:

“Preclinical Intravital Microscopy of the Tumour-Stroma Interface:
Invasion, Metastasis, and Therapy Response.”

Alexander S¹, Weigelin B², Winkler F³ & Friedl P^{1,2,4}

Curr Opin Cell Biol 2013; 25(5):659-71.

¹ David H.Koch Center for Applied Research of Genitourinary Cancers, Department of Genitourinary Medical Oncology, The University of Texas MD Anderson Cancer Center, Houston, TX, USA

² Department of Cell Biology, Radboud University Nijmegen Medical Centre, Nijmegen, The Netherlands

³ Department of Neurooncology, Neurology Clinic and National Center for Tumor Diseases, University of Heidelberg and German Cancer Research Center (DKFZ), Heidelberg, Germany

⁴ Cancer Genomics Center (CGC.nl), The Netherlands

4D imaging of the tumor stroma to understand cancer progression and (immuno) therapy response

As central aspect of this thesis, novel approaches to visualize connective tissues, the extracellular matrix (ECM) and stromal cells, and their impact on tumor biology were developed (Chapter 3) and applied to identify mechanisms of invasion and the interaction of immune effector cells with the tumor (Chapters 3, 6). *In vivo*, both, moving tumor and immune cells face complex and structurally heterogeneous 3D tissue architecture consisting of molecular and physical interfaces of different composition, length scale and stiffness, which provide space and guidance or act as a physical barrier and restrict cell motility. Thereby, multiple cell and ECM parameters are integrated by migrating cells to determine type, direction and efficiency of migration. Thus, to understand cellular function it is mandatory to visualize cell behavior within tissue context. When assessed with multiphoton excitation, most tissue structures generate intrinsic signals (higher harmonic generation) which can be exploited for label-free visualization of 3D tissue topography. In interstitial tissues, SHG (frequency doubling of photons) is elicited by collagen fibers and striated muscle myosin, detecting tumor-associated remodeling of collagen-rich ECM^{1,2}. As novel imaging modality in cancer research, THG (frequency tripling of photons) was introduced (Chapter 3) to detect water-lipid or water-protein scaffold interfaces, including cellular membranes, tissue discontinuities and interfaces along blood vessels, myofibers, nerves, and adipocytes. While fluorescence provides information about specifically labeled molecules, higher harmonic generation microscopy provides structural information and serves as a framework within which the fluorescence signals can be interpreted. Thus, when combined, SHG, THG, and fluorescence detection enable multispectral analysis of cell-tissue interactions and reveal connective tissue as remarkably heterogeneous in density and organization, which impacts guidance of moving cells (Fig. 1). The data show the efficacy and tolerability of backward THG compared with SHG and fluorescence detection in tumor-free and B16F10 melanoma-bearing tissue in live mice³ and thus establish THG as important complement to SHG and fluorescence imaging for the longitudinal monitoring of cancer biology in the context of tissue organization, blood flow and the dissemination of microparticles.

Principles of melanoma cell migration in complex environments

By establishing THG to detect migration-enhancing and –impeding tissue structures in live tumors, this thesis provided a first microanatomic classification for plasticity of tumor cell invasion strategies in response to tissue organization, with relevance for therapy design (Chapter 3).

Invading melanoma cell guidance is provided by cleft-like tracks along collagen bundles, myofibers, nerves, and vessels, or complex-shaped space within loose collagen networks or adipocytes (Fig. 1b). The underlying geometries of guidance tracks thus comprise 1D fibrillar strings of individual collagen fibers, porous 3D meshwork of ECM fibrils, and cleft-like 3D tracks between 2D ‘inner surfaces’ along and between collagen bundles, myofibers, nerve tracks, and vessels (Fig. 1b, c). The heterogeneity of tissue geometry is reflected and respected by invading tumor cells (Chapter 3) and further, these tissue tracks overlap with trafficking routes of leukocytes, likely representing constitutive ‘highways’ exploited by adaptive tumor cells³. The data suggest that the plasticity of cell migration modes, ranging from single-cell and multicellular streaming to collective invasion is determined by tissue topography, consistent with physical principles of cell migration such as haptotaxis and contact guidance. *In vivo* tumor cell invasion thus occurs preferentially via tissue tracks of least resistance without apparent signs of structural destruction. The concept of tissue-guided invasion provides new rationales for designing molecular targeting of cancer invasion and could explain why therapeutic inhibition of matrix degrading MMPs in clinical trials was not sufficient to prevent metastasis formation in patients^{5,6}. Thus, multi-modal microscopy reinforces the long-established pathological concept of tissue-guided interstitial tumor migration by providing direct evidence through intravital imaging.

Impact of the tumor stroma on immune cell positioning and function

Besides shaping tumor cell invasion patterns, the stroma determines infiltration routes and positioning of tumor-infiltrating immune cells. For apoptosis induction, cytotoxic T lymphocytes (CTL) depend upon efficient infiltration of the tumor lesion to form direct cell-cell contacts with tumor cells. To ensure that rare antigen-specific target cells are not overlooked, CTL employ a scanning behavior which is best described as random walk (Brownian motion) and generalized Lévy walk migration^{7,8} but appears independent of large-range chemokine gradients which were shown to guide neutrophil swarming towards sites of acute tissue damage⁹. Intravital microscopy further suggests that migrating effector CTL are guided by ECM fibers and blood vessels¹⁰, similar to the ‘guided random walks’ used by naive T cells in lymph nodes^{11,12}. Following adoptive transfer, CTLs efficiently infiltrate solid tumors but their distribution is heterogeneous and often limited to the tumor periphery¹³, suggesting that the tumor core escapes immune surveillance. In Chapter 6, CTL infiltration of solid tumors was reconstructed until 300 μm depth and revealed a wide heterogeneity of variable ET ratios ranging from ET 1:1 in the tumor margins to complete lack of CTL infiltration in deep tumor regions.

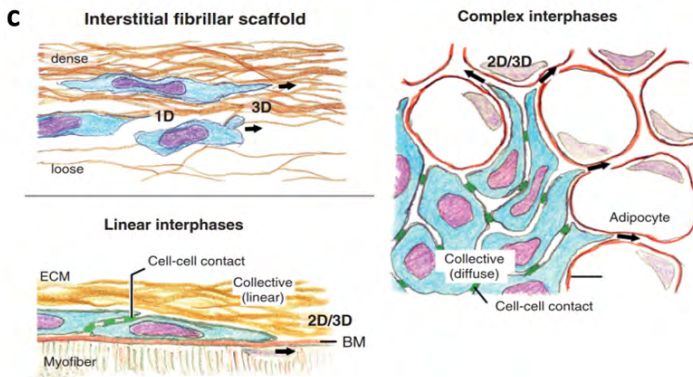
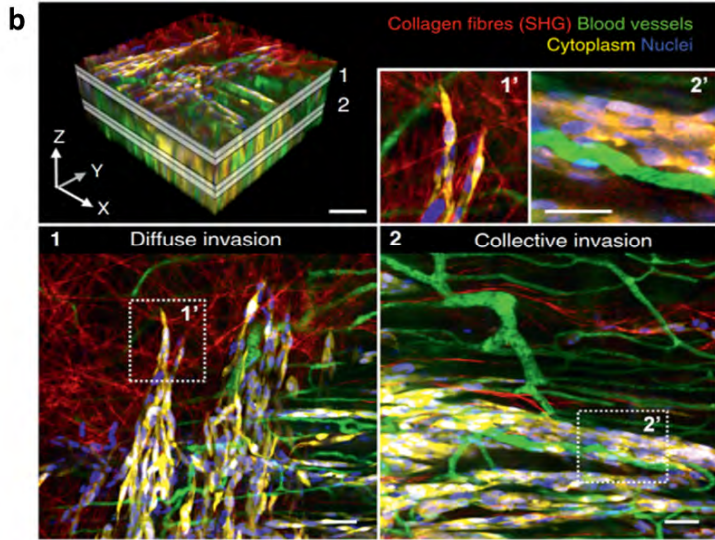
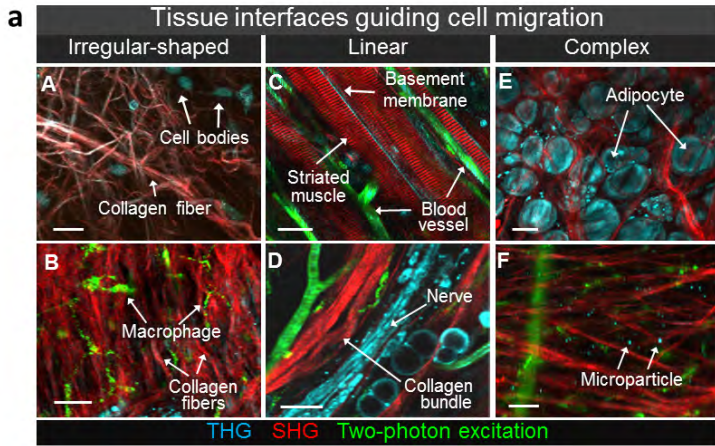


Figure 1. Multi-parameter 3D mapping of tumor invasion into interstitial stroma. (a) Diversity of the microanatomy of connective tissue (mouse dermis), visualized by intravital MPM. Collagen-rich loose (A) and dense (B) interstitial tissue. Interface-dependent tissue discontinuities along (C) myofibers and accompanying blood vessels and (D) between nerves and collagen-rich stroma. (E) Fat tissue showing interfaces along adipocytes (asterisk) and interstitial collagen fibers, resulting in complex geometries. (F) Detection of microparticles drifting through spaces between collagen fibers. (b) Plasticity of tumor cell invasion into the mouse dermis, in dependence of encountered tissue structures. 3D tissue reconstruction displaying two invasion zones ('niches') at different depth with either diffuse or compact collective invasion. Zoomed images show tip cells (10) and the multicellular core (20) of the invasion zone. Scale bars: 50 μ m. (c) Concepts of tissue-guided invasion modes derived from IVM. Interstitial collagen-rich connective tissue supports predominantly individual-cell dissemination, whereas movement along complex interfaces enables linear-ordered or diffuse collective invasion. Abbreviations: BM, basement membrane; ECM, extracellular matrix; SHG, second harmonic generation; THG, third harmonic generation. Reproduced from Ref. 4.

The concerted impact of mechanisms mediating exclusion of tumor-infiltrating CTL from central tumor regions remains unclear. Dysfunctional endothelium of core neo-vessels which prevents CTL adhesion and extravasation¹⁴ as well as lack of nutrients and oxygen are possible factors that limit deep tumor infiltration. In addition, aligned ECM fibers which encapsulate human lung cancer lesions were shown to misdirect and trap migrating CTL in peripheral tumor areas¹⁵. Compromised infiltration may further result from dendritic cell networks within solid tumors which attract and immobilize CTLs in non-productive engagements and thereby deviate or exhaust effector activity in irrelevant interactions^{16,17}. Consequently, limited tumor infiltration restricts therapeutic efficacy¹⁸ and thus, represents a relevant target with the potential to improve immunotherapy.

Principles of cytotoxic T cell cooperation and additive cytotoxicity

By using dynamic imaging, Chapter 6 of this thesis discovered the cooperation of multiple CTL as mandatory to overcome melanoma cell resistance to CTL-mediated killing and thus, further emphasizes the relevance of CTL migration concomitant to sufficient local CTL densities for reaching tumor regression. In contrast to immunogenic B cell targets^{19–21}, CTL effector function against melanoma cells is an inefficient process with a high failure rate which is rarely completed by a single CTL interaction, but requires a sequence of sublethal hits (Fig. 2). Apoptosis induction is, thus, not a binary event but instead implies the accumulation of a death signal within the target cell over time ("additive cytotoxicity").

This further implies that target cells may resist CTL attack by degrading cytotoxic mediators and repairing received damage between serial hits. The requirement for synergistic effects of multiple CTL to kill a target cell may represent a safety mechanism,

by creating a local threshold to autoimmunity in absence of significant or sustained antigen-specific CTL tissue infiltration. Concomitantly, CTL cooperation may strengthen the killing efficacy of CTL populations in immunosuppressive environments by compensating for compromised hits of individual CTL with multiple additive hits at high local CTL densities. The concept of additive cytotoxicity further opens the possibility that distinct subthreshold cytotoxic mechanisms may converge in the target cell, e.g. cytotoxic hits of NK cells and CTL or distinct apoptosis pathways such as Fas-FasL and perforin-mediated cytotoxicity. Likewise, however, interactions with or factors released by suppressive cells of the immune system may modulate CTL effector function by weakening the impact of CTL hits similar to immune suppressive mechanisms during CTL activation²¹⁻²³, thereby increasing, locally, the threshold to apoptosis. In addition, the microenvironment may promote target cell recovery between serial hits, e.g. by anchorage-mediated survival signaling or presence of growth factors. Thus, CTL effector function is not a binary process but instead integrates multiple synergizing or interfering parameters which tune the damage versus recovery in the target cell.

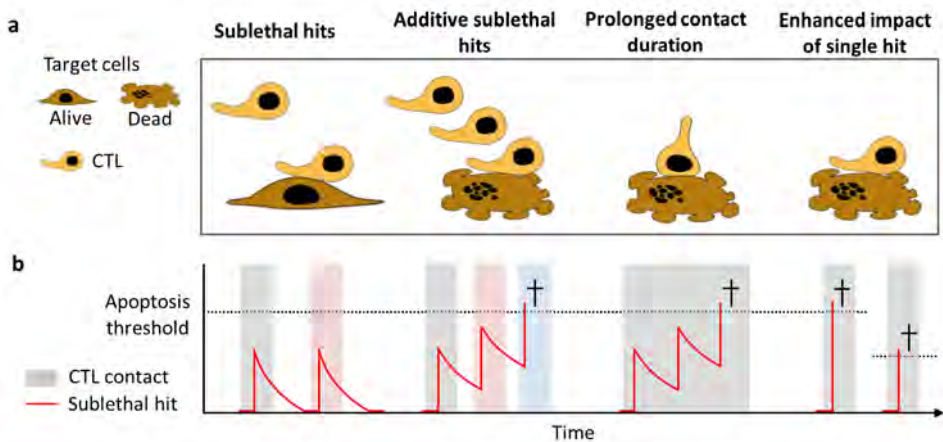


Figure 2. CTL cooperation and additive cytotoxicity. (a) CTL-target cell contact types and outcome. **(b)** Predicted accumulation of cytotoxic but often sublethal hits and recovery over time. Black cross, target cell apoptosis.

Tumor niches susceptible for immunological targeting

The concept of additive cytotoxicity predicts CTL-mediated killing *in vivo* to critically depend on local CTL density and migration capability which jointly mediate sufficient CTL contact frequencies for killing. In Chapter 6 and 7, intravital microscopy was used to monitor CTL migration, interactions with and apoptosis of tumor cells in the context of the 3D tissue microenvironment to identify regions permissive or ablative for CTL

effector function. After adoptive CTL therapy of invading B16F10 melanoma, adequate CTL densities for killing were only reached in the tumor margin and invasion zones. Dynamic multiphoton microscopy combined with higher harmonic generation (SHG/THG) revealed tissue guidance tracks that support both, CTL migration and density, thereby enhancing serial CTL conjugations and consequently, increasing target cell killing. This validates the concept of additive cytotoxicity and provides additional relevance of the invasion niches identified in Chapter 3, as it shows the shared use of tissue tracks by tumor and immune cells with detrimental outcome for tumor cell survival. Thus, dynamic imaging *in vitro* and intravital multiphoton microscopy *in vivo* reveals novel microenvironmental niches that control success or failure of anti-tumor immune effector mechanisms.

Therapeutic routes to focus and enhance cancer immunotherapy

Additive cytotoxicity describes CTL lethal hit delivery as gradual and thus, tunable process, which is amenable for therapeutic targeting by increasing either the impact of single hits or their frequency (Fig. 2). To enhance the frequency of serial CTL-tumor cell engagements, it will be mandatory to increase and sustain CTL infiltration of solid tumors. In addition, homogeneous CTL distribution including targeting of CTL to tumor regions which exclude CTL invasion will be required for complete response and to prevent tumor regrowth from resistance niches. Combinations of immunotherapy and anti-angiogenic therapy may improve CTL access to poorly infiltrated regions²⁴⁻²⁷ by normalizing dysfunctional vessel endothelium and enhancing expression of adhesion molecules which facilitate CTL extravasation²⁸. The long lag-times between initial CTL contact and tumor cell apoptosis emphasize strategies to either shorten the lag phase or to prolong CTL survival and to sustain CTL function over sufficient time periods to increase the probability of apoptosis induction. This may be achieved by repetitive adoptive CTL transfer or by combined IL-2 or immunomodulatory antibody therapy²⁹. Another route to increase CTL efficiency is to enhance the impact of individual cytotoxic hits. This can be achieved by either increasing the amount of cytotoxic mediators delivered per hit, by stabilizing CTL-target cell contacts to facilitate repetitive hits delivered by the same CTL, or by reducing the threshold to apoptosis induction in target cells (Fig. 2). Several approaches were developed to increase the efficacy of cytotoxic hit delivery. Immunomodulatory antibodies which activate costimulatory pathways during CTL activation and effector phase increase the expression of genes associated with enhanced effector function (Chapter 7). CTL-tumor cell contacts may be stabilized by using bispecific antibodies³⁰⁻³² that connect CTL and target cell or by blocking contact destabilizing inhibitory molecules expressed by tumor cells³³. However, balancing CTL

motility between swarming to promote serial CTL contacts and tumor infiltration, and arrest to promote stable contact formation with target cells, will be required for optimized serial CTL conjugation and killing efficacy. Lastly, chemotherapy^{34,35}, irradiation^{36,37}, or molecular targeted therapy to reduce stroma-derived anti-apoptotic signals^{38,39} may synergize with CTL-mediated cytotoxicity by lowering the target cell threshold to apoptosis. Thus, the concept of additive cytotoxicity provides a mechanistic explanation of immunotherapy failure in solid tumors and a rationale for improving combinatorial treatment schemes.

Conclusions and outlook

In the past decades, great advances have been made in our understanding of immune responses against cancer. A variety of *in vitro* and *ex vivo* methods has been applied to understand signaling pathways for immune cell activation and the molecular processes underlying immune effector function. However, much of our knowledge derived from these studies is static, or is obtained from reductionistic *in vitro* models, and does not fully reflect the natural dynamics of immune processes. To combine both, dynamic imaging and tissue complexity, intravital microscopy (IVM) of live tumors has evolved as powerful technique that allows capturing cell dynamics and function simultaneously and over time, at sub-cellular resolution and within the natural environment of living tissues. Visualizing immune cells in their physiological environment is particularly crucial because cellular function is controlled by many parameters including local cytokine concentrations, interactions with other cells, metabolic factors and nutrient availability as well as anatomical compartmentalization. Thus, combining molecular cell analysis *in vitro* and intravital microscopy of immune effector function will resolve important remaining questions, such as: How do immune cells navigate and interact inside complex tumor tissues and during the evolution of a tumor lesion? How do specific tumor subregions evade immune control? How does the microenvironment influence immune effector phase and how can we address such niche-dependent evasion by molecular targeting? The work in this thesis thus re-emphasized the importance of studying immune effector function in the context of 3D structural environments and cell navigation as integrating process. In addition, this thesis establishes the physiological relevance for principles of cell migration in confined spaces, which was rapidly applied for inspired biotechnical tissue engineering to model plasticity of cell migration in tunable defined environments^{40,41}. Further, kinetic imaging of adoptively transferred CTL in melanoma lesions revealed how 3D tissue topography determines immune effector function success or failure. Thus, to better predict the efficacy of adoptively transferred

CTL, the use of organotypic *in vitro* assays is required which integrate CTL migration capability and contact stability with tumor cells in their readout.

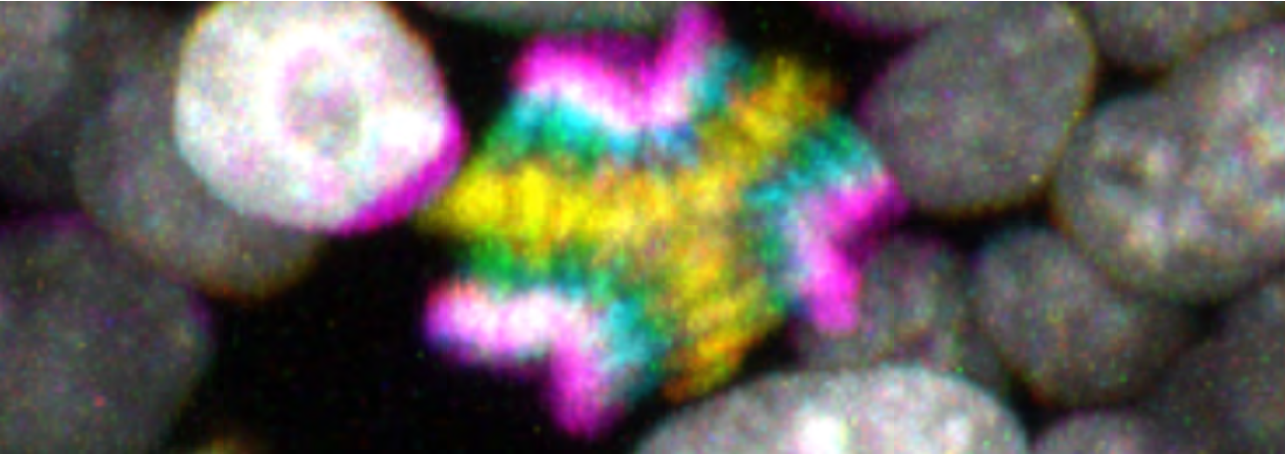
With the continuing development of new fluorescent mouse models, improved optical reporters and enhanced detection systems, IVM will contribute to an improved level of understanding complex processes of tumor biology and antitumor immune reactions within tissues. Implementation of multicolor tracers for simultaneous detection of multiple immune cell subsets will deliver mechanistic insight in the reciprocal interactions of CTL with supportive or suppressive immune cells, such as dendritic cells, CD4⁺ T cells, Foxp3⁺ T_{reg} and M1/M2 macrophages. By monitoring distribution and ratios of distinct immune cell subsets and the enrichment of external factors such as cytokines or metabolic parameters⁴² in relation to local CTL function, tumor resistance niches can be identified and characterized. Advanced molecular sensors will further allow simultaneous recording of CTL interactions and their consequences on CTL activation, e.g. by visualizing Ca²⁺ signaling or NFAT translocation⁴³. Likewise, consequences of CTL hits on target cells and their effect on cell viability may be monitored using fluorescent reporters for Ca²⁺ levels, cell cycle stage, caspase activation or DNA damage^{44–47}. By combining functional readouts with high spatiotemporal resolution, IVM will provide the foundation for an integrating, systems-level understanding of CTL function in the tumor microenvironment. Thus, multimodal IVM will reach the maturity to visualize tumor resistance niches, define their molecular, structural and cellular components and thereby deliver novel mechanistic insight into tumor immune escape strategies to provide new rationales for targeted immunotherapy design.

References

1. Provenzano, P. P. *et al.* Collagen reorganization at the tumor-stromal interface facilitates local invasion. *BMC Med.* **4**, 38 (2006).
2. Brown, E. *et al.* Dynamic imaging of collagen and its modulation in tumors in vivo using second-harmonic generation. *Nat. Med.* **9**, 796–800 (2003).
3. Weigel, B., Bakker, G.-J. & Friedl, P. Intravital third harmonic generation microscopy of collective melanoma cell invasion: Principles of interface guidance and microvesicle dynamics. *IntraVital* **1**, 9–20 (2012).
4. Alexander, S., Weigel, B., Winkler, F. & Friedl, P. Preclinical intravital microscopy of the tumour-stroma interface: invasion, metastasis, and therapy response. *Curr. Opin. Cell Biol.* **25**, 659–71 (2013).
5. Coussens, L. M., Fingleton, B. & Matrisian, L. M. Matrix metalloproteinase inhibitors and cancer: trials and tribulations. *Science* **295**, 2387–92 (2002).
6. Dormán, G. *et al.* Matrix metalloproteinase inhibitors: a critical appraisal of design principles and proposed therapeutic utility. *Drugs* **70**, 949–64 (2010).
7. Harris, T. H. *et al.* Generalized Lévy walks and the role of chemokines in migration of effector CD8+ T cells. *Nature* **486**, 545–8 (2012).
8. Weninger, W., Biro, M. & Jain, R. Leukocyte migration in the interstitial space of non-lymphoid organs. *Nat. Rev. Immunol.* **14**, 232–46 (2014).
9. Lämmermann, T. *et al.* Neutrophil swarms require LTB4 and integrins at sites of cell death in vivo. *Nature* **498**, 371–5 (2013).
10. Mrass, P. *et al.* Random migration precedes stable target cell interactions of tumor-infiltrating T cells. *J. Exp. Med.* **203**, 2749–61 (2006).
11. Cahalan, M. D. & Parker, I. Choreography of cell motility and interaction dynamics imaged by two-photon microscopy in lymphoid organs. *Annu. Rev. Immunol.* **26**, 585–626 (2008).
12. Bajénoff, M. *et al.* Stromal cell networks regulate lymphocyte entry, migration, and territoriality in lymph nodes. *Immunity* **25**, 989–1001 (2006).
13. Boissonnas, A., Fetler, L., Zeelenberg, I. S., Hugues, S. & Amigorena, S. In vivo imaging of cytotoxic T cell infiltration and elimination of a solid tumor. *J. Exp. Med.* **204**, 345–56 (2007).
14. Buckanovich, R. J. *et al.* Endothelin B receptor mediates the endothelial barrier to T cell homing to tumors and disables immune therapy. *Nat. Med.* **14**, 28–36 (2008).
15. Salmon, H. *et al.* Matrix architecture defines the preferential localization and migration of T cells into the stroma of human lung tumors. *J. Clin. Invest.* **122**, 899–910 (2012).
16. Boissonnas, A., Licata, F. & Network, C. T Cells Are Trapped in the Tumor-Dendritic. **15**, 85–94 (2013).
17. Engelhardt, J. J. *et al.* Marginating dendritic cells of the tumor microenvironment cross-present tumor antigens and stably engage tumor-specific T cells. *Cancer Cell* **21**, 402–17 (2012).
18. Quezada, S. a *et al.* Limited tumor infiltration by activated T effector cells restricts the therapeutic activity of regulatory T cell depletion against established melanoma. *J. Exp. Med.* **205**, 2125–38 (2008).
19. Purbhoo, M. a, Irvine, D. J., Huppa, J. B. & Davis, M. M. T cell killing does not require the formation of a stable mature immunological synapse. *Nat. Immunol.* **5**, 524–30 (2004).

20. Stinchcombe, J. C., Bossi, G., Booth, S. & Griffiths, G. M. The immunological synapse of CTL contains a secretory domain and membrane bridges. *Immunity* **15**, 751–61 (2001).
21. Mempel, T. R. *et al.* Regulatory T cells reversibly suppress cytotoxic T cell function independent of effector differentiation. *Immunity* **25**, 129–41 (2006).
22. Tadokoro, C. E. *et al.* Regulatory T cells inhibit stable contacts between CD4+ T cells and dendritic cells in vivo. *J. Exp. Med.* **203**, 505–11 (2006).
23. Fife, B. T. *et al.* Interactions between PD-1 and PD-L1 promote tolerance by blocking the TCR-induced stop signal. *Nat. Immunol.* **10**, 1185–92 (2009).
24. Bellone, M. & Calcinotto, A. Ways to enhance lymphocyte trafficking into tumors and fitness of tumor infiltrating lymphocytes. *Front. Oncol.* **3**, 231 (2013).
25. Shrimali, R. K. *et al.* Antiangiogenic agents can increase lymphocyte infiltration into tumor and enhance the effectiveness of adoptive immunotherapy of cancer. *Cancer Res.* **70**, 6171–80 (2010).
26. Terme, M. *et al.* Modulation of immunity by antiangiogenic molecules in cancer. *Clin. Dev. Immunol.* **2012**, 492920 (2012).
27. Mauge, L., Terme, M., Tartour, E. & Helley, D. Control of the adaptive immune response by tumor vasculature. *Front. Oncol.* **4**, 61 (2014).
28. Palazón, A. *et al.* Agonist anti-CD137 mAb act on tumor endothelial cells to enhance recruitment of activated T lymphocytes. *Cancer Res.* **71**, 801–11 (2011).
29. Melero, I., Grimaldi, A. M., Perez-Gracia, J. L. & Ascierto, P. A. Clinical development of immunostimulatory monoclonal antibodies and opportunities for combination. *Clin. Cancer Res.* **19**, 997–1008 (2013).
30. Hoffmann, P. *et al.* Serial killing of tumor cells by cytotoxic T cells redirected with a CD19-/CD3-bispecific single-chain antibody construct. *Int. J. Cancer* **115**, 98–104 (2005).
31. Baeuerle, P. a. & Reinhardt, C. Bispecific T-cell engaging antibodies for cancer therapy. *Cancer Res.* **69**, 4941–4 (2009).
32. Deguine, J. *et al.* Cutting edge: tumor-targeting antibodies enhance NKG2D-mediated NK cell cytotoxicity by stabilizing NK cell-tumor cell interactions. *J. Immunol.* **189**, 5493–7 (2012).
33. Vasaturo, A. *et al.* Clinical Implications of Co-Inhibitory Molecule Expression in the Tumor Microenvironment for DC Vaccination: A Game of Stop and Go. *Front. Immunol.* **4**, 417 (2013).
34. Shalapour, S. *et al.* Immunosuppressive plasma cells impede T-cell-dependent immunogenic chemotherapy. *Nature* **521**, 94–8 (2015).
35. Zitvogel, L., Galluzzi, L., Smyth, M. J. & Kroemer, G. Mechanism of action of conventional and targeted anticancer therapies: reinstating immunosurveillance. *Immunity* **39**, 74–88 (2013).
36. Lugade, A. a. *et al.* Local radiation therapy of B16 melanoma tumors increases the generation of tumor antigen-specific effector cells that traffic to the tumor. *J. Immunol.* **174**, 7516–7523 (2005).
37. Sharon, E., Polley, M.-Y., Bernstein, M. B. & Ahmed, M. Immunotherapy and radiation therapy: considerations for successfully combining radiation into the paradigm of immuno-oncology drug development. *Radiat. Res.* **182**, 252–7 (2014).
38. Sulzmaier, F. J., Jean, C. & Schlaepfer, D. D. FAK in cancer: mechanistic findings and clinical applications. *Nat. Rev. Cancer* **14**, 598–610 (2014).

39. Mendelsohn, J. & Baselga, J. The EGF receptor family as targets for cancer therapy. *Oncogene* **19**, 6550–65 (2000).
40. Stroka, K. M., Gu, Z., Sun, S. X. & Konstantopoulos, K. ScienceDirect Bioengineering paradigms for cell migration in confined microenvironments. *Curr. Opin. Cell Biol.* **30**, 41–50 (2014).
41. Yevick, H. G., Duclos, G., Bonnet, I. & Silberzan, P. Architecture and migration of an epithelium on a cylindrical wire. *Proc. Natl. Acad. Sci.* **112**, 5944–5949 (2015).
42. Zhao, W. *et al.* Cell-surface sensors for real-time probing of cellular environments. *Nat. Nanotechnol.* **6**, 524–31 (2011).
43. Marangoni, F. *et al.* The Transcription Factor NFAT Exhibits Signal Memory during Serial T Cell Interactions with Antigen-Presenting Cells. *Immunity* **38**, 237–49 (2013).
44. Chen, T.-W. *et al.* Ultrasensitive fluorescent proteins for imaging neuronal activity. *Nature* **499**, 295–300 (2013).
45. Yang, K. S., Kohler, R. H., Landon, M., Giedt, R. & Weissleder, R. Single cell resolution in vivo imaging of DNA damage following PARP inhibition. *Sci. Rep.* **5**, 10129 (2015).
46. Figueroa, R. A. *et al.* Anchored FRET sensors detect local caspase activation prior to neuronal degeneration. *Mol. Neurodegener.* **6**, 35 (2011).
47. Haass, N. K. *et al.* Real-time cell cycle imaging during melanoma growth, invasion, and drug response. *Pigment Cell Melanoma Res.* **27**, 764–76 (2014).



Summary

Samenvatting

Acknowledgements

Curriculum Vitae

List of publications

Summary

Cancer growth and invasion as well as therapy response are complex processes which depend upon both, cell intrinsic mechanisms and the tumor microenvironment. Besides conventional anti-cancer therapy, immunotherapy is a promising approach for a range of cancer types with the potential to raise a specific, adaptive and long-lasting anti-cancer protection. For immunological control of tumor progression, the activation and expansion of tumor-specific cytotoxic T-lymphocytes (CTL) is required followed by efficient infiltration of the tumor lesion, direct CTL-tumor cell contact formation and successful apoptosis induction. In this thesis, organotypic *in vitro* models and intravital microscopy were applied to visualize both, tumor and immune effector cells in the context of the tumor microenvironment to address central aspects of melanoma progression, including dynamic interactions of invading tumor cells with the tumor stroma and the local regulation of tumor infiltrating CTL.

CTL effector function in tumors depends on both, “immunological” mechanisms, such as TCR-mediated recognition and signaling, and coordinated CTL positioning and migration within the tumor tissue. **Chapter 2** summarizes the molecular and biophysical parameters that govern CTL migration in interstitial and tumor tissue. In the three-dimensional tumor microenvironment, tissue topography can form barriers or provide guidance for CTL infiltration of solid tumors and may locally determine tumor resistance niches by misrouting or excluding CTL from tumor regions. Thus, visualizing tissue topography simultaneous to CTL dynamics is required to understand the mechanisms of successful or failed CTL effector function in tissues.

In **Chapter 3** multimodal intravital MPM was established which combines infrared-excited two-photon fluorescence, second harmonic generation and, as novel modality in cancer research, third harmonic generation (THG) microscopy for label-free visualization of the structural microenvironment of melanoma growing in the mouse dermis. The data provide a framework for tissue cues guiding melanoma cell invasion. Melanoma cells invade connective tissue along constitutive interfaces which form routes of least resistance, including tissue tracks and spaces along blood vessels, myofibers, nerves, between adipocytes and collagen bundles, without immediate anatomic tissue remodeling or destruction. By using a novel imaging approach, this thesis provides a first microanatomic classification for plasticity of tumor cell invasion strategies in response to 1D, 2D and 3D tissue organization, with relevance for therapy design for targeting invading tumor cells.

In **Chapter 4**, a 3D collagen-based *in vitro* assay was established which simulates the connective tissue environment and allows real-time imaging of CTL function, including the observation of active migration, interaction, dissociation and serial engagements of

CTL with single target cells over extended time periods. This novel migration-based assay promotes the natural dynamic CTL behavior and thus provides improved physiologically relevant information on CTL killing kinetics. In **Chapter 5** the mechanisms of CTL effector function are reviewed and fluorescent histone-2B labeling is established as readout for CTL-mediated apoptosis induction in tumor cells.

In **Chapter 6** dynamic imaging of organotypic 3D assays of tumor cells confronted with migratory CTL and intravital multiphoton microscopy identified a cooperation mechanism dependent on sequential CTL-tumor cell interactions and the accumulation of sub-lethal hits to overcome melanoma cell resistance to CTL-mediated apoptosis ('additive cytotoxicity'). Consistently, in orthotopic melanoma *in vivo*, tumor regions with high CTL density supported additive cytotoxicity and correlated with high local apoptosis rates. Highest CTL densities and apoptosis induction occurred at the invasive tumor front, where invading tumor cells and CTL both move and accumulate along the same anatomic trails of least resistance, suggesting invading tumor cells as target for immunotherapy.

In **Chapter 7** the immune-augmenting impact of agonistic anti-CD137 antibodies on CTL effector phase was addressed by immunological and intravital imaging approaches. Prolonged CTL contacts with tumor cells and sustained effector function of adoptively transferred CTL over extended time periods enhanced tumor remission, providing direct evidence of synergistic effects of α -CD137 mAb and adoptive CTL transfer.

Thus, in summary, in this thesis kinetic imaging and intravital microscopy were applied to deepen the mechanistic understanding of immune cell function within complex tissues which provides a basis for novel, rationale design of immunotherapies.

Samenvatting

De groei, het invasief gedrag en de respons van kankercellen op antikanker therapie zijn complex gereguleerde processen die afhankelijk zijn van zowel celintrinsieke factoren als de extracellulaire tumoromgeving. Naast traditionele antikanker therapieën, is immuuntherapie een veelbelovende nieuwe behandeling met de potentie om specifieke, adaptieve en langdurige bescherming te bieden tegen diverse soorten kanker. De immunologische remming van tumorprogressie begint met een activering en een toename van tumorspecifieke cytotoxische T-lymfocyten (CTL's). Deze CTL's doden tumorcellen door aan deze cellen te binden, wat vervolgens celdood door apoptose veroorzaakt. Een succesvolle eliminatie van de tumor wordt daarom niet alleen bepaald door een expansie van de tumorspecifieke CTL populatie, maar ook in de mate waarin de CTL's in de tumor kunnen infiltreren en in hoeverre zij een stabiele interactie met de tumorcellen kunnen aangaan. In dit proefschrift worden nieuwe organotypische in vitro modellen en intravitale microscopische technieken beschreven die CTL's en tumoren en hun onderlinge interactie in de context van tumorweefsel in beeld brengen. Hiermee konden belangrijke aspecten van de tumorprogressie van melanoom, waaronder de dynamische interacties van invasieve tumorcellen met het tumorstroma, en de lokale regulering van tumorinfiltrerende CTL's worden bestudeerd.

De effector functie van CTL's wordt niet alleen gereguleerd door "immunologische" mechanismen, waaronder signaalherkenning en signaaloverdracht via de TCR, maar ook door de gecoördineerde positionering en migratie van CTL's binnen het tumorweefsel. **Hoofdstuk 2** beschrijft de moleculaire en biologische parameters die de migratie van CTL's binnen het tumorweefsel bepalen. In de 3-dimensionale tumor omgeving kan de topografie van het tumorweefsel enerzijds een barrière vormen, maar anderzijds ook als routemarkering voor CTL's in de tumor fungeren. Als gevolg hiervan is het mogelijk dat CTL's sommige delen van de tumor niet kunnen bereiken waardoor er locale tumorresistentie niches ontstaan. Door de dynamiek van CTL's en weefseltopografie tegelijkertijd in beeld te brengen, wordt het mogelijk om factoren die van belang zijn voor een effectieve CTL functie in weefsels in kaart te brengen.

In **Hoofdstuk 3** is de ontwikkeling beschreven van multimodale intravitale multifoton microscopie (MPM), waarbij infrarood-geëxciteerde tweefoton microscopie, tweede harmonische generatie, en derde harmonische generatie (TGH) werd gecombineerd. De toepassing van THG microscopie is een nieuwe microscopie modaliteit in kankeronderzoek, en is hier gebruikt om op een labelvrije manier de structurele micro-omgeving van een melanoom in de dermis van de muis in beeld te brengen. De in dit hoofdstuk beschreven resultaten scheppen een kader voor hoe bepaalde "markeringen"

die in het weefsel aanwezig zijn een rol kunnen spelen bij de invasie van melanoom cellen.

De invasie van melanoomcellen in het omliggende bindweefsel verloopt vaak via “de weg van de minste weerstand”, waarbij gebruik wordt gemaakt van al aanwezige anatomische “routes”. Voorbeelden hiervan zijn: de oppervlakte van bloedvaten, spierweefsel of zenuwen, of de ruimtes tussen collageen bundels of tussen vetcellen. Door gebruik te maken van deze ruimtes blijft de anatomie van het bestaande weefsel grotendeels behouden. Met behulp van de nieuwe microscopische technieken die in dit proefschrift worden beschreven, kan nu, voor de eerste keer, de plasticiteit van tumorcel invasie gedrag als gevolg van specifieke weefselstructuren worden geclassificeerd. Deze kennis kan toegepast worden om specifieke therapieën tegen tumorcel invasie te ontwikkelen.

Hoofdstuk 4 beschrijft de ontwikkeling van een 3D *in vitro* toetsmodel waarin de structuur van bindweefsel wordt nagebootst en waarin de functie, migratiegedrag, en de (seriële) interacties en dissociaties van CTL's met individuele tumorcellen gedurende langere tijd gevolgd kan worden. Dit model is in het bijzonder fysiologisch relevant om de kinetiek van CTL-geïnduceerde celdood te bestuderen, omdat het CTL migratie en CTL-tumor cel interacties in een relevante weefselcontext nabootst. **Hoofdstuk 5** geeft een overzicht van de mechanismen die betrokken zijn bij CTL-gemedieerde apoptose in tumorcellen, en laat zien hoe apoptose met behulp van fluorescent gelabeld histon-2B kan worden geanalyseerd.

In **Hoofdstuk 6** wordt met behulp van intravitale MPM en organotypische 3D *in vitro* assays (zie Hoofdstuk 3 en 4) gedemonstreerd dat een combinatie van opeenvolgende, subletale interacties van CTL's met apoptosis-resistente melanoomcellen, in staat zijn om deze resistentie op te heffen in het *in vitro* model (“additieve cytotoxiciteit”). Consistent met deze bevindingen zijn de resultaten verkregen in een *in vivo* model van een orthotoop melanoom, waarin een positieve correlatie werd gevonden tussen tumorgebieden met een hoge concentratie CTL's en de mate van apoptose. De hoogste concentratie CTL's werd met name waargenomen aan het invasieve tumorfront, waar zowel de invasieve tumor cellen als de CTL's de lokale weefselanatomie gebruikten als “weg van de minste weerstand”, zoals beschreven in Hoofdstuk 3. Deze bevindingen zijn een aanwijzing dat invasieve tumorcellen specifiek gevoelig kunnen zijn voor immuuntherapie.

In **Hoofdstuk 7** werd het immunostimulerend effect van agonistische anti-CD137 antilichamen op de CTL effector fase onderzocht met behulp van immunologische methoden en intravitale microscopie. De behandeling van CTL's met anti-CD137 antilichamen voorafgaande aan adoptieve CTL transfer verlengde het contact van CTL's

met tumorcellen, verhoogde de effector functie van CTL's en stimuleerde langdurige tumorremissie. Deze resultaten demonstreren daarom een synergistisch effect van adoptieve CTL transfer en anti-CD137 behandeling.

Samenvattend kan worden gesteld dat in dit proefschrift kinetische- en intravitale microscopische methoden worden toegepast, welke diepgaand inzicht verschaffen in de werkingsmechanismen van immuuncellen in een complex weefselmilieu. Deze kennis kan leiden tot verbeteringen in de rationele ontwikkeling van nieuwe immuuntherapieën.

Acknowledgements

The final pages of this thesis shall be dedicated to all the people I met along the way, with who I shared the ups and downs and whose contributions and support made this thesis possible.

First of all I would like to thank my promotor. **Peter**, I remember our first meeting where you showed me movies of tumor cells moving through collagen and T cell serial killers. I was immediately fascinated. But it takes more to explain why I'm still around after all these years and you certainly have a role in it. I especially want to thank you for always taking my ideas seriously and (even when I couldn't fully convince you) giving me the freedom to follow my own beliefs and to shape my projects. Also your openness for "hidden treasures", meaning unexpected discoveries and their development into side projects, is unique. And while some may criticize it as lack of straight-forwardness, for me this is what makes science fun and what triggers innovation - the open mind for the unexpected result. Thank you for that. And the success proves this right: all of the "distractions" eventually turned into successful projects. You were also always reachable for advice and feedback whenever needed. I also greatly appreciate that you gave me the opportunity to travel and to represent the group and my work at many conferences and meetings, which created many opportunities for me. Without your support I would not be where I am today, thank you for everything!

Mirjam, my co-promotor, thank you for your support in the final phase of the thesis and particularly for the Dutch translations. I think your Dutch version partially sounds better than the English original 😊 Thank you for always being open for discussing science and giving advice whenever I needed it!

Esther, I cannot imagine how this thesis would look without all your help. I admire your efficiency (of course, who could not...), but even more importantly I greatly value your critical thinking and common sense and all the discussions about experiments we have. I find it funny to see, how we usually have a common way of thinking. With your enthusiasm and involvement in each project it is just fun to work with you, as it makes all the difference to have someone to share the unavoidable disappointments of failed experiments and the happiness of successful ones. I also greatly appreciate your helpfulness, you always sense when and where your support is needed and from that, a kind of synergy evolves which is more than just the work of both of us combined. That effect might be the reason for our notorious over-optimistic plannings ... but no ... it is just true ... we can do absolutely everything in one week 😊! I feel honored that you will stand beside me at my defense, thank you for everything!

Samuel, we shared our entire PhD time together, the beginning in Würzburg and the move to Nijmegen, the emotional ups and downs of scientific work, the late night and

weekend experiments (where the real science is done), scientific and philosophical discussions in front of the panoramic view on Nijmegen, some Football Championships in the German Unit, excessive red wine parties in PRIME ☺ ... Your enthusiasm for science and glycans is fun to see and very contagious! Thank you for always being there and for always listening! It is priceless to feel understood. Some people believe we could have done the PhD in half of the time because most of the day we spent talking to each other ... haha ... well, whatever ... I sure don't want to miss any moment of it!

Gert-Jan, with you I shared many of my scientific “magic moments” during my PhD. Do you remember the first intravital imaging sessions and our first movies of the funny cell division and the migration of cells “in the wrong direction” in the tissue tracks? Or when we discovered the first THG tissue structures wondering what we are actually seeing? Without you, large parts of this thesis would not exist, because I still believe the multiphoton microscope functions only as long as you stay within a radius of a few kilometers ☺. You have a unique way of thinking and I always enjoy our scientific discussions! Thank you for your interest in my projects and all your input!

My students, it was a lot of fun working with all of you! **Marina**, your discovery and elimination of all technical “teething troubles” of our Multiphoton platform really got the imaging work started. I'm glad the difficult project did not scare you off and you decided to come back for your PhD! **Jasper**, your enthusiasm for science, your creativity and ideas led to novel design of models and techniques! **Sarah**, you brought the 3D spheroid model to perfection and we could finally get some first real data of CTLs killing a tumor spheroid. It is great to have you back again for your PhD! **Marit**, with your EM skills you started a novel sideline and moved the “tissue-guided migration” project a huge step forward! **Daphne**, in your short internship time you learned an incredible amount of techniques and accumulated a large set of data! Thank you all for your valuable contributions!

Many chapters of this thesis include input from collaborators from near and far who I want to acknowledge specifically. **Nacho**, **Elixabet** and **Ivan**, thank you for this fruitful, enjoyable and successful European team effort! Maybe we should think of a sequel? Successful movies usually are continued as trilogy... **Kelly**, we met on our first PhD retreat and the human male-cells attacking T cells you had accidentally isolated turned out to be an important contribution to my project. Thank you for the nice collaboration! **Johannes**, your expertise and statistical analysis of our data really completed the manuscript. Thank you for your effort and valuable input!

A large part of my time I spend across the street in the CDL and in PRIME and there I met many people I want to specifically thank for contributing to this thesis. **Connie** and **Nicole**, thank you for all the help with technical and administrative problems and for

always finding a solution. Also all biotechnicians of the CDL and PRIME team, particularly **Jeroen**, you did a great job to keep the nestin-mice healthy, and **Bianca, Henk, Iris, Kitty, Alex, Mike** and **Saskia** I want to thank for taking such very good care of our mice!

Dear **TIL colleagues** and **Carl** and **Gosse**, it was an enriching experience to join your DLM mouse seminars, thank you for your interest in my projects and your immunological feedback on my work. I noticed that Immunology and Cell Biology are like two very different cultures but nevertheless, or better because of that your input was very valuable! **Lotte, Annemiek, Fernando, Luis** and **Jolanda** it was nice to collaborate with you and to contribute my expertise on cell migration assays. **Ingrid**, thank you for sharing mice and advice, which was priceless in the start-up time after moving to Nijmegen!

Christina and **Luis**, from colleagues we soon became friends, I think because we share a common view on many aspects of life and a common humor. I always loved the vacation-like weekends we spent together and many memories still make me laugh 😊

Long time ago, but not forgotten is my time in Würzburg with all my dear German colleagues. **Steffi** and **Markus**, thank you for introducing me to the world of mice and microscopes! I will not forget the late night experiments and all-day-long imaging sessions. It was a great time. Thank you for everything! **Annemieke**, you had started the T cell project in the lab, thank you for introducing me to your T cell world. I enjoyed working with you! **Kata, Margit, Moni, Angelika, Julian, Ute, Eva, Andrea, Martina**, vielen Dank für die tolle Zeit, eure Hilfsbereitschaft in allen Bereichen und die vielen Gespräche. Ich hoffe, dass wir die Tradition der Weihnachtsessen noch eine Weile beibehalten!

Olga, Samuel, Mariska, and **Kata**, being the “founding members” of the Cell Dynamics group in Nijmegen we went together through the phase of building-up, settling in and reconditioning the new microenvironment. It was a special time and I absolutely enjoyed spending it with you! **Kata**, thank you especially for all the conversations, advice and the good collaborations on many little projects over the years! **Cindy**, it was great to have you join the T cell project. Together we got through the difficult times (sick T cells...) and successfully established the theme of tumor immunology in the cell dynamics lab. Thank you for all your input and your advice over the years! **Linda**, thank you for your help with all administrative issues and for always finding a way! **Anna, Antoine, Gert-Jan, Cindy, Esther, Mirjam, Steffi, Harsha, Angela, Cornelia, Sarah, Marina, Manon, Pavel, Julia, Jan-Hendrik, Sjoerd, Lianne**, thank you all for the friendly and supporting atmosphere in the lab and the many great conversations and discussions that we have within the group, in the cell culture, at the coffee machine, in PRIME, in the lab, over lunch and over skype. I think we have a great team spirit in the group which even expands over the Atlantic to our Houston colleagues.

Steffi, Steve, Michael, Veronika, Eleonora, Lying, Stefano, Weihua, over the years the labs have grown together and I greatly value all the input from your side! I'm looking forward to be on the other side of the skype-screen next year!

The department of Cell Biology I want to thank for the warm welcome and for integrating us on the 6th floor. **Bé**, I greatly appreciate that you were always available for advice when needed, thank you for that! **Wiljan**, without your help we'd have been lost in the GGO legislation jungle! Thank you for your support over all these years! **Jack**, thank you for all the help around microscopes and for patiently and regularly reminding me to back up my files to clean up the MIC server ☺ Thank you also for the nice collaboration and the amazing EM images, I'm looking forward to continue this work with you! **Mietske**, since I started I hoped for an opportunity to get some beautiful EM images ... I'm glad we finally found a scientific justification for doing these experiments ☺ Thanks for your help! **Huib**, there is no problem in the lab you don't have a solution for, from simple empty batteries to broken state-of-the-art confocal microscopes and locked doors, thank you for always making time to help! **Marieke**, thank you for generously sharing vectors and for your enthusiastic support on many occasions! **Jan**, your ability to find a solution to impossible cloning problems is legendary and many times I was glad to rely on your skills, thank you! **Magda**, bedankt voor jou hulp in administratie en jou onvermoeibare inzet om mijn Nederlands te verbeteren! ☺

Further I wish to thank all other current and former members of the Cell Biology department, **Ineke, Frank, Walther, Rinske, Ad, Ingeborg, Remco vH, Michiel, Rick, Ellen, Irene, Gerda, Lieke, Anchel, Susan, Claire, Marieke, Mirthe, Annika, Anke, Remco, Lauréne, Leontien, Monique**, your support and scientific input during numerous times along the way was always very helpful! In addition to the scientific aspect, thanks to all members of the 6th floor, including my **Animal Physiology colleagues** for the nice atmosphere, the Christmas and Sinterklaas evenings (I will never forget the dead fish), the Easter Lunchs, the Dagje Uits and Movie Nights. Although I must admit, I still don't understand why you dress up funny for a Christmas dinner... maybe because a Halloween party is missing? ☺

Mein besonderer Dank geht auch an meine **Familie und Freunde**. Ihr habt immer an mich geglaubt. Besonders Mama und Papa, danke für Eure Unterstützung, ohne Euch stände ich jetzt nicht hier.

Claudius, ich bin froh, dass Du in all den Jahren immer an meiner Seite warst und bist. Zu wissen, mich immer auf Dich verlassen zu können ließ alle Schwierigkeiten überwindbar aussehen. Danke für all dein Verständnis und deinen starken Rückhalt!

Bettina

Curriculum Vitae

Bettina Weigelin was born on March 20th, 1982 in Bernburg, Germany. She studied Biology with a focus on biomedical science at the in Würzburg, Germany and received her diploma in 2007. Thereafter she started her PhD studies at the Clinic for Dermatology at the University of Würzburg in the group of Prof. Dr. Peter Friedl. Together with the lab she moved to the Radboud University Nijmegen, The Netherlands, in 2008 and joined the Department of Cell Biology in the Radboud Institute of Molecular Life Sciences where she completed her experimental PhD thesis work with the title “Cytotoxic T cell functions in solid tumors: principles and implications for immunotherapy”. Following the PhD project, in 2012 she continued as PostDoc in the same department, concentrating on understanding the cellular dynamics of cancer invasion, metastasis and anti-cancer immune responses within the tumor microenvironment by visualizing cellular functions within live tissues using multiphoton microscopy. Her work was presented on numerous national and international conferences including presentations as invited speaker. Beginning of 2016 she will move to the MD Anderson Cancer Center, USA, to establish novel strategies to target prostate cancer bone metastasis with immunotherapy.

List of Publications

- Friedl P & **Weigelin B**. Interstitial leukocyte migration and immune function. **Nat Immunol** 2008; 9:960–9.
- Weigelin B** & Friedl P. A three-dimensional organotypic assay to measure target cell killing by cytotoxic T lymphocytes. **Biochem Pharmacol** 2010; 80:2087–91.
- Hagemann C, **Weigelin B**, Schommer S, Schulze M, Al-Jomah N, Anacker J, Gerngas S, Kühnel S, Kessler A F, Polat B, Ernestus RI, Patel R & Vince G H. The cohesin-interacting protein, precocious dissociation of sisters 5A/sister chromatid cohesion protein 112, is up-regulated in human astrocytic tumors. **Int J Mol Med** 2011; 27:39–51.
- Weigelin B**, Krause M & Friedl P. Cytotoxic T lymphocyte migration and effector function in the tumor microenvironment. **Immunol Lett** 2011; 138:19–21.
- Weigelin B**, Bakker GJ & Friedl P. Intravital third harmonic generation microscopy of collective melanoma cell invasion: Principles of interface guidance and microvesicle dynamics. **IntraVital** 2012; 1:9–20. Cover story of 1st edition.
- Bonetto F, Srinivas M, **Weigelin B**, Cruz LJ, Heerschap A, Friedl P, Figdor CG & De Vries IJ M. A large-scale (19) F MRI-based cell migration assay to optimize cell therapy. **NMR Biomed** 2012; 25:1095–103.
- Alexander S, **Weigelin B**, Winkler F & Friedl P. Preclinical intravital microscopy of the tumour-stroma interface: invasion, metastasis, and therapy response. **Curr Opin Cell Biol** 2013; 25(5):659-71.
- Cruz LJ, Tacke PJ, Zeelenberg IS, Srinivas M, Bonetto F, **Weigelin B**, Eich C, de Vries IJ & Figdor CG. Tracking targeted bimodal nanovaccines: immune responses and routing in cells, tissue, and whole organism. **Mol Pharm** 2014; 11(12):4299-313.
- Friedl P & **Weigelin B**. A Swiss army knife for CTL. **Immunity** 2014; 41(6), 873–5.
- Weigelin B***, Bolaños-Mateo E*, Teijeira A, Martínez-Forero I, Labiano S, Azpilicueta A, Morales-Kastresana A, Quetglas JI, Wagena E, Rodríguez A, Chen L, Friedl P⁺ & Melero I⁺. Focussing and sustaining the antitumor CTL effector killer response by agonist anti-CD137 mAb. (*⁺contributed equally). **Proc Natl Acad Sci USA** 2015; 112(24): 7551–7556.
- Weigelin B**, Bakker GJ & Friedl P. Third harmonic generation microscopy for label-free imaging of tissues. **J Cell Sci**. Accepted.

IN REVISION, SUBMITTED OR IN PREPARATION:

Weigelin B, den Boer A, Wagena E, Broen K, de Boer R, Dolstra H, Figdor CG, Textor J, & Friedl P. Cancer cell elimination requires cytotoxic T cell cooperation. **In revision.**

Schmidt S, **Weigelin B**, te Riet J, Lelli B, Rognoni L, Messent AJ, Mayer U, Marlow R, Eble J, Bröcker EB, Humphries MJ, Gottschalk KE & Friedl P. Integrin-independent glyocalyx-mediated amoeboid modes of cell migration. **In revision.**

Hude S, **Weigelin B**, Wolf K, Wilk G, Tretiakov KV, Iwasa M, Banaszak M, Soh S, Pilans D, Makurath M, Friedl P, Borisy GG, Kandere-Grzybowska K & Grzybowski BA. Predatory, Lévy walks of metastatic cancer cells and their reprogramming into benign, diffusive migrations. **Submitted.**

Weigelin B, de Beer M, Fransen J, Häger A, Bakker GJ & Friedl P. Guided cell migration along tissue highways. **In preparation.**

Weigelin B, Wagena E & Friedl P. Proliferation induced cell jamming induces collective tumor cell migration. **In preparation.**